

**Microgel Iron Oxide Nanoparticles for
Tracking of Stem Cells through
Magnetic Resonance Imaging**

Eddy Shoo Ming LEE

**A thesis submitted for the degree of
Doctor of Philosophy**

National University of Singapore

Abstract

Stem cell therapy is an emerging field of regenerative medicine that has the potential to treat diseases by transplanting therapeutic cells to replace or support the repair of damaged host cells. An important step of the therapeutic success is the homing of transplanted cells to the desired site. Magnetic resonance imaging (MRI), coupled with cellular markers, offers a non-invasive method of following the fate of cell transplants during the therapeutic period. However, clinically and commercially-available markers do not offer sufficient image contrast for the detection of small groups of cells. The aim of this thesis is to investigate the development of particulate cellular markers that will improve the tracking of stem cells in an animal model through MRI.

Current markers for cellular labelling are composite, magnetic particles that measure less than 100 nm or greater than 1 micron in diameter. As the intermediate range has not been investigated, microgel iron oxide particles (MGIO) with the diameters of 89 to 765nm were synthesised and characterised in terms of their physical properties. The magnetic resonance relaxation characteristics of MGIO were measured and shown to largely agree with the values predicted by theoretical models.

The efficiency of MGIO was tested on human fetal mesenchymal stem cells (fMSC). With simple incubation, MGIO provided equal or better uptake in fMSC compared to a clinical particle, ferucarbotran, with MGIO-600nm achieving three-fold higher uptake. Labelled fMSC was characterised in terms of proliferation rate, multilineage differentiation capacity and global gene expression to show that labelling with MGIO does not affect stem cell functions. To further verify the safety of MGIO, human

endothelial progenitor cells were labelled and shown to retain phenotype and function after labelling.

A rat stroke injury model was developed to observe cellular migration. Labelled-fMSC was transplanted intracerebrally or intravenously and shown via MRI to home to the injury site. MGIO labelling provided superior detection of cells compared to ferucarbotran labelling. Histological analysis showed that MRI reliably detected the location of fMSC for up to 5 days post-transplantation after which fMSC were rejected by the host due to the nature of the animal model used. This study shows that MGIO is an efficient label that enables improved detection of transplanted cells during *in vivo* imaging.

In all, this thesis describes the development of a high contrast MRI cellular label with superior performance over commercially-available iron particles, with possible applications for *in vivo* tracking of transplanted stem cells.

Acknowledgements

This thesis has been funded by the Singapore Bio-Imaging Consortium (SBIC) of the Agency for Science, Technology and Research (A*STAR).

First of all, I would like thank Professor Wang Shih-chang and Professor Teoh Swee Hin for their supervision and guidance throughout this study. I would like express special gratitude to Dr Jerry Chan for his tireless inspiration, patience and hands-on approach to the guidance of this thesis.

The overseas collaborators of this study, Professor André Briguet, Dr Olivier Beuf and Dr Claire Billotey deserve special mention for the training in animal imaging I received at their facilities in Lyon, France. I am grateful to A/Prof Mahesh Choolani for sharing his wealth of experience in experimental design and analysis. I would also like to thank Professor Michael Tam for his advice on chemical synthesis and Dr Borys Shuter for the hours we spent discussing about imaging physics and A/Prof Ding Jun his advice in material science.

I would like to thank my colleagues Lay Geok, Mark, Zhiyong, Yiping, Durrghah and Brenda for their technical support and their company during the darkest hours of experimentation. I am also indebted to Wai Leng, Serena, Ginny and Pascale for their administrative support and Mathieu for the French translation of the abstract.

I would like to thank my family – my parents Lawrence and Florence Lee, and sister Alicia Lee for their support of this endeavour. Most of all, I would like to thank my wife, Debbie for her love, patience and presence, and God for this opportunity in life.

Table of Content

Abstract	1
Acknowledgements	3
Table of Content	4
List of Figures	8
List of Tables	14
Abbreviations	16
Chapter 1 Introduction	18
1.1 Stem Cell Therapy.....	19
1.2 Mesenchymal Stem Cells	23
1.2.1 Origin of MSC	23
1.2.2 MSC Sources	25
1.2.3 MSC Characteristics	26
1.2.4 Homing and Migration.....	31
1.2.5 Engraftment.....	33
1.2.6 Clinical trials of MSC Therapy.....	42
1.3 Monitoring of Cell Therapy	49
1.3.1 Histological Methods.....	49
1.3.2 <i>In vivo</i> Imaging Modalities	51
1.4 MR Contrast	54
1.4.1 T2* Relaxation	55
1.4.2 T2 Relaxation.....	56
1.4.3 Contrast agents.....	58
1.4.4 Theoretical Relaxation Induced by Homogenous Magnetised Spheres	60
1.5 Iron Oxide Particles.....	67
1.5.1 Iron Oxide Particle Synthesis.....	67
1.5.2 Encapsulation of Iron Oxide Particles	68
1.5.3 Particle Size Measurement by Light Scattering.....	70
1.6 Cellular MRI	74
1.6.1 MRI in Tissue Engineering.....	74
1.6.2 MRI in Cellular Transplantation.....	75
1.6.3 MRI in Homing and Migration Studies	75
1.6.4 Clinical Trial of Cellular MRI	76
1.6.5 Cellular Imaging with Iron Oxide Particles	77
1.6.6 Mechanisms of Cellular Uptake.....	82

1.6.7 Controlling Cellular Uptake of Particles.....	89
1.6.8 Transgenic Methods.....	97
1.6.9 Challenges of Cellular MRI.....	100
1.7 Summary.....	105
1.7.1 Hypothesis.....	106
Chapter 2 Methods	107
2.1 Synthesis of Particles.....	108
2.1.1 Synthesis of Precursor Migrogel.....	108
2.1.2 Synthesis of MGIO.....	111
2.2 MGIO Characterisation.....	114
2.2.1 Transmission Electron Microscopy.....	114
2.2.2 Thermogravimetric Analysis.....	114
2.2.3 Vibrating Sample Magnetometry.....	115
2.2.4 SQUID Magnetization.....	115
2.2.5 Dynamic Light Scattering.....	116
2.2.6 MR Relaxation Rate.....	117
2.3 Ethics and samples.....	119
2.4 fMSC isolation and differentiation.....	119
2.5 EPC Isolation.....	120
2.6 EPC Immunostaining.....	121
2.7 Cellular labelling protocol and iron quantification.....	122
2.8 Iron Quantification.....	123
2.9 Cellular TEM.....	124
2.10 Genome wide Microarray Expression Analysis.....	125
2.10.1 RNA Extraction.....	125
2.10.2 Characterisation of RNA Purity.....	125
2.10.3 Analysis of Microarray Data.....	129
2.11 <i>In vivo</i> imaging.....	131
2.11.1 Cellular Migration Stroke Model.....	131
2.11.2 Transplantation of fMSC.....	134
2.11.3 MRI.....	136
2.11.4 Histology.....	137
2.12 Statistics.....	138
Chapter 3 Results I: MGIO Synthesis and Characterisation	139
3.1 Synthesis of PMG.....	141
3.2 Synthesis of MGIO.....	142
3.3 Characterisation of MGIO.....	143

3.3.1 Transmission Electron Microscopy	143
3.3.2 Thermogravimetric Analysis	145
3.3.3 Vibrating Sample Magnetometry.....	153
3.3.4 SQUID	157
3.3.5 Dynamic Light Scattering.....	160
3.3.6 Relaxation	167
3.4 Discussion	174
Chapter 4 Results II: Labelling of Stem Cells.....	176
4.1 Isolation and Characerisation of fMSC.....	178
4.2 Uptake of MGIO by fMSC	179
4.3 Proliferation of Labelled fMSC	183
4.4 Multi-Lineage Differentiation of Labelled fMSC.....	185
4.5 Microarray Analysis of Labelled fMSC.....	187
4.5.1 Development and Analysis of Microarray Data	187
4.6 Uptake of MGIO by EPC.....	203
4.7 Function of Labelled EPC.....	204
4.8 Discussion	207
Chapter 5 Results III: MR Tracking of MGIO-fMSC.....	211
5.1 Cellular Migration Stroke Model.....	213
5.1.1 Internal and Middle Cerebral Artery Occlusion	213
5.1.2 Photochemical Cerebral Thrombosis.....	214
5.2 Tracking fMSC in Stroke Animals	215
5.3 Histology.....	220
5.4 Discussion	231
Chapter 6 General Discussion.....	233
6.1 Hypothesis.....	234
6.2 Summary of Findings.....	235
6.3 Limitations	236
6.4 Future Directions for Research	239
6.5 Conclusion.....	241
Chapter 7 Appendix.....	242
7.1 List of Overexpressed genes	243
7.1.1 M600-Labeling Up-Regulated Genes (Top 50).....	243
7.1.2 M600-Labeling Down-regulated Genes (Top 50)	244
7.1.3 Ferucarbotran-Labeling Up-regulated Genes	245
7.1.4 Ferucarbotran-Labeling Down-regulated Genes.....	246

7.2 Record of Experimental Animals.....247

7.3 Publications249

References251

List of Figures

- Figure 1: General differentiation potential of pluripotent embryonic stem cells and multipotent adult stem cells. The pluripotent embryonic stem cells from the inner cell mass can differentiate into any cell in the body. In comparison, the multipotent stem cells from various adult tissues are committed but can still differentiate into multiple cell types. 22
- Figure 2: Mesenchymal stem cells (MSCs) differentiation is multistep, involving committal development of cells towards a particular lineage. They have the potential to differentiate into various tissue including bone, cartilage, muscle, marrow stroma, tendon/ligament, fats, and other connective tissues. (Caplan, 2005). 29
- Figure 3: Various modalities of cellular imaging adapted from Arbab et al (Arbab, 2008). CEST: Chemical exchange-dependent Saturation Transfer, CT: computer tomography, PET: positron emission tomography, SPECT: single photon emission computed tomography, mAb: antibodies, IM: intravital microscopy, FRI: fluorescence reflectance imaging, BLI: bioluminescence imaging, US: ultrasound. Sensitivity: the minimum number of cells detectable. Reporter gene: whether transgenic cells can carry a reporter gene that generates contrast. 53
- Figure 4: A plot of the transverse magnetization decaying at a rate of $1/T_2^*$ rate. If a refocusing pulse is applied at an interval of τ , the signal reaches another maxima at time $2\tau = TE$ (Haacke, 1999). 56
- Figure 5: Applying multiple, regularly spaced refocusing pulse at $(2n-1)\tau$ and acquiring signals at $2n\tau$, where n is 1, 2, 3, (Haacke, 1999). 57
- Figure 6: Relaxation rate dependence on particle diameter, d 61
- Figure 7: Illustration of scattering of the incident beam and detection of the scattered beam. 71
- Figure 8: Possible pathways of cellular uptake of nanoparticles. Uptake of particles can occur through phagocytosis (1), macropinocytosis (2), clathrin-mediated endocytosis (3), non-clathrin-, non-caveolae-mediated endocytosis (4), caveolae-mediated endocytosis (5) or diffusion (6). (Unfried, 2007). 83
- Figure 9: Pinocytosis. This process, as known as ‘cell-drinking’ or fluid-phase endocytosis, internalizes particles in uncoated intracellular vesicles called pinosomes. The pinocytosis of larger particles may be called macropinocytosis and the resulting vesicles are known as macropinosomes. 85
- Figure 10. TEM of Formation of Clathrin Pits. The micrographs shows the sequence of extracellular debris internalization via clathrin-mediated endocytosis. The event is initiated by (a) induction of membrane curvature, followed by (b) formation of coated pits and membrane invagination, (c) constriction and fission and finally the containment of debris in clathrin-coated vesicle. Following these events, the vesicle fuses with early endosome that can mature into late endosome and lysosome (Perry, 1979). 87
- Figure 11. TEM of Caveolae invaginations. Caveolae are flask-shaped plasma invaginations. After internalization, caveolae-driven vesicles travel to caveosomes, which are distinct from endosomes in content and pH. Thereafter, caveosome content is sorted to the Golgi complex or the endoplasmic reticulum (Rothberg, 1992). 87
- Figure 12: Uptake of polystyrene (open symbols) and phenylated polyacrolein (closed symbols) particles in absence of serum (greater uptake) and 10% serum (lesser uptake), showing maximal uptake within a range of sizes (Tabata, 1988). 92
- Figure 13 Schematic of PMG. The molar ratio of methacrylic acid (MAA) and ethyl acrylate (EA), and the wt% of crosslinker di-allyl phthalate (DAP) are represented by x , y and z respectively. 110

Figure 14: Electrogram showing crisp 28S and 18S bands.....	127
Figure 15: Procedures of stroke induction by photochemical thrombosis. (a) Animal is mounted on a stereotatic frame and skull was exposed. (b) Through a 3mm aperture, green-filtered white light was applied to the skull while Rose Bengal was injected via a tail vein cannula.....	133
Figure 16: Animals is mounted on a stereotaxic frame and (a) a 1mm burr hole was made to expose the dura and (b) the Hamilton syringe was lowered and cells were injected slowly over a 10 min period.....	135
Figure 17: (a-e) Transmission micrographs of M600 air-dried on copper grid. (a-c) MGIO are spherical particles that are 50-70nm when dried. The primary iron oxide (PIO) nanoparticles, being more electron dense than the polymer matrix of PMG, appear as dark spots in each MGIO. (d-e) High magnification images show that the PIO are 2-5nm each. (f) Selected area electron diffraction of a single MGIO particle showing interplanar pattern typical of composite particle containing magnetite.....	144
Figure 18: Transmission micrographs of ferucarbotran air-dried on copper grid. (a) Dried ferucarbotran are about 50nm in diameters, they appear spherical but aggregated when dried. (b) 3 individual particles of ferucarbotran that have diameters 40-60nm and they contain PIO, just like MGIO.....	145
Figure 19 Schematics of anhydrite formation during PMG degradation. (a) Between two MAA neighbours, an ethanol molecule is removed. (a) Between a neighbouring MAA and EA, a water molecule is removed.....	146
Figure 20: Thermogram of M100. Weight % curve (green) shows that the sample weight was decreased from 100% at room temperature to 97% after evaporation of absorbed water and further decreased to 74% at 850°C. The first minimum of the derivative weight (blue) was taken as the temperature where absorbed water had been removed.....	148
Figure 21: Thermogram of M150. Weight % curve (green) shows that the sample weight was decreased from 100% at room temperature to 97% after evaporation of absorbed water at the first minimum of the derivative weight (blue) and further decreased to 80% at 850°C.	148
Figure 22: Thermogram of M250. Weight % curve (green) shows that the sample weight was decreased from 100% at room temperature to 97% after evaporation of absorbed water at the first minimum of the derivative weight (blue) and further decreased to 45% at 850°C.	149
Figure 23: Thermogram of M300. Weight % curve (green) shows that the sample weight was decreased from 100% at room temperature to 97% after evaporation of absorbed water at the first minimum of the derivative weight (blue) and further decreased to 65% at 850°C.	149
Figure 24: Thermogram of M400. Weight % curve (green) shows that the sample weight was decreased from 100% at room temperature to 97% after evaporation of absorbed water at the first minimum of the derivative weight (blue) and further decreased to 64% at 850°C.	150
Figure 25: Thermogram of M500. Weight % curve (green) shows that the sample weight was decreased from 100% at room temperature to 97% after evaporation of absorbed water at the first minimum of the derivative weight (blue) and further decreased to 62% at 850°C.	150
Figure 26: Thermogram of M600. Weight % curve (green) shows that the sample weight was decreased from 100% at room temperature to 94% after evaporation of absorbed water at the first minimum of the derivative weight (blue) and further decreased to 36% at 850°C.	151
Figure 27: Thermogram of M750. Weight % curve (green) shows that the sample weight was decreased from 100% at room temperature to 96% after evaporation of absorbed water at the first minimum of the derivative weight (blue) and further decreased to 33% at 850°C.	151

Figure 28: Magnetization curves for M400 to M750 measured by VSM. (a-e) Magnetization was measured while the samples were subjected to a static field that was varied stepwise from 10^3 to -10^3 G. (f) Magnification of the origin when curves of M400 to M750 are superimposed show a small amount of hysteresis.	155
Figure 29: Average magnetization of M400 to M750. (a) By superimposing the magnetization curves, the average magnetization (b) at each field strength can be obtained and plotted.	156
Figure 30: ZFC/FC of lyophilised M600 from 0 to 320K. The two curves did not intersect at temperatures below 300K, hence the blocking temperature is above 300K. The blocking temperature is probably slightly above 320K as the curves were almost intersecting at 320K.	157
Figure 31: ZFC/FC of aqueous M600. The results were similar to those with lyophilized sample. The curves were nearly intersecting at 320K, indicating that the blocking temperature was not much further.	158
Figure 32: DLS plots of ferucarbotran and M100 to M750. All particles had unimodal size distributions. The peak of each distribution curve was taken as the mean hydrated diameter.	161
Figure 33: DLS distribution curves of Ferucarbutran from repeated measurements of one sample.....	163
Figure 34: DLS distribution curves of M100 from repeated measurements of one sample.....	163
Figure 35: DLS distribution curves of M150 from repeated measurements of one sample.....	164
Figure 36: DLS distribution curves of M250 from repeated measurements of one sample.....	164
Figure 37: DLS distribution curves of M300 from repeated measurements of one sample.....	165
Figure 38: DLS distribution curves of M400 from repeated measurements of one sample.....	165
Figure 39: DLS distribution curves of M600 from repeated measurements of one sample.....	166
Figure 40: DLS distribution curves of M750 from repeated measurements of one sample.....	166
Figure 41: Example of a plot of relaxation rates against concentration to determine relaxivity. The gradient of CPMG relaxation rates and GRE relaxation rates corresponded to relaxivity r_2 and r_2^* , respectively.	167
Figure 42: Relaxation rates of particles at 0.1mM Fe. R_2^* increased with diameter and reaches a plateau at M250. R_2 is the same as R_2^* but as diameters increased beyond M250, R_2 decreased.....	168
Figure 43: Comparison of relaxation rates to distinct regimes theory of motional averaging (MAR), static dephasing (SDR) and echo limited regime (ELR). Measurement fit the theoretical models in general.....	169
Figure 44: Comparison of Muller's simulation, distinct regime and continuous theory. Muller's simulated relaxation rates fit both theories better than the measurements of MGIO.	171
Figure 45: Representative sketch of composite particles such as MGIO that consist of multiple primary iron oxide nanoparticle cores (PIO) held together by a polymer matrix like microgel. Each composite particle is equivalent to one with a single homogenous core with diameter d_{mag} . (a) For large MGIO, the diameter determined by dynamic light scattering (d_{DLS}) approximates d_{mag} . (b) For ferucarbotran or small MGIO, d_{DLS} and d_{mag} deviates.....	172
Figure 46: (a) Light micrograph of M600-labelled fMSC with iron stained with Prussian Blue. (b) TEM of labelled fMSC with insert showing MGIO in double-walled membrane organelle.....	179

Figure 47: Micrographs of (a) M600, (b) mock and (c) ferucarbotran-labelled fMSC on a haemocytometer show that labeled cells are separated and their sizes in suspension remain 15-25 μm in diameter, as indicated by the lines of the (d) Neubauer haemocytometer, regardless of labelling. 180

Figure 48: Intracellular iron mass when labelled with different particles showed a particle size-dependent quantity of uptake. All MGIO sizes showed the same or higher uptake than ferucarbotran with M600 providing the highest uptake. 181

Figure 49: Intracellular iron as a function of labelling concentration. As iron concentration in the labeling medium was increased, the iron loading of the cells were increased and the difference in loading between ferucarbotran and M600 became more significant. 182

Figure 50: Retention of intracellular iron over 3 passages. Individual points indicate the quantity of iron at each particular population doubling. Lines are one-phase decay fits to each particle to show that intracellular iron was approximately halved each time a cell divided with R^2 showing goodness of fit. 183

Figure 51: Population doublings at each passage. The number of population doubling at each of the three passages post-labelling were not affected by the particles used. 184

Figure 52: Cell viability at each passage. The effect of labelling on the cell viability, as assessed by Trypan blue exclusion assay, was insignificant for three passages post-labelling. 184

Figure 53: Trilineage differentiation of fMSC post-labelling. Labelling with either ferucarbotran or M600 did not affect the multipotent capacity of fMSC as shown by their differentiation into osteoblasts (black extracellular crystals by von Kossa staining), adipocytes (oil red O staining) or chondrocytes (micromass pellet cultures were stained red by Safranin O and blue by Alcian blue). 186

Figure 54: Scatter plot showing the 1504 M600-labelled probes that had significant difference in expression compared to the mock-labelled counterparts. Out of these probes, 114 were more than 2-fold upregulated and 102 were more than 2-fold downregulated. 189

Figure 55: Scatter plot showing the 895 ferucarbotran-labelled probes that had significant difference in expression compared to the mock-labelled counterparts. Out of these probes, 32 were more than 2-fold upregulated and 29 were more than 2-fold downregulated. 189

Figure 56: Heatmaps of 114 upregulated (left) and 102 downregulated (right) probes due to M600-labelling. Ferucarbotran-labelling resulted in the upregulation and downregulation of the same genes, except for the group circled blue and yellow. 190

Figure 57: Heatmaps of 32 upregulated (left) and 29 downregulated (right) probes due to ferucarbotran-labelling. M600-labelling resulted in the upregulation of the same genes, except for the group circled blue. M600-labelling resulted in the downregulation of the same genes (circled in yellow) except the the uncircled group. 191

Figure 58: Staining of (a) intracellular iron by Prussian blue and (b-d) cellular function of mock, M600 and ferucarbotran –labelled EPC. Labelled EPC retained the capacity to (b) form tubes, (c) take up Dii-acLDL and (d) be stained for vWF. 205

Figure 59: Staining of mock, M600 and ferucarbotran-labelled cells for endothelial phenotypic surface markers. Labelled EPC retained the expression of (a) CD144 and (b) CD31. 206

Figure 60: Consecutive 2mm brain sections of rats with photo-thrombotic stroke were stained by TTC. Mitochondria activity is stained red while the infarct region remains colourless. 214

Figure 61: Comparison of (a) TTC stain and (b) T2-weighted MR image of the approximate section shows that TTC can reliably verify infarct extent 214

Figure 62: *In vivo* imaging with turbo spin echo (TSE, Day -1) and gradient echo sequence (GRE, Day -1 through Day 12). A focal cortical stroke (yellow arrows) was induced at Day -2 and cellular transplantation took place on Day 0 by contralateral intracerebral (green arrows) or systemic injection (IV) (a) An area of hypointensity appeared in the area of the stroke (red arrows) noticeable at Day 5, and increased over time to Day 12 in M600-fMSC injected animals. (b) A similar observation was made in Ferucarbotran-fMSC injected animals, albeit with a smaller area of hypointensity seen. (c) Animals injected with M600-fMSC intravenously showed appearance of hypointensity in the stroke region by Day 5, which increased over time to Day 12. (d) In comparison, there was no hypointensity at the contralateral cerebral cortex where no stroke injury had been induced. 216

Figure 63: *In vivo* imaging with SSFP sequence. The images are of the same animals and were taken immediately after those in Figure 62. A focal cortical stroke (yellow arrows) was induced at Day -2 and cellular transplantation took place on Day 0 by contralateral intracerebral (green arrows) or systemic injection (IV) (a) An area of hypointensity appeared in the area of the stroke (red arrows) noticeable at Day 5, and increased over time to Day 12 in M600-fMSC injected animals. (b) A similar observation was made in Ferucarbotran-fMSC injected animals, albeit with a smaller area of hypointensity seen. (c) Animals injected with M600-fMSC intravenously showed appearance of hypointensity in the stroke region by Day 5, which increased over time to Day 12. (d) In comparison, there was no hypointensity at the contralateral cerebral cortex where no stroke injury had been induced. 219

Figure 64: Immunohistological analysis of animals transplanted with 2×10^4 M600-fMSC on Day 1. (a-c) Prussian blue/haematoxylin-eosin staining demonstrated iron-laden cells at the injection site, but not the stroke site. (d-f) Immunohistochemical staining of adjacent sections showed these to be mainly human vimentin-positive fMSC (green), infiltrated by ED1-positive rat macrophages (red). (g-h) Examination of the stroke area demonstrates presence of ED1-positive cells and no vimentin-positive fMSC. Nuclei were stained with DAPI (blue). 221

Figure 65: Immunohistological analysis of animals transplanted with 2×10^4 M600-fMSC on Day 5. By Day 5, (a-c) the presence of iron-laden cells can be seen at the stroke site through DAB enhancement of Prussian blue staining (brown, b-c). (d-f) Immunohistological staining of adjacent sections showed the presence of fMSC (green vimentin positive cells, f, z-stacked confocal) surrounded with ED1-positive macrophages at the stroke site. 222

Figure 66: Immunohistological analysis of animals transplanted with 2×10^4 M600-fMSC on Day 12. By Day 12, Prussian blue staining demonstrated increased iron-laden cells at the stroke site (a-c), which were exclusively ED1-positive when stained for both ED1 and human vimentin on adjacent sections (d-e). Both vimentin-positive and ED1-positive cells were found in the injection site (f). 223

Figure 67: Immunohistological analysis of animals transplanted with 2×10^4 ferucarbotran-fMSC on Day 12. (a-c) Prussian blue/haematoxylin-eosin staining demonstrated a large number of iron-laden cells at the stroke site. (d-e) Immunohistochemical staining of adjacent sections at the stroke site revealed a large infiltrate of ED1 positive cells with no human-vimentin positive fMSC seen at the stroke site. Nuclei were stained with DAPI (blue). 225

Figure 68: Immunohistological analysis of animals transplanted with 2×10^6 M600-fMSC by tail vein injection on Day 19. (a-c) Prussian blue/haematoxylin-eosin staining demonstrated iron-laden cells at the stroke site. (d-f) Immunohistochemical staining of adjacent sections revealed that these cells to be ED1 positive macrophages. There were no human vimentin positive fMSC cells seen at the stroke area. Nuclei were stained with DAPI (blue). 226

Figure 69: Immunohistological analysis of animals transplanted with 2×10^4 mock-labelled-fMSC at Day 12. (a-c) Prussian blue/haematoxylin-eosin staining demonstrated absence of iron-laden cells at the injection and stroke site. (d-e) Immunohistochemical staining of adjacent sections revealed infiltration of ED1 positive cells with a few human vimentin-positive fMSC (green) at the (d) injection site but not the (e) stroke site. Nuclei were stained with DAPI (blue). 227

Figure 70: Immunohistological analysis of animals without stroke but transplanted with 2×10^4 M600-fMSC on Day 19. (a-b) Prussian blue/haematoxylin-eosin staining demonstrated iron-laden cells at the injection site, but not the contralateral site. (c-e) Immunohistochemical staining of adjacent sections

showed infiltration of ED1-positive rat macrophages (red) and presence of human vimentin-positive fMSC (green) at the injection area. (g-h) Magnified images shows many ED1-positive cells and only few vimentin-positive fMSC. Nuclei were stained with DAPI (blue). 228

Figure 71: Histological sections on Day 12 of animal with stroke induced but no injection. (a-c) No iron-laden cells were found at the Prussian blue/haematoxylin-eosin staining. (d-e) Immunohistochemical staining of adjacent sections shows infiltration of ED1-positive rat macrophages (red) but no human vimentin-positive fMSC (green) at the stroke area. (e) Magnification of the stroke area shows many ED1-positive cells and and no vimentin-positive fMSC. Nuclei were stained with DAPI (blue). 229

Figure 72: Immunohistochemical analysis of various animals with stroke induced and transplanted with 2×10^4 M600-fMSC and sacrificed at Day 1, 5 or 12. Sections, adjacent those shown in Figure 64 to Figure 66, demonstrate progressive increase of CD8 (green) cytotoxic T cell in stroke site from Day 1 to 12 but only negligible change of CD8+ cells in the injection site, suggesting that an adapted immune response was mounted against the stroke site only but not the injection site. 230

List of Tables

Table 1: Immunophenotype of human fetal MSC (O'Donoghue, 2006). + Positive, - Negative, ± Weakly Positive or Low Expression.....	28
Table 2: Molecules responsible for MSC migration. Adhesion molecules mediate MSC transendothelial migration. Once in the perivascular space, chemokine receptors direct MSC migration along chemokine gradients and metalloproteinases breakdown ECM while MSC migrates.....	33
Table 3: Clinical trials for cardiac diseases adapted from Rosenzweig et al. Overall results of trials show that bone marrow cell infusion may improve cardiac function but the effect may not be permanent (Rosenzweig, 2006).....	45
Table 4: Masses of reagents required to form six models of precursor microgel particles (PMG) of different sizes by altering the micellar and MAA to EA ratios.....	110
Table 5: Masses of reagents and the PMG models required to synthesize MGIO of approximately 100 to 750nm as denoted by models M100 to M750.....	112
Table 6: Characteristics of total RNA obtained from labelled cells in triplicates.....	126
Table 7: Iron oxide content of various MGIO models expressed in terms of weight % (IOwt%).....	152
Table 8: Magnetization measurements determined by VSM. M10kOe is the magnetization when field strength is 10^3 G; M_s is the saturation magnetization when field $\rightarrow \infty$; M_r is the remnant magnetization and H_c is the coercivity.....	156
Table 9: Hydrated diameter of particles expressed as mean \pm SEM.....	162
Table 10: Matching genes (column List 1) upregulated by M600 labelling to associated GO terms at various hierarchical levels and comparing the match with other genes in the genome (column Genome).....	193
Table 11: Significant GO terms that are associated with the upregulation of 114 genes due to M600-labelling.....	194
Table 12: Matching genes (column List 1) downregulated by M600 labelling to associated GO terms at various hierarchical levels and comparing the match with other genes in the genome (column Genome).....	195
Table 13: Significant GO biological process terms that are associated with downregulation of 102 genes due to M600-labelling.....	197
Table 14: Significant GO biological process and molecular function terms that are associated with downregulation of 102 genes by M600-labelling.....	198
Table 15: Matching genes (column List 1) upregulated by ferucarbotran labelling to associated GO terms at various hierarchical levels and comparing the match with other genes in the genome (column Genome).....	199
Table 16: Significant GO terms that are associated with upregulation of 32 genes due to ferucarbotran-labelling.....	200
Table 17: Matching genes (column List 1) downregulated by ferucarbotran labelling to associated GO terms at various hierarchical levels and comparing the match with other genes in the genome (column Genome).....	200

Table 18: Significant GO terms are associated with downregulation of 29 genes due to ferucarbotran-labelling201

Table 19: Record of experimental animals used in our study classified by the experimental groups. .248

Abbreviations

AMNP	Anionic magnetic nanoparticle (30nm)
APC	Antigen presenting cells
BBB	Blood brain barrier
BMC	Bone marrow cells
BMT	Bone marrow transplantation
cDNA	Complementary deoxyribonucleic acid
CM10	Culture medium with 10% fetal bovine serum
CNS	Central nervous system
CPMG	Carr-Purcell-Meiboom-Gill sequence
CyA	Cyclosporin A
DAP	Di-allyl phthalate
DLS	Dynamic light scattering
EA	Ethyl acrylate
ED1	Cytoplasmic marker for rat macrophages/microglia
ELR	Echo limited regime
EPC	Endothelial progenitor cells
ESC	Embryonic stem cells
FC	Field cooled magnetization curve
FISH	Fluorescent <i>in situ</i> hybridisation
GFP	Green fluorescent protein
GRE	Gradient echo pulse sequence
fMSC	Human fetal mesenchymal stem cells
HLA	Human Leukocyte Antigen
HSC	Haematopoietic stem cells
ICP	Inductively coupled plasma
MAA	Methacrylic acid
MAR	Motional averagering regime

MGIO	Microgel iron oxide particles
MHC	Major histocompatibility complex
MION	Monocrystalline iron oxide nanoparticle
MNC	Mononuclear cells
MMP	Metalloproteinases
MRI	Magnetic resonance imaging
MSC	Mesenchymal stem cells
PB	Prussian blue
PIO	Primary iron oxide nanoparticle cores
PMG	Precursor microgel particles
RME	Receptor mediated endocytosis
RNA	Ribonucleic acid
SDR	Static dephasing regime
SPIO	Superparamagnetic iron oxide nanoparticle
TEM	Transmission electron microscopy
TGA	Thermogravimetric analysis
TTC	2,3,5-triphenyltetrazolium
USPIO	Ultrasmall SPIO
VIM	Human vimentin
VSOP	Very small iron oxide particle (8nm)
ZFC	Zero field cooled magnetization curve

Chapter 1 Introduction

1.1 Stem Cell Therapy

Stem cell therapy is a rapidly emerging field of regenerative medicine where transplanted stem cells either directly replace or ameliorate the repair of damaged host tissue. Several clinical trials are already in progress for the treatment of various diseases, such as ischemic stroke (Bang, 2005), skeletal dysplasia (Horwitz, 2001), spinal cord injury (Callera, 2007) and myocardial infarction (Meyer, 2006). The complexities and complete mechanisms by which cell-based therapies work need not be fully understood to be used clinically. Instead, the key determinants for the use of such therapies are safety and efficacy.

The first attempt of cellular transplantation in the literature was performed by W.G. Thompson in the late nineteenth century. When allogeneic neocortex from a dog was transplanted to another dog, the tissue showed “vitality to survive for seven weeks the operation of transplantation without wholly losing its identity as brain substance” (Thompson, 1890; Chen, 2008). Since that report, a myriad of transplantation strategies have been performed in both humans and experimental animals, with little understanding of the biology of the graft at times. Today, bone marrow transplantation (BMT) has been used successfully for many years to treat leukaemia and other haematological malignancies, and clinical trials using autologous and even allogeneic stem cell transplantation therapies are being run concurrently with laboratory efforts to better understand stem cell biology.

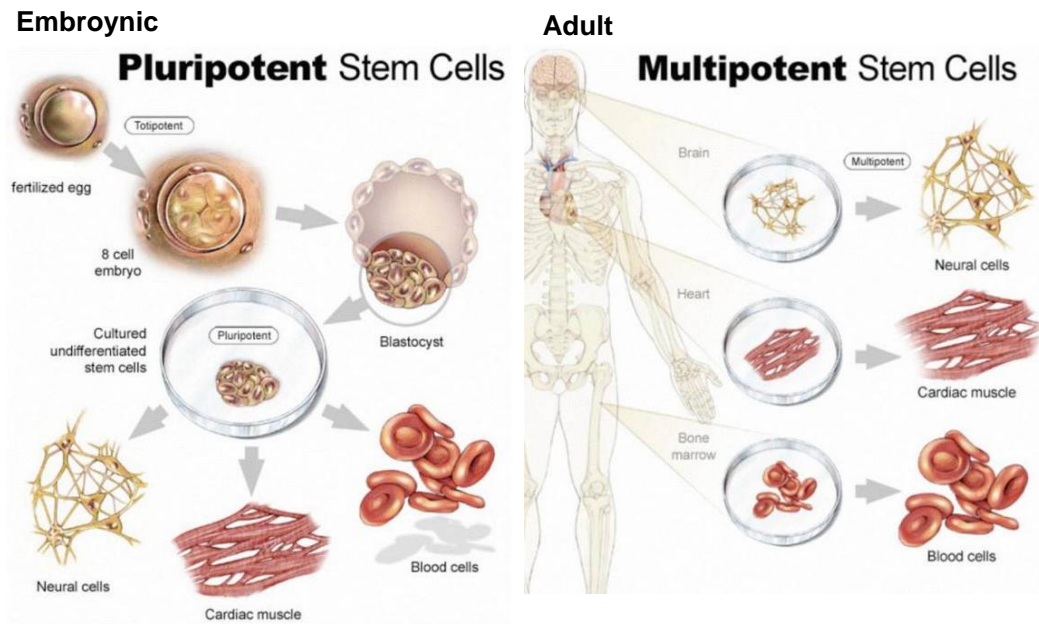
Stem cells are immature cells that possess the ability of self-renewal and differentiation into various cell types. These cells can be broadly classified into three categories based on their capacity for differentiation. Totipotent stem cells, such as

the zygote or cells from early (1 to 3 days post fertilisation) embryos, have the ability for each cell to develop into a complete individual. Pluripotent stem cell can form all three germ layers of the body (endoderm, mesoderm and ectoderm), an example of which is the embryonic stem cells (ESC) isolated from the inner cell mass of blastocyst (5 to 14 days) (please refer to Figure 1). Multipotent stem cells are committed cells that can still form a number of other tissues, but not all three germ layers. An example of a multipotent stem cell is the haemopoietic stem cell (HSC) which can derive both lymphoid and myeloid lineage blood cell types.

Recent developments in the understanding of multipotent stem cells from non-embryonic sources have sparked new excitement in the field. Multipotent cells, such as the mesenchymal stem cells (MSC), appear to possess greater plasticity than dictated by established paradigms of embryonic development (Phinney, 2007). As MSC can differentiate from primitive cells into mature cell types, they can be used for cell replacement therapy, tissue engineering, regenerative medicine and vehicles for gene therapy (Gafni, 2004). Unlike ESC which are reliably generated only with the sacrifice of human embryos, multipotent cells from adult or terminated fetuses are subjected to fewer ethical questions. These attributes of multipotent cells make them promising candidates for future clinical use.

As stem cells are isolated from more adult tissue sources (often termed “niches”), the definition of bona fide stem cells becomes important. The differences between stem cells have prompted the need for detailed cell line classification methods such as global gene expression profiling and clustering (Muller, 2008). Definitions aside, the most important question is how we can use stem cell as therapeutic agents.

Stem cells can be administered to a patient at the site of injury or less invasively through an intravenous injection. When given intravenously, stem cells have the ability to home and migrate to sites of tissue injury, where they may participate in therapeutic activities. However, transplanted stem cells may also end up in other parts of the body. Therefore, a method of tracking these transplanted cells is urgently required. By combining nanoparticle technology and magnetic resonance imaging, we can now visualise transplanted cells. Prior to their transplantation, stem cells can be encouraged to engulf limited amounts of MR-visible particles which turn them MR-visible, albeit only in large numbers grouped together. Better detection sensitivity is required when tracking small groups of cells that migrate to remote locations or when studying how cells accumulate at the boundary of an injury site. One method to improve sensitivity is to encourage the cells to engulf more MR-visible particles. This project aims to improve the stem cell uptake of particles with diameter between 100 and 900 nm, a size range which has not been studied.



www.isscr.org

Figure 1: General differentiation potential of pluripotent embryonic stem cells and multipotent adult stem cells. The pluripotent embryonic stem cells from the inner cell mass can differentiate into any cell in the body. In comparison, the multipotent stem cells from various adult tissues are committed but can still differentiate into multiple cell types.

1.2 Mesenchymal Stem Cells

Mesenchymal stem cells (MSC) are multipotent cells that have received much attention in recent years as a promising source of autologous or allogeneic cell type for cellular therapy. They can be isolated from a number of adult (da Silva Meirelles, 2006) and fetal organs and tissues. It is believed that they reside in various niches for the purposes of tissue maintenance and regeneration. Adult and fetal MSC share the characteristics of self-renewal and differentiation down multiple mesenchymal lineages, although human fetal MSC (fMSC) are more primitive and are capable of greater proliferative and differentiation capabilities (Zhang, 2009).

1.2.1 Origin of MSC

The term, mesenchyme, is derived from Greek meaning “middle” (meso) “infusion” and refers to the ability of mesenchymatous cells to spread and migrate in early embryonic development between the ectodermal and endodermal layers. The middle embryonic layer, the mesoderm, gives rise to all of the body’s skeletal elements (Arnold, 1991).

During the period of haemopoietic stem cell discovery in the 1950s, Urist et al observed that bone marrow could form new bone when transplanted to an ectopic site (Urist, 1952). It was later identified that there exists a cell population in bone marrow that could regenerate bone (Friedenstein, 1968). The isolation and culture of cells from bone marrow that could form this ectopic bone was first demonstrated by Friedenstein et al (Friedenstein, 1970). It was not until a decade later that a similar adherent cell population from human bone marrow was isolated (Hann, 1983). Only

more recently was the self-renewal and multipotency of fetal MSC demonstrated with MSC cultured from first trimester fetal blood, liver and bone marrow (Campagnoli, 2000; Campagnoli, 2001).

After isolation, such cells can be separated from haemopoietic cells by their adherence to plastic culture dishes and proliferation from an initially heterogeneous population towards a more homogenous, spindle-shaped cell type with subculturing / passaging. MSC exist in the adult bone marrow as rare cells, with a frequency of one in 10^4 to 10^6 mononuclear marrow cells (Pittenger, 1999; Friedenstein, 1970; Castro-Malaspina, 1980). They were originally called “colony forming unit – fibroblast” (CFU-F), for their ability form colonies of fibroblast-like cells. The nomenclature developed from CFU-F to multipotent stromal cells or mesenchymal stem cells, with the latter popularized by Caplan in the 1990s (Caplan, 1991).

Due to the heterogeneous nature of these cells, critics have argued against the use of the term “stem” to describe the whole isolated cell population (Horwitz, 2005). Although not yet rigorously defined, “stemness” refers to the capacity for self-renewal, differentiation and function. Demonstration of MSC surviving *in vivo* for long periods with multi-lineage differentiation, self-renewal and tissue repopulation has been more difficult than for haemopoietic stem cells (HSC) (Thomas, 2008; Horwitz, 2005). Moreover, *in vivo* integration and differentiation have been proven by teratoma formation with embryonic stem cells (ESC) (Thomson, 1998) and reconstitution in irradiated host with multipotent adult progenitor cells (MAPC) (Reyes, 2001; Jiang, 2002), but not MSC. It was proposed that “mesenchymal stem cells” should be reserved for only the subpopulation of cells that exhibit “stemness”. Some researchers have preferred to call these cells bone marrow stromal stem cells, stromal precursor

cells, recycling stem cells, marrow isolated adult multilineage inducible stem cells (MIAMI) (DiIppolito, 2004) or MAPC. For the purpose of consistency, I have chosen the terminology “mesenchymal stem cells” in this dissertation.

Of the above cell types the MIAMI and MAPC cells stand out as special types. They have higher proliferative and differentiative potential compared to classical MSC (DiIppolito, 2004). MAPC can differentiate into HSC (Serafini, 2007) and have the capacity for arterial (Aranguren, 2007) and endothelial lineages (Reyes, 2002). It has been suggested that they may represent a more primitive subset of stem cells that could be the common precursor to MSC. If indeed so, the relationship between these precursors and the hemangioblast will have to be determined as the latter is regarded as the mesodermal precursor of haemopoietic and endothelial lineages (Park, 2005).

1.2.2 MSC Sources

Apart from adult MSC isolated from bone marrow, other MSC niches have more recently been identified (da Silva Meirelles, 2006). The sources of fetal MSC are generally the same as their adult counterpart. An early clue to the existence of non-haemopoietic stromal cells in fetal life was reported in the early 1970s (Macek, 1973). Fetal MSC could be identified in the embryonic aorta-gonad-mesonephros (AGM) region and yolk sac of rodents (Van Den Heuvel, 1987). Developmental studies demonstrated that cells from the stage-24 chick bud limb could turn into various mesenchymal cells depending on culture conditions (Arnold, 1991). Fetal MSC can be found in fetal circulation starting from 7 weeks gestation, declining to insignificant numbers by the beginning of the second trimester (Campagnoli, 2001). They have been identified in fetal blood, liver and bone marrow (Campagnoli, 2000;

Campagnoli, 2001), metanephros (Almeida-Porada, 2002), dermis (Zhao, 2005), pancreas (Hu, 2003) and thymus (Rzhaninova, 2005). Recently, second and third trimester amniotic fluid has been explored as a source of MSC that could have been released from fetal urinary, gastrointestinal, respiratory and amniotic interfaces (Tsai, 2004; Zhao, 2005; De Coppi, 2007). The placenta was also identified as an MSC source, though 80% of cells were of maternal origin (in't Anker, 2004). MSC can also be found in term umbilical cord blood (UCB), though at low and inconsistent frequencies. Mareschi et al could not isolate MSC from UCB in culture conditions that were permissive for bone marrow MSC (Mareschi, 2001). Others reported CFU-F per 10^6 monocuclear cells (MNC) plated that ranged from 0.35 to 0.5 (Erices, 2000; Goodwin, 2001), which is much lower than first trimester fetal blood (8.2 CFU-F / 10^6 MNC) (Campagnoli, 2001). By using high volumes of UCB and addition of cytokines to stimulate cell proliferation in culture, MSC could be isolated, albeit from less than a third of collected samples (Bieback, 2004; Lee, 2004).

1.2.3 MSC Characteristics

Pittenger et al have defined MSC as cells that exhibit self-renewal in adherent culture, differentiate to multiple mesenchymal lineages and present specific surface proteins (Pittenger, 1999). In order to standardise the nomenclature and characteristics of MSC, the International Society for Cellular Therapy has published a consensus statement which largely follows on from Pittenger et al's earlier work (Dominici, 2006). While there is no marker specific for MSC, it is generally accepted that MSC from any source do not express haematopoietic markers such as CD14, CD34 and CD45 and are negative for the endothelial markers CD31 and von-Willebrand factor (vWF). They express a number of adhesion molecules such as CD44 (hyaluron), CD29 (β 1

integrin), CD49e ($\alpha 5$ integrin), CD62 and a number of intracellular markers such as vimentin, laminin, fibronectin and surface epitopes like CD105 (SH2) and CD73 (SH3/4). MSC express intermediate amounts of HLA Class I and do not express HLA Class II. However, variable expression of CD90 (Thy1.1), CD117 (ckit), CD105, CD73 and STRO-1 may occur between cultures and species, underlying the heterogeneous nature of MSC and the different microenvironments required for haemopoietic support (Javazon, 2004). A comparative table on their respective phenotypes is shown in Table 1.

CD reference	Name	Blood ^{6,7}	Bone Marrow ^{6,7}	Liver ^{6,7}	Lung ^{13,15}	Kidney ¹⁶	Pancreas ^{17,18}	Thymus ²⁰	Dermis ¹⁹	Amniotic fluid ^{21,22,23}
CD45	LCA	-	-	-	-	-	-	-	-	-
CD14	LPS-R	-	-	-	-	-	-	-	-	-
CD68	Macrosialin	-	-	-	-	-	-	-	-	-
CD34		-	-	-	± ¹³ - ¹⁵	-	-	-	-	-
CD38	T10	-	-	-	- ¹⁵	-	- ¹⁸	-	-	-
CD31	PECAM	-	-	-	-	-	-	-	-	-
CD58	LFA-3	-	-	-	±	-	-	-	-	-
CD71	T9	-	-	-	±	-	- ¹⁸	+	-	-
CD29	B-1 integrin	+	+	+	+ ¹⁵	+	+	-	-	+
CD44	H-CAM	+	+	+	+	+	+	+	-	+
CD50	ICAM-3	-	-	-	-	-	-	-	-	-
CD54	ICAM-1	-	-	+	+	-	-	±	-	-
CD106	VCAM-1	+	+	+	-	±	-	-	-	-
CD11a	LFA-1	-	-	-	-	-	-	-	-	-
CD105	SH2, endoglin	±	±	±	+	±	-	+	-	±
CD73	SH3	+	+	+	+	-	-	-	-	+
CD73	SH4	+	+	+	+	-	-	-	-	+
CD13	Aminopeptidase N	-	-	-	+ ¹⁵	-	+	-	-	-
CD90	Thy-1	-	-	-	+	+	+ ¹⁸	+	+	±
CD147	Neurothelin	-	-	-	-	-	+ ¹⁸	-	-	-
CD117	SCF-R, c-kit	-	-	-	-	-	- ¹⁸	-	-	-
CD133	AC 133	-	-	-	- ¹⁵	-	- ¹⁸	-	-	-
CD49b	VLA-2	+ ⁷	+ ⁷	+ ⁷	-	-	-	-	-	-
CD49d	VLA-4	+ ⁷	+ ⁷	+ ⁷	-	±	-	-	-	-
CD49e	VLA-5	+ ⁷	+ ⁷	+ ⁷	+	-	-	-	-	-
	HLA-DR	-	-	-	-	-	-	-	-	-
	Oct-4	-	-	-	-	-	-	-	-	+
	Vimentin	+	+	+	-	+	+ ¹⁸	+	-	+
	Laminin	+	+	+	-	±	-	-	-	-
	Fibronectin	+	+	+	-	-	-	-	-	-
	Type I collagen	-	-	-	-	+	+	-	-	+

Table 1: Immunophenotype of human fetal MSC (O'Donoghue, 2006). + Positive, - Negative, ± Weakly Positive or Low Expression.

A defining characteristic of the MSC is its ability to differentiate into osteoblasts, adipocytes and chondroblasts under appropriate culture conditions (Dominici, 2006). In addition, myogenic differentiation of MSC from various sources has been shown (Gang, 2004; Chan, 2006). Some reports have shown that MSC can transdifferentiate down the neuroectodermal lineage into neurons (Wislet-Gendebien, 2005; Cho, 2005) and the endodermal lineage into hepatocytes (Aurich, 2007; Banas, 2007), but this has not been reproducible in many laboratories. The possible lineages of MSC are illustrated in Figure 2.

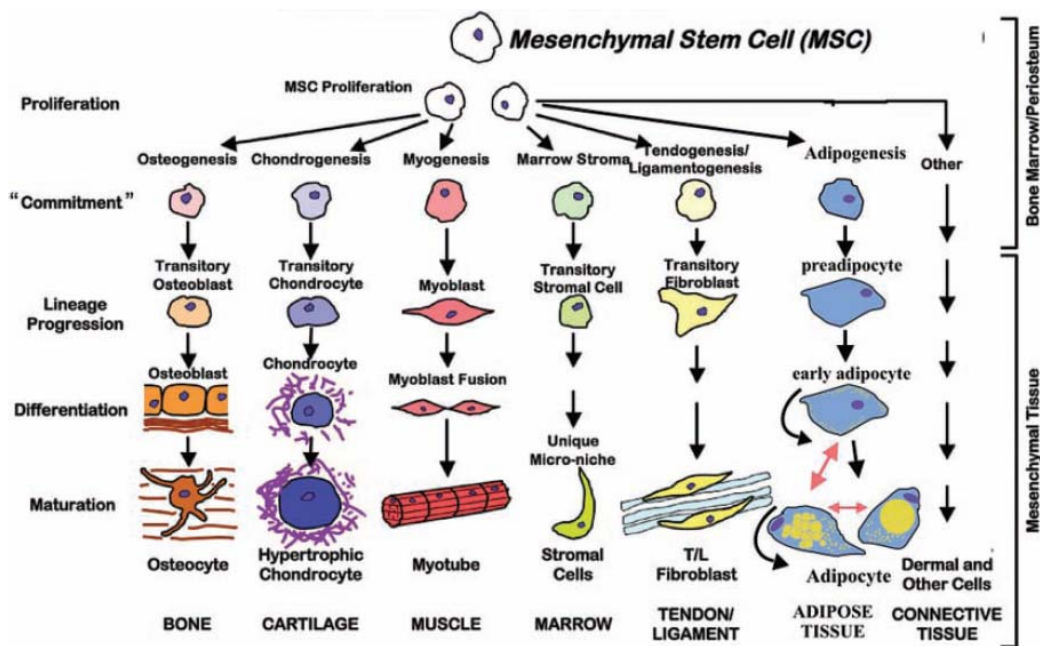


Figure 2: Mesenchymal stem cells (MSCs) differentiation is multistep, involving committal development of cells towards a particular lineage. They have the potential to differentiate into various tissue including bone, cartilage, muscle, marrow stroma, tendon/ligament, fats, and other connective tissues. (Caplan, 2005).

Clonal analysis of MSC and their differentiation capacity has revealed the heterogeneous nature of this cell type. It has been shown that a majority of clones can differentiate into osteoblast, but fewer into adipocytes and chondroblasts. Only a third

of clones can differentiate into all three lineages with adipogenesis and chondrogenesis lost with greater population doublings (Muraglia, 2000). In addition, there are tri-potent (osteogenesis, adipogenesis and chondrogenesis), bi-potent (osteogenesis and chondrogenesis) and uni-potent (osteogenesis only) clones (DiGirolamo, 1999).

Compared to MSC derived from adults, fetal tissue-derived MSC (also known as human fetal MSC [fMSC]) have several advantages that may be exploited in cellular transplantation applications. Firstly, fMSC have been shown to proliferate faster than adult MSC (Gotherstrom, 2003) and can undergo many more population doublings before senescing (Campagnoli, 2001), thus allowing the generation of clinically relevant cell numbers for clinical transplantation. Secondly, fMSC may have greater differentiation capacity than adult MSC, with reports demonstrating superior osteogenic capacity (Zhang, 2009), and oligodendrocyte (Kennea, 2003; Kennea, 2009) and haemopoietic differentiation (MacKenzie et al. 2001). Thirdly, expression of markers associated with pluripotency, such as Oct-4, have been demonstrated in fMSC at the mRNA and protein level (Guillot, 2007; Zhang, 2009), suggesting their primitive origin. Lastly, fMSC from fetal blood, liver and BM have been shown to express a higher level of telomerase activity and have longer telomeres compared to MSC derived from adult tissues (Guillot, 2007). Telomeres are double-stranded DNA (TTAGGG)_n repeat sequences of <20kb long, with a single strand of the repeated sequence acting as a protective cap for the chromosomal ends. As DNA polymerase does not duplicate end sequences completely, telomeres shorten with successive cell division until a critical length where division is arrested (Guillot, 2007). Telomerase activity coincides with lengthening of telomeres by enzymes, thereby maintaining self-renewal of cells such as the ESC.

1.2.4 Homing and Migration

There has been emerging evidence that systemically delivered MSC migrate towards damaged or inflamed tissue, such as that found in stroke injuries (Jendelova, 2003). Although fMSC trafficking is not yet fully understood, such cells are likely to migrate using similar mechanisms to adult MSC. Circulating adult MSC adhere to vascular endothelial cells through specific adhesion molecules and chemokines, enter the perivascular space through transendothelial migration and move along chemokine gradients towards sites of tissue damage. Steingen and colleagues showed that transmigration is dependent on the endothelial phenotype, with MSC co-cultured with human umbilical vein endothelial cells the most effective and exhibiting cytoplasmic podia (Steingen, 2008).

The mechanisms of leukocyte transendothelial migration have been established since the early 1990s (Butcher, 1991; Springer, 1994). The coordinated sequence of adhesion steps is initiated by surface tethering, which are mainly mediated by P and E selectins and their ligands. Following tethering, the captured cells roll and encounter chemokines, which eventually activate integrins to result in firm arrest. The subsequent transendothelial migration is mediated by the platelet/endothelial cell adhesion molecule 1 (PECAM-1 or CD31) (Muller, 1995).

Compared to leukocytes, less is known about the transendothelial migration mechanisms of MSC. A number of adhesion molecules are expressed on fMSC, including integrins $\alpha 2$, $\alpha 4$, and $\alpha 5$ (de la Fuente, 2002) (please see Table 2). Other adhesion molecules found on adult MSC include VLA-4, VCAM-1 and CD44 (Krampera, 2006). The adherence of MSC to endothelial cells has been shown to involve VLA-4 and VCAM-1 (Steingen, 2008).

The mechanisms of MSC transendothelial migration are similar to those of leukocytes, as shown by intravital microscopy (Ruster, 2006). Leukocytes express P-selectin glycoprotein ligand 1 (PSGL1) which interacts with the P-selectin on endothelial cells during rolling. MSC rolling and adherence is a P-selectin-dependent process but MSC do not express PSGL1, therefore MSC express an unknown P-selectin ligand (Ruster, 2006). Moreover, PECAM-1 is expressed on leukocytes but not on MSC, bringing to question the mechanism responsible for MSC passage through endothelial cell gaps (Muller, 1995).

After entering the perivascular space, MSC move along chemokine gradients. Chemokines or chemotactic cytokines, are a large superfamily of small (8 – 10 kDa) glycoproteins that are involved in a diverse range of biological processes. The difference between chemokines and other cytokines are the ability of the former to bind to G-protein coupled receptors to mediate directional migration (Baggiolini, 2001; Chamberlain, 2007). Only a few recent studies probed for most or all receptor expression on MSC and correlated with cellular migration in response to chemokine stimuli with chemotaxis assays (Honczarenko, 2006; Ringe, 2007; Ponte, 2007; Prockop, 2009) (Table 2). MSC express a broad spectrum of chemokine sub-family receptors, although with much variability between reports, further alluding to their heterogeneity.

After entering the perivascular space, MSC move along chemokine gradients, and encounter the extracellular matrix of the basement membranes. Metalloproteinases (MMPs) are expressed by MSC to overcome these barriers. It was shown that MSC express MMP-2, MT1-MMP, TIMP-1 and 2 (please see Table 2), and cannot traverse the basement membrane when MMPs are inhibited (Ries, 2007).

Adhesion molecules on MSC (de la Fuente, 2002; Krampera, 2006; Steingen, 2008)	
$\alpha 2$ and $\alpha 4$	integrins
VLA-4 or $\alpha 4\beta 1$	very late antigen 4 integrin
VCAM-1 or CD106	vascular cell adhesion molecule-1
CD49e	$\alpha 5$ integrin
CD29	$\beta 1$ intrgrin
CD44	hyaluron
Chemokine Receptors on MSC (Honczarenko, 2006; Ringe, 2007; Ponte, 2007)	
CCR1, 2, 3, 7, 8, 9	CC chemokine receptors
CXCR 1, 2, 3, 4, 5, 6	CXC chemokine receptors
Metalloproteinases secreted by MSC (Ries, 2007)	
MMP-2	Matrix metalloproteinase 2
MT1-MMP	Membrane type 1 MMP
TIMP-1 and 2	Tissue inhibitor of MMP 1 and 2

Table 2: Molecules responsible for MSC migration. Adhesion molecules mediate MSC transendothelial migration. Once in the perivascular space, chemokine receptors direct MSC migration along chemokine gradients and metalloproteinases breakdown ECM while MSC migrates.

1.2.5 Engraftment

Engraftment refers to the ability of transplanted cells to stably survive and integrate with host tissue without rejection by the host immune system. Transplantation of MSC, in particular to the central nervous system, is challenged by several factors related to engraftment.

1.2.5.1 Host Immune Response to Cell Therapy

An important consideration for cell therapy is the host immune response to the transplanted cells. Immune-rejection by the host can compromise the efficacy of stem

cells from either allogeneic or xenogeneic sources. The immune responses in the brain and the periphery are different due to capacity of the brain to reduce or delay immune response in a phenomenon known as ‘immune privilege’, which will be discussed later. The magnitude of the response is generally dependent on the phylogenetic distance between donor and host; a strong host immune response is mounted against discordant xenograft from a distantly-related species (Pakzaban, 1994). In addition to the type of transplant, the strength of the response is not only host organ dependent, but also transplant site dependent. For example, grafts transplanted in the cerebral parenchyma show better survival rate than near the ventricular systems (Oertel, 2004). Possible reasons for strong immunoreactivity near the ventricular system include partial lack of blood-brain barrier (BBB) in the ventricular system and extensive antigen drainage to cervical lymph nodes.

1.2.5.1.1 Immune Response of the CNS

There are two parts to the mammalian immune response to pathogens such as bacteria and viruses. The first is the innate immune response which is the immediate and generic response of the host to the presence of any pathogen. An important cell type of the innate immune system within the central nervous system (CNS) is the microglia (Aloisi, 2001). Microglia are macrophage-like cells that reside throughout the CNS parenchyma and respond to the presence of antigen through pattern recognition receptors (PRR) such as toll-like receptors (TLR) (Olson, 2004). They play a surveillance role until activation by injury or the presence of foreign antigens (Nimmerjahn, 2005). Their function as intrinsic phagocytic cells of the CNS is well established. They have limited function as antigen presenting cell (APC) but can

mature into macrophages and dendritic cells for full APC capacity (Santambrogio, 2001).

A growing pool of evidence implicated astrocytes as the other cell type involved in the innate immune system (Farina, 2007). Astrocytes are the most populous glial cells of the CNS, and they form a major part of the blood brain barrier and provide metabolic support of neurons. Upon recognition of foreign antigen with PRR such as TLR, mannose and complement receptors, they activate neighbouring cells with immune mediators, including the granulocyte macrophage colony stimulating factor which regulates microglial activity (Fischer, 1999). Other astrocyte-secreted mediators modify BBB permeability and attract extravasation of immune cells in support of the adaptive immune system.

The adaptive immune response is the second line of defence of vertebrates for the long-term defence against specific pathogens (Alberts, 2007). It has “memory” for previously encountered pathogens and mounts stronger attacks each time the pathogens are encountered. There are two broad classes of such responses - *antibody response* and *cell-mediated immune response*, and they are carried out by different lymphocytes, called B cells and T cells, respectively.

In the antibody response, B cells are activated to secrete antibodies specific to the antigen. The antibodies distribute throughout the host and bind specifically to the foreign antigen that stimulated their production. Antigen binding inactivates viruses and microbial toxins by inhibiting their ability to bind to receptors on host cells. Antibody binding also marks the pathogens for destruction, mainly by making it easier for phagocytic cells of the innate immune system to ingest them.

1.2.5.1.2 Cell-mediated Immune Response Against Foreign Grafts

There are two classes of MHC proteins: MHC I which present foreign antigens to cytotoxic, CD8+ T cells and MHC II which presents antigens to helper, CD4+ T cells. Often, the MHC proteins expressed on the transplanted cells (with the exceptions of autologous and syngenic grafts) are different from those of the host cells. Cell-mediated immune response is the main mechanism of immunity against transplanted foreign cells in an allogeneic or xenogeneic cell graft. It occurs in three phases: the induction, the attack and the quiescent phase (Lawrence, 1990). The activity of the induction phase is similar to the innate immune response. Transplanted grafts usually suffer partial necrosis and become surrounded by cytokine expressing macrophages for up to 6 days. Transplanted cells carry major histocompatibility complex (MHC) different from that of host cells. When APC of the innate immune response, such as the dendritic cells engulf necrotic cells, the APC can enzymatically break down the foreign cells into peptides and migrate to the T cell rich peripheral lymph node. At the lymph nodes, the foreign peptides complexed with the host MHC molecules on the host APC are presented to T cells. When T cells bind to the MHC-peptide complex through T cell receptors, they become activated, proliferate, differentiate into effector cell subsets carry the same MHC-peptide on their surface, proliferate and enter the circulation. BBB disruption during injury or intracerebral transplantation assists the extravasation of T cells at the inflammation site. At this stage, the main source of MHC I is from donor cells, but the host tissue may present MHC I when injury occurs during the transplantation. It has been shown that the mechanical damage of an intracerebral transplantation was a cause of elevated host MHC I at the injection tract and vicinity (Modo, 2002).

The attack phase can occur from 6 to 40 days of the transplantation. During this time, T cells in the vicinity of the inflammatory site stimulate the microglia with interferon- γ . The T cells recognise B cells, CD8⁺ cells carrying the MHC-peptide, and also the target cells carrying the foreign MHC. The CD4⁺ cells help to stimulate the response of B cells and CD8⁺ cells which on identifying the foreign cells, reorganise their cytoskeleton at the T cell/ target cell interface to form an immunological synapse. Once bound, the cytotoxic T cells induce the target cells to undergo apoptosis through perforin protein or Fas – Fas ligand directed caspase. At the same time, debris and dead cells are phagocytosed by microglia. At the quiescent phase, which can last up to 5 months, the graft rejection is at its late or complete state and the graft site has few remaining T cells.

1.2.5.2 Suppression of Immune Response

Although the brain is immunologically privileged to a certain extent, the use of immunosuppression ensures the best survival chances of a cerebral graft. Immunosuppressive drugs interfere with the activation and to some degree, the proliferation of T cells. Cyclosporin A (CyA), a commonly used immunosuppressive drug improves intracerebral xenograft survival, but immunosuppression can be improved when CyA is combined with other drugs such as prednisolone or mycophenolate mofetil (Wennberg, 2001). It has also been shown that the combination of a calcineurin-dependent (FK506) and a non-calcineurin-mediated inhibitor (rapamycin) allowed human fetal neural stem cells to survive in mice for more than 2 months, compared to as little as one week for FK506 or CyA alone (Yan, 2006).

CyA, a calcineurin inhibitor, is a potent immunosuppressant that reduces the production of several growth factors (especially interleukin 2). Ryffel et al reviewed the role of CyA as a carcinogenic agent (Ryffel, 1992) and concluded that CyA may allow dose-dependent growth of initiated tumor cells *in vivo* and Epstein-Barr virus-infected B cells might escape the control of specific cytotoxic T cells. A study of short term CyA showed that donor marrow stem cells migration and outgrowth in intact striatum were delayed (Irons, 2004), although the long term effects remain unknown. Other therapeutic roles of CyA have been documented, including the potential as a treatment for Parkinson's disease (Seaton, 1998).

The use of immunosuppression drugs, including CyA, poses an increased risk of post-transplantation lymphoid neoplasia, a group of lymphoproliferative disorders that develop in recipients of solid organs and bone marrow allograft (Cobo, 2008). The incidence of lymphoma in the transplanted population is <2% and is influenced by the intensity of the immunosuppression. It remains to be determined if the type of immunosuppressive drug alters the incident rate.

1.2.5.3 Immune Privilege of the Brain

'Immune privilege' is a phenomenon where immune-mediated inflammation and allograft rejection are reduced in certain organs, such as the eye, pregnant uterus and the CNS (Niederhorn, 2006). Immune-mediated inflammation can have deleterious effects to the eye and brain, which have limited regeneration capacity. The term 'immune privilege' was first used by Medawar (Medawar, 1948) who proposed that certain sites, like the brain do not allow entrance of immune cells or exit of antigen due to the presence of blood-tissue barrier, absence of antigen-presenting cells (APC)

and sparse lymphatic drainage. This view was accepted until it was shown that the brain does not possess absolute privilege. Activated T cells can cross the brain-tissue barrier and enter the brain (Hickey, 1991), and microglia have APC function and lymphatic drainage into deep cervical lymph nodes do exist. After cerebral ischemia, the initial inflammatory response is followed by upregulation of cytokines, adhesion molecules and chemokines, all of which promote recruitment of leukocytes that mediate further cerebral infarction (Huang, 2006). Moreover, recent evidence points to the failure of “immune privilege” mechanisms as a contributor to the conditions of multiple sclerosis, corneal allograft rejection or immune-mediated miscarriages (Nieder Korn, 2006).

Cells in the brain do possess surface molecules that moderate the immune response. Several cell types, including astrocytes, neurons and microglia express FasL (CD95L) and can trigger the apoptosis of Fas+ (CD95) activated T cells (Bechmann, 1999). Complement activation is a stimulus of the innate immune response, but it can be moderated by complement regulatory proteins (CRP) in the eye and the fetus. Two main CPR, the membrane cofactor protein and CD59, are found in the brain (Harrower, 2004), although their role in immune privilege of the brain remains to be determined. On the other hand, major histocompatibility complex (MHC) class I molecules are absent or weakly expressed on oligodendrocytes and neurons in the brain (Massa, 1993), reducing cell lysis by cytotoxic T-cells.

Aside from cell membrane molecules, immune privilege is also maintained by soluble anti-inflammatory and immunosuppressive molecules. One such molecule in the brain is the macrophage migration inhibitory factor (Calandra, 2003), which reduces natural killer cell-mediated cytotoxicity (Apte, 1998).

1.2.5.4 Variability of Graft Survival

Graft survival after transplantation in rodent models has been found to be highly variable by several authors (Mason, 1986; Lawrence, 1990; Modo, 2002). In a murine-rat xenograft transplantation stroke model, the number of surviving murine neural stem cells after 2 weeks varied from none to >80 per 25 μ m thick brain section (Modo, 2002). In an intra-muscular allograft to nude mice, only 30% of transplanted muscle precursor cells survived after 1 hr and the survival rate dropped to 1% after 1 day (Beauchamp, 1999). In an intracerebral allograft to rats, transplanted MSC survived for 7 days in the striatum and hippocampus with CyA immunosuppression (Coyne, 2006). The allograft rejection by ED1+ microglia/macrophages started on day 3 and was nearly complete on day 14. In a xenogeneic human-murine transplantation, transplanted fMSC survived with chimerisms of up to 5% for up to 19 weeks duration (Chan, 2007; Guillot, 2008). Intracerebral fetal injections in a similar model led to oligodendrocytic differentiation and survival for at least 35 days (Kennea, 2009). Finally, post-natal transplantation of fMSC in adult *scid* mouse muscle resulted in their survival up to 28 days post-transplantation (Chan, 2006). Taken together, the survivability of primary cell grafts like fMSC is highly variable and is related to the immunocompetence of the host species.

1.2.5.5 Immunogenicity of MSC

MSC are considered non-immunogenic and may induce immuno-modulatory tolerance when co-grafted with other immunogenic cells. As MSC are MHC I positive, they may activate host cytotoxic T cells, but being negative for MHC II, FAS ligand and other co-stimulation molecules prevents full T cell stimulation by MSC alone (Tse, 2003). MSC retain similar human leukocyte antigen (HLA; the MHC in human)

expression even after differentiation into bone, fat or cartilage (Le Blanc, 2003). In addition, cytosolic HLA Class II in fMSC required 7 full days of interferon- γ to be upregulated (Gotherstrom, 2004), compared to just 2 days for adult MSC (Le Blanc, 2003). Interestingly, interferon- γ induced adult MSC still do not elicit an alloreactive lymphocyte proliferative response in culture (Le Blanc, 2003). It was proposed that allogeneic MSC suppress lymphocyte alloreactivity through an HLA-independent mechanism, as seen from *in vitro* mixed lymphocyte cultures (Krampera, 2003).

The immuno-tolerance of MSC *in vivo* is varied among different reports and less well-understood. In agreement with the ability to suppress alloreactive lymphocytes in mixed lymphocyte cultures (Krampera, 2003), co-transplanted MSC exert immunomodulation of host response against immunogenic allografts. Evidence of this comes from prolonged survival of allogeneic skin graft in immunocompetent baboons when MSC are administered (Bartholomew, 2002). Another evidence is the formation of tumours from melanoma cells in immunocompetent mice only when they are co-injected with MSC (Djouad, 2003). The immunomodulatory mechanism has not been confirmed and there have been contradicting reports (Nasef, 2008). Initial clinical experience with MSC showed promising potential for therapy-resistant severe acute graft-versus-host disease, tissue repair, treatment of rejection of organ allografts and autoimmune disorders (Le Blanc, 2007). However, contradictory results on the immuno-tolerance of MSC were shown when erythropoietin-releasing allogeneic MSC transplanted into MHC-mismatched mice caused only a transient rise in haematocrit compared to syngeneic hosts. Moreover, subsequent transplantation showed refractoriness in haematocrit levels consistent with alloimmunization against donor MSC (Eliopoulos, 2005).

1.2.6 Clinical trials of MSC Therapy

MSC have been considered for clinical application in a wide range of fields, including haematologic malignancy, cardiovascular disease, osteogenesis imperfecta and stroke. The cell type is favourable because of its capacity for expansion in culture, multilineage differentiation and immunomodulatory properties. Some clinical trials have already begun despite some unanswered questions relating to possible decrease in immunity against infection or tumorigenesis (Houghton, 2004; Ringden, 2006).

1.2.6.1 Hematological Malignancy

MSC have been shown to exert immunosuppression. It was shown that MSC suppress lymphocytes in culture (Krampera, 2003) and prolong survival of skin graft in immunocompetent hosts (Bartholomew, 2002). Graft versus host diseases (GVHD) is a major cause of morbidity and mortality following allogeneic HSC transplantation where donor lymphocytes start attacking the host cells (Ferrara, 2006). It was proposed that the immunomodulatory effects of MSC can be a prevention or treatment for GVHD.

During a feasibility study on the intravenous infusion of autologous MSC alone, no deleterious effect was observed (Lazarus, 1995). Cotransplantation of autologous MSC with HSC in patients who have received myeloablative therapy was also shown to be safe (Koc, 2000). In an acute leukaemia patient given allogeneic HSC, where rejection or severe GVHD risk is high, she was also given HLA-haploidentical MSC and no GVHD was observed for two and a half years after transplantation (Lee, 2002). In a more extensive study on haematological malignancies, 46 patients had MSC co-

infused with HSC from HLA identical siblings (Lazarus, 2005). Neither MSC-related adverse effect nor severe GVHD was observed in 23 of 46 patients and 2-year progression-free survival was 53%. Chimerism of MSC was demonstrated in only 2 of 19 patients at 6 and 18 months after transplantation.

In a clinical trial involving 8 patients with the same disease, GVHD disappeared in 75% of the patients given allogeneic MSC and survival was improved over the 16 patients without MSC transplantation (Ringden, 2006). In another study involving 13 patients with the same disease, 15% of patients responded to the allogeneic MSC infusion and a further 45% responded after addition concomitant transplantation and immunosuppression therapy (von Bonin, 2009). The results of a phase II study of this treatment showed that recipients of MSC had higher survival 2 years post-transplantation and the response rate was not related to donor HLA-matching (Le Blanc, 2008).

Taken together, these results showed that allogeneic MSC transplantation is safe and promising for the treatment and prevention of GVHD. Donor HLA-matching may not be important and engraftment may not be stable even in immunocompromised patients.

1.2.6.2 Myocardial Infarction

Myocardial infarction (MI) leads to cardiomyocyte loss and contractile dysfunction of the heart. Formation of scar tissue follows as the ischemic tissue persists and negative remodelling can result in total failure (Rivera, 2006). Much excitement was generated when Orlic and colleagues suggested that marrow cells replaced lost heart muscle and improved cardiac function (Orlic, 2003). Although later challenged by views from

other laboratories that the transplanted cells did not themselves become cardiac muscle cells (Murry, 2004; Balsam, 2004), clinical trials on whole and fractionated marrow cells were already underway.

The largest clinical trial of the disease was the Reinfusion of Enriched Progenitor Cells and Infarct Remodeling in Acute Myocardial Infarction (REPAIR-AMI) trial, a multicenter trial of infusing patient with marrow mononuclear cells (MNC, consisting of haemopoietic, mesenchymal and endothelial cells) after percutaneous coronary intervention (Schachinger, 2006). Left ventricular ejection fraction (LEVF), measured only at 4 months was greater in treated patients compared to the placebo group. One year post-transplantation data showed lower rate of adverse clinical events. Bone Marrow Transfer to Enhance ST-Elevation Infarct Regeneration trial (BOOST) reported that the relative improvement in LEVF after infusion of MNC at 6 months, as compared with no infusion, was no longer significant at 18 months, suggesting that the main effect was an acceleration of recovery (Wollert, 2004; Meyer, 2006). Results contradicting to these trials were shown by Autologous Stem Cell Transplantation in Acute Myocardial Infarction (ASTAMI) (Lunde, 2006). No significant improvement in LVEF at 6 months was observed in the MNC group. The inconsistent findings were somewhat disappointing, but can be attributed to difference in cell culture protocol (Lunde, 2006). The other trials are summarized in Table 3.

Trial	Setting	Design	Cell Number	Results
BOOST	Percutaneous coronary intervention (PCI) after acute MI	30 patients received bone marrow cells (BMC) 30 did not receive infusion	2.5×10^9 unfractionated BMC	6 mo: LVEF 6% greater in BMC group 18 mo: no difference
Janssen et al	PCI after acute MI	33 patients received BMC 33 received placebo	3×10^8 ficoll-separated BMC	4 mo: no difference in LVEF, decreased infarct size, better regional function in BMC group
TOPCARE-CHD	Chronic left ventricular dysfunction	28 patients received BMC 23 did not receive infusion	2×10^8 ficoll-separated BMC	3 mo: 2.9% greater increase in LVEF in BMC group
ASTAMI	PCI after acute MI	47 patients received BMC 50 did not receive infusion	7×10^7 ficoll-separated BMC	6 mo: no difference in LVEF
REPAIR-AMI	PCI after acute MI	101 patients received BMC 98 received placebo	2.4×10^8 ficoll-separated BMC	4 mo: greater increase in LVEF in BMC group 1 yr: reduced adverse clinical events in BMC group

Table 3: Clinical trials for cardiac diseases adapted from Rosenzweig et al. Overall results of trials show that bone marrow cell infusion may improve cardiac function but the effect may not be permanent (Rosenzweig, 2006)

1.2.6.3 Osteogenesis Imperfecta

Osteogenesis imperfecta (OI) is a genetic disorder characterized by production of defective type I collagen, the principal protein in bone. The patients have numerous painful fractures and retarded bone growth with progressive deformation. At present, there is no cure and only empirical bisphosphonate treatment has been proven to be partially effective. The first clinical studies of MSC transplantation for OI started in the late 90s (Horwitz, 1999; Horwitz, 2001; Horwitz, 2002). Children were infused with MSC from HLA-identical or single antigen mismatched siblings after ablative therapy. Donor osteoblast engraftment, new dense bone formation and increase in total bone mineral content was observed with increase in growth velocity and reduced frequencies of bone fracture.

In a female fetus with bilateral femur fractures diagnosed with OI, *in utero* therapy with male HLA-mismatched fMSC was performed (Le Blanc, 2005). Biopsy indicated engraftment of donor cells (up to 12%) and histology showed regularly arranged and configured bone trabeculae. At 2 years of life, fewer fractures than typical OI patients were noted, and psychomotor development was normal. This is intriguing as the genotype suggests a more severe form of OI than what was observed. This shows that fMSC can engraft and differentiate into bone in a human fetus even when the recipient is immunocompetent and HLA-incompatible.

1.2.6.4 MSC therapy in stroke

MSC have been extensively studied in therapy of stroke in rodent models and only limited clinical results are available. When administered post-stroke they home to the

infarct region from the circulation or from the contralateral hemisphere, across the striatum (Jendelova, 2003). They have been shown to exert therapeutic effect including angiogenesis, neurogenesis, restoration of blood brain barrier and motor function recovery (Chen, 2001; Chen, 2003; Chen, 2004; Borlongan, 2004; Shen, 2007). Available animal and clinical results suggest that the route, timing of delivery may affect the efficacy of MSC therapy in terms of angiogenesis, neuroplasticity and immunomodulation.

Intravascular delivery appears to be the best route of MSC delivery. Recent clinical trials have used intravascular delivery of MSC (Bang, 2005) or bone marrow mononuclear cells (Mendonca, 2006). In contrast to the rodent brain, teratocarcinoma-derived neuronal cells showed limited migration in the human adult brain when transplanted intracerebrally (Nelson, 2002). The role of MSC in stroke therapy can be direct replacement cells or as source of neurotrophic and angiogenic factors. The role may affect the choice of delivery route. The distribution of MSC by the intravascular route was widespread (Borlongan, 2004), although only 4% of transplanted hMSC reached the rodent brain when given intravenously post-stroke (Li, 2002). Despite the small cell number that reached the infarct locality, the resulting functional recovery suggests that direct cell replacement or localized protein secretion may not be necessary. Moreover, intracarotid delivery can increase the proportion reaching the brain to about 20% of the rMSC given (Li, 2001).

The timing of cell delivery appears to affect the fate of MSC in the brain, particularly when cells are injected intracerebrally. The infarcted brain is a hostile environment for cell grafts, with radical oxygen species and inflammatory cells present. Reports on intravascular transplantation have focused on the delivery of MSC between 1 day and

1 week post-stroke with few reports on later transplantation. Although human neural cells showed significantly better survival when transplanted 3 weeks post-stroke as compared to 5-7 days post-stroke (Kelly, 2004; Grabowski, 1994), the early delivery of MSC may exert a different therapeutic effect on the infarct. As early as 30 minutes post-stroke, the disruption of the blood brain barrier allows the transmigration of immune cells such as leukocytes and macrophages (Dirnagl, 1999). As MSC are likely to transmigrate in a similar manner as leukocytes, the early delivery of MSC can allow an influx of immunomodulators to provide neuroprotection from early inflammatory damages caused by immune cells. MSC delivered early have been shown to improve angiogenesis (Liu, 2006) and neurogenesis (Shen, 2006) in the infarct periphery. Given the therapeutic effects of early intravascular delivery and graft survival of late intracerebral injection, the optimal delivery timing or the effects of multiple deliveries remain to be determined.

1.3 Monitoring of Cell Therapy

While the therapeutic capability of cell therapy is under investigation, knowledge of the whereabouts of transplanted cells is critical to the evaluation of transplantation route, timing, dosage and cell type. The temporal and spatial information of the cells will provide feedback on their engraftment efficiency and functional capacity to allow monitoring and optimising of the therapeutic process. As opposed to endpoint histological analysis of sacrificed animals, *in vivo* imaging throughout the therapeutic period will allow serial monitoring of patients and reduction in experimental animals numbers.

1.3.1 Histological Methods

A few techniques are available to identify donor cells from host tissue of sacrificed animals, for example by fluorescent confocal microscopy. The simplest method is to apply donor specific markers on histological tissue sections. Sex-mismatched transplantation has been employed where fluorescent *in situ* hybridisation (FISH) technique is used to locate the Y chromosome (van Dekken, 1989; Hocht-Zeisberg, 2004). FISH can also be used to identify the origin of cells in xenotransplantations. As the targets are small, being nucleotides or centromeres at best, their identification can be challenging against the autofluorescence of tissue sections. In xenogeneic transplantations, donor cells can be identified from host tissue by species-specific, antibody markers, such as vimentin (Chan, 2006; Guillot, 2008) or human nuclear marker MAB1281 (Lu, 2007).

To improve the signal from implanted cells, they can be labelled with exogenous labels, such as fluorescent thymidine analogues (Chen, 2001) or lipophilic carbocyanine (Arbab, 2008) before implantation. Although this method can be used when donor and recipient are of the same species or sex, it can be complicated by the transfer of labels to host cells, resulting in the failure to identify donor cells (Pawelczyk, 2006; Burns, 2006; Coyne, 2006). This complication often results from the engulfment of dead donor cells by host phagocytic cells. Moreover, cells loaded with *in vitro* dyes may suffer from label dilution following cellular proliferation or optical quenching due to limited lifespan of the dyes.

The transduction of cells with reporter genes aims to circumvent these drawbacks by encouraging cells to produce markers. While reporter genes that produce green fluorescent protein (GFP) have successfully identified hMSC xenotransplants in non-human primates (Irons, 2004), transplantation of transgenic cells still faces issue of variable expression within the host (Swenson, 2007) and safety concerns in translational studies.

Histological techniques have the potential for highly specific detection of donor cells although there are a few inherent drawbacks. Firstly, animals need to be sacrificed for each time point in a longitudinal study. Moreover, they suffer from inter-animal differences between control and experimental group which translate to the requirement for more animals to improve statistical significance. Therefore, there is need for methods to locate and follow the fate of transplanted cells in living animals over the entire study period.

1.3.2 *In vivo* Imaging Modalities

A number of cellular imaging modalities are under investigation but only a few are clinically relevant (Arbab, 2008). Clinical translation requires a modality that provides sufficient imaging resolution and depth of penetration through the human body while maintaining ionising radiation exposure within safety limits. Ultrasound is inexpensive and widely available compared to other modalities, but such requirements limit its application in cellular imaging. The inherent tradeoff between resolution and depth of ultrasound may restrict it to mammography and the imaging of the subcutaneous regions, the limbs and the neck.

Optical techniques offer superior resolution, but suffer from limited depth of penetration. The limitation is acceptable in applications such as intravital microscopy (IM). Donor cells can be identified with fluorescent transgenic materials, such as reporter genes or xenogeneic antibodies. By inserting luciferase transgene into cells, they can be located with bioluminescence imaging (BLI) in rodents. However, transgenic and xenogeneic materials are unlikely to receive clinical approval in the near future. Therefore, optical methods are likely to remain an imaging modality for small animals or superficial visualization in patients.

With modalities that require ionising radiation such as computer tomography (CT), positron emission tomography (PET) and single photon emission computed tomography (SPECT), patient exposure to radiation needs to be limited. In cellular imaging by CT, radiation exposure is the limiting factor at the resolution required to identify small groups of cells. SPECT also uses ionising radiation, but is limited by the period of monitoring when using practical isotopes such as ^{111}In . PET is a

promising modality that is not restricted by depth but has limited spatial resolution. It can be limited by patient radiation exposure, and suffers from generally very short tracer isotope half-lives. However, gene transfection methods have been devised to overcome the latter limitation. Prior to transplantation, donor cells are transduced with herpes simplex virus thymidine kinase genes such that they can be tracked by positron emitters (Cao, 2006). PET researchers have focused on improving spatial resolution and efficiency with miniature PET detectors (Park, 2007), pinhole inserts (Wu, 2008) and better signal processing (Fontaine, 2007).

By comparison, MRI edges out PET in terms of resolution, but the bane of MRI for cellular imaging is the lack of sensitivity at cellular resolutions. Researchers have been working to improve specificity by using spectrally distinct agents such as ^{19}F and chemical exchange-dependent saturation transfer (CEST) agents, which in theory can acquire signal only from the cells and without interference from the background. There have been also attempts to use specialised sequences for optimal cellular detection or simply increase the amount of contrast agent per cell. The following section describes the current state of cellular MRI research.

Modality	MRI			CT	PET	SPECT	Optical			US
	1H	19F	CEST				IM	FRI	BLI	
Spatial Resolution	10 – 100 μm	>100 μm	>100 μm	<10 μm	1-2 mm (animal scanner) 3-5 mm (clinical)		1 μm	2-3 mm	2-3 mm	50 μm
Depth of penetration	Unlimited	Unlimited	Unlimited	Unlimited	Unlimited	Unlimited	0.4 mm	<1 cm	1 cm	Unlimited
Sensitivity	1-1000	7500	25000	Poor	hundreds	?	?	?	10	1
Reporter gene	In progress	No	Yes	No	Yes	No	Yes	No	Yes	No
Longevity	Good	Good	Excellent	Good	Excellent	Poor	Excellent	Good	Excellent	Good
Label approach	Exogenous label	Exogenous label	Reporter gene	Exogenous label	Reporter gene	Decaying Isotope	Reporter gene	Exogenous label	Reporter gene	Exogenous label
Cellular Quantification	Possible	Yes	Possible	Possible	Possible	Yes	No	No	Possible	Possible
Ionising radiation	No	No	No	Yes	Yes	Yes	No	No	No	No
Clinical Translation	Yes	Yes	Yes	Possible	Yes	Yes	Limited	No	No	Yes
Characteristics	Gd, Mn, FeO Soft tissue contrast	19F Good specificity	Ln or peptides Good specificity	Iodine	18F, 11C, 15O, 64Cu Cyclotron needed	111In, 123I, 99mTc mAb imaging	GFP	GFP, NIR fluoro-chrome Rapid molecular diagnostics	Luciferins Gene expression	Perfluoro- carbon, μ bubble Vascular interventional

Figure 3: Various modalities of cellular imaging adapted from Arbab et al (Arbab, 2008). CEST: Chemical exchange-dependent Saturation Transfer, CT: computer tomography, PET: positron emission tomography, SPECT: single photon emission computed tomography, mAb: antibodies, IM: intravital microscopy, FRI: fluorescence reflectance imaging, BLI: bioluminescence imaging, US: ultrasound. Sensitivity: the minimum number of cells detectable. Reporter gene: whether transgenic cells can carry a reporter gene that generates contrast.

1.4 MR Contrast

MR imaging rests on the ability to manipulate, with a combination of magnetic fields, and then detect the precession of the protons spins in different tissue such as water and fat. To understand the principles of magnetic resonance relaxation, we begin by considering a set of randomly oriented protons spins. When an external magnetic field, B_0 is applied, a net number of spins are aligned parallel to B_0 . Although thermal energy causes each spin to adopt a parallel or an anti-parallel alignment to B_0 , the population of parallel spins is slightly larger, albeit in the order of parts per million of total spins. As each spin is charged, a resulting magnetic moment, known as the longitudinal magnetization vector, is aligned parallel to B_0 .

The magnetization vector, with a magnitude M_0 , can be imagined to be a spinning top that can remain upright (aligned to B_0), or precess around the vertical axis at its Larmor frequency, ω_0 when tipped. To tip the magnetization vector, an electromagnetic field at the radiofrequency range (rf pulse) is supplied from a nearby ‘transmit’ coil. The rf pulse that tips the magnetization vector from the vertical z-axis through an angle of 90° into the transverse plane xy-plane is called a $\pi/2$ -pulse. The resulting ‘transverse magnetization’ produces a time-varying magnetic flux that induces a voltage in a nearby ‘receive’ coil.

To performing imaging, spatial encoding of the signal from the transverse magnetization is required. As the Larmor frequency is proportional to the applied field B_0 , an additional coil (linear gradient coil) that changes the original B_0 linearly in a specific direction, say z, also creates spins of linearly varying frequency in that direction. On application of a finite bandwidth rf pulse centered at the Larmor

frequency, a layer or 'slice' of spins orthogonal to that gradient becomes excited. By employing more gradient coils, the signal can be encoded in all directions.

1.4.1 T2* Relaxation

The T2* relaxation is best measured and demonstrated with a gradient echo pulse sequence (GRE). To initiate a GRE sequence, an excitation rf $\pi/2$ -pulse is applied so that the spins are tipped onto the transverse plane and allowed to precess freely. The measured transverse magnetization will undergo an exponential decay in the form of

$$M_{xy}(t) = M_{xy}(0)e^{-t/T_2^*}$$

The decay time T2* represents a combination of static field induced (T2') and thermodynamic (T2) effects and the decay rate or R2* relaxation rate is

$$R_2^* = \frac{1}{T_2^*} = \frac{1}{T_2} + \frac{1}{T_2'}$$

During a GRE sequence, no π refocusing pulse is applied, and the acquired signal will decay at the rate of $1/T_2^*$, also known as the R2* relaxation rate. However, in a pulse sequence with π refocusing pulses (eg spin echo), the effects of static field inhomogeneity (T2') are partially removed, such that the measured signal will decay at the rate of $1/T_2$. The decaying signal is shown below.

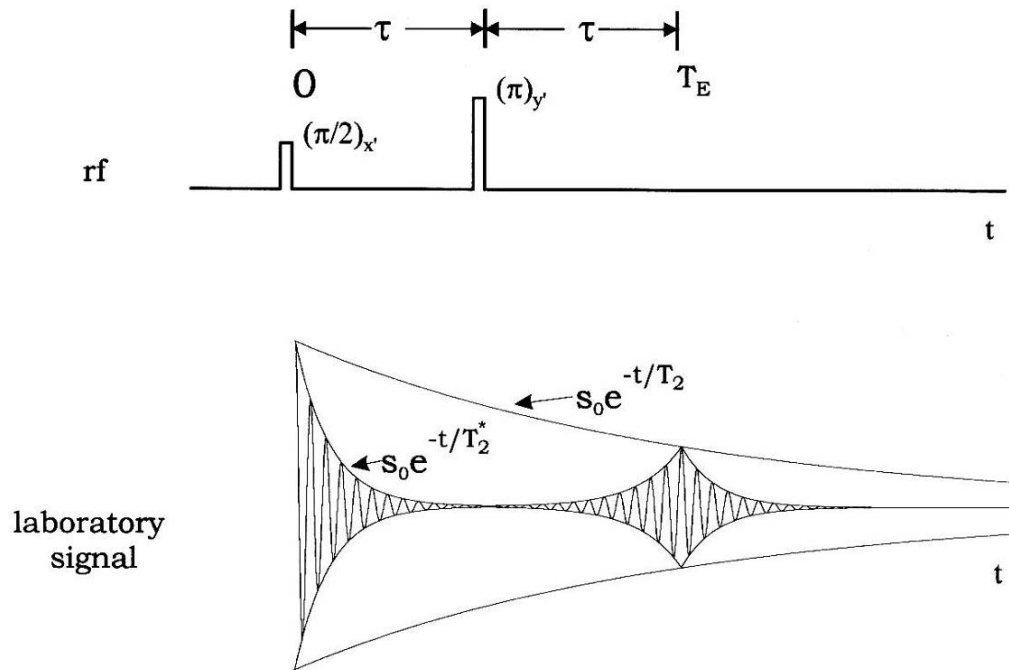


Figure 4: A plot of the transverse magnetization decaying at a rate of $1/T_2^*$ rate. If a refocusing pulse is applied at an interval of τ , the signal reaches another maxima at time $2\tau = T_E$ (Haacke, 1999).

1.4.2 T2 Relaxation

There are two components to T2 relaxation, namely the intrinsic and the diffusion-induced component.

Intrinsic T2: Intrinsic T2 decay is a result of rapid, random fluctuations in the local fields experienced by the spins while precessing in the transverse plane. As the inhomogeneities in these internal fields do not stay fixed in time after the π -pulse, phase accumulation changes with time and the signal decay cannot be recovered with refocusing pulses. As such signal decay occurs without yet taking into consideration the effects of diffusion, this is called the intrinsic T2 decay or also known as the spin-spin relaxation.

Diffusion-induced T2: As mentioned, spin echo methods can only partially recover signal loss from the effects of external field inhomogeneity (T_2'). While a refocusing pulse can help fixed-position spins to rephase, diffusion causes change in position of spins after each π -pulse. The spin echo cannot recover this type of loss of phase coherence.

One method of R_2 measurements is based on the Hahn spin echo sequence where a π refocusing pulse is applied at time = τ after the rf excitation, such that the signal is refocused and acquired at time = $2\tau = TE$. By changing the TE, a decay plot of M_{xy} against TE can be obtained with the decay rate rate being the $1/T_2$ or the R_2 relaxation rate.

However, spins are subjected to various amounts of diffusion effect depending on TE. To minimize a build-up of phase accumulation from diffusion, a Carr-Purcell-Meiboom-Gill (CPMG) sequence can be used to insert a series of spin flips between the $\pi/2$ pulse and signal acquisitions as shown in Figure 5.

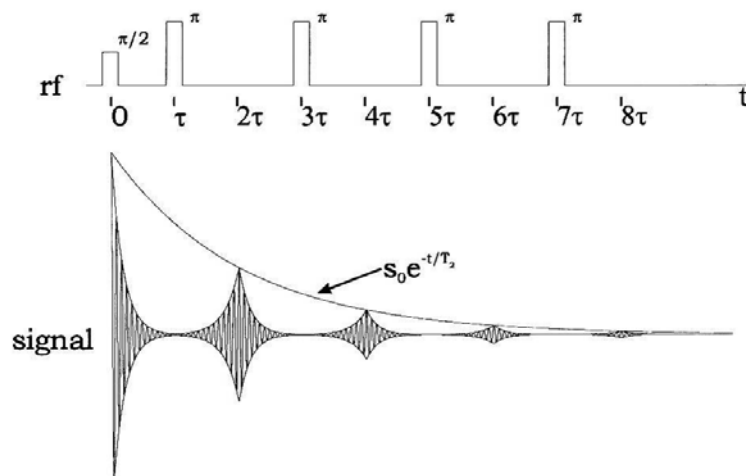


Figure 5: Applying multiple, regularly spaced refocusing pulse at $(2n-1)\tau$ and acquiring signals at $2n\tau$, where n is 1, 2, 3, (Haacke, 1999)

Similarly, a decay plot of M_{xy} against $2n\tau$ can be obtained with the decay rate being the R2 (CPMG) relaxation rate. When τ is short, the time allowed for spins to diffuse between refocusing is low and the amount of recovered signal is large.

1.4.3 Contrast agents

Contrast agents are typically injectable substances that have affinity for specific tissue, and can increase the signal intensity difference between the specific tissue and background tissue. Contrast agents are substances that can increase the signal intensity difference between the target tissue and background tissue. Their ability to alter contrast can be quantified by the relaxation times or rates. There are 3 types of relaxation times: the T1 longitudinal, T2 transverse and T2* transverse relaxation times. The inverse of the relaxation times are the relaxation rates, which are denoted as R1, R2 and R2* respectively. The relaxation rate per unit concentration is known as the relaxivity, denoted as r1, r2 and r2* respectively. Iron oxide based contrast agents are known as T2 agents as they induce the most contrast change in T2 or T2*-weighted MRI sequences. The relaxivities r2 and r2* are therefore important parameters of an iron oxide agent. In cellular MRI, contrast agents are attached to or contained within the transplanted cells such that the cells become brighter or darker and hence become identifiable on images.

1.4.3.1 T1 Contrast Agents

Low molecular weight paramagnetic T1 organic molecular agents generate positive contrast by increasing the signal intensity (hyperintensity) in their vicinity on T1-weighted images. In 1988, gadopentetate dimeglumine (Gd-DTPA) became the first paramagnetic MRI contrast agent to be marketed in the United States for clinical use

(Nelson, 1995). Gd-DTPA and other small molecule chelates of gadolinium extravasate rapidly into the extracellular space and are typically used for the contrast enhancement of differentially perfused tissue. In culture, they are taken up by cells via diffusion and at limited amounts. Attempts to improve cellular loading of Gd include mounting Gd chelates on a macromolecular backbone (Modo, 2002) and encapsulation of Gd chelates in polymeric particles (450 nm diameter) to tap on more efficient internalisation pathways (Tokumitsu, 1999). The inherent difficulty of using T1 agents is the requirement for water molecule access to the Gd inner coordination sphere electrons for contrast enhancement. When cellular loading is increased, intracellular Gd experience less water access and the proximity among Gd ions induces a susceptibility T2 effect and compromises T1 enhancement.

1.4.3.2 T2 Contrast Agents

T2 or susceptibility effect agents generate negative contrast by decreasing signal intensity (hypointensity) in their vicinity on T2-weight images. T2 agents include small molecule agents like Eu-DTPA and Yb-DTPA, and particulate agents. The latter, generally known as superparamagnetic iron oxide nanoparticles (SPIO) offer the best sensitivity in cellular MRI to date. They typically consist of multiple iron oxide primary crystalline nanoparticles, held together or by a polymeric matrix. When cells are sufficiently loaded with SPIO, they behave like magnetized spheres in the order of microns in diameters (Bowen, 2002). In this dimension, they generate the maximum possible signal intensity change per mole of agent (Gillis, 2002). (Further details about such signal change can be found in Section 1.4.4.2). It is also theoretically possible to quantify cell count per imaging voxel and also differentiate between intra and extracellular SPIO (Kuhlpeter, 2007).

A group of negative contrast agents depends on the chemical exchange saturation transfer (CEST) effect. Specific off-resonance pulses reduce the signal intensity of water protons associated with the agent (exchangeable protons) by transferring saturation magnetization of these protons to the bulk water. Paramagnetic lanthanide chelates (PARACEST agents) help to widen the resonance frequency difference between the exchangeable protons and bulk water to improve specificity. By labelling different cell types with PARACEST agents of different frequencies prior to their injection into an animal, the cells can be tracked independently. (Aime, 2005). Subtraction of images taken with and without the off-resonance pulse will theoretically produce images of only the labelled cells, although this introduces the possibility of misregistration due to physiologic and macroscopic motion.

Another off-resonance imaging approach utilized perfluoropolyether emulsion particle labelled cells to enable detection through fluorine-19 (^{19}F) MRI (Ahrens, 2005). This is useful for increasing the specificity of cellular tracking, as tissues produce negligible signal at the resonance frequency of ^{19}F . *In vivo* application of these techniques is challenged by signal to noise issues and chemical shift artefacts from the body.

1.4.4 Theoretical Relaxation Induced by Homogenous Magnetised Spheres

Theoretical models have been proposed to describe the transverse relaxation of a two phase system consisting of only homogenous magnetised particles distributed within a homogenous medium, eg water. The particles in these models are motionless and magnetically independent from one another, while protons diffuse freely among the particles. The models propose that, within the limits of low particle concentration and

high particle magnetization, the relaxation rates $R2^*$ and $R2$ are dependent on the particle diameter (d). The relationship is made up of three regimes (Figure 6) separated by ranges of d :

- Motional averaging regime (MAR): $d < d_{\text{SDR}}$
- Static dephasing regime (SDR): $d > d_{\text{SDR}}$
- Echo-limited regime (ELR): $d > d_{\text{EL}}$

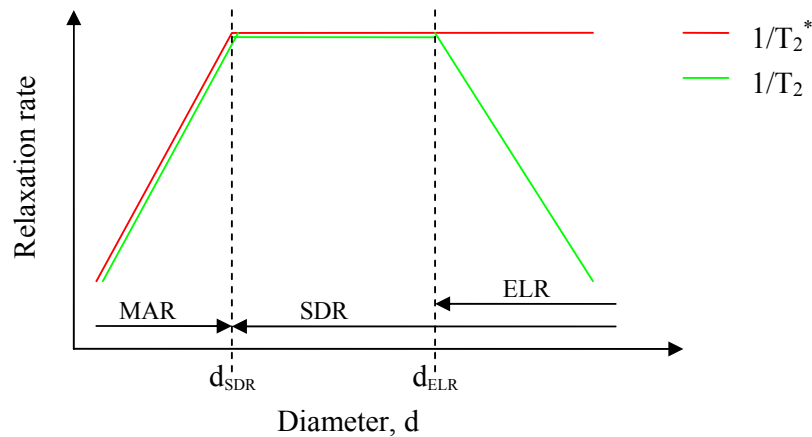


Figure 6: Relaxation rate dependence on particle diameter, d .

Relaxation takes place in distinct regimes due to two components that contribute to proton relaxation: a coherent component that is related to protons experiencing slightly different local fields and an incoherent component that results from protons interchanging positions due to diffusion (Ziener, 2005). The correlation time τ_D relates to the time a proton stays with a particular local field and is dependent on the particle diameter, d . When d or τ_D is large, the incoherent component (diffusion) becomes negligible and the coherent component (spatial) dominates. This is because

the source of inhomogeneous field is so large that even as protons diffuse over time τ , the change in local field is negligible such that the protons appear static, hence the theory of static dephasing regime. Therefore with large particles and without π refocusing pulses, relaxation is in the SDR, while with refocusing pulses, it is in the ELR.

1.4.4.1 Motional Averaging Regime

This regime of relaxation occurs under the conditions of

- $d < d_{\text{SDR}}$
- long interval between refocusing echo pulse, ie $\tau_{CP} \gg \tau_D$
- $\tau_D \ll (1/\Delta\omega_r)$

In this regime, the relaxation effect due to diffusive motion of spins is much greater than that due to spatial variations of field created by the magnetic particles. The diffusive motion of spins thus averages out effects of the individual particle and the system is in a motionally averaged situation. The relaxation rate is given by the outer sphere relaxation theory (Roch, 2005).

$$1/T_2 = 1/T_2^* = (16/45)v\tau_D(\Delta\omega_r)^2$$

where v is the fraction volume, d is the particle diameter, and τ_D the diffusion time is given by

$$\tau_D = d^2 / 4D$$

and is defined as the time taken for a water molecule to diffuse a distance of $d / \sqrt{2}$.

$\Delta\omega_r$ is the rms angular frequency shift at the particle equator,

$$\Delta\omega_r = \gamma B_{eq}$$

where B_{eq} is the equatorial field of the particle and γ is the proton gyromagnetic ratio.

The outer sphere relaxation describes the variation of relaxation rate with particles size, for a constant v and $\Delta\omega_r$. The proton diffusion rate with respect to the particles ($1/\tau_D$) is large compared to $\Delta\omega_r$, hence it determines the relaxation rates. Therefore, as τ_D increases, the effect of spatial variation of field created by particle increases. In other words, the outer sphere relaxation shows that the same amount of magnetized material is much more effective in causing proton relaxation when distributed as fewer large particles than as a greater number of smaller ones (Gillis, 1987).

1.4.4.2 Static Dephasing Regime

This regime of relaxation is valid under the conditions of (Gillis, 2002)

- $d > d_{SDR}$
- long interval of refocusing echo pulse, ie $\tau_{cp} \Delta\omega_r \geq 1.35$
- $\tau_D \gg (1 / \Delta\omega_r)$

In the MAR, the relaxation rates increase as particles become larger. As particle diameter increases further, the signal decay due to the local differences in precessing frequencies occurs faster than the proton diffusion phenomena manage to average out the phases of different nuclei. This is the so-called static dephasing regime (the word “static” refers not to proton spin rotation but to proton translational motion)

(Yablonskiy, 1994). In this regime, the T_2^* relaxation rate is (Brooks, 2001; Brown, 1961)

$$1/T_2^* = (2\pi\sqrt{3}/9)v\Delta\omega_r$$

The relaxation rate is at the maximum and is independent of diameter when $d > d_{SDR}$

$$d_{SDR} = \pi\sqrt{15}/(4\Delta\omega_r)$$

Moreover, when the relaxation is not interrupted by refocusing pulses in the diameter range of $d_{SDR} < d < d_{EL}$, then $1/T_2^* = 1/T_2$

1.4.4.3 Continuous Theories

The MAR and SDR are discontinuous theories which operate at the limits of $\tau_D \ll (1/\Delta\omega_r)$ and $\tau_D \gg (1/\Delta\omega_r)$, respectively. A few approaches have been used to describe the theoretical relaxation rate with respect to variation in d or τ_D , continuously across the two regimes. One is the Gaussian approximation that assumes spins within a voxel have normally distributed precessional frequencies (Kennan, 1994). The other approach approximates the spin diffusion with stochastic transitions dynamics (Ziener, 2005).

The third approach is with the use of empirical models where the relaxation rate was found to be (Yung, 2003)

$$R_2^* = \frac{v\delta\omega(0.52)x^2}{1+0.39x^2}$$

where

$$x = \frac{d}{2} \sqrt{\frac{\delta\omega}{D}}$$

Unfortunately, there is no empirical model for the continuous relaxation regime using a CPMG sequence.

1.4.4.4 Echo-Limited Regime

The ELR describes the relaxation rates when dephasing spins are refocused by multiple refocusing pulses placed at a fixed interval τ_{CP} apart, such as with CPMG sequences. There are two types of ELR, one with strongly magnetised spheres where $\tau_{CP}\Delta\omega_r > 1.35$ (Gillis, 2002). The other is with weakly magnetised spheres where $\tau_{CP}\Delta\omega_r < 1$. With weakly magnetized particles, it is possible that $d_{ELR} < d_{SDR}$, such that SDR cannot be reached (Brooks, 2001). The relaxation rates with strongly magnetised spheres will be discussed first.

With strongly magnetised spheres, SDR is reached as diameter increases and R2 and R2* relaxation rates become independent of diameter. Gillis et al proposed that protons sufficiently close to the particles experience gradient so strong that their magnetization decay too rapidly to be observed on MRI (Gillis, 2002). They showed that as the diameter increases further, T2 relaxation rate becomes (Gillis, 2002)

$$1/T_2 = (2.25\nu / \tau_D) x^2 y^5$$

where $x = \Delta\omega_r \tau_{cp}$ and $y = [(\alpha + \beta\nu x) / x]^{1/3}$

Gillis obtained $\alpha \approx 1.35$ and $\beta \approx 1$ which were close to numerical simulation results of $\alpha \approx 1.34$ and $\beta \approx 0.99$. The simulation was carried out with the parameters:

- small ν (<10 ppm)
- $\tau_D \geq 0.01$ ms
- $B_{eq} = 1$ T
- $\tau_{cp} = 0.1$ to 20 ms

The particle diameter where ELR intersects SDR is (Gillis, 2002)

$$d_{ELR} = 2.58x\sqrt{Dy^5 / \Delta\omega_r}$$

With weakly magnetised spheres where $\tau_{cp}\Delta\omega_r < 1$, SDR will not be reached as $d_{EL} < d_{SDR}$. Instead, the ELR intersects with the MAR and the T_2 relaxation is described by $1/T_2 = (2.25\nu / \tau_D)x^2y^5$ with $y = 1$ (Brooks, 2001).

Interestingly, when cells are loaded with iron oxide particles, they seem to have relaxation properties similar to those large magnetic spheres. Ferumoxtran or ferucarbotran were compartmentalised in cells, they produce less signal on T2-weight images but similar signal T2*-weighted images (Simon, 2006; Henning, 2009). These results suggest that the labelled cells, like large magnetic spheres, produce relaxation in the ELR regime.

1.5 Iron Oxide Particles

The majority of particles used for cellular MRI are from commercial sources. The two most commonly used particles, approved for clinical liver imaging are ferumoxide (trade name in Europe: Endorem, trade name in US and Japan: Feridex, AMAG Pharmaceuticals, Lexington, MA, USA) (Reimer, 1998) and ferucarbotran (trade name in Europe and Japan: Resovist®, Bayer Schering Pharma, Berlin, Germany) (Reimer, 2003). The usage of ferucarbotran in future is in doubt, as Bayer-Schering recently withdrew it from global marketing, citing insufficient clinical utilisation as the primary reason. At the moment, only ferumoxide can be purchased from commercial sources. In this section, we will look at the synthesis methods and properties of SPIO and other iron oxide particles.

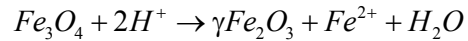
1.5.1 Iron Oxide Particle Synthesis

The synthesis methods for iron oxide particles are fairly simple without the need for complex purification procedures like ultracentrifugation or size exclusion chromatography. There are two main synthesis methods: alkaline coprecipitation of iron salts and thermal decomposition of iron organic precursors.

The co-precipitation method was first described by Massart more than 2 decades ago (Massart, 1981). Iron oxide in the form of magnetite is formed by aging stoichiometric mixture of ferrous and ferric salts in an inert atmosphere at pH between 9 and 14 by the following reaction



Magnetite particles appear as a lustrous black powder. While magnetite has the highest magnetization among iron oxides, it is sensitive to oxidation by atmospheric oxygen to become maghemite by the following reaction (Laurent, 2008).



Ferucarbotran is an example where maghemite instead of magnetite was used. This co-precipitation method allows some form of control over particle diameter by adjustment of the pH, ionic strength, temperature or ratio of Fe^{2+} to Fe^{3+} salts to achieve a size range from 4 to 15 nm. Co-precipitating reverse micelles that contain iron salts can provide better size control but this method requires prior preparation of stable micelles (Lee, 2005).

The thermal decomposition route offers even greater control on particle diameter and produces more uniformly sized particles. Diameters of 5 to 22nm were produced by heating a complex of iron chloride and oleic acid (Park, 2004). By changing the iron precursor, for example to $Fe(CO)_5$, diameter control in steps of 1 or 2 nm was achieved (Park, 2005).

1.5.2 Encapsulation of Iron Oxide Particles

The naïve iron oxide particle surface is uncharged and neither hydrophilic nor hydrophobic. An additional coating is necessary to provide repulsive forces to keep particles from aggregating in a dispersing medium. In the classical ferrofluid, this is achieved by a coat of oleic acid such that the particles are suspendable in organic solvents like hexane. A requirement of particles for biomedical application is the ability to suspend in aqueous media, hence the need for a hydrophilic particle surface. An early method of achieving hydrophilic coating is through the *in situ* incorporation

of polysaccharide during the co-precipitation process followed by size selection membrane filtration (Groman, 1989). The size and structure of the resulting composite particle is dependent on the type and molecular weight of the polysaccharide, due to the polar interactions of the polymer with iron oxide surfaces during co-precipitation (Pardoe, 2001). While ferumoxide is coated with dextran, carboxydextran is absorbed on the surface of ferucarbotran. Based on the narrow size distribution of ferucarbotran in comparison to ferumoxide, it is likely to have undergone filtration to select for particles of about 60nm in diameter. Ferucarbotran is synthesized by Meito Sanyo Co. Ltd. (Japan) (Reimer, 2003), and the details of the method are pending patent approval and inaccessible (Briel, 2007).

Other stabilizing molecules have been used to produce particles <30nm, including 4.5 generation dendrimers (Bulte, 2001), dimercaptosuccinic acid (Wilhelm, 2003) or citric acid (Stroh, 2005). Larger particles of 120nm were produced by coating with poly(ethylene glycol) or its derivatives (Kim, 2003). Particles up to micrometers in diameter (from Bangs Laboratories, Fishers, IN, USA) were prepared by an alternative route in which pre-formed divinyl benzene microspheres are expanded in an organic solvent, infused with iron oxide particles and the solvent replaced by an aqueous medium (Hinds, 2003). The strategy of using pre-formed polymer particles has allowed high iron oxide weight content (IOwt%) of over 60%, as seen with the 0.9 μ m Bangs particles (Hinds, 2003). Such weight content is considerably high given that large particles usually has lower IOwt% than small particles and ferucarbotran has a IOwt% of 58.4% (Reimer, 2003). The IOwt% of ferumoxide cannot be found in the literature.

1.5.3 Particle Size Measurement by Light Scattering

The main application of quasi-elastic light scattering is measurement of water-suspended particles sizes. A proper explanation of the phenomenon of light scattering was first given by Lord Rayleigh in late 19th century. In the early days, chaotic light sources, such as the mercury arc lamp were used, restricting measurement to time-averaged or static properties, hence the name ‘static light scattering’ (SLS). An example of an SLS application is the determination of particle size by forward light scattering. With the advent of coherent light sources, it became possible to measure the temporal characteristics of scattered light, hence the term dynamic light scattering (DLS). Modern instruments record the scattered light with digital autocorrelators, instead of spectrum analyzers, thus giving DLS the alternative acronym of photon correlation spectroscopy (PCS).

DLS starts with the interaction of light with matter. Light, being an oscillating electromagnetic field, can bring the charged surface atoms on the particle surface into oscillatory motion. The acceleration of charges results in the release of electromagnetic field in all directions (Rayleigh scattering), which is the scattered light in this case. In a perfectly homogeneous material, the light scattered by individual atoms or molecules interferes destructively so that no scattered light is observed. With a suspension of particles, the observed scattered light is due to the difference in refractive index between the particles and the dispersing medium.

The light source is typically a collimated, monochromatic laser beam known as the incident beam, with a wave vector \vec{k}_i where magnitude $|\vec{k}_i| = 2\pi m_1 / \lambda_0 = m_1 \omega_0 / c$, where m_1 is the refractive index of the liquid, and λ_0 and ω_0 are the wavelength and

circular frequency of light in vacuum, respectively. When the incident beam hits an immobile particle, a scattered beam, with wave vector \vec{k}_s is produced as shown in

Figure 7, with $|\vec{k}_i| \approx |\vec{k}_s|$

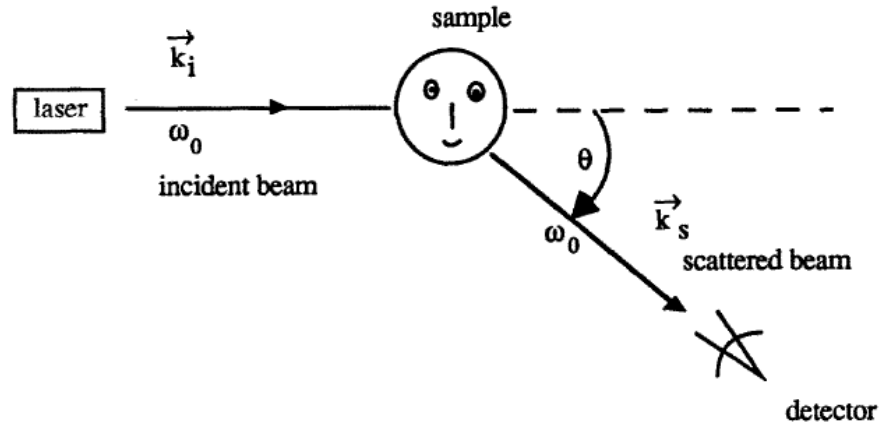


Figure 7: Illustration of scattering of the incident beam and detection of the scattered beam

With scatter wave vector defined as $\vec{q} = \vec{k}_i - \vec{k}_s$, the magnitude,

$$|\vec{q}| = q = \frac{4\pi m_1}{\lambda_0} \sin \theta / 2$$

In reality, all the particles are in Brownian motion, each with a different velocity. The scattered beam frequency of an immobile particle is unchanged but that of a mobile particle is $\omega_0 + \Delta\omega$, where $\Delta\omega$ is the frequency shift due to one particle. As each particle has a different velocity and the average frequency shift is related to the half height half width $\Delta\omega_{1/2}$ of a Lorentzian distribution, given by

$$\Delta\omega_{1/2} = Dq^2$$

where D is the translational diffusion coefficient of the particle.

With digital autocorrelators, this measurement can be made in the time domain with the intensity autocorrelation function $g_2(\tau) = \langle I(t) \cdot I(t+\tau) \rangle$, which is the averaged product of two intensity, I acquired time delay τ apart. With short delays, correlation is high and $g_2(\tau)$ is large. As the delay increases, particles diffuse and $g_2(\tau)$ diminishes. Data are typically collected over a delay range of 100ns to several seconds. The resulting intensity autocorrelation function when plotted against τ is described by

$$g_2(\tau) = A + Bg_1^2(\tau) \quad [1]$$

and the field autocorrelation function, $g_1(\tau)$ is a monoexponential decay for non-interacting spherical particles,

$$g_1(\tau) = \exp(-\Gamma \tau)$$

with decay rate $\Gamma = Dq^2$.

The measured autocorrelation functions can be solved by numerically fitting them to functions of known decay rates. And the particle diameter is related to D by the Stokes-Einstein expression

$$d_H = \frac{kT}{3\pi\eta D}$$

where k is Boltzmann's constant, T is absolute temperature, η is viscosity of the medium and d_H is hydrated particle diameter.

Practically, the particles under measurement do not have a common discrete size, but rather a distribution of diameters d_i that are related to different decay rates Γ_i , such that the sum of exponential for $g_1(\tau)$ is

$$g_1(\tau) = \sum_{i=0}^n c_i \exp(-\Gamma_i \tau)$$

where c_i is the normalized intensity weight for particles with decay rate Γ_i . And in the continuous form, $g_1(\tau)$ is

$$g_1(\tau) = \int_0^{\infty} C(\Gamma) \exp(-\Gamma \tau) d\Gamma$$

where $C(\Gamma)$ is the normalized intensity-weighted distribution of decay rates. $C(\Gamma)$ is obtained from the inverse Laplace Transformation of $g_1(\tau)$ and often plotted against hydrated diameter, d_H to show the size distribution.

1.6 Cellular MRI

There has been much interest in cellular tracking by MRI, as its balance of spatial resolution and sensitivity, as well as its lack of ionising radiation, makes it an attractive and practical modality for cellular detection. MRI has been used to track the movement and incorporation of administered cells in tissue engineering, myocardial cellular transplantation, and cellular homing and migration studies.

1.6.1 MRI in Tissue Engineering

Tissue engineering has progressed from just the use of artificial scaffold to the incorporation of cells or tissue onto biocompatible materials prior to their implantation to improve tissue regeneration. With the integration of imaging techniques, the participation of cells in tissue repair can be monitored. The approach by various research groups is similar: to first label cells with a clinical iron oxide contrast agent, seed the labelled cells on an engineered implant (the sequence of the first two steps can be reversed) and introduce the cell-loaded implant into a disease animal. MRI of ferumoxide-labelled human adult MSC on collagen scaffold has been demonstrated *in vitro* (Terrovitis, 2006), as have labelled MSC within gelatine sponge *in vivo* (Ko, 2007). By labelling aortic smooth muscle cells with ultrasmall superparamagnetic iron oxide particles (USPIO) prior to seeding them on a polymeric vascular graft, researchers were able to evaluate the graft performance *in vivo* (Nelson, 2008). The cells were visualised to have successfully remained in the scaffold vicinity for up to several weeks. The success of MR monitoring may be limited by the MR properties of implants used. Ferrous metallic implants and

voluminous, water-impenetrable implants may cause susceptibility artefacts and may not provide sufficient contrast to identify the hypointense cells (Nelson, 2008).

1.6.2 MRI in Cellular Transplantation

In therapeutic attempts without engineered scaffolds but where static cells are monitored, labelled stem cells were directly injected into myocardial infarcts. Ferumoxide-labelled (Kraitchman, 2003) and micron-size iron oxide particles (MPIO)-labelled (Stuckey, 2006; Hill, 2003) allogeneic MSC have been injected intramyocardially into infarcted hearts and their location studied up to 16 weeks in various animal models. In a different study, intravenously injected iron oxide-labelled, allogeneic MSC homed to the myocardial infarct in a canine model and persisted for at least one week (Kraitchman, 2005). However, the successful identification of hypointense cells may be complicated by haemorrhage from microvascular obstruction during infarct reperfusion (van den Bos, 2006). Haemorrhage causes susceptibility-induced signal voids that are similar to iron oxide induced ones.

1.6.3 MRI in Homing and Migration Studies

The homing of intravenously injected MSC has been demonstrated in other disease models as well. The arrival of ferumoxide-labelled MSC at injured arteries (Gao, 2007) and atherosclerotic plaques (Qiu, 2007) was monitored by MRI. When intravenously injected into animals with cerebral infarcts, ferumoxide-labelled MSC homed to the lesion periphery as soon as six days post injection (Jendelova, 2003). The use of MRI tracking to optimise cellular delivery was also demonstrated. Ferumoxide-labelling provided evidence of better MSC engraftment when cells were

given through the inner carotid artery rather than intravenously in a rodent stroke model (Walczak, 2008).

A number of cell types have been shown to be able to migrate towards the infarct periphery when transplanted intracerebrally. Ferumoxide-labelled MSC (Jendelova, 2003), ferumoxide-labelled neural stem cells (NSC) (Zhu, 2006) or USPIO-labelled ESC (Hoehn, 2002) were transplanted and shown to migrate from the contralateral hemisphere and across the corpus callosum to the infarct periphery. The same phenomenon was demonstrated using NSC labelled with a gadolinium-dextran T2 agent (Modo, 2002). When transplanted to the ipsilateral side of the stroke, ferumoxide-labelled NSC were reported to migrate along the infarct periphery (Guzman, 2007). In a Huntington's disease model where lesions were induced by quinolinic acid, ferumoxide-labelled MSC showed a distinct migration route toward the lesions (Sadan, 2008).

1.6.4 Clinical Trial of Cellular MRI

To date, there have only been two reports of MRI cellular tracking in clinical trial. Autologous dendritic cells (DC) were labelled with ferumoxide or ¹¹¹In-oxine prior to their injection into the lymph nodes of 11 stage-III melanoma patients (de Vries, 2005). Post-injection verification by MRI was found to be superior to just ultrasound-guided injection alone. Among 3 out of 8 patients, MRI showed unsuccessful intranodal delivery and the observation corresponded to the lack of DC migration to the draining lymph nodes. Detection of migrated DC to draining lymph nodes was more reliable by MRI compared to scintigraphy, as verified by histology of resected nodes. An inherent advantage of MRI is the anatomical localisation of DC at injection

sites or after migration. Scintigraphy is the superior quantification modality and ^{111}In -oxine labelling may remain a useful co-label with MRI contrast agent until MRI quantification matures. The other clinical trial involved patients with traumatic, open head injuries where loose neural tissue is cultured in a media known to proliferate NSC (Zhu, 2006). Following NSC labelling with ferumoxide, the cells were injected intracerebrally at four sites around the lesion. Weekly MRI assessment showed that the lesion periphery began to darken progressively while injection site hypointensity faded from 1 to 3 weeks post-transplantation. This was not observed in the control patient that received unlabelled NSC. As the patient survived the trauma and transplantation, histology has not been possible.

The two clinical trials showed that MRI labels are safe and that clinical detection of the labelled cells is possible. To achieve the goal of clinical cellular MRI, more off-label use of approved contrast agents, such as ferumoxide or ferucarbotran in cellular therapy clinical trials is needed. Currently, the FDA requires preclinical studies to be performed in experimental diseases models using labelled and unlabelled cells along with sham controls to assess the toxicity and any alteration in morbidity and mortality (Arbab, 2008). Serum chemistry analysis, histology correlation and experimentation in a clinical grade manufacturing practice (CGMP) facility are probable requirements in the future.

1.6.5 Cellular Imaging with Iron Oxide Particles

The development of iron oxide particles as MRI contrast agents took place more than two decades ago. During that time, Gd-DTPA was a commonly used contrast agent (Saini, 1987), but it did not improve the detection of liver carcinoma in clinical

studies (Carr, 1984). In fact, liver metastases were often obscured due to the extracellular distribution of Gd-DTPA into both neoplastic tissue and normal liver (Saini, 1986). This limitation was largely due to the poor temporal resolution of clinically available spin echo imaging sequences at that time, but this limitation has been overcome by recent development and implementation of fast breath-held spoiled gradient echo sequences. Till today, gadolinium-based dynamic contrast enhancement remains the key method for the detection and characterisation of liver masses in most centres. Because of the limitations of Gd-enhanced T1-weighted MRI in the late 1980's and early 1990's, superparamagnetic iron oxide particle (SPIO) attracted attention as an alternative for this application because of their large magnetic moment in a magnetic field, absence of remnant magnetization when the field is removed (superparamagnetism) and their unique biodistribution (Mendonca, 1986; Saini, 1987).

When injected intravenously, these particles home to the reticuloendothelial system (Saini, 1987) and are taken up by macrophages in the liver, known as Kupffer cells. Presence of SPIO causes darkening of normal hepatic tissue on T2-weighted MR images, while liver carcinomas and metastases remain bright. This application of SPIO led to the 1996 FDA approval of ferumoxide (US trade name: Feridex®, Europe trade name: Endorem®, research name: AMI-25, generic name: ferumoxide), which is administered by dilution in 5% dextrose and slow infusion. Ferumoxide is a composite particle that consists of multiple 5nm iron oxide nanoparticle cores coated with dextran and its hydrated diameter is 120-180 nm (Raynal, 2004). In 2001, European market approval was granted to a smaller SPIO, ferucarbotran (trade name: Resovist®, research name: SHU 555A, generic name: ferucarbotran), which can be given intravenously, undiluted by bolus injection. Ferucarbotran has nanoparticle

cores of 4nm coated with carboxydextran and its hydrated diameter is 62nm (Reimer, 1995; Reimer, 2003).

Smaller than SPIO is a class of particles known as ultrasmall SPIO (USPIO), with diameters less than 30nm (Weissleder, 1990). USPIO provides a mixture of paramagnetic blood pool positive enhancement and intracellular superparamagnetic reticuloendothelial cell negative enhancement, and has been injected intravenously to differentiate between darkened normal lymph nodes and metastatic ones that remain bright (Weissleder, 1990). An USPIO undergoing clinical trials is ferumoxtran (trade name: Sinerem/Combidex®, research name: AMI-227, generic name: ferumoxtran) which has a 5nm iron oxide core and 17-20 or 21-30nm hydrated diameter as a result of its dextran coat (Sharma, 1999; Jung, 1995). A preclinical particle of similar size as USPIO is the monocrystalline iron oxide nanocompound (MION) developed by Massachusetts General Hospital (Shen, 1993). Each particle has a single 4-5nm core coated with dextran, resulting in a hydrated diameter of 20nm. Two other ultrasmall preclinical particles that are coated with monomers are the citrate-coated very small superparamagnetic iron oxide particles (VSOP, 5nm core, 8nm hydrated diameter) (Taupitz, 2000) and the dimercaptosuccinic acid-coated anionic magnetic nanoparticle (AMNP, 8nm core, 30nm hydrated diameter) (Wilhelm, 2008).

The imaging of inflammation processes has made use of the ability of macrophages to take up iron oxide particles *in vivo*. The imaging of macrophages involved in atherosclerotic plaques was demonstrated by an intravenous injection of SPIO (Ruehm, 2001; von Zur Muhlen, 2007). Moreover, it was found that USPIO uptake was in predominantly ruptured and rupture-prone atherosclerotic lesions, differentiating such lesions from intact ones (Kooi, 2003).

Iron oxide particles can also be used for the imaging of neuroinflammation following ischemic stroke. The first use of SPIO in a stroke study was in 1989, where rats were injected with ferumoxide 1 to 24 hours after a stroke by middle cerebral artery occlusion (Bradley, 1989). Ischemic volume was estimated as normal brain tissue was darkened while ischemic tissue remained bright from lack of perfusion. Macrophages infiltrating an ischemic stroke can be differentiated from resident macrophages. By intravenously (IV) injecting rodents with SPIO 24 hours prior to imaging, MR images showed darkened stroke periphery at day 6 or darkened stroke core at day 8 post-stroke. The specific darkening was due to iron-laden macrophages infiltrating the stroke site (Kleinschnitz, 2003). Interestingly, when SPIO/USPIO were IV delivered two to five hours post-stroke, the stroke periphery was darkened as well but was due to the focal accumulation of SPIO/USPIO in the occluded vessels (Kleinschnitz, 2005; Wiart, 2007). Therefore, the IV administration of SPIO/USPIO can provide the monitoring of: i) ischemic development and ii) macrophage infiltration into the stroke site (Bendszus, 2007), and clinical phase II trials have been explored for imaging neuroinflammation (Saleh, 2004).

Another application of iron oxide particles was the *ex vivo* labelling of target cells to enable MR tracking of the labelled cells post-transplantation, which was first reported by Ghosh et al (Ghosh, 1990). The particles were introduced into the culture medium of cells and incubated for hours to encourage particle uptake by endocytosis into intracellular compartments. The labelled cells appeared as hypointense regions on MR images, similar to Kupffer cells that have taken up intravenously injected SPIO. In the early 1990s, neural tissues (Norman, 1992) and T cells (Yeh, 1993) were labelled with iron oxide particles and transplanted into healthy animals to demonstrate that the labelled cells can be visualized *in vivo*.

Since the early successes, the method has been applied to label more cell types, including monocytes, glioma cells, macrophages and oligodendrocytes progenitors (Bulte, 2004). Despite the apparent ability to label virtually any cell type, the detection of target cells has been restricted by the amount of particles taken up. The quantity of iron oxide attached to a cell is an absolute determinant of cell detectability. With a greater amount of iron oxide loading per cell, there is less emphasis on hardware requirements and imaging duration to achieve the required SNR and resolution for cellular detection (Heyn, 2005).

The quantity of particles taken up by cells appears to increase with concentrations of particle in the culture medium, although high concentrations have been associated with free radical generation, decrease in cell proliferation and apoptosis (van den Bos, 2003). Cell labelling can be achieved by binding iron oxide particles onto the cellular surface or incorporating them into the intracellular space. The latter is favoured as particles at the cell surface can hinder cell-cell interaction by the blockage of cell surface receptors. Even when the particles are internalised, it is important that the particles do not alter the properties or functions of the cell, particularly with high amounts of iron loading. Hence, labelled cells are often compared with intact cells in terms of viability and proliferation, and in addition, the differentiation capacity for stem cells. A potential problem with using exogenous label is the reliability of the iron oxide particle in reporting the true location or fate of the transplanted cell. For example, internalised particles may be exocytosed *in vivo* or transplanted cells may die due to label toxicity, and cell debris and particle may be engulfed by host macrophages giving rise to false positives (Coyne, 2006). Hence, it is important to develop methods of increasing cellular uptake while retaining cellular functions.

1.6.6 Mechanisms of Cellular Uptake

The amount of iron oxide particles internalised by cells is often expressed as picograms of iron per cell. The amount of iron per cell determines the MR detectability of the cells. High iron loading can relax the hardware requirements to detect few cell numbers. When labelling phagocytic cells like macrophages, high amounts of iron loading (61 pg/cell) can be achieved with clinically available SPIO (Heyn, 2006). However, the labelling of non-phagocytic cells such as MSC with SPIO has been less efficient, with approximately only 9 pg/cell (Mailander, 2008), and may require improvement of the labelling method to achieve higher iron loading. An understanding of the uptake mechanism is therefore important.

The various mechanisms of cellular uptake of particle have been reviewed in detail by Unfried et al (Unfried, 2007). With reference to Figure 8, the possible pathways of cellular uptake of nanoparticles are phagocytosis (1), macropinocytosis (2), clathrin-mediated endocytosis (3), non-clathrin-, non-caveolae-mediated endocytosis (4), caveolae-mediated endocytosis (5) or diffusion (6). During phagocytosis, particles become engulfed via specific membrane receptors (e.g., scavenger receptors), leading to the formation of an early phagosome (1A) Subsequent particle processing includes phagosome maturation which is described to be dependent on the involved receptor and may include the formation of a late phagosome (1B) and a lysosome (1C). Processes 2-5 are collectively known as receptor mediated endocytosis (RME). During particle ingestion via macropinocytosis, a macropinosome (2A) is formed which also passes various maturation steps resulting into the formation of a lysosome (1C). Clathrin-mediated endocytosis occurs at specific membrane regions, referred to as clathrin coated pits (3A). Following formation of a clathrin-coated vesicle (3B) and

its uncoating (3C) with clathrin monomer recycling, particles are subsequently processed by early endosomes (3D), multivesicular bodies (3E) and late endosomes (3F). Endocytotic processes without involvement of clathrin or caveolin are referred to as non-clathrin, non-caveolae-mediated endocytosis (4). Better known is the particle uptake via so called lipid rafts (5A), which leads to the formation of caveosomes (5B) with possible particle transfer into the cytosol or the endoplasmic reticulum (5C). Finally, particles may translocate into cells via diffusion (6), which in contrast to all aforementioned pathways, is a non-active process.

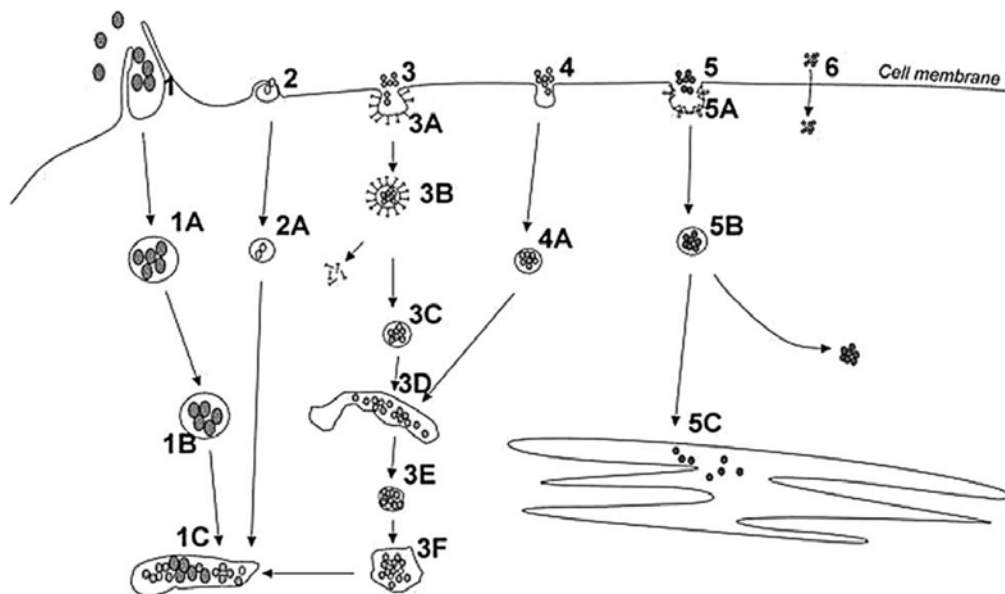


Figure 8: Possible pathways of cellular uptake of nanoparticles. Uptake of particles can occur through phagocytosis (1), macropinocytosis (2), clathrin-mediated endocytosis (3), non-clathrin, non-caveolae-mediated endocytosis (4), caveolae-mediated endocytosis (5) or diffusion (6). (Unfried, 2007)

With respect to particle size, the mechanism of cellular internalisation can be classified into 3 broad categories: phagocytosis, endocytosis and diffusion, in the order of decreasing particle sizes. The exact size range of each mechanism is presently unknown, as each cell type has unique characteristics and there has been no

study on the uptake mechanism with a single type of particle across a wide range of sizes (please see Section 1.6.7).

1.6.6.1 Phagocytosis

Phagocytosis is a mechanism unique to a subset of bone marrow-derived cells, including neutrophils, monocytes, macrophages and dendrite cells. It is involved in the uptake of large particles in an actin-dependent process. In a study of phagocytosis of large particles, polystyrene particles of 30 nm to 1.1 μm in diameter were taken up by macrophages (Pratten, 1986). The inhibition with cytochalasin B or colchicine affected small particles more severely than the 1.1 μm particles. The result suggested that the 1.1 μm particles were taken up mainly by phagocytosis and that there was no radical switch from pinocytosis to phagocytosis, but rather, the contribution of phagocytosis increases with particle diameter.

There have been conflicting reports on the uptake of micron-sized particles by non-phagocytic cell types. Murine melanoma cells internalised 50 – 500 nm polystyrene particles by RME and did not take up 1 μm ones (Rejman, 2004) and human T cells internalised 33 – 107 nm dextran particles and 207 - 289 nm polystyrene particles but showed limited uptake for 1.4 μm silica particles (Thorek, 2008). On the contrary, breast cancer cells were shown to uptake 0.9 μm polystyrene particles readily (Heyn, 2006), suggesting that beside particle size, the quantity of uptake depends on cell type and other particle properties.

1.6.6.2 Endocytosis

Current literature suggests that individual particles or aggregates of diameter 22nm or larger can be internalised by endocytosis (Stearns, 2001; Geiser, 2005). When 22nm titanium oxide particles were incubated with epithelial cells (Stearns, 2001) or macrophages (Geiser, 2005), they appear as clusters within intracellular vesicles. One of the ultrasmall iron oxide particles, AMNP with a diameter of about 30nm was localised to vesicles in macrophages as well (Wilhelm, 2003). It was suggested that particles tend to aggregate in culture medium (Geiser, 2005) or on the cellular surface (Wilhelm, 2003) before they were internalised by endocytic pathways.

The endocytotic pathway is characterised by its energy dependence on ATP and is inhibited at low temperature (4°C). To differentiate the activation of this pathway or the diffusion pathway, cellular uptake can be compared at 37°C and 4°C. For example, AMNP uptake by Hela cells was inhibited at 4°C and TEM showed particle clustering on cell surfaces without internalisation (Wilhelm, 2008).

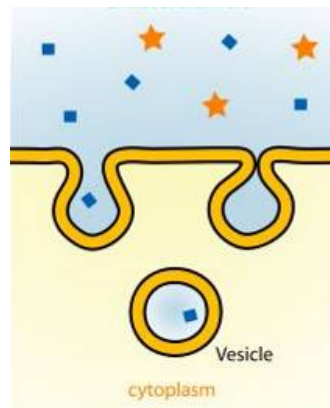


Figure 9: Pinocytosis. This process, as known as ‘cell-drinking’ or fluid-phase endocytosis, internalizes particles in uncoated intracellular vesicles called pinosomes. The pinocytosis of larger particles may be called macropinocytosis and the resulting vesicles are known as macropinosomes.

Endocytosis can be further classified into the pathways of pinocytosis, clathrin-mediated and caveolae-mediated endocytosis. Pinocytosis, also known as fluid phase endocytosis or ‘cellular drinking’, is a constitutive internalisation pathway and is not specific to the substance transported. This pathway was reported for the uptake of MION, a 20nm monocrystalline, dextran-coated iron oxide particle, that internalised into glioma cells and resided in large pinosomes (Moore, 1997), and also for 3.5 nm gold particles that caused micropits on cell membrane and localised in perinuclear vesicles (Shukla, 2005). It has been described that macrophages take up ferumoxide via the pinocytosis pathway (Raynal, 2004). Scavenger receptors have been shown to be involved during the endocytosis, through inhibition studies with polyinosinic acid and fucoidan (Raynal, 2004).

In comparison to pinocytosis, clathrin and caveolae-mediated endocytosis show specificity to the material being internalised, and requires specific membrane proteins for activation. They also require dynamin for the scission of new vesicles from the cellular membrane. A key difference between the two pathways is that the clathrin-mediated process transports extracellular particles into endosomes, and the caveolae-mediated one envelopes particles with caveosomes and brings them to the Golgi complex or endoplasmic reticulum, as illustrated in Figure 10.

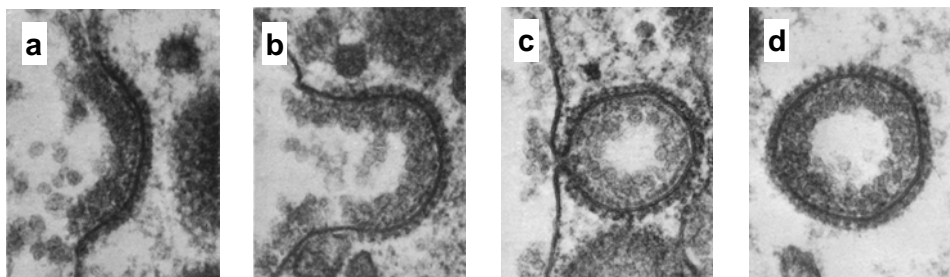


Figure 10. TEM of Formation of Clathrin Pits. The micrograph shows the sequence of extracellular debris internalization via clathrin-mediated endocytosis. The event is initiated by (a) induction of membrane curvature, followed by (b) formation of coated pits and membrane invagination, (c) constriction and fission and finally the containment of debris in clathrin-coated vesicle. Following these events, the vesicle fuses with early endosome that can mature into late endosome and lysosome (Perry, 1979).

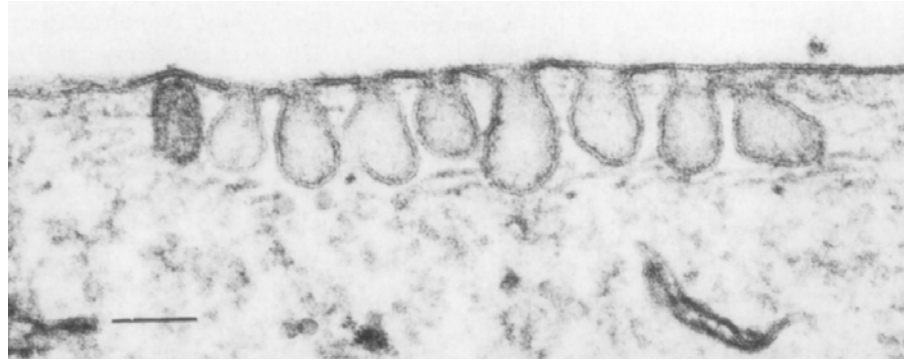


Figure 11. TEM of Caveolae invaginations. Caveolae are flask-shaped plasma invaginations. After internalization, caveolae-driven vesicles travel to caveosomes, which are distinct from endosomes in content and pH. Thereafter, caveosome content is sorted to the Golgi complex or the endoplasmic reticulum (Rothberg, 1992).

Macrophages have unique receptors called scavenger receptors that are involved in the process of clathrin-coated pit formation. Through inhibition studies on murine melanoma cells, it was shown that polystyrene particles of 50 to 200 nm in diameter were internalised by clathrin-mediated endocytosis, compared to 500 nm particles that underwent a caveolae-mediated uptake (Rejman, 2004). The uptake of particles between 50-200 nm, but not the 500 nm particles, were inhibited by potassium depletion or presence of chlorpromazine or EPS15 construct that perturbs transferrin endocytosis. In contrast, only 500 nm particles were inhibited by filipin and genistein and the particles colocalise to LacCer, a caveolae marker.

Further evidence that 500 nm particles do not enter via macropinocytosis came from inhibition studies demonstrating that the pathway was uninhibited by 5-(N,N-

dimethyl)amiloride hydrochloride, unaffected by cytochalasin D and did not ruffle cellular membranes.

1.6.6.3 Diffusion

The smallest particles enter cells by diffusion, which is an energy-independent process. To test for internalisation via diffusion, cellular uptake at 37°C and 4°C can be compared (Wilhelm, 2003; Pratten, 1986; Rejman, 2004). The diffusion pathway is not inhibited by low temperature, unlike other pathways. Further evidence for the existence of a diffusion pathway lies with the non-specific and non-vesicle location of particles in cells. In comparison, larger particles reside in intracellular vesicles after their internalisation, suggesting a different mechanism for their uptake (please refer to Section 1.6.6.1 and 1.6.6.2).

It was reported that well-dispersed titanium oxide particles of 22nm diameter were found in fibroblast, epithelial and endothelial cells in rats after inhalation of the particles in aerosol form (Geiser, 2005). Particles were located mainly in the cytosol, unbound by intracellular vesicles and to a lesser extent, within the cell nucleus. On the contrary, gold particles 5-8 nm in diameter were found in intracellular vesicles in epithelial cells as individual particles or with slight aggregation when inhaled by rats (Takenaka, 2006). It was suggested that cellular response to different particle surfaces resulted in the different internalisation pathway and particle location. The diffusion mechanism could not be easily demonstrated with *in vitro* cell cultures due to the aggregation of small, uncoated particles in culture medium (Geiser, 2005).

1.6.7 Controlling Cellular Uptake of Particles

In the attempt to improve the efficiency of iron oxide particle uptake by the cells, factors relating to the interaction between particles and cellular surface need to be considered. The uptake efficiency depends on the physicochemical properties of the particles (chemical composition, size/geometry, surface charge, coating/ligands, aggregation status), the cell type (professional phagocytes versus other cell types), as well as the labelling medium. Most cell labelling studies have not addressed the kinetics and pathways of uptake. We shall now look at those that have.

1.6.7.1 Particle Surface Composition and Charge

The iron oxide particles in biomedical applications are often coated with dextran or other formulation. The coating material, at times carrying electrostatic charges, can mediate both interparticle and particle-cellular interactions. Bare iron oxide particles cannot be well-suspended in water. While in a dispersing medium, particles are in Brownian motion due to random collision from water molecules, and they experience interparticle attractive and repulsive forces. When attractive forces (Van der Waal's forces or magnetic dipole-dipole interactions resulting from residual magnetic moment) dominate, particles aggregate, become too large to remain suspended by Brownian motion and sink. Polymer coating around the iron oxide particles provides repulsive forces between particles in the form of electrostatic repulsion or steric hindrance to enable stable suspension in water. Clinically available SPIO such as ferumoxide or ferucarbotran are well suspended in water due to the steric hinderance offered by their dextran or dextran-derivative coating (Hunter, 1995).

Various particle coatings have been engineered to enhance or avoid specific particle-cell interactions (Nath, 2004). Both macromolecules and monomers have been used as coating material. An example of macromolecular coating is the ‘PEGylation’ of iron oxide to allow for a long circulation time by avoiding opsonisation and uptake by the macrophages of the reticuloendothelial system (Lee, 2006). PEG represents poly(ethylene glycol). The PEGylated surface is hydrophilic, electrostatically neutral and without hydrogen donor or acceptors. Hence the lack of attractive forces between PEG and opsonising protein is exploited in this application.

Particles that are stabilized by monomer coating remain suspended due to the electrostatic repulsion between particles. Examples of charged particles that have anionic surfaces are the citrate-coated VSOP (8nm) and dimercaptosuccinic acid-coated AMNP (30nm). The surface charge on particles plays an important role in the efficiency of particle uptake by cells. VSOP showed improved uptake by macrophages compared to uncharged particles of similar size (Fleige, 2002). In a separate study, AMNP (21 – 30 nm) showed greater uptake by macrophages and Hela cells than dextran-coated ferumoxtran (of similar size) which carries no charge (Wilhelm, 2003; Jung, 1995).

In addition to surface charges, charge polarity can also affect particle uptake by cells. Positively and a negatively-charged particles with diameters similar to SPIO (100nm) were compared in terms of uptake by Hela cells (Harush-Frenkel, 2007). The anionic polylactide-based particles provide poorer uptake than their aminated, cationic cousins. Furthermore, Hela cells were transfected with clathrin hub or K44A, dominant negative mutant of dynamin I, to elicit the pathways of particle uptake. It was shown that the cationic particles used the clathrin- and caveolae-mediated

endocytic pathways, but not the anionic ones. Interestingly, when the clathrin/caveolae pathway was inhibited, the HeLa cells took up the cationic particle through a possible compensatory, macropinocytic pathway.

1.6.7.2 Surface Ligand

A method to improve cellular uptake takes advantage of the use of biological ligands that encourage receptor-mediated endocytosis. Attachment of HIV tat peptide to aminated, dextran-cross-linked iron oxide particles (CLIO-tat, ~45nm) improved particle uptake by human CD34+, human CD4+ and mouse splenocytes (4 – 8 pg/cell) compared to CLIO alone (<2 pg/cell) when labelled at 0.1 mg Fe/ml (Lewin, 2000). However, the particles were located in the cell nucleus instead of the usual endosomal location of other particles. This raises the question whether CLIO-tat is more likely than other particles to alter cellular function through interfering with nuclear activity. Instead of using peptides, it is possible to direct receptor-mediated endocytosis with antibodies (Ab) as well. The transferrin receptor is abundant on numerous cell types. SPIO tagged with anti-transferrin Ab can improve the iron loading of human haemopoietic progenitor cells (9.8 pg/cell) over the use of SPIO alone (2.4 pg/cell) (Daldrup-Link, 2003). These particles were internalised in contrast to another report where transferrin-coupled SPIO only bound to the surface of human dermal fibroblast (Berry, 2004). Other Ab under exploration include the CD11c, which increased SPIO uptake in dendritic cells. (Ahrens, 2003).

An inherent problem with Ab-directed RME is the species-specific attachment to the target receptor. This requires each Ab-SPIO to be tailored to the target species and

cell type. Moreover, as Ab are raised in animals as such mouse, this method will have to contend with regulations on xenogeneic contamination of transplants.

1.6.7.3 Particle size

The rate and quantity of particle of cellular uptake are dependent on the particle diameter. In an early study of the effect of particle size on uptake in macrophages, it was shown that the volume of particles taken up increased with increasing particles diameters, with a maximum reached at about 2 μm (Tabata, 1988). As particles diameters increased from 2 to 4.6 μm , the amount of particles taken up actually decreased as shown in Figure 12

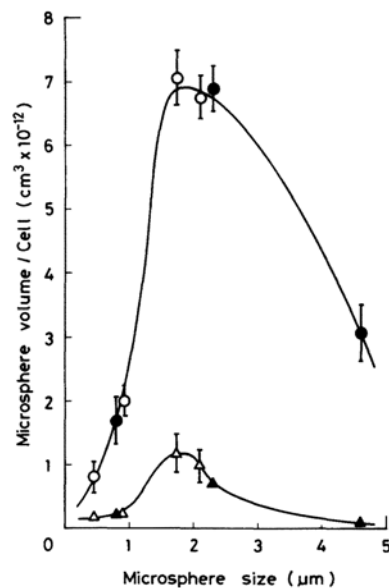


Figure 12: Uptake of polystyrene (open symbols) and phenylated polyacrolein (closed symbols) particles in absence of serum (greater uptake) and 10% serum (lesser uptake), showing maximal uptake within a range of sizes (Tabata, 1988)

This result was supported by observations that the uptake rate and quantity increased for increasing polystyrene particle diameter between 30 nm and 1.1 μm (Pratten,

1986). It was also shown that leukocytes obtained by density centrifugation of human blood took up the greatest amount of styrene-based particles of diameter 500 nm to 1 μm , compared to particles of other sizes (Kawaguchi, 1986). A similar result was shown with dextran-coated iron oxide particles where macrophages took up more 60nm SPIO than 20nm USPIO (Zhang, 2001).

There have been few studies on how particle size affects uptake by non-phagocytic cells. From the limited studies available, non-phagocytic cells showed a different uptake pattern compared to macrophages. Rejman et al demonstrated that the uptake into murine melanoma cells decreased as polystyrene particles diameter is increased from 50 to 500 nm, and was absent when 1 μm particles were used (Rejman, 2004). In a study of labelling human T cells with aminated particle of size between 33nm and 1.4 μm by Thorek et al, 107nm particle provide the best cellular loading (Thorek, 2008). Cellular uptake decreased with increasing particle diameters from 207nm to 1.4 μm , in agreement with Rejman's results. Contrary to Rejman's results, the cellular uptake increased for increasing particles diameters from 33 to 107nm. However, it is difficult to infer the pattern of T cell uptake with particle diameters, as Thorek's study used a variety of particle coatings at different sizes: dextran (33 - 107 nm), styrene (207 - 289 nm) and silica (1.4 μm) coated particles.

It is possible to use transfection agents during labelling to generate particle aggregates of different sizes. However, results relating aggregate size and uptake have been contradictory, as aggregate surface composition and charge had not been kept constant in these experiments (Matuszewski, 2005; Song, 2007).

The study of the relationship between particle size and cellular uptake requires a set of particles of similar surface composition but with diameters that cover

the range of 100nm to 1µm. There has been no such study to date, in part due to the difficulty of achieving such a wide diameter range with uniform composition.

1.6.7.4 Labelling Duration and Concentration

The amount of internalised particles correlates positively to the duration and concentration of incubation with the cells. Current evidence shows that the uptake amount increases and saturates with increasing labelling duration and concentration, independent of particle type, size or cell type. The uptake of sub-100 nm dextran, 200-300 nm styrene and 1.4 µm silica particles increased with incubation duration but was saturated by 4 hours with non-phagocytic T cells (Thorek, 2008). The same study also demonstrated that the saturating concentration varied for different particle sizes. Labelling concentration is commonly expressed as mass of iron per unit volume of labelling medium, for example mg Fe / ml or simply mg/ml. The uptake for sub-100 nm dextran particle saturates at 0.025 mg/ml and 200-300 nm styrene particles and 1.4 µm silica particles are saturated at 0.1 mg/ml. When 30nm AMNP was used to label Hela cells and macrophages, the saturating durations were 5 and 10 hrs, respectively while the saturating concentration was 0.5 mg/ml for both cell types, further demonstrating the variability of labelling efficiency between cell types (Wilhelm, 2003).

The longest reported labelling duration was 72 hrs where ferumoxide was incorporated into bone marrow cells (Jendelova, 2003). Most studies kept to a maximum labelling duration of 24 hours and a maximum concentration 0.2 mg/ml as it has been shown that long duration and high concentration, in particular the combination of both, can result in cytotoxicity (van den Bos, 2003; Neri, 2008).

1.6.7.5 Electroporation and Transfection Agents

Using DNA transfection technologies, electroporation and transfection agents (TA) have been used in the attempt to improve uptake of particles into cells. When ferumoxide labelling was assisted by electroporation, iron loading of 11.5 pg/rMSC was achieved compared to just 3 pg/rMSC with simple incubation alone (Walczak, 2005). However, this technique may require careful tuning of the electrical parameters to avoid affecting cell viability (Daldrup-Link, 2005).

Poly-L-lysine (PLL), a common cationic TA, binds with DNA to form complexes of <100nm. By complexing PLL with ferumoxide prior to their incubation with hMSC, iron loading between 13 pg/cell (Arbab, 2003) and 16 pg/cell (Frank, 2003) has been reported. As an alternative to PLL, protamine sulphate, an FDA-approved TA has been complexed with ferumoxide to achieve loading of 11 pg/hMSC (Arbab, 2004). However, no comparison against the uptake by simple incubation was done in these studies with TA.

Although the iron loadings achieved with TA are promising, a few potential disadvantages are associated with this method. It was reported that hMSC labelled with ferumoxide-PLL could not undergo chondrogenesis (Kostura, 2004), although the use of ferumoxide-protamine sulphate did not encounter the same problem (Arbab, 2004). It was suggested that the inhibition was due to the use of PLL as the TA rather than the presence of ferumoxide (Bulte, 2004), although no detailed study had been done to examine the effect of PLL and protamine sulphate alone on the chondrogenicity of MSC.

Despite an apparent increase in iron loading, it was reported that TA-mediated labelling may result in only cell surface attachment rather than internalisation of SPIO (Montet-Abou, 2007). In this study, the TA lipofactamine resulted in SPIO attaching to the surface in contrast to protamine sulphate, which allowed the complete internalisation of feridex in mouse neural progenitor cells but not in other cell types. These results suggest that the internalisation of SPIO may be dependent on TA, labelling condition and cell type.

Another distinctive feature of TA-mediate labelling is the iron loading with respect to iron concentration of the labelling medium. Labelling with naïve ferumoxide or other SPIO resulted in cellular uptake that increases with iron concentration of the labelling medium, and reaching a saturated iron load at high labelling concentrations. PLL-mediated particle uptake on the other hand, varies non-linearly with the labelling concentration (Kim, 2008), and may present difficulty in optimising cell labelling conditions for different cell types.

This observation may be due to the dynamic nature of the complex formation between TA and SPIO, which is less understood compared to the complex formation between TA and DNA. The formation of PLL and DNA complexes, depending on the relative amounts of the constituents, results in structures that range from spheres to rods and toroids (Liu, 2001) and have sizes that are dynamic over several hours (Lai, 2001). The complex formed by TA and SPIO has a hydrated diameter that depends on the relative amount of the constituents and may form precipitations at certain ratios (Montet-Abou, 2007). Therefore, the use of TA-mediated labelling requires careful optimisation of labelling condition for each cell type to be labelled.

1.6.7.6 Labelling medium

During the labelling of cells, the physicochemical properties of particles are influenced by the microenvironment. Studies on the effects of the labelling medium have shown that the use of 10% serum increases the uptake of ferumoxide compared to serum-free medium (Rogers, 2005). Similar results were reported with monocrystalline iron oxide particle (MION). MION was opsonised by fresh plasma, purified and incubated with macrophages or cancer cell, resulting in six and two fold increase in uptake, respectively, compared to naïve MION (Moore, 1997). It was suggested that opsonised MION was taken up by scavenger and complement receptors of macrophages and naïve MION entered cells through fluid-phase endocytosis. This suggestion was supported by reports that the macrophage uptake of albumin-coated particles is C3b-complement (a component of opsonisation) dependent (Roser, 1998). On the contrary, opsonised AMNP show reduced uptake by Hela cells (1 pg/cell) compared to naïve AMNP (16 pg/cell) (Wilhelm, 2003). It was also reported that macrophage uptake of polystyrene and phenylated polyacrolein between 0.5 to 4.5 μm was higher in serum-free media (Tabata, 1988). Therefore, the presence of serum in media can influence the uptake of particle and the change in uptake is dependent on the cell type.

1.6.8 Transgenic Methods

Living organisms possess specialized iron storage mechanisms involving ferritin, transferrin and transferrin receptor. The expression of these proteins on certain cells may be accompanied by an increase in intracellular iron storage, which will allow the cells to be detected through MRI. An application is the use of these proteins as markers to monitor of the gene expression during gene therapy. These proteins can

also be applied to the imaging of endogenous gene expression during development and pathogenesis in transgenic animals.

1.6.8.1 Transferrin

Free iron in the circulation is captured by the plasma protein transferrin (Tf) and iron-loaded Tf is transferred into cells after binding to the transferrin receptor (TfR). TfR is naturally abundant on some cell types and has been utilised to improve the uptake of Tf-conjugated SPIO (Daldrup-Link, 2003). When human Tf-conjugated MION were administered by IV, the particles bound specifically to the rat gliosarcoma cells that have been transfected to express human TfR (Weissleder, 2000; Moore, 2001). Therefore, TfR becomes a model marker for the MR visualisation of *in vivo* gene expression.

1.6.8.2 Ferritin

Ferritin is a ubiquitous and highly conserved iron-binding protein (Harrison, 1996). In vertebrates, the cytosolic ferritin is a heteropolymer composed of variable proportions of H and L subunits. The H subunit has ferroxidase activity that promotes iron oxidation and incorporation, and the L subunit facilitates the activity of the H-chain by offering sites for iron nucleation and mineralization. Twenty-four ferritin subunits assemble to form the apoferritin shell. Each apoferritin molecule of 450 kDa can sequester up to 4500 iron atoms, depending on the tissue type and physiologic status of the cell. MRI has been shown to detect abnormality of iron metabolism where ferritin and iron storage was elevated (Grabill, 2003). The T2 relaxation properties of iron-loaded ferritin have also been studied *in vitro* (Gossuin, 2000).

An early study on transfecting cells to overexpress H-chain ferritin showed upregulation of TfR and increased intracellular iron (Cozzi, 2000). In a separate study, the change in cellular iron was detected as a 7% change in MR relaxation rate when the ferritin gene were switched on (Cohen, 2005). Inducible ferritin expression was also detected in the liver and heart of transgenic, fetal mice with 25% change in relaxation rates (Cohen, 2007).

Poor sensitivity is a limitation of these attempts to image gene expression as turning on the ferritin gene increased cellular iron content by only 0.2 pg/cell (Cohen, 2005). Sensitivity was not improved by the co-transfection of both ferritin and TrR genes, which yielded an iron content increase of only 14 fg/cell (Deans, 2006). However, studies are ongoing to improve the sensitivity of imaging ferritin expression by controlled aggregation of ferritin to increase relaxation rate for the same iron quantity per cell (Bennett, 2008).

1.6.8.3 MagA

Magnetotactic bacteria are motile prokaryotes that synthesize intracellular magnetic structures and move in relation to the earth's magnetic field (Bazylinski, 2004). The synthesized structures, called magnetosomes, consist of multiple iron oxide crystals surrounded by a lipid membrane. One of the genes identified to be involved in magnetosome production is *magA*. When 293FT cells, a common human packaging cell line, were transfected with *magA*, the cells produce sub-micron sized magnetosomes that contained multiple iron oxide crystals each measuring 3-5nm in diameter (Zurkiya, 2008). Induction of the gene *magA* increased intracellular iron by 0.55 pg / cell and produced up to four-fold change in measured relaxation rate. The

use of *magA* is in its infancy, but current results make the gene a promising candidate as an MR reporter.

1.6.9 Challenges of Cellular MRI

Cellular MRI faces numerous challenges in the pursuit of a cell marking method that can be translated to the clinic. Being non-phagocytic, stem cells do not internalise sufficient amount of clinically-available SPIO by simple incubation. The use of transfection agents may be complicated by alteration of cellular function such as differentiation capacity and difficulty in optimizing labelling parameters. The option of electroporation to encourage uptake may require extensive optimization of labelling protocols to avoid cellular toxicity.

1.6.9.1 Label Transfer

Even with sufficient iron loading of cell, the route and timing of cellular delivery may have significant effects on cellular survival and engraftment. When cellular grafts encounter hostile host immune response and are destroyed, the transfer of label to the host immune cells may occur. When cells are labelled with exogenous fluorescent labels such as 5-bromo-2-deoxyuridine (BrdU) and bis benzamide (BBZ) prior to transplantation, the transfer of label to host macrophages can potentially cause erroneous diagnosis of cellular engraftment or differentiation. (Pawelczyk, 2006; Burns, 2006; Coyne, 2006). Iron oxide MRI labels face the same potential problem. Hence secondary methods of identifying donor cells by means of FISH or sex mismatch may be an essential procedure to verify MRI observations in preliminary experiments.

1.6.9.2 Cellular Quantification

The quantification of cells through the use of radioactive methods like scintigraphy is well-established. Quantification of cells by iron oxide MRI on the other hand is in its infancy, but there have been some promising reports. The principle of cellular quantification is based on the bulk magnetic susceptibility relaxation mechanism of cells labelled with iron oxide particles. Iron oxide particles that are compartmentalised into cells have relaxation rates that are higher than homogeneously distributed particles (Bowen, 2002). When a cell is labelled with SPIO or USPIO, its relaxation is like that of a large magnetic sphere operating in the SDR (Ziener, 2005). The geometry of signal voids created by the iron oxide labelled cells extends beyond the cell membrane, making it easier to identify the cells on an image (Pintaske, 2006). More importantly, the relaxation rate of each cell is in the SDR which means that the relaxation rate remains constant even when cells group together in clusters. Therefore, when iron mass per cell is known, the $R2^*$ relaxation rate is directly proportional to the number of cells per voxel.

The accurate measurement of $R2^*$ relaxation rate is beset with artefacts from macroscopic magnetic susceptibility of tissue-air interfaces leading to overestimates of $R2^*$. A number of methods have been proposed to compensate for the susceptibility artefacts, including increasing spatial resolution, alternating slice selection, tailoring rf pulses or utilizing 3D z-shimming. A method that combined 3D high-resolution ΔB_0 maps and image postprocessing was reported to provide improved $R2^*$ measurements that would have been a two-fold overestimate if left uncorrected (Dahnke, 2005). Using this method, the detection limit during brain

imaging was 2.4 $\mu\text{g Fe/ml}$, which is equivalent to 600 cells/voxel (voxel size: 1 x 1 x 5 mm) at 20 pg Fe/cell.

Besides improving cellular iron loading, improvement in hardware and image processing can increase detection sensitivity. Nevertheless, it remains a considerable challenge to detect small numbers of cells against native low signals from, for example, haemosiderin or haemorrhagic artifacts or the presence of metals such as calcium. Furthermore, the detection of labelled cells is limited by partial volume effects, in which void detection is dependent on the resolution of the image (Heyn, 2005). A post-processing algorithm based on phase map cross correlation was proposed for robust identification of labelled cells even in images with low SNR (Mills, 2008). Deoxyhemoglobin in small, slow flowing vessels is another source of native hypointensity that can have similar appearances to labelled cells, especially in 2D images. The problem can be circumvented by the administration of paramagnetic contrast agent prior to cellular imaging (Anderson, 2005) or the use of carbogen inhalation (95% O_2 and 5% CO_2) to allow vasodilation by CO_2 (Himmelreich, 2005).

1.6.9.3 Positive Contrast

Gadolinium-based T1 contrast agents have been in clinical use for over two decades and radiologists are used to identifying positive contrast or hyperintense image features. As a result, new methods for display of magnetically induced dark signal pixels have been developed. There are two main methods of creating positive contrast from iron oxide labelled cells.

The first is based on the design of pulse sequences to detect the susceptibility-induced, off-resonance barbell geometry around labelled cells (Pintaske, 2006). Selective

imaging of the off-resonance signals around cells was proposed (Cunningham, 2005). As an extension to this method, an inversion recovery on-resonance water suppression (IRON) sequence places an additional saturation pulse to negate on-resonance water signal far away from cells (Stuber, 2007). Positive contrast can also arise from diffusion-mediated off-resonance saturation (ORS) sequence (Zurkiya, 2006). In this method, bulk water protons are imaged with and without the presence of an ORS pulse. Unlike chemical exchange dependent saturation transfer (CEST) contrast agents which function by reducing the water proton signal through a chemical exchange site, this method relies on diffusion of water molecules around the labelled cells. The “white marker” or Gradient Echo Acquisition for Superparamagnetic Particle (GRASP) technique takes a slightly different approach (Seppenwoolde, 2003; Mani, 2006). GRASP rely on the introduction of a dephasing gradient on the slice-select axis to spoil the signal across the sample, so that a positive contrast is gained only in one direction.

The second method takes a different approach by deriving positive contrast through post-processing of images (Posse, 1992). The local magnetic gradients induced by magnetic susceptibilities lead to echo-shifts in k-space with gradient echo imaging. The effect is exploited by applying a shifted reconstruction window in k-space (Bakker, 2006). Recently, a susceptibility gradient mapping (SGM) technique has been proposed that generates susceptibility vectors from a regular complex gradient echo dataset to develop positive contrast in 3D (Dahnke, 2006).

Some of the above positive contrast methods have been compared by imaging labelled glioma cells transplanted to the flanks of nude rats (Liu, 2007). Positive contrast was generated from the presence of labelled cells, but it remains to be determined whether

positive contrast yielded better cellular detection. However, positive contrast images lack anatomical detail, and are best supplemented with traditional T2 or T2*-weighted hypointensity imaging. Overlain or “fused” images combining the positive contrast and anatomic images are possible, in a manner analogous to that used in clinical PET-CT, although this type of display is susceptible to misregistration artifacts.

1.7 Summary

Stem cell therapy has the potential to improve the treatment of numerous diseases. Mesenchymal stem cells (MSC) can be isolated from a number of sources such as adult bone marrow, umbilical cord blood and fetal bone marrow. These cells are defined by their ability to self-renew, and differentiate into osteoblasts, adipocytes and chondroblasts under suitable culture conditions. In animal models, MSC have been shown to home to injured tissue, such as a cerebral infarct, but stroke treatment is challenged by our incomplete knowledge of the central nervous system immunology, especially towards a new allogeneic MSC. Although classically considered an immune privileged organ, there is evidence of brain graft rejection, and graft survival in target tissue is often variable.

Longitudinal studies of experimental animals or monitoring of cellular therapy in subjects require non-invasive methods that reports cellular function, or at least their location. Magnetic resonance imaging has an appropriate balance of sensitivity and resolution required for tracking transplanted cells. By employing sensitive contrast agents like superparamagnetic iron oxide particles (SPIO) to label cell prior to their transplantation, cellular migration can be tracked. However, cellular imaging has been hampered so far by poor uptake of particles by non-phagocytic cells such as MSC. Sub-150nm SPIO have failed to label MSC sufficiently to relax hardware requirements and enable detection of small cell numbers *in vivo*. There have been conflicting results in labelling non-phagocytic cells with particles $>0.9\mu\text{m}$ in diameters. The dependence of uptake mechanism on particle size is a known phenomenon, yet MRI particles of similar formulation and composition in the size

range between 100 to 900 nm have not been investigated. An important property of a contrast agent is its MR relaxation. The relaxation of particles in this sub-micron size range has been theoretically derived and numerically simulated, but has not been investigated with actual particles.

A set of these particles may serve the dual purpose of cell tracking and verification of MR relaxation models. Labelling with such particles may reveal unreported particle internalising efficiency by non-phagocytic cells. Studying the relaxation of these particles may provide the first experimental verification of theoretical models with actual particles.

1.7.1 Hypothesis

- Magnetic microgel iron oxide particles (MGIO) can be synthesized such that they have:
 - diameters that cover the range of 100nm to 1 μ m
 - similar composition between different sizes
- MGIO can provide a physical means of verifying theoretical models of particle magnetic resonance relaxation
- MGIO can be used as a label for non-phagocytic cell type, such as fMSC and provide better labelling efficiency than clinically-available labels, such as ferucarbotran, without deleterious effects to the cells
- MGIO-labelled fMSC can be transplanted to an animal model of cerebral stroke such that the cellular migration to the injury site can be tracked by MRI

Chapter 2 Methods

2.1 Synthesis of Particles

Magnetic microgel iron oxide particles (MGIO) are synthesized in a two-step process where precursor microgel particles are formed by emulsion polymerisation followed by the alkaline co-precipitation of iron oxide in the precursors to form MGIO.

2.1.1 Synthesis of Precursor Migrogel

Non-magnetic precursor microgel (PMG) was synthesized using conventional semi-continuous emulsion polymerisation modified from the protocol described by Tan et al (Tan, 2004). A monomer mixture was prepared by dispersing in a bottle, ethyl acrylate (EA), methacrylic acid (MAA) (both from Sigma Aldrich), di-allyl phthalate (DAP) and 75% Aerosol OT surfactant (American Cyanamid, Stamford, Connecticut). The mixture was charged to a 50ml graduated monomer-feed cylinder. An initiator feed mixture comprising of sodium persulfate, sodium bicarbonate (both from Sigma Aldrich) and distilled de-ionized water was prepared in another container and was charged to a 20ml syringe pump. In a third container, sodium persulfate was dissolved in water to form the initial catalyst solution. An initial reactor charge consisting of distilled de-ionized water, 2-sulfoethyl methacrylate (Hampshire Chemical Corp., Nashua, NH, USA) and 75% Aerosol OT surfactant were charged into the reactor, a 500ml resin flask. Under nitrogen purge, 10% of monomer mixture was added and the reactor was heated. The temperature of the reactor was controlled by an immersion mineral oil bath which was heated with a hot plate controlled by a thermostat. When the reactor temperature reached 80°C, the initial catalyst solution was added to initiate polymerization. After a reaction time of 30 min to form an *in-situ* seed product, the

remaining monomer and initiator feed mixtures were conveyed to the reaction vessel at a rate of 0.4 and 0.05 g/min, respectively, while the reaction mixture was maintained under continuous stirring, nitrogen atmosphere and a reaction temperature of 80°C. After the complete discharge of the monomer and initiator feed, the reaction was allowed to persist for another hour under the same conditions, for the complete reaction of the residual monomer. The completed colloidal product was cooled, filtered through a 200-mesh nylon cloth, transferred to regenerated cellulose tubular membrane and dialyzed against distilled de-ionized water. Distilled de-ionised water was replaced twice a week and the dialysis process was carried out over a month to purify PMG by removing unreacted reagents. Six models of PMG were prepared with the masses of reagents summarised in the following table.

Masses of Reagents (grams) in the Synthesize PMG						
PMG Model	1	2	3	4	5	6
Reactor Charge						
a. Water	330	230	230	230	230	230
b. 10% monomer mix	2.2	3.27	2.91	2.81	3.21	2.71
c. Aerosol OT	1.52	1.17	0.21	0.21	0.01	0.0078
d. 2-Sulfoethyl Methacrylate	0.85	1.31	0.24	0.24	0.02	0.0088
e. Micellar ratio	1.4	2.8	12.9	13.4	321.0	347.4
Initial Catalyst						
a. Water	2.79	2.79	2.79	2.79	2.79	2.79
b. Sodium Persulfate	0.63	0.63	0.63	0.63	0.63	0.63
Monomer mix						
a. MAA	9.58	11.01	4.40	11.01	11.01	11.01
b. EA	7.28	12.69	20.31	12.69	12.69	12.69
c. Diallyl Pthalate	0.68	0.95	0.95	0.95	0.95	0.95
d. Aerosol OT	0.74	5.72	1.03	1.03	0.066	0.038
e. Water	3.4	2.37	2.37	2.37	2.37	2.37
Sub-total	21.68	32.7	29.07	28.1	32.1	27.1
MAA-EA ratio, x:y	60:40	50:50	20:80	50:50	50:50	50:50
Feed oxidizer / initiator feed						
a. Water	5	3.49	3.49	3.49	3.49	3.49
b. Sodium Persulphate	0.226	0.32	0.32	0.32	0.32	0.32
c. Sodium Bicarbonate	0.56	0.08	0.08	0.08	0.08	0.08
PMG Size						
Hydrated diameter, d_H (nm)	-	-	70.2	129.9	-	-

Table 4: Masses of reagents required to form six models of precursor microgel particles (PMG) of different sizes by altering the micellar and MAA to EA ratios.

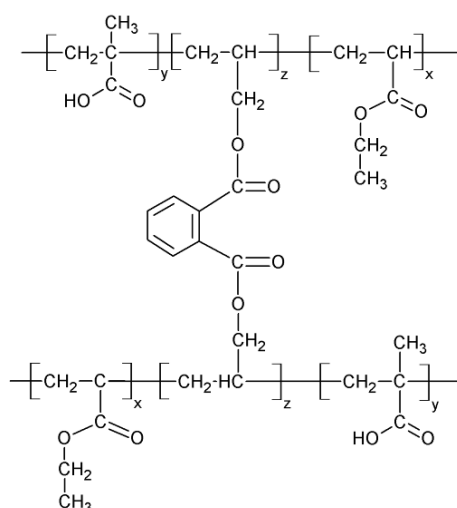


Figure 13 Schematic of PMG. The molar ratio of methacrylic acid (MAA) and ethyl acrylate (EA), and the wt% of crosslinker di-allyl phthalate (DAP) are represented by x, y and z respectively.

Precursor microgel (PMG) is made up of polymerized methacrylic acid (MAA) and ethyl acrylate (EA) cross-linked with di-allyl phthalate (DAP) (Figure 13). Six models of PMG were synthesized, each differing in micellar ratio and the molar ratio of MAA to EA, which is represented by x:y. The micellar ratio is defined as the weight ratio of 10% of monomer mix to Aerosol OT. The wt% of crosslinker di-allyl phthalate (DAP) against the total weight of MAA and EA, z, was maintained at 4%. The total amount of monomer for each model is 22 to 33g.

The PMG diameters depend on the micellar ratio and x:y. At the initial stage of PMG synthesis, the Aerosol OT and 10% of monomer mixture form micelles or seeds that grow when more monomers polymerize onto their surfaces to form PMG. When the micellar ratio is large, there are few available seeds for the monomers to polymerize onto, thus forming larger PMG.

PMG diameters are dependent on the x:y and the wt% of DAP. As PMG consists of methacrylic acid that possesses the carboxyl group, they are considered soft particles that expand in response to increase in pH. When the pH is raised, there is less protonation of the carboxyl group, resulting in greater electrostatic repulsion between negatively-charged groups. The amount of expansion is limited by the amount of carboxyl groups available and the amount of DAP crosslinker present (Tan, 2004).

2.1.2 Synthesis of MGIO

MGIO was synthesized by the alkaline coprecipitation of iron oxide primary particles within the PMG. Some intermediate products of MGIO synthesis are prone to oxidation by atmospheric gases, as such the reagents were deoxygenated by bubbling with nitrogen for at least 15 min prior to use. Briefly, 120ml of 0.5 wt% PMG was

adjusted to a pH of 6.5 with 1M NaOH and deoxygenated in a 500ml, three-neck reaction flask. $\text{FeSO}_4 \cdot 7\text{H}_2\text{O}$ was dissolved in 30ml of deoxygenated, 4°C deionised water and added at a rate of 10ml/min into the reactor while under gentle mechanical stirring and nitrogen blanket. After an interval of 2 hours for sufficient infusion of Fe salts into PMG, the temperature of the reactor was raised to 35 °C and under vigorous stirring, NaNO_2 and 28% NH_4OH were added. The reaction was allowed to continue for one hour, after which the suspension was centrifuged at 22k x g. The supernatant was discarded and the pelleted residues were redispersed for 30 min via an ultrasonic bath filled with iced water to prevent excessive heating of the particles. The centrifugation and redispersion were repeated twice. After the last redispersion, the suspension of a low speed centrifugation at 4k x g was retained. The discarded residue contained aggregated composite particles, including aggregates of iron oxide primary particles that formed outside the PMG. The suspension was passed through a high magnetic field separation column to separate out non-magnetic particles. The remaining magnetic fraction was MGIO. Eight models of MGIO were achieved by using the masses of reagents in the following table.

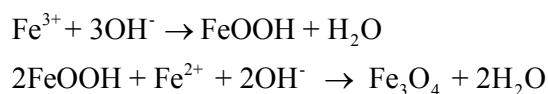
Masses of Reagents in the Synthesis of MGIO				
MGIO Model	PMG Model	$\text{FeSO}_4(\text{g})$	$\text{NaNO}_2(\text{g})$	$\text{NH}_4\text{OH}(\text{g})$
M100	1	0.3	0.1	6
M150	1	1.0	0.1	6
M250	2	1.0	0.1	6
M300	3	1.0	0.125	15
M400	3	1.5	0.25	15
M500	4	2.5	0.25	15
M600	5	1.5	0.15	12
M750	6	2.5	0.25	15

Table 5: Masses of reagents and the PMG models required to synthesize MGIO of approximately 100 to 750nm as denoted by models M100 to M750.

When the pH of PMG was raised to 6.5, the protonation of carboxyl groups on MAA decreased resulting in a larger proportion of charged carboxylate groups that increased the driving force for the incorporation of Fe cations into PMG. When Fe²⁺ was introduced, 2 hours was given for the infusion of Fe salts into PMG. Infused Fe²⁺ coordinated with the carboxyl groups of MAA and some remained outside PMG to form a cloudy, greenish suspension. It is possible to perform dialysis on the suspension to remove Fe²⁺ that remains outside the particles, but due to lack of equipment for dialysis in an deoxygenated atmosphere, this step was omitted. When ammonia and oxidiser NaNO₂ were introduced, Fe²⁺ and newly formed Fe³⁺ reacted with ammonia to form a green suspension, which turned into a black precipitate after one hour, by the classical equation.



It is also believed that the formation of magnetite is a two-step process, with the green intermediate being FeOOH, as shown below (Tao, 2008).



Soluble impurities from unreacted reagents, eg ammonia were removed by high-speed centrifugation while unsuspendable impurities of iron oxide particles that formed outside PMG were removed by low speed centrifugation. Non-magnetic products, including PMG or FeOOH, were removed by magnetic separation.

2.2 MGIO Characterisation

2.2.1 Transmission Electron Microscopy

Air-dried MGIO structure was analysed by transmission electron microscopy (TEM). A 10 μ L sample was placed on a film-coated 200-mesh copper grid laid on a filter paper. Water was immediately drawn from the sample by the filter paper and the retained MGIO was allowed to dry for a 10 min prior to loading in the TEM (JEOL JEM-100CX microscope, Tokyo, Japan). Microscopy images of various magnifications were obtained in transmission mode and selected area diffraction (SAD) of a single MGIO was obtained.

2.2.2 Thermogravimetric Analysis

The iron oxide weight content (IO%) of MGIO was measured by thermogravimetric analysis (TGA 2950, TA Instruments, New Castle, DE, USA). MGIO suspension was frozen at -20°C overnight and lyophilized for 24 hours prior to the characterisation by TGA. 10-20 mg of lyophilized MGIO was heated from 25 to 900°C at a rate of $10^{\circ}\text{C}/\text{min}$ in a 99.99% nitrogen flow of 50ml/min while the weight of the sample was measured. The plot of weight versus temperature and its first derivative was produced on Universal Analysis 2000 Ver 3.4c, an analysis software from TA Instruments. The IO% of MGIO was taken as the quotient of dividing residue weight at 850°C by the dry weight of MGIO at about $110\text{-}130^{\circ}$. The weight of residue from polymers was considered negligible (Lin, 2005).

2.2.3 Vibrating Sample Magnetometry

MGIO suspension was frozen at -20°C overnight and lyophilized for 24 hours prior to the characterisation by vibrating sample magnetometry (VSM). Magnetometry (Oxford Instruments, Oxfordshire, UK) was performed on each of M400-750, using sample masses of 2.2 to 14.9 mg. Magnetization was measured at 300K while the field was swept from 0 to 10^4 A/m, and from 10^4 to -10^4 A/m, then back to 0 A/m. The M_{10kAm} is the average of magnetization at 10^4 A/m. Magnetization against the applied field was plotted with a graphing and analysis software (Origin 8, OriginLab, Northampton, MA, USA).

2.2.4 SQUID Magnetization

A lyophilized sample of M600 and an aqueous one with a concentration of 320 mM Fe were prepared. The aqueous sample was obtained in increasing the concentration of stock M600 with centrifugation and resuspension. Each sample was characterized by a superconducting quantum interference device (SQUID; MPMS XL, Quantum Design, San Diego, CA, USA) while the temperature of the sample was varied to determine the zero-field-cooled (ZFC) and field-cooled (FC) magnetization curves. In a ZFC measurement, the sample was cooled from 300 to 10 K without applying an external field. After reaching 10 K, a 100 A/m field was applied and the magnetization was recorded as the temperature increased. For FC experiments, the same was done except that the samples were cooled while under an external field of 100 A/m. As temperature is increased, the ZFC magnetization is expected to increase, reach a maximum and meet the FC curve. The temperature at the ZFC maximum is related to the average blocking temperature, T_B of the particles, while the temperature

at which the FC and ZFC curves meet corresponds to the blocking temperature of the largest particles (Maity, 2008). The blocking temperature is defined as the temperature above which a particle possess sufficient thermal energy to switch between energy states rapidly (become unblocked) such that the particle moment fluctuates and is zero when time-averaged. If the blocking temperature is below 300K, the particle is considered to be superparamagnetic and exhibits absence of remnant magnetization at 300K.

2.2.5 Dynamic Light Scattering

The hydrated diameter of MGIO suspension was determined by dynamic light scattering (DLS, Brookhaven Instruments Corp BI-200SM, Holtsville, NY, USA) using a vertically-polarised 488nm argon laser source. The sample concentration was kept at about 0.02 wt% during measurement to minimize interference from particle interaction, as MGIO exert inter-particle electrostatic repulsion. Prior to each measurement, the sample was subjected to ultrasonic agitation in a water bath to disperse aggregated particles. The laser was turned on for at least 30 min prior to the measurements to ensure stability of the light source. With the laser power set to 100 – 150mW and the pinhole size adjusted, count rates of 10^5 to 10^6 per second were achieved, which signified good signal to noise ratio of measurement. The photo detector was adjusted to receive scattering at the angles of 45, 60, 75, 90, or 120 degrees. The inverse Laplace transformation of acquired data was complicated by the presence of polydispersed or multi-modal decay rates. This was handled by Gendist, a software that used an algorithm known as the Regularized Positive Exponential Sum (REPES) (Jake, 1995). Gendist performed the transformation on $g_2(\tau)$ (please refer to the principle of DLS in Section 1.5.3 of the Introduction) rather than $g_1(\tau)$ and

used a variable degree of regularization with a second degree regularizer. It presented the distribution in terms of decay time, $1/\Gamma$, from which the diameter distribution was determined.

2.2.6 MR Relaxation Rate

Volumes of 20ml of MGIO suspensions at concentrations of 0.01 to 0.4 mM Fe were prepared. Since relaxation rates are dependent on concentration and MGIO diameter, which in turn is dependent on pH, steps were taken to ensure that desired concentration and constant pH were achieved in the samples. The procedure started with the preparation of a 50mL sample of 0.4 mM Fe with pH corrected to the desired value by 1M NaOH or HCL using a 20 μ L micropipette. A 400mL volume of DI water with the same pH was prepared. Serial dilution of the initial 0.4 mM sample with the pH-adjusted water was performed to prepare 20mL samples with concentrations of 0.2, 0.1, 0.05, 0.025 or 0.0125 mM Fe. The pH consistency was ensured by measuring the pH of all samples. The same sample preparation procedure was used for ferucarbotran.

The relaxation rates of suspended particles were determined on a Siemens Symphony 1.5T imager (Siemens Medical Solutions, Erlangen, Germany). Prior to each imaging sequence, the scanner was shimmed with 20mL water in bottle(s) identical to those containing particles and placed upright at selected position(s) in the quadrature head coil. After shimming, the bottle(s) of water was carefully replaced with bottle(s) of the prepared particle at concentrations of 0.01 to 0.4 mM Fe. GRE images were acquired at 4 to 5 echo times for individual bottles as single 2D coronal slices (FOV: 6.4cm; Matrix: 64x64; Voxel dimensions: 1mm x 1mm x 5mm; TR/TE/FA: 1.6s / 5 to

60ms / 90°; Pixel BW: 260Hz). Spin echo Carr-Purcell-Meiboom-Gill (CPMG) images were acquired for five or six bottles of different concentration simultaneously (FOV: 18cm; Matrix: 256x256; Voxel dimensions: 0.7mm x 0.7mm x 5mm; TR/TE/ETL/FA: 2s/15ms/32/90°; Pixel BW: 130Hz).

The DICOM datasets were exported for image processing using an in-house software package (MATLAB V7.1: MathWorks, Natick, MA, USA). A region-of-interest (ROI) was drawn on within the GRE image of each bottle, with care to maximize ROI area and avoid interface artifact. The mean ROI intensity of each bottle was plotted against the echo time at which the image was acquired. Non-linear least square means fitting was performed to the following equation

$$S_{xy}(t) = S(0)e^{-t/T_2^*} + B$$

where S was the mean ROI signal intensity and B was the image noise. The transverse relaxation time (T_2^*) of each concentration was computed from the time constant obtained from the fit of a first order mono-exponential decay curve to the GRE signal intensity of each bottle against TE. The relaxivity, r_2^* , was taken as the gradient of a linear fit of R_2^* ($= 1/T_2^*$) against iron concentration. The same process was repeated for the CPMG images to obtain the relaxivity, r_2 .

To ensure the reliability of MGIO sample suspension stability, DLS measurements were carried out for duplicate samples of 0.0125 mM that have and have not been used for MR measurements. As MGIO are magnetic and inter-particle attraction at high field may cause irreversible particle aggregation. Although MGIO were once exposed to high field during magnetic separation, exposure to high field for the duration of the MR measurements may also have decreased inter-particle distance

enough to hinder redispersion outside the magnet. Therefore, particle diameters were randomly remeasured after MR measurements.

2.3 Ethics and samples

All human tissue collection was approved by the Domain Specific Review Board of the National University Hospital, and was in compliance with international guidelines regarding the use of fetal tissue for research (Polkinghorne, 1989). In all cases, patients undergoing clinically-indicated termination of pregnancies or normal delivery gave separate written consent for the use of the collected tissue. Female Wistar rats (200-250gm) were acquired from the Centre for Animal Resources (Singapore) and all procedures were approved by the Institutional Animal Care and Use Committee at the National University of Singapore.

2.4 fMSC isolation and differentiation

I isolated fMSC from human fetal bone marrow from terminated pregnancies as previously described (Chan, 2005). Two donors at 8 and 12 week gestation were used. Briefly, bone marrow cells were flushed from the femurs using a 22-gauge needle into a culture medium (CM10), consisting of 10% fetal bovine serum (FBS, Sigma-Aldrich, St. Louis, MO, USA) in Dulbecco's modified Eagle's medium (DMEM) (Sigma-Aldrich, Singapore) supplemented with 2 mM L-glutamine, 50 IU/ml penicillin, and 50 mg/ml streptomycin (Invitrogen, Carlsbad, CA, USA). Single cell suspension was plated in 100mm dishes at 10^5 nucleated cells per ml and cultured in CM10, at 37°C in 5% CO₂. After 3 days, non-adherent cells were removed and the medium was replaced. Adherent cell colonies were detached with 0.25% trypsin

EDTA (Stemcell Technologies, Vancouver, BC, Canada), expanded to sub-confluence, trypsinized, resuspended in freezing medium comprising of 10% DMSO, 30% FBS and 60% DMEM, cooled from room temperature to -80°C at 1°C/min, and stored in liquid nitrogen as frozen stocks.

fMSC were characterised by immunocytochemistry for CD14, CD34, CD45, CD31, von Willebrand factor, CD105 (SH2), CD73 (SH3, SH4) (Abcam, USA), Vimentin, Laminin, CD29 (Chemicon, USA), CD44 (BD, USA), CD 106, CD 90 (Chemicon, USA), HLA I, HLA II (Dako, USA), Oct-4 and Nanog (Abcam, USA) while flow-cytometry was used to screen for Stro-1 (Chemicon, USA) as previously described (Campagnoli, 2001). Cells at passages 5 to 6 were used in all the experiments. Osteogenic, adipogenic and chondrogenic differentiation and their respective assays were performed as previously described (Campagnoli, 2001; Zhang, 2009).

2.5 EPC Isolation

Umbilical cord blood endothelial progenitor cells (EPCs) were derived as described by Ingram et al (Ingram, 2005). Briefly, mononuclear cells were retrieved from umbilical cord blood by density centrifugation and cultured in EPC medium comprising EGM-2 (Cambrex East Rutherford, NJ, USA) supplemented with 10% fetal bovine serum (Gibco®, Invitrogen, Carlsbad, CA, USA) at 37°C in 5% CO₂. Typical cobblestone colonies appeared after 2 weeks, and were subcultured at subconfluence. Cells from passage four were used in these experiments. Cells were characterised by immunocytochemistry to confirm their phenotype and plated on Matrigel (BD Bioscience, San Jose, CA, USA) to evaluate their capacity to form a network of tubular structures or aligned cells in an in vitro angiogenesis assay.

2.6 EPC Immunostaining

Cells grown on collagen-coated cover slips were rinsed with PBS, fixed with ice-cold 1:1 acetone–methanol for 10 min, washed and transferred to a blocking solution consisting of PBS with 3% bovine serum albumin (Sigma-Aldrich) and 0.1% TritonX-100 (Sigma-Aldrich). After 1 h, the blocking solution was replaced with 200 μ l of primary antibody (diluted to 10 μ g/ml in 10% blocking solution) for 1 h at room temperature. Primary antibodies were removed by repeated PBS washes before incubation in 200 μ l of Alexa Fluor 594 conjugated secondary Ab (10 μ g/ml) for 1 h. Samples were then removed and mounted with Vectashield containing DAPI (Vector Laboratories, Peterborough, UK) for the visualisation of cell nuclei. Antibodies used were obtained from Dako Inc., and are listed as follows: rabbit (Rb) anti-human (Hu) vascular-endothelial cadherin, mouse (Ms) anti-Hu PECAM and Ms anti-Hu von Willebrand Factor (vWF). Ac-LDL uptake was carried out based on manufacturer's instructions as follows: samples were washed with PBS and incubated with 10 mg/ml Dii-Ac-LDL (Invitrogen) in EGM-2 for 4 h. The coverslips were retrieved, washed and mounted for analysis.

2.7 Cellular labelling protocol and iron quantification

Prior to labelling, 5×10^5 fMSC were cultured for 24 hr at 2×10^3 cells / cm^2 in CM10. The cells were labelled with MGIO or ferucarbotran by incubation at 0.025 to 0.2 mg iron/ml within a labelling culture medium (CM2: 2% FBS in DMEM supplemented with 2 mM L-glutamine, 50 IU/ml penicillin, and 50 mg/ml streptomycin) at 37°C in 5% CO₂. After 24 hours, adherent cells were repeatedly washed with fresh changes of phosphate buffered saline (PBS) until the PBS appears free of particle under light microscopy to remove unattached particles. The cells were then trypsinized, resuspended in CM10 and layered on Ficoll-paque PLUS (Amersham Biosciences, Piscataway, NJ, USA) for density centrifugation at 100 x g for 30 min to remove loosely attached, extracellular particles. Labelled fMSC were recovered at the interface between CM10 and Ficoll-paque PLUS and washed with PBS by centrifugation to remove remaining Ficoll-paque. Mock-labelled cells were used as controls where fMSC were subjected to the above procedures but without exposure to any particles. The same procedure was used to label EPC, with the exception that CM10 and CM2 were replaced with EGM-2.

2.8 Iron Quantification

Labelled cells were counted and the total iron content analysed to determine the iron mass per cell. Each 100mm dish provided $3.3 \pm 0.3 \times 10^6$ cells for analysis. After counting, the cells were pelleted by centrifugation at $400 \times g$ for 5min, and the supernatant replaced by 0.2ml of aqua regia. The cell pellet was subjected to 15min of homogenization in an ultrasonic bath and kept at 60°C overnight to allow cellular lysing and reduction of iron oxide to complete. The lysate was reconstituted to 5ml with distilled water and analysed by inductively coupled plasma using optical emission spectroscopy (ICP-OES. Optima 5300V, PerkinElmer, Waltham, MA, USA). The iron mass of the mock-labelled control was below reliable ICP-OES detectability of 0.01ppm (<0.1 pg/cell).

2.9 Cellular TEM

The internal structure of labelled and mock-labelled fMSC was analysed by TEM. Cells trypsinized, pelleted and fixed using a fixative mixture containing 2.5% glutaraldehyde in PBS. Post fixation was performed with 1% OsO₄ in PBS pH 7.4 for 2 hours at room temperature and washed in distilled water for 5-10 minutes twice. Dehydration procedure ensued by subjecting the pellet to a series of increasing ethanol then acetone concentration. The sample was washed twice in 100% acetone for 10 minutes. Araldit resin was added to the sample maintained at room temperature for 30 min before the temperature was stepped up to 40°C, 45°C and 50°C for 1 hour at each temperature. The resin was discarded in exchange for fresh resin and maintained at 60°C for 24 hours where polymerisation occurred. Using a Reichert Ultracut E (Leica Microsystems, Wetzlar, Germany) resin-embedded samples were cut into 0.1 µm slices, copper grid mounted, post-stained with lead citrate on copper grid and viewed at 5×10^3 to 100×10^3 times magnifications (Leica) (Myriam, 2008).

2.10 Genome wide Microarray Expression Analysis

2.10.1 RNA Extraction

Total RNA was extracted from 3×10^6 M600, ferucarbotran and mock-labelled fMSC in biological triplicates, using the Qiagen kit (RNAeasy Mini Kit; Qiagen, Valencia, CA) in accordance with the manufacturer's protocol. Briefly, the cell samples were first lysed with surfactant provided by the kit and then homogenised. Ethanol was added to the lysate to provide ideal binding conditions. The lysate was then loaded onto the RNeasy silica-gel membrane to which the RNA binds and all the contaminants that did not were washed away. Pure, concentrated total RNA was eluted with 30 or 40 μ l of water.

2.10.2 Characterisation of RNA Purity

The method of total RNA extraction may result in contamination from DNA. Immediately after eluding total RNA with water, the total volume was measured, 2 μ l of RNA was aliquoted for characterisation and the rest stored at -80°C . The purity of RNA, with respect to contamination from DNA, was determined by placing 1 μ l of RNA on a UV/Vis analyser, NanoDropTM 1000 Spectrophotometer (ND-1000, Thermo Scientific, Wilmington, DE, USA). The total RNA concentration is ideally more than 500 ng/ μ l and the purity, as indicated by A_{260}/A_{280} , between 1.9 and 2.1. The following information of each sample of total RNA sample was obtained

Sample No.	Volume of tRNA (ul)	260/280	260/230	Conc (ng/ul)	A260-10mm	A280-10mm
C1	30	2.09	1.86	1256.3	31.41	15.02
C2	40	2.09	1.81	173.5	-	-
C3	40	2.10	2.15	2315.9	57.90	27.35
F1	30	2.08	2.17	1742.2	43.56	20.97
F2	40	2.06	2.06	2122.5	-	-
F3	40	2.12	2.14	1591.8	39.79	18.73
M1	30	2.08	2.23	1347.5	33.69	16.19
M2	40	2.07	2.15	2018.9	-	-
M3	40	2.13	1.8	1580.1	39.50	18.56

Table 6: Characteristics of total RNA obtained from labelled cells in triplicates.

Sample number C, F and M represents the mock-labelled control, ferucarbotran-labelled and M600-labelled cells, respectively, while the numbers 1, 2 or 3 indicates the triplicates of each group. Less eluant than the recommended volume was used to ensure that the concentration of each RNA sample was high to facilitate analyses that required highly concentrated samples. Even the concentration of sample C2 proved to be sufficient for the subsequent microarray analysis. The measured 260/280 ratios were within the ideal range of 1.9 to 2.1, with the exception of F3 and M3. The measured ratios were acceptable as the ideal value of 2.0 is a rule of thumb. For example, a ratio of greater than 2 is expected if there is a high Uracil to Thymine ratio but a ratio below 1.9 may indicate the presence of protein, phenol or other contaminants that absorb at or near 280 nm (Wilfinger, 1997).

The total RNA integrity was checked with QIAxcel System (Qiagen), formerly known as eGene HDA-GT12 (eGENE, Irvine, CA, USA) short for high-performance DNA analyzer for genotyping on 12 channels. This capillary electrophoresis system replaces time-consuming slab gel electrophoresis methods used to separate segments

of DNA or RNA. 1ul of total RNA was used in accordance to the manufacturer's protocol and the resulting electropherogram should ideally consist of two well-defined peaks corresponding to the 28S and 18S ribosomal RNA in the approximate ratio of 2:1. The resulting electrograms for sample C1, F1 and M1 are shown below.

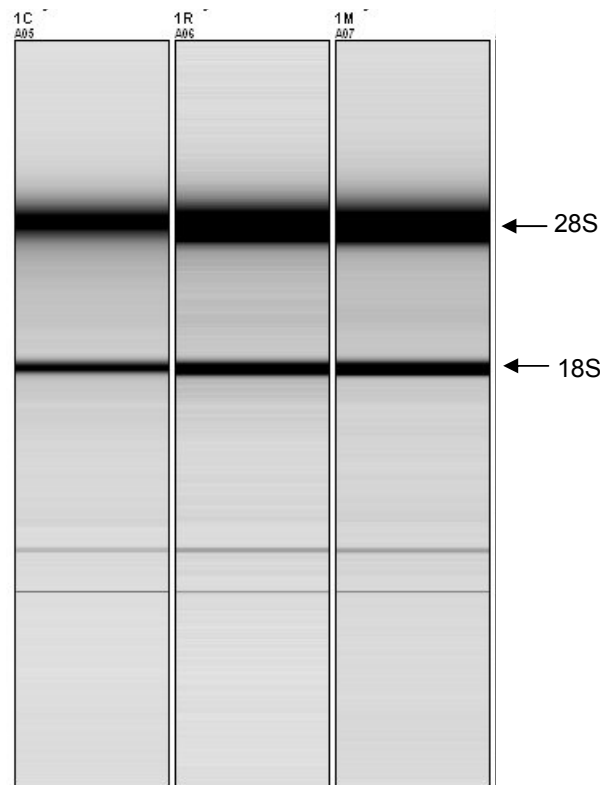


Figure 14: Electrogram showing crisp 28S and 18S bands

The electrogram shows the relative ratio of the 28S and 18S ribosomal RNA (rRNA) sub-units. 28s is the larger sub-unit and rRNA sub-unit naming are based on their molecular weights. The electrogram shows that 28S and 18S are two well-defined bands in the approximate ratio of 2:1. This method relies on the assumption that rRNA quality and quantity reflect that of the underlying mRNA population. Because mammalian 28S and 18S rRNAs are approximately 5 kb and 2 kb in size, the theoretical 28S:18S ratio is approximately 2.7:1; but a 2:1 ratio has long been considered the benchmark for intact RNA. While crisp 28S and 18S rRNA bands are

indicative of intact RNA, it remains to be determined how well the integrity of relatively stable and abundant rRNA reflect the quality of the underlying mRNA population, which turns over much more rapidly (Imbeaud, 2005).

2.10.2.1 Development of cDNA and cRNA

To develop cDNA from the total RNA, 10 µg of total RNA was used for a one-cycle cDNA synthesis, followed by synthesis of Biotin-labelled cRNA and fragmentation of the cRNA in accordance to the protocol given in GeneChip® One-cycle Target labelling and control reagents (Affymetrix, P/N: 900493).

2.10.2.2 Hybridisation of cRNA to Microarray

10 µg of fragmented and labelled cRNA from each sample was hybridized with control oligonucleotides B2 and hybridization controls (*bioB*, *bioC*, *bioD* and *cre*) on each Human Genome U133 Plus 2.0 Array (Affymetrix, Santa Clara, CA, USA) at 45 °C overnight at 60 rpm. The washing and scanning were carried out as stated in the manufacturer's wash and stain protocol for GeneChip® Hybridization (Affymetrix). The washed arrays were scanned using GeneChip Scanner 3000 GeneChip Operating Software 1.0 (GCOS, Affymetrix) and data collected to generate the data files which contained the intensities and the flag values of present, absent or marginal of 54675 probes.

2.10.3 Analysis of Microarray Data

The GCOS data files were imported into GeneSpring GX 7.3.1 (Agilent Technologies, Inc., Palo Alto, CA) to filter out probes that were unaltered by labelling. The software was used to filter out unwanted probes in the following steps.

- The control strength of all samples groups (M600, ferucarbotran, mock) was identified. Control strength is the cut-off intensity value such as any probe with intensity below which may be considered less reliable and can be omitted from further analysis. Only probes with raw signals above control strength in at least 1 of 3 samples groups were considered
- The probes which have triplicates from all sample groups flagged absent were removed, to avoid unnecessary comparison of low signals.
- A t-test was performed to identify M600-labelling probes that have mean intensities that were significantly different from the mean mock-labelling probes. The same was done for ferucarbotran-labelling probes. The 2-fold up and down regulated list for M600 and ferucarbotran-labelling can now be identified.

As genes do not function individually but in concert to elicit a particular function (Hallikas, 2006), the functions associated with our set of differentially regulated genes can be identified in a process known as functional profiling. Bioinformatician have established a fixed set of vocabulary, called gene ontology (GO) terms to describe the various functions. Since each gene is associated with one or more gene ontology (GO)

terms, which are classified into biological processes, cellular components and molecular functions, the 2-fold differentially expressed gene list can be enriched based on their associated GO terms. A web-based software, FatiGO (Al-Shahrour, 2006), was used to obtain GO terms that were significantly associated with the genes list. FatiGO takes the gene list, generates a second list consisting of the genome less the gene list, and generates the GO terms associated with each of these lists. Then a Fisher's exact test for 2×2 contingency tables is used to check for significant over-representation of GO terms in the gene list with respect to the rest of genome. Multiple test correction to account for the multiple hypothesis tested (one for each GO term) is applied to correct for multiple testing using the false discovery rate (FDR) procedure of Benjamini & Hochberg (Benjamini, 1995). The FDR is necessary to control the number of false positives given the large number of simultaneous tests. Each associated GO term is assigned a p-value and an adjusted p-value. The p-value was derived from the Fisher's exact test while the adjusted p-value uses the FDR procedure.

2.11 *In vivo* imaging

2.11.1 Cellular Migration Stroke Model

To verify the sensitivity and efficacy of MGIO as a cellular label for MRI tracking, an injury model to demonstrate stem cell homing is required. The brain was chosen as the target organ as it provides a reasonably homogenous and hyperintense background for the observation of hypointense, migrating cells. The mouse brain is often imaged with dedicated MRI equipment, but the rat brain at approximately the size of an adult's thumb, is more easily imaged on the available clinical MR scanner. Cerebral infarction by focal ischemia is a clinically relevant injury model which can result from thrombosis or embolism.

2.11.1.1 Internal and Middle Cerebral Artery Occlusion

Middle cerebral artery occlusion (MCAo) is a commonly used method to induce ischemia with the option of reperfusion. In this model, only large (25-84mm²) infarcts are reproducible but they result in motor deficit and contralateral circling (Menzies, 1992). Small infarcts are desired as the migrated cells can be more easily located. The MCAo can be produced by craniectomy or by advancing an end-rounded suture through the internal carotid artery (ICA) to occlude the origin of the MCA (Longa, 1989). The advancing suture method is less invasive to the animal but is more technically demanding as it requires dextrous fingers to feel the resistance on the suture when its end reaches the MCA origin.

2.11.1.2 Photochemical Cerebral Thrombosis

The photochemical cerebral thrombosis is an alternative and well-established thrombotic stroke injury model in rats (Watson, 1985; Kim, 2000; Jendelova, 2004). The principle behind this method of infarct creation lies in the absorption of green light by intravascular Rose Bengal. The resulting triplet state of the sensitizer molecule generates singlet oxygen, starting a chain process of peroxidation that produces microrupture of endothelial cell membranes, and causes platelet aggregation that eventually leads cerebral infarction and necrosis. In this highly reproducible model, the size of the infarct depends on the Rose Bengal dose and delivery rate, light intensity and area exposed.

Focal cortical stroke was induced in Wistar female rats via a photochemical method (Watson, 1985; Jendelova, 2004). The rats were anaesthetized with 7.5mg/100g BW ketamine (Parnell Laboratories, Alexandria, NSW, Australia) and 1mg/100g BW xylazine (Troy Laboratories, Smithfield, NSW, Australia) intraperitoneally and mounted in a stereotactic frame. A 7.5 mg/ml solution of Rose Bengal in saline was filtered (0.22 μ m) and injected via a tail vein cannula at 1 mg/ 100 g BW at a rate of 0.2 ml/min. Simultaneously, the skull at AP = -2 mm, ML = -3 mm from the bregma, was exposed to 60W of blue-green passband-filtered (BG39; Schott, Duryea, PA, USA) white light from a halogen lamp via a fibre optic waveguide for 10 min to generate a photochemical cortical stroke. The spot size was adjusted to a diameter of approximately 3mm with an optical aperture. The selected coordinates corresponded to the sensory cortex and were easily assessable for light exposure. The motor cortex was avoided to minimize distress to the animal, although contralateral motor deficit could have been a convenient manner to verify the success of infarct induction.

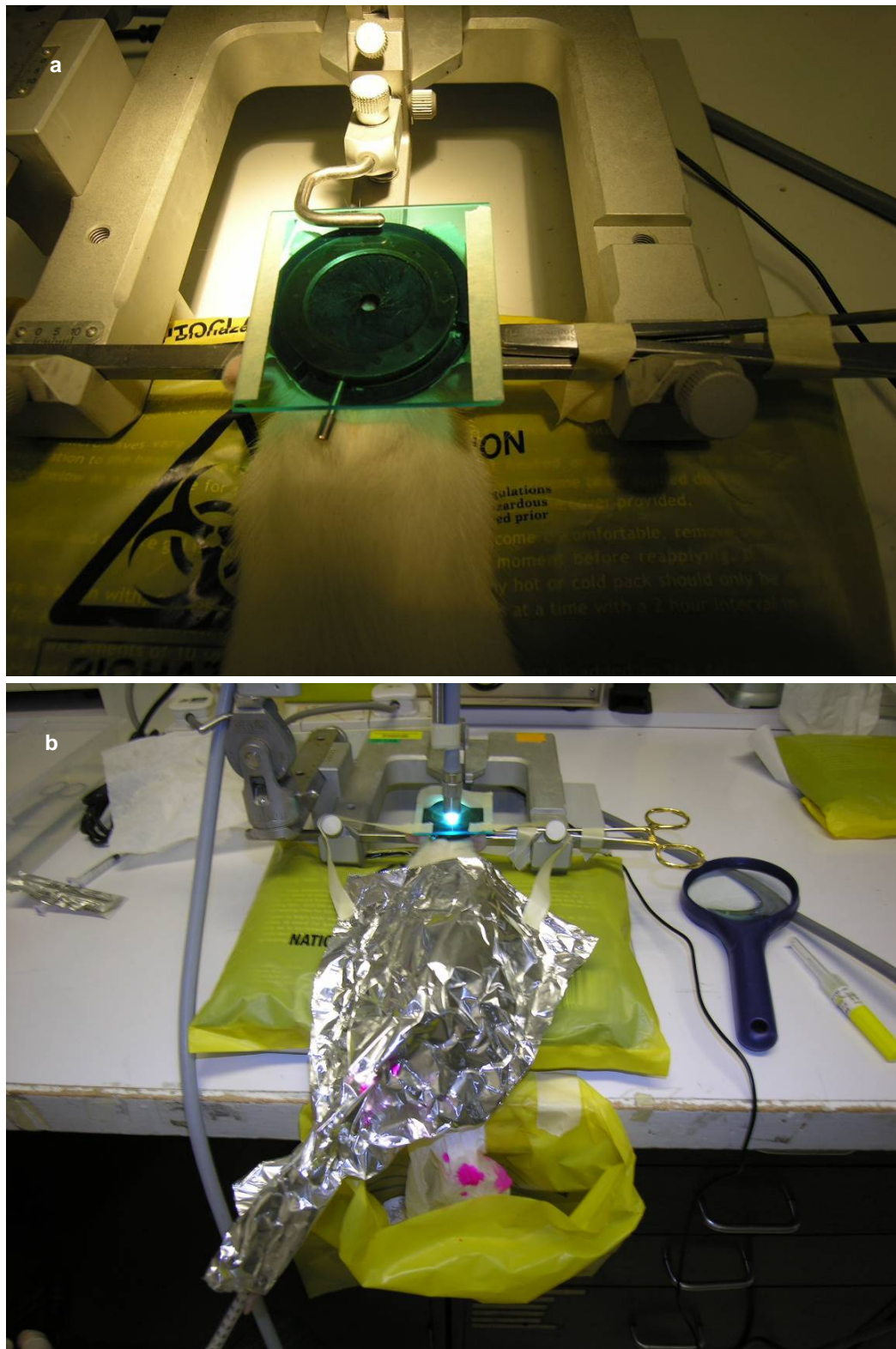


Figure 15: Procedures of stroke induction by photochemical thrombosis. (a) Animal is mounted on a stereotatic frame and skull was exposed. (b) Through a 3mm aperture, green-filtered white light was applied to the skull while Rose Bengal was injected via a tail vein cannula.

2.11.2 Transplantation of fMSC

Two days after induction of photo-thrombotic injury to the cerebral cortex (Day 0), xeno-transplantation of (a) 2×10^4 M600-labelled fMSC (M600-fMSC, n=22) or (b) 2×10^4 ferucarbotran-labelled fMSC (ferucarbotran-fMSC, n=7) into the contralateral cerebral cortex was performed. A third group had (c) 2×10^6 M600-labelled fMSC infused intravenously through the tail vein (n=4), and (d) a control group of animals without cortical injury were transplanted with 2×10^4 M600-fMSC (n=3). A further two control groups consisted of animals with contralateral stroke injury either without cellular transplantation (n=10), or transplanted with mock-labelled fMSC (n=1).

For cortical injection contralateral to the stroke site, a burr hole (1 mm) was made on the right side of the skull to expose the dura overlying the cortex (Figure 15a). fMSC were kept on ice, resuspended immediately before injection by repeated pipetting before loading into a Hamilton syringe. 2×10^4 cells in 5 μ l of PBS were injected slowly over a 10 min period using a 33G needle into the contralateral hemisphere at AP = -2 mm, ML = 3 mm, and DV = 3.5 mm from the bregma (Figure 15b). For IV delivery, 2×10^6 cells in 0.5 ml PBS were injected into the lateral tail vein. Immunosuppression with intraperitoneal cyclosporin (20 mg/kg BW on alternate days, Sandimmune Injection, Novartis Pharma, Switzerland) was initiated at the time of cellular transplantation and maintained throughout the experimental duration.

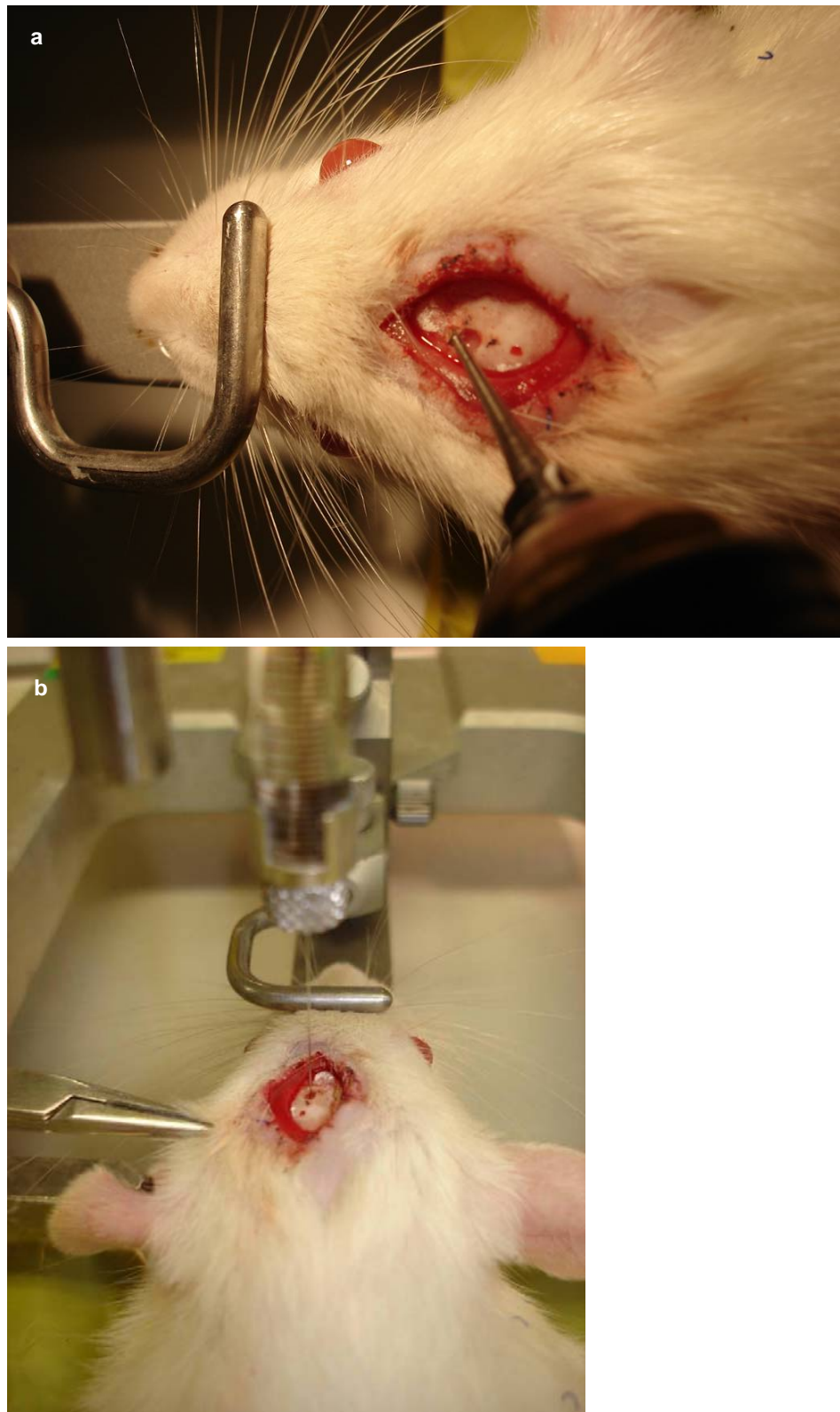


Figure 16: Animals is mounted on a stereotaxic frame and (a) a 1mm burr hole was made to expose the dura and (b) the Hamilton syringe was lowered and cells were injected slowly over a 10 min period.

2.11.3 MRI

In vivo MRI was performed on a 1.5 T whole-body clinical MR scanner with a clinical wrist rf coil (General Electric, GE, Fairfield, CT, USA). Anaesthesia was induced with 4% isoflurane and maintained with 1.5-2.5% isoflurane in 100% oxygen delivered through a cone mask. *In vivo* transverse images were obtained using turbo spin echo (TSE - FOV: 5cm; Matrix: 192x192 and zero-filled to 512x512; Voxel dimensions: 260 μ m x 260 μ m x 1.5mm TR/TE/ETL/FA/NEX: 2s/81ms/16/90°/12; Acquisition Time: approximately 9min) and gradient echo (GRE - FOV: 5cm; Matrix: 160x160 and zero-filled to 512x512; Voxel dimensions: 313 μ m x 313 μ m x 1.5mm; TR/TE/FA/NEX: 280ms/20ms/20°/15; Acquisition Time: approximately 9min) pulse sequences as ten 2D slices. SSFP sequence produced sixteen 3D slices (FOV: 6cm, Matrix: 160x160 and zero-filled to 512x512; Voxel dimensions: 375 μ m x 375 μ m x 1mm TR/TE/FA/NEX: 11.2ms/5.6ms/70°/20).

A method was developed to quantify the number of hypointense voxels on an MR image to facilitate a direct comparison of MR images other than a qualitative visual analysis. A voxel was considered hypointense if its signal intensity was below the signal intensity threshold (S_H). Using Rose's criterion, the S_H of a day 5 or day 12 image was determined with respect to a reference signal (S_R) and the image standard deviation (SD_R), as:

$$S_H = S_R - k \cdot SD_R$$

The S_R was determined from the corresponding day -1 GRE image as the mean signal intensity of an 8 mm² ROI positioned at the cortical region contralateral to the stroke. The SD_R was calculated from the standard deviation of MR signal from the air,

reduced by a factor of 0.655 to account for the non-Gaussian noise of magnitude images. The contrast to noise ratio, k , was assumed to be 5.

2.11.4 Histology

In order to confirm the generation of a thrombotic stroke, selected rats ($n=3$) were anaesthetized and perfused intracardially with 250ml of 2% 2,3,5-triphenyltetrazolium (TTC, Sigma-Aldrich) 24 hrs after stroke induction. Following recovery of the brain, 1 mm sections were further incubated in TTC at 37 °C for 10 min, laid onto slides, and visualised under light microscopy. For histological analysis of transplanted cells at various time points, the rats were anesthetized and transcardiacally perfused with PBS followed by 4% paraformaldehyde. The brain was harvested, processed and paraffin embedded, Ten micron coronal sections on polylysine-coated slides were prepared for staining.

Prussian blue (PB) iron staining was performed by incubating the dewaxed sections with freshly prepared 5% potassium ferrocyanide in 5% HCl 1:1 for 30 min and washing with deionised water. For 3,3'-diaminobenzidine (DAB)-enhancement of PB staining (Schroeter, 2004), sections were incubated in 3% H₂O₂ for 3min pre-PB staining, PB stained, incubated in 0.05% DAB in PBS for 5min followed by another incubated in 0.05% DAB in PBS and 0.03% H₂O₂ for 3 min.

Immunohistochemical staining was done after de-paraffinisation, rehydration and an antigen retrieval step performed at 95°C for 30 mins using H-3300 buffer (Vector Laboratories, Peterborough, UK). Sections were blocked with 5% goat and fetal calf serum, and the nuclear envelope permeabilized with 0.2% Triton X-100 for 1 hr, before being incubated overnight at 4 °C with primary antibodies of mouse anti-rat

ED1 1:100 (MCA341R, AbD Serotec, Oxford, UK) and rabbit anti-human vimentin 1:100 (ab16700, Abcam, Cambridge, UK). After washing of the slides with PBS, incubation with secondary antibodies, either goat anti-rabbit Alexa Fluor 488 or goat anti-mouse Alexa Fluor 594 at 1:100 for 30 min was performed. Sections were then mounted with 4,6-diamidino-2-phenylindole (DAPI) or propidium iodide for nuclear visualisation (both from Vector Laboratories).

Fluorescent *in situ* hybridisation (FISH) was done after de-paraffinisation, rehydration and antigen retrieval at 95°C for 30 mins with H-3300, citrate buffer pH6, or Tris-EDTA. The FISH staining was done on sections with or without prior staining with the above immunohistochemical procedure. Each section was dehydrated in ethanol, exposed to the 8ul (25% dilution in hybridisation buffer) of Starfish pan-centromeric probe (1695-Cy3-02; Cambio, Cambridge, UK), covered cover-slip sealed with nail varnish. In a hybridisation chamber, denaturation took place at 71°C for 7 minutes followed by hybridisation at 37°C for 4 hours, in a humid atmosphere. Cover slip was removed during post-hybridisation washes in 2x sodium citrate buffer (SSC; 3 M NaCl, 0.3 M sodium citrate, pH 7) followed by washing in 0.4x SSC at 72° C for 2 mins and in 2x SSC at 37° C for 2 mins. Sections were then mounted with DAPI or propidium iodide for nuclear counterstaining.

2.12 Statistics

Parametric data are shown as mean \pm standard error of the mean. Iron loading at various labelling concentrations was analysed using two-way ANOVA with post-hoc Bonferroni correction, or with a *t*-test. A p-value<0.05 was considered indicative of a statistically significant result.

**Chapter 3 Results I: MGIO Synthesis and
Characterisation**

MGIO was synthesized in a two-step process consisting of emulsion polymerisation to form PMG, followed by co-precipitation of iron oxide within PMG to form MGIO. Manipulation of reagent masses and proportions during both steps of synthesis resulted in MGIO with diameters that cover the sub-micron range. The physicochemical properties of MGIO were measured, including the MR relaxation properties, which were compared against existing theoretical models.

Hypothesis:

Magnetic microgel iron oxide particles (MGIO) can be synthesized such that they have similar composition across the diameter range of 100nm to 1 μ m. Moreover, the measurements of the magnetic resonance relaxation of MGIO can provide a physical means of verifying theoretical model predictions.

3.1 Synthesis of PMG

The synthesized PMG Models 1 to 6 were in the order of increasing particle diameter. They had similar composition where the DAP was kept at 4% for all models and x-y ratios were 60:40, 50:50 or 20:80. Dialysis was performed to remove unreacted chemicals, including unpolymerised EA. The presence of EA in the dialysate is characterised by a strong odour of solvent that gradually disappears 2 weeks into the dialysis process. The resulting PMG has pH of 1.8 to 2.2 and solid weight (wt) % of about 10%.

The quantity of reagents for the various models of PMG differed mainly in the micellar ratio, which is inversely proportional to the PMG diameter. For example, the quantities of reagents in Model 4 and 5 were similar but Model 5 was larger as the monomers were polymerized onto fewer micelles. The effect of a larger amount of MAA is exemplified by PMG Model 3 and 4. Both had similar micellar ratio but as Model 4 had a higher MAA to EA weight ratio, its hydrated diameter was 130.9 nm compared to 71.1 nm of Model 3 (Tan, 2004). The diameters of the other models were not determined, although the effects of varying micellar ratio and MAA to EA ratio were expected to apply to them as well.

3.2 Synthesis of MGIO

Alkaline co-precipitation of iron salts to form iron oxide particles is a synthesis route that was established more than 2 decades ago (Massart, 1981). The method has been adapted for the *in situ* co-precipitation of iron oxide primary particle within PMG to form MGIO particles. Synthesized MGIO consist of multiple iron oxide (IO) primary nanoparticles cores (~5nm each) held within soft polymeric matrices. The synthesized MGIO had a 9-fold range of hydrated diameters (87–765 nm) as determined by DLS.

The PIO size of 5 nm or less is expected at the precipitation temperature of 35 °C given that the particle sizes created by the alkaline co-precipitation process is dependent on temperature (Davies, 1993). Elevated temperature would result in larger PIO that have higher saturation magnetization and magnetic remnance (Murbe, 2008). Attempts with co-precipitation at 35 to 80°C were made, but they failed to produce stable MGIO above 40°C as the PMG became unstable during the Fe²⁺ salt infusion process. The unstable PMG lost their ability to suspend in the Fe²⁺ salt solution and formed visible aggregates, some of which settled to the bottom of the reactor as soon as mechanical stirring stopped. The co-precipitation temperature was selected to be 35 °C to give sufficient margin from the onset of instability at higher temperatures.

3.3 Characterisation of MGIO

3.3.1 Transmission Electron Microscopy

The transmission electron microscopy (TEM) was used to show that MGIO consisted of numerous electron dense sub-5nm structures held together by a mesh of lower electron density (Figure 17a-e). The sub-5nm structures were the primary iron oxide nanoparticle cores (PIO) which were more electron dense than the polymeric matrix holding them together. The composition of MGIO was confirmed by selected area electron diffraction (SAD) (Figure 17f), which shows a pattern with interplanar spacing typical of composite particles that contain both amorphous material (polymer) and crystalline magnetite. From the micrographs, the geometry of MGIO was approximately spherical but the particle size was far lesser than the hydrated diameter reported by DLS. This is due to the collapse of the polymeric matrix when absorbed water is removed when the sample is air-dried prior to TEM. Indeed, microgels are capable of changing their sizes by several times in response to change in their environment, for example change in temperature (Nayak, 2005).

In comparison to MGIO, air-drying ferucarbotran seems to induce greater aggregation, as suggested by the TEM micrographs in Figure 18. Moreover, the diameter of air-dried ferucarbotran is approximately 50 - 70nm, which is similar to its hydrodynamic diameter (62nm). This again suggests that the polymer matrix of MGIO differs greatly from that of ferucarbotran. The disparity in the extent of collapse is probably due to the difference in the capacity of hydrogel and carboxy-dextran to absorb water.

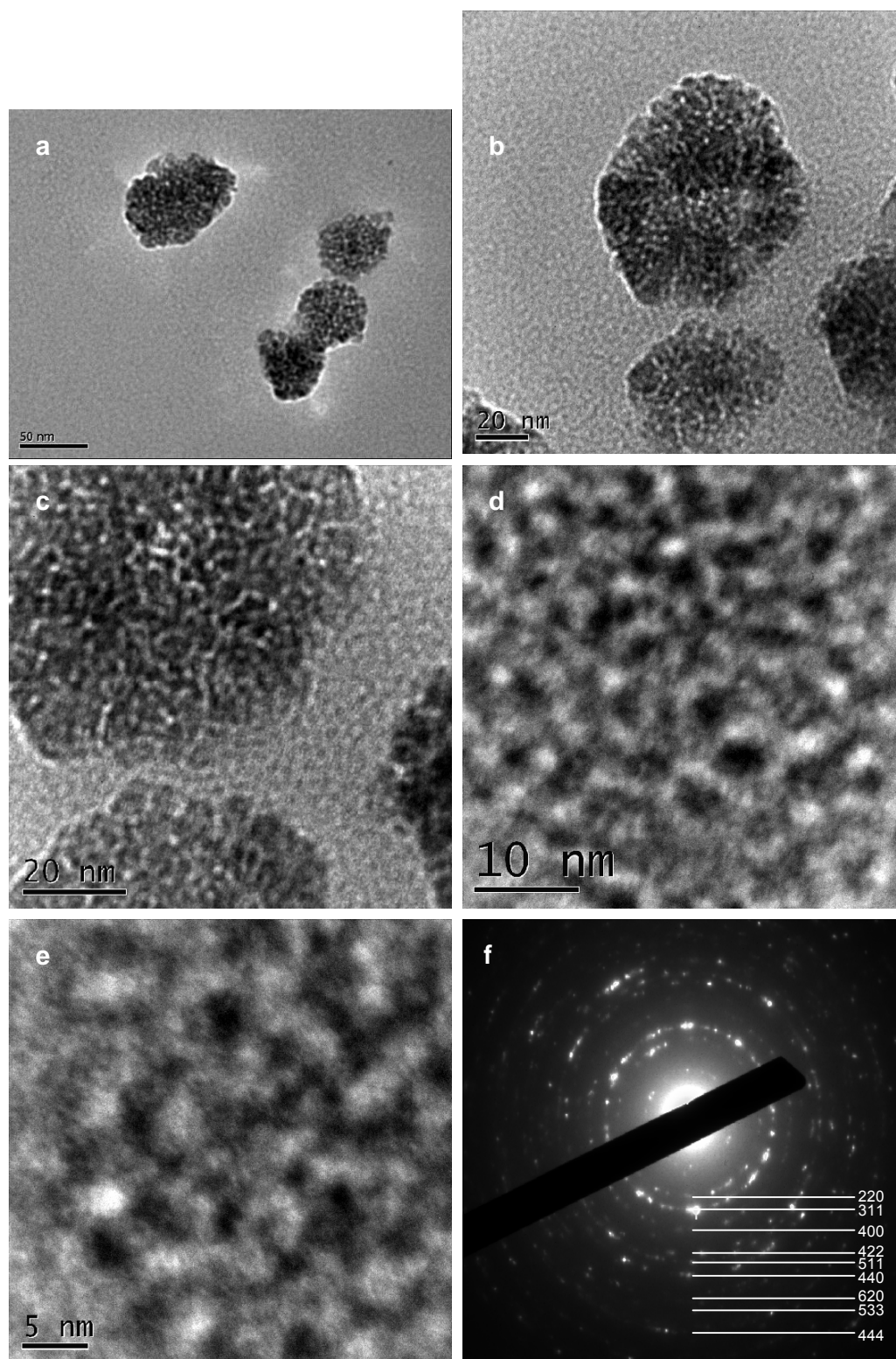


Figure 17: (a-e) Transmission micrographs of M600 air-dried on copper grid. (a-c) MGIO are spherical particles that are 50-70nm when dried. The primary iron oxide (PIO) nanoparticles, being more electron dense than the polymer matrix of PMG, appear as dark spots in each MGIO. (d-e) High magnification images show that the PIO are 2-5nm each. (f) Selected area electron diffraction of a single MGIO particle showing interplanar pattern typical of composite particle containing magnetite

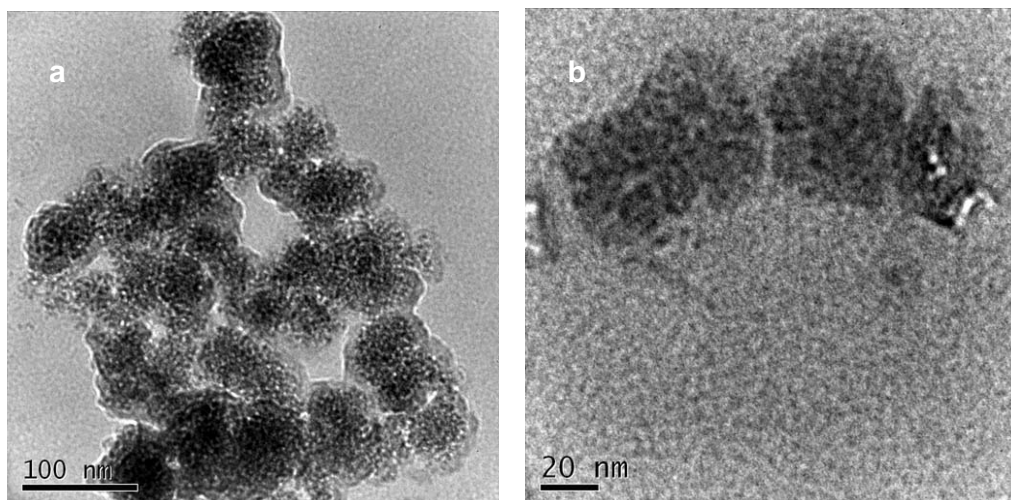


Figure 18: Transmission micrographs of ferucarbotran air-dried on copper grid. (a) Dried ferucarbotran are about 50nm in diameters, they appear spherical but aggregated when dried. (b) 3 individual particles of ferucarbotran that have diameters 40-60nm and they contain PIO, just like MGIO.

3.3.2 Thermogravimetric Analysis

Thermogravimetric analysis (TGA) of MGIO was performed by heating lyophilised MGIO up to 900°C to determine the iron oxide weight %. The TGA thermograms were plotted to show the weight and the first derivative with respect to temperature. The weight loss occurred in four stages. The first loss occurring below 200°C was due to water absorbed in the MGIO. The weight loss from absorbed, tightly bound water was about 3-4 %. Removal of bound water that coordinated to the carboxyl groups occurs before 200°C, which is similar to the TGA of poly(acrylic acid) (Maurer, 1987). The minimum of the derivative, T_{dry} , occurring at about 140 – 160 °C, was taken as the temperature at which MGIO became completely dry with intact carboxyl groups. The next stage of weight loss occurred between the 160 to 285 °C where a water or ethanol side chain was eliminated in the anhydrite formation process shown below (Bajaj, 1994).

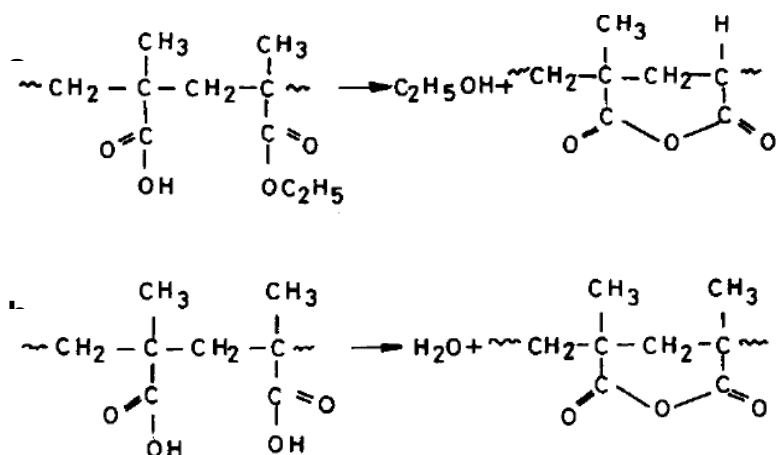


Figure 19 Schematics of anhydrite formation during PMG degradation. (a) Between two MAA neighbours, an ethanol molecule is removed. (a) Between a neighbouring MAA and EA, a water molecule is removed.

The third (300 – 500 °C) and fourth (500°C – 800 °C) stage of weight loss involved the decomposition of the polymer backbone with the release of different decomposition products. In this temperature range, the anhydrite chains were fragmented into gaseous products. When polyacrylic acid was analysed by TGA, it was shown by mass spectrometry that at the third stage, methacrylic acid, and carbon dioxide were given off, and at the fourth stage, the by-products were propene, isobutylene and dodecanoic acid (Schild, 1993; Bajaj, 1994). Although I have not performed mass spectrometry of the output gaseous during TGA, the by-products can be expected to be similar due to the similar composition of acrylic acid and MAA.

At the temperature range of 750 – 900 °C, a weight gain was observed for some of the samples. This was due to the oxidation of MGIO magnetite to γ -hematite below 500 °C and to α -hematite beyond 500 °C by the traces of oxygen in the 99.99% nitrogen gas used during TGA (Forsmo, 2005). The weight gain from oxidising magnetite is dependent on the amount of oxygen during TGA. The amount varies depending on the purity of nitrogen used during the analysis. In air, the weight gain from oxidising

maghemite is about 3.5%. In a completely oxygen free-atmosphere, the weight gain is less than 0.1% and is still less than 1% in 99.99% nitrogen (Ishikawa, 1998). Therefore, this is a negligible error in our calculations. Nonetheless, the weight of the final product was taken at a temperature T_{final} of 850 °C instead of 900 °C to minimize this error. The residue consisted of iron oxide and minute amounts of solid polymeric decomposition products. Based on previous TGA studies, the residue weight % of PMG, R, was about 4% at 600°C and less at higher temperature (Bajaj, 1994). Therefore, the iron oxide weight % can be defined as,

$$\text{wt}\% = X = \frac{W_{\text{IO}}}{W_{\text{IO}} + W_{\text{P,dry}}}$$

Where W_{IO} is the weight of iron oxide in MGIO and $W_{\text{P,dry}}$ is the weight of PMG at T_{dry} . Given that the initial weight of MGIO at room temperature, W_{sample} , is known, the following equations can be established.

$$\begin{aligned} W_{\text{sample}}P_{\text{dry}} &= W_{\text{IO}} + W_{\text{P,dry}} \\ W_{\text{sample}}P_{\text{final}} &= W_{\text{IO}} + R(W_{\text{P,dry}}) \end{aligned}$$

Where P_{dry} and P_{final} are the weight % of the sample at T_{dry} and T_{final} , respectively. The wt% can be expressed as

$$\text{wt}\% = X = \frac{\frac{P_{\text{final}}}{1-R} - R}{\frac{P_{\text{dry}}}{1-R}}$$

Under this TGA condition, R can be accurately determined by performing TGA on PMG alone, but this experiment was not done. The error due to R was considered negligible small for other workers to have omitted it from their calculations (Lin, 2005). MGIO particles contained between 33 to 82 % by weight of IO as determined by this method. The thermograms of each MGIO can be found in the following pages.

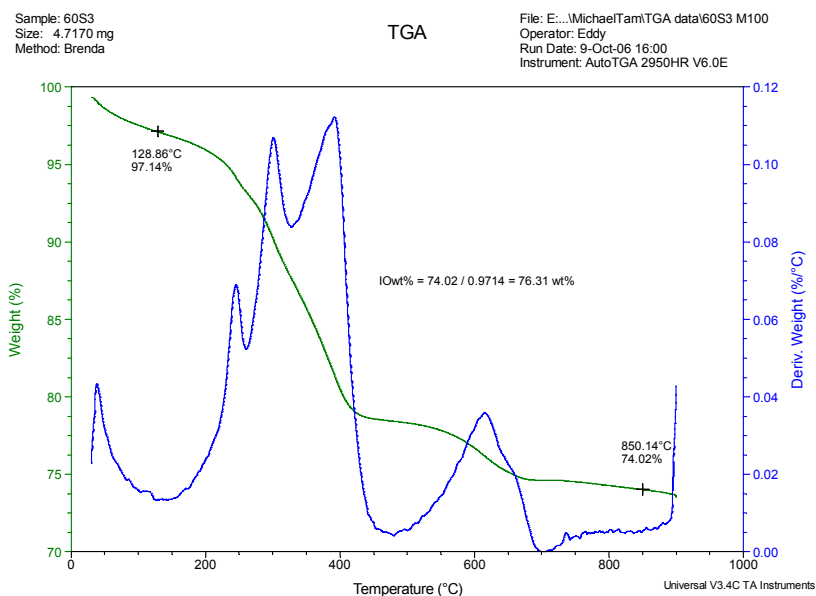


Figure 20: Thermogram of M100. Weight % curve (green) shows that the sample weight was decreased from 100% at room temperature to 97% after evaporation of absorbed water and further decreased to 74% at 850°C. The first minimum of the derivative weight (blue) was taken as the temperature where absorbed water had been removed removed.

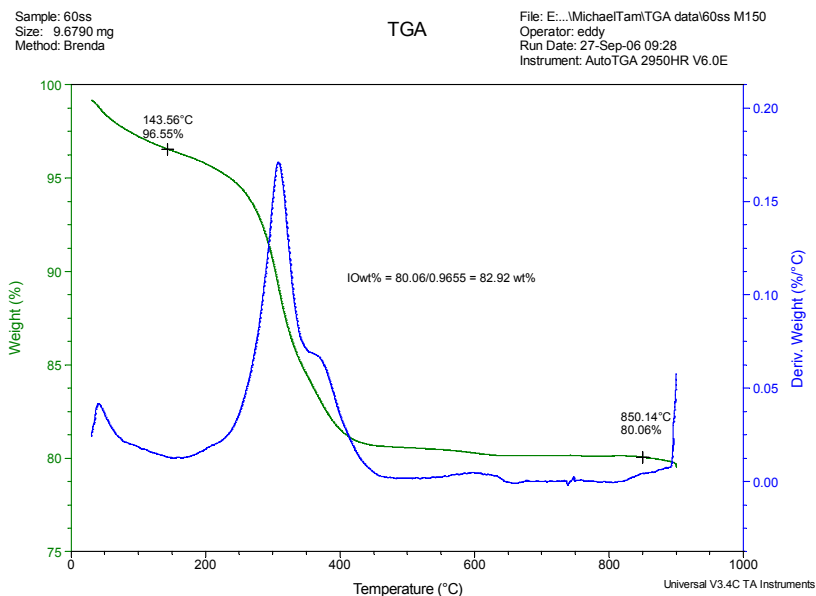


Figure 21: Thermogram of M150. Weight % curve (green) shows that the sample weight was decreased from 100% at room temperature to 97% after evaporation of absorbed water at the first minimum of the derivative weight (blue) and further decreased to 80% at 850°C.

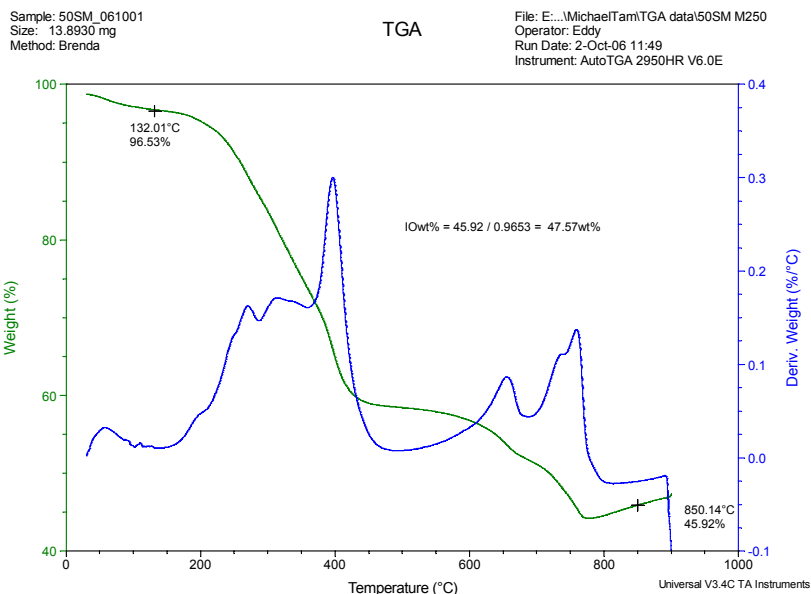


Figure 22: Thermogram of M250. Weight % curve (green) shows that the sample weight was decreased from 100% at room temperature to 97% after evaporation of absorbed water at the first minimum of the derivative weight (blue) and further decreased to 45% at 850°C.

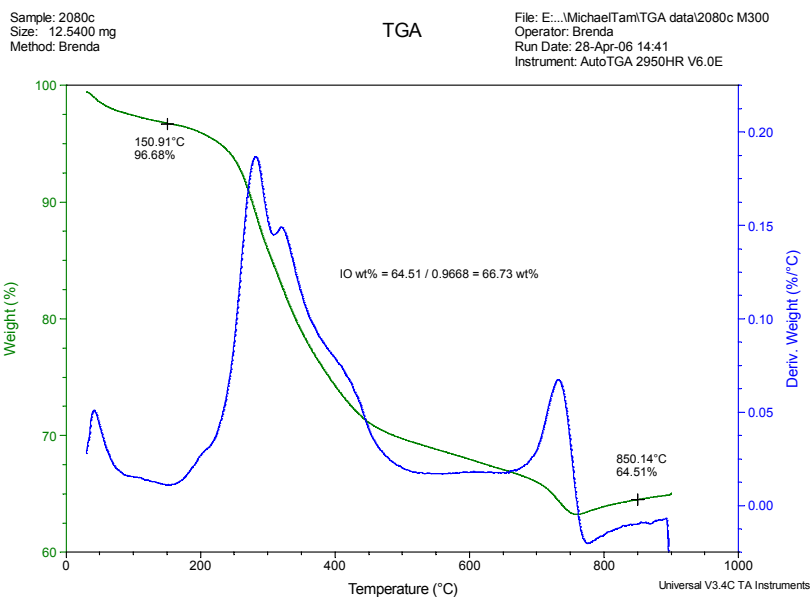


Figure 23: Thermogram of M300. Weight % curve (green) shows that the sample weight was decreased from 100% at room temperature to 97% after evaporation of absorbed water at the first minimum of the derivative weight (blue) and further decreased to 65% at 850°C.

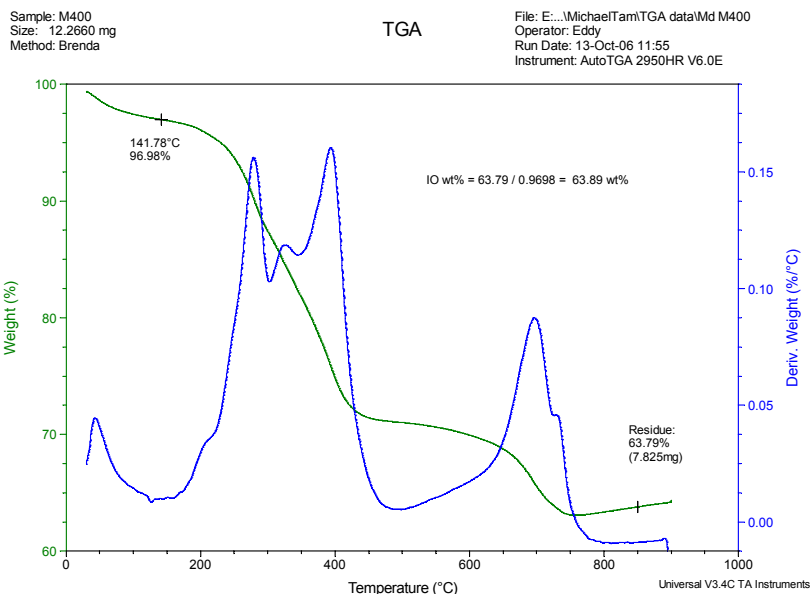


Figure 24: Thermogram of M400. Weight % curve (green) shows that the sample weight was decreased from 100% at room temperature to 97% after evaporation of absorbed water at the first minimum of the derivative weight (blue) and further decreased to 64% at 850°C.

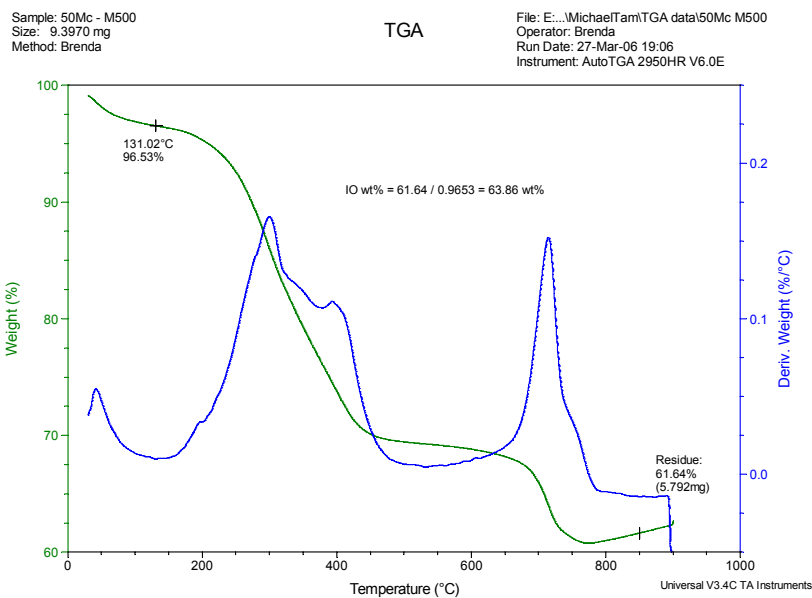


Figure 25: Thermogram of M500. Weight % curve (green) shows that the sample weight was decreased from 100% at room temperature to 97% after evaporation of absorbed water at the first minimum of the derivative weight (blue) and further decreased to 62% at 850°C.

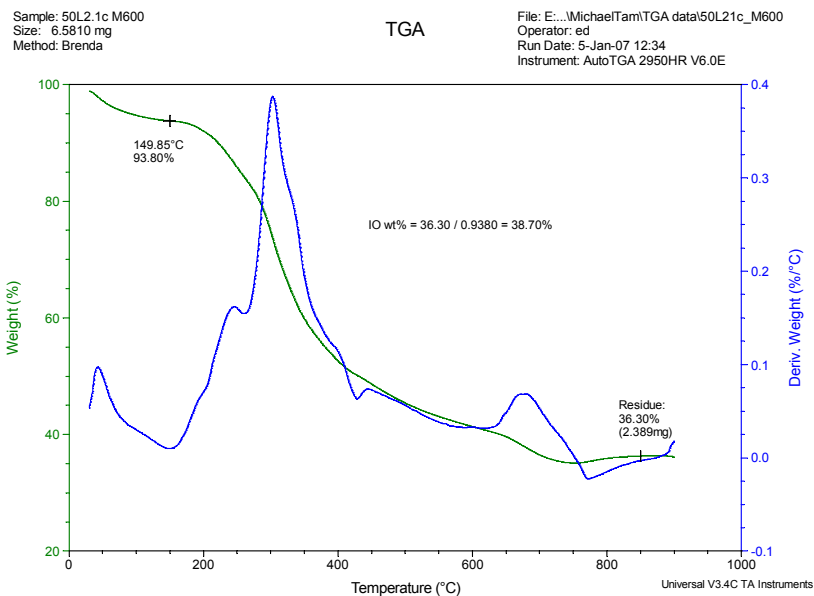


Figure 26: Thermogram of M600. Weight % curve (green) shows that the sample weight was decreased from 100% at room temperature to 94% after evaporation of absorbed water at the first minimum of the derivative weight (blue) and further decreased to 36% at 850°C.

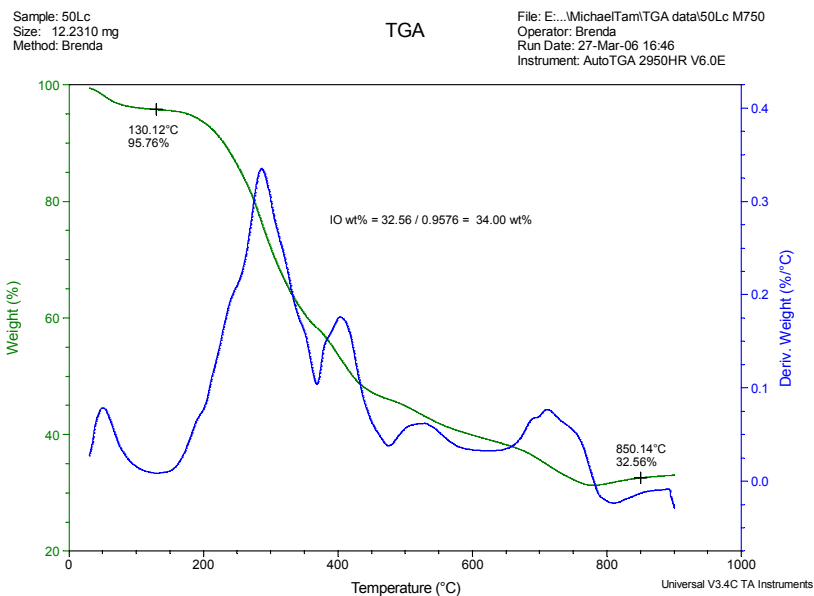


Figure 27: Thermogram of M750. Weight % curve (green) shows that the sample weight was decreased from 100% at room temperature to 96% after evaporation of absorbed water at the first minimum of the derivative weight (blue) and further decreased to 33% at 850°C.

In summary, the IO wt% is shown in the following table

MGIO Model	IO wt%
Ferucarbotran	58.4% (Reimer, 2003)
M100	76.%
M150	83%
M250	46%
M300	67%
M400	64%
M500	64%
M600	43%
M750	34%

Table 7: Iron oxide content of various MGIO models expressed in terms of weight % (IOwt%).

Having a high IOwt% is an advantage when MGIO is used as a cell label, as only the iron oxide portion of the particle make the cells MR-visible. There is no obvious relationship between particle diameter and IOwt%. M100, M150, M300, M400, M500 have IO wt% higher than ferucarbotran, but the MGIO models have lower IO wt%.

Between M100 and M150, M150 was expected to have a higher IOwt% because both were synthesized from the same PMG model (Model 1), but M150 was infused with 1.0g of iron salt while M100 received only 0.3g. M150 and M250 were co-precipitated under the same conditions but M250 was synthesized from a larger PMG model (Model 2) that have a MAA:EA ratio of 50:50, while that of PMG Model 1 was 60:40. The greater availability of MAA in M150 may explain its higher IOwt%, since MAA provide carboxyl groups that coordinate with iron salts. Comparing M300 and M400, they were based on the same PMG model (Model 3), although M400 received a larger amount of iron salt. M400 was expected to have a higher IOwt% but

did not, suggesting that the iron oxide loading of PMG Model 3 was saturated by 1.0 or 1.5g of iron salt.

M500, M600 and M750 had similar co-precipitation conditions and they were based on PMG Model 4, 5, and 6, respectively, which had the same MAA:EA ratio but differed in diameter. With these three MGIO models, the IOwt% were inversely proportional to the diameters of the PMG used, suggesting that the iron oxide loading of large PMG is less efficient. This may be due to insufficient time for infusion of iron salts to the centre of large PMG, thus restricting iron oxide formation to the particle surface region. We may require longer period of iron salt infusion, a process that is currently given two hours. On the other hand, the PMG may have been homogeneously infused but when ammonia was added, the formation of iron oxide near the particle surface may have impeded ammonia from reaching the iron salt at the PMG centre quickly. Moreover, the addition of ammonia may have increased the ionic strength of dispersion medium, which resulted in collapse of the matrix (Tan, 2005) and leakage of inner iron salts before they can be co-precipitated.

3.3.3 Vibrating Sample Magnetometry

The vibrating sample magnetometry at 300K was used to obtain the magnetization plot against an externally applied field that varied from -10 to 10^4 A/m. The applied field is also called the magnetic flux density or magnetic field strength and is measured in the unit of A/m, equivalent to 10^{-4} Tesla (T). This analysis was used to determine the dc magnetization and the hysteresis characteristics as the field was stepped past the origin. The average magnetization at $\pm 10^4$ A/m (M_{10kAm}) was 83.7 ± 3.3 Am² / kg of iron oxide for M400 to M700. While it is acceptable to take the

magnetization at 10^4 A/m as the saturation magnetization of each sample a more precise magnetization at infinite field can be obtained through non-linear regression or a Lineweaver-Burk plot by treating the magnetization values at positive fields to be a Langevin function (Lineweaver, 1934). Essentially, it is a plot of magnetization against the reciprocal of field. The saturated magnetization (M_s) obtained through this method is 85.9 ± 3.1 Am²/kg of iron oxide. This value is comparable to the M_s of magnetite particle of sizes similar to the primary iron oxide nanoparticles in MGIO, which have values of 85.7 to 87.0 Am²/kg (Ramirez, 2003).

All MGIO samples have saturation magnetization lower than bulk magnetite magnetization of 92 Am² / kg (Cullity, 1972) except for M400. The random canting of surface spins of the primary iron oxide particles within MGIO causes a reduction in saturation magnetization compared to bulk magnetite. A reduction in saturation magnetization of ferrimagnetic particles such as PIO is expected as opposed to an increase for ferromagnetic particles (Batlle, 2002). The larger than expected M_s for M400 could be due to the experimental error during weight measurement of the VSM sample. A 2.2mg sample of M400 was measured using a digital weighing scale with error of ± 0.1 mg, implying that a weight measurement error of up to 5% can be expected. Therefore, a 5% error may have been introduced into the magnetization per unit mass measurements, and the M_s of M400 is within the margin of this error. The remanence magnetization, M_r and coercivity, H_c are the magnetization at $H=0$ and field at $M=0$, respectively. They were obtained by b-spline interpolation of the magnetization curves around the origin to determine the y and x-intercept, respectively. The low M_r/M_s remanence ratio and low coercivity H_c indicate that there is negligible amount of remanent magnetization when the external field is removed,

implying that the primary iron oxide nanoparticles within MGIO are moderately well separated (Morup, 1995).

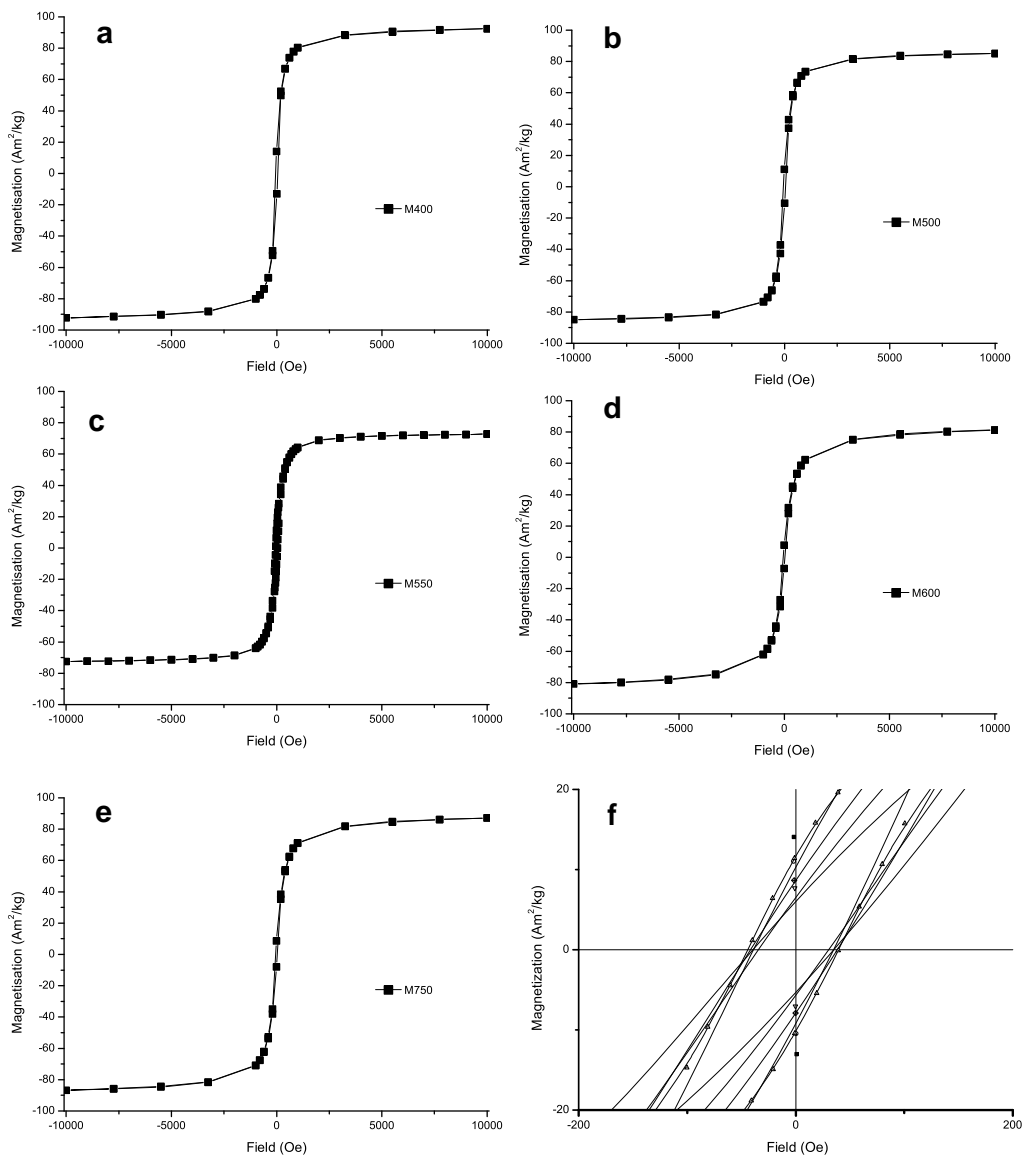
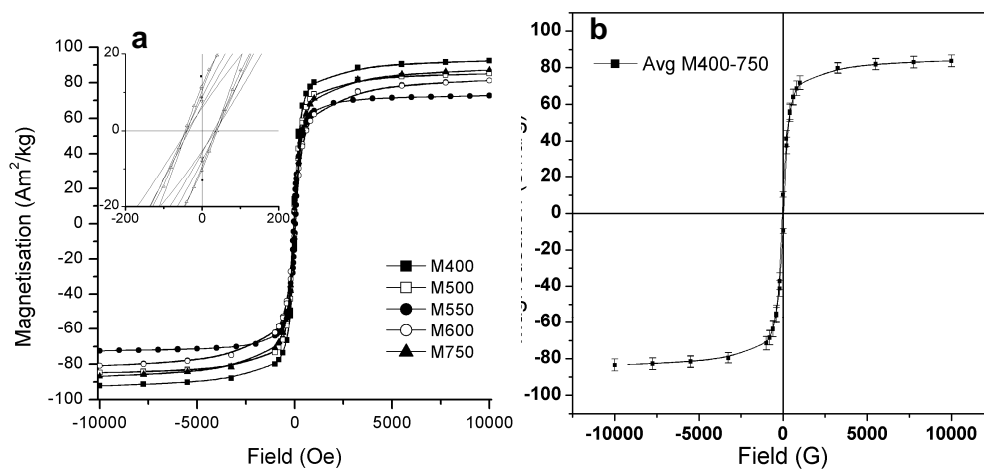


Figure 28: Magnetization curves for M400 to M750 measured by VSM. (a-e) Magnetization was measured while the samples were subjected to a static field that was varied stepwise from 10^3 to -10^3 G. (f) Magnification of the origin when curves of M400 to M750 are superimposed show a small amount of hysteresis.



MGIO Model	Sample Mass (g)	M_{10kG} (Am ² /kg)	M_s (Am ² /kg)	M_r (Am ² /kg)	M_r/M_s	H_c (Oe)
M400	2.2	92.38	93.56	4.157	0.044	0.4374
M500	3.3	85.07	87.42	6.429	0.074	0.958
M550	14.9	80.83	83.29	5.750	0.069	0.7084
M600	3.5	81.18	83.78	5.127	0.061	0.455
M750	9.0	87.05	89.29	2.836	0.032	0.7202
average	-	85.30±2.12	87.47±1.89	4.860±0.629	0.056±0.008	0.656±0.097

Table 8: Magnetization measurements determined by VSM. M_{10kOe} is the magnetization when field strength is 10^3 G; M_s is the saturation magnetization when field $\rightarrow \infty$; M_r is the remnant magnetization and H_c is the coercivity.

3.3.4 SQUID

The remanence of M600 was further analysed by measuring its ZFC and FC magnetization curves. Analysis of lyophilised M600 produced the curves below.

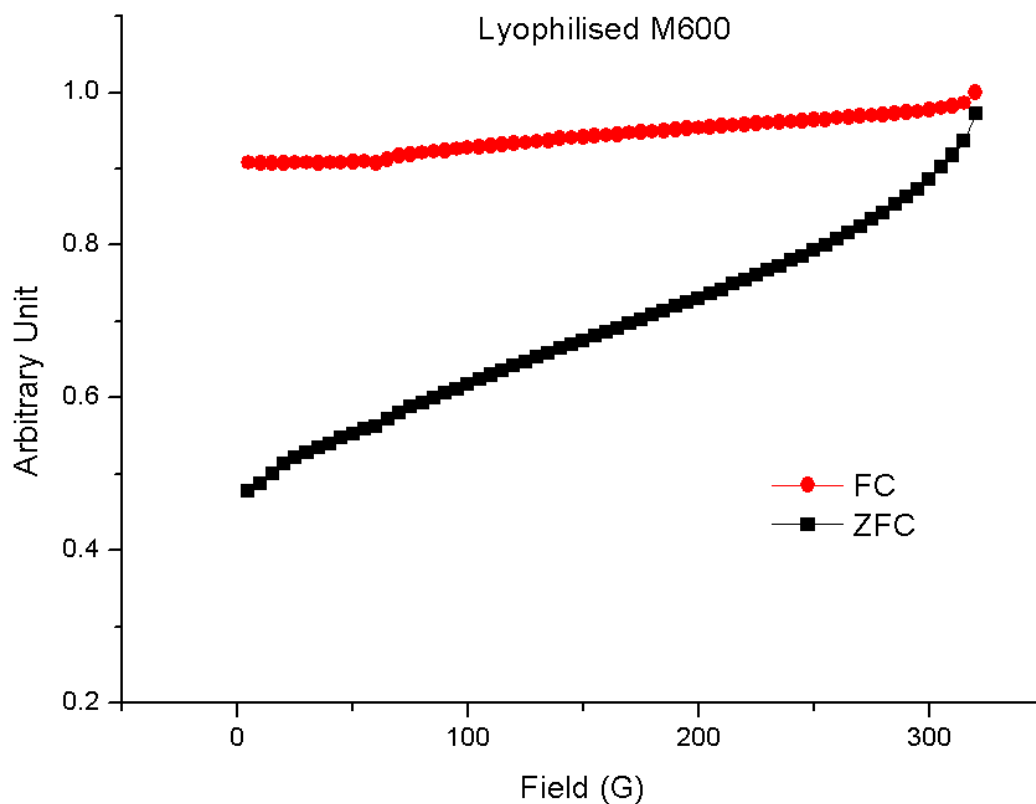


Figure 30: ZFC/FC of lyophilised M600 from 0 to 320K. The two curves did not intersect at temperatures below 300K, hence the blocking temperature is above 300K. The blocking temperature is probably slightly above 320K as the curves were almost intersecting at 320K.

Since the ZFC neither showed a maximum nor met the FC curve at temperatures below 300K, the blocking temperature was above 300K and the sample was not superparamagnetic. The two curves were nearly intersecting at 320K, indicating that the blocking temperature is slightly above 320K.

The lyophilising of MGIO may have decreased the inter-particle distance between the primary iron oxide nanoparticles, and enhanced particle dipole and exchange

interaction (Morup, 1995). Since MGIO are used in its aqueous state during cell labelling applications, further measurement were carried out on aqueous MGIO, to obtain the following cooling curves.

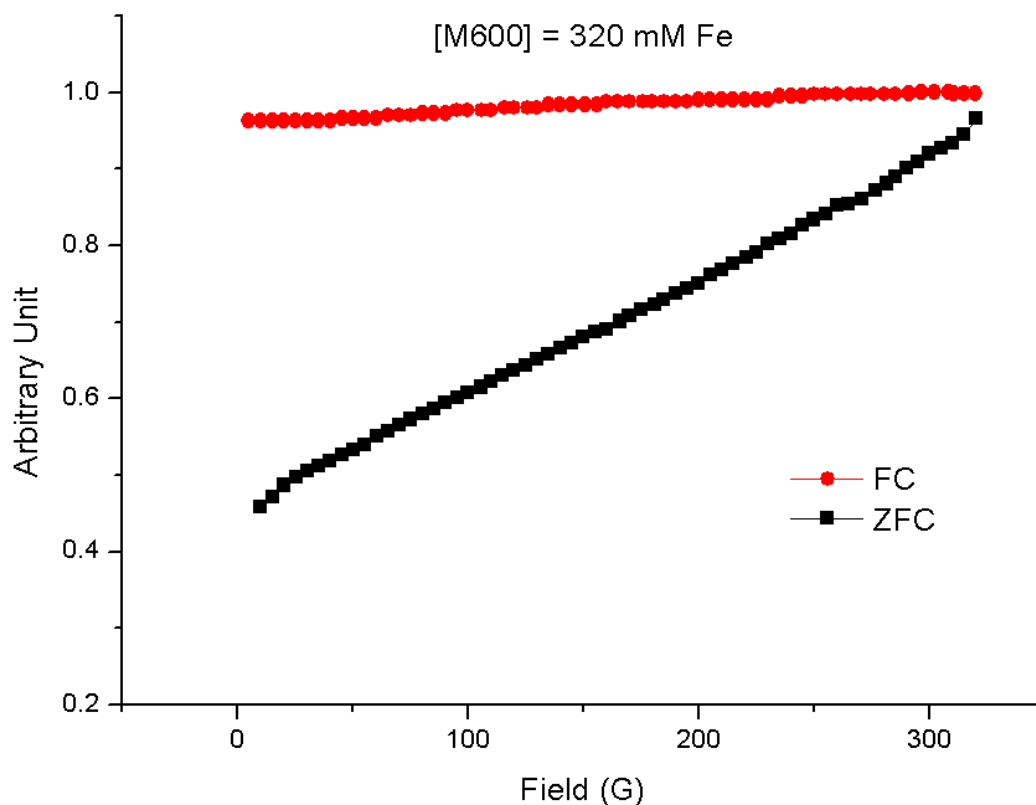


Figure 31: ZFC/FC of aqueous M600. The results were similar to those with lyophilized sample. The curves were nearly intersecting at 320K, indicating that the blocking temperature was not much further.

The results with aqueous M600 were similar to those of the lyophilised sample. Given that the primary iron oxide nanoparticles (PIO) are approximately 5nm as assessed by TEM, they are within the size limit of superparamagnetism, as particles of less than approximately 15nm are expected to exhibit superparamagnetism (Bean, 1959). Therefore the T_B is expected to be below 300K but is greater than 320K instead. This phenomenon may be due to the interaction or dipole-coupling between PIO. ZFC curves approached a broad-based maximum that had shifted to temperatures beyond

300K, indicating that PIO are interacting in groups with sizes larger than the superparamagnetic limit. Moreover, the FC curves did not follow the Curie-Weiss law, suggesting the presence of strong interparticle interactions (Testa, 2001). This interpretation is supported by observations of Bizdoaca et al. PIO of diameter 4 and 13 nm had T_B of 23 and 185K, respectively (Hyeon, 2001). However, Bizdoaca synthesized composite particles of 750nm diameter by fusing PIO (~12nm) on the surface of polystyrene cores, resulting in similar T_B as M600 (Bizdoaca, 2003). Bizdoaca concluded that the elevated T_B was a result of dipole-coupling between PIO on the composite particles.

Dry samples are preferred to aqueous ones as a greater dry sample mass can be accommodated in the instrument, which improved measurement accuracy. Excessively high concentration on the aqueous sample may be the cause for the dipole interactions. Therefore, further experimentation with concentrations lower than 320 mM Fe may be required, albeit at the loss of accuracy with small sample quantity.

3.3.5 Dynamic Light Scattering

The inverse Laplace transformation of acquired data was performed by Gendist software and the results were presented in the form of intensity autocorrelation as a function of time delay between intensity measurements, τ . Each dynamic light scattering (DLS) measurement was taken at a particular angle, θ . With the following relationships, the particle diameter, d_H can be expressed in terms of τ

$$\begin{aligned} |\vec{q}| = q &= \frac{4\pi m_1}{\lambda_0} \sin \theta / 2 \\ \Gamma = 1 / \tau &= Dq^2 \\ d_H &= \frac{kT}{3\pi\eta D} \end{aligned}$$

The intensity autocorrelation curve was normalised and expressed in arbitrary units (A.U.). With every DLS measurement, one such plot can be generated. A plot of each particle was selected and showed in the chart below.

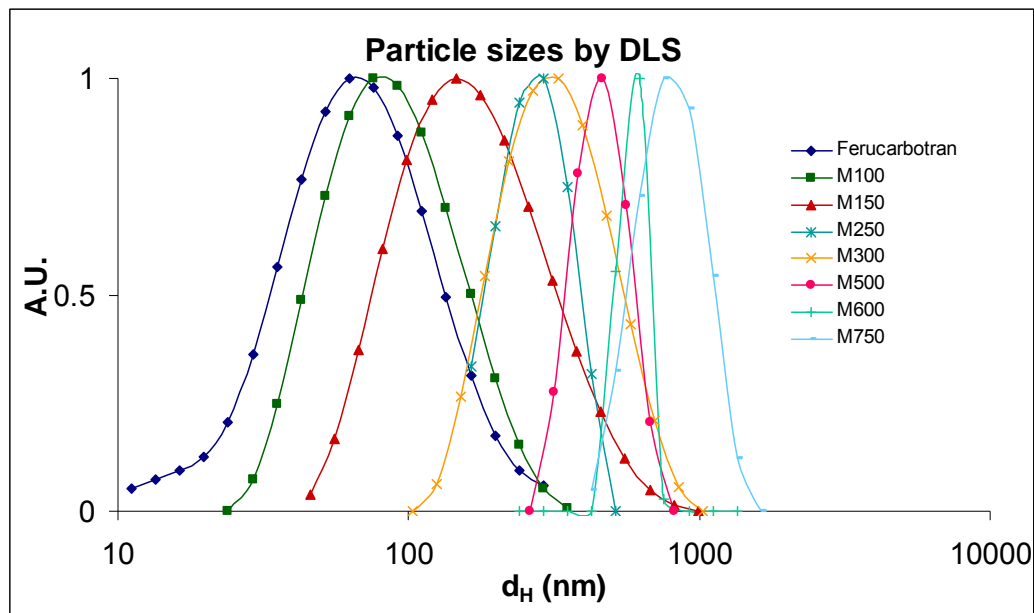


Figure 32: DLS plots of ferucarbotran and M100 to M750. All particles had unimodal size distributions. The peak of each distribution curve was taken as the mean hydrated diameter.

For each particle, three to six repeated measurements were taken with the photo-detector set at different angles. Gendist software provided the diameter at which each intensity autocorrelation curve peaks, and the mean of these peaks was taken as the particle hydrodynamic diameter, d_H and are shown below.

Particle	Hydrodynamic diameter, d_H (nm)
Ferucarbotran	64 ± 2
M100	87 ± 5
M150	152 ± 9
M250	263 ± 3
M300	329 ± 30
M400	414 ± 10
M500	479 ± 24
M600	602 ± 20
M750	766 ± 20

Table 9: Hydrated diameter of particles expressed as mean \pm SEM.

The diameter distribution of suspended particles including SPIO, is dependent on the weighting used (Jung, 1995). Intensity weighting is commonly used to report DLS sizes and it may be biased towards large particles in polydispersed samples. However, MGIO were monodispersed as the diameter distributions had single dominant peaks. Therefore, the intensity weighting is a reliable method to present the diameter distribution of MGIO. The details of the normalised curves against d_H of each particle are presented in the following pages:

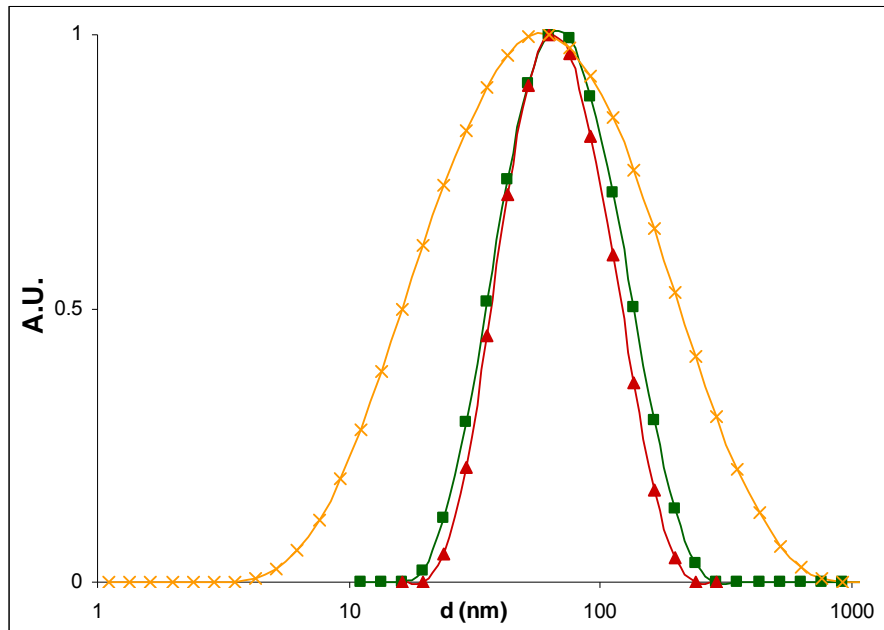


Figure 33: DLS distribution curves of Ferucarbutran from repeated measurements of one sample

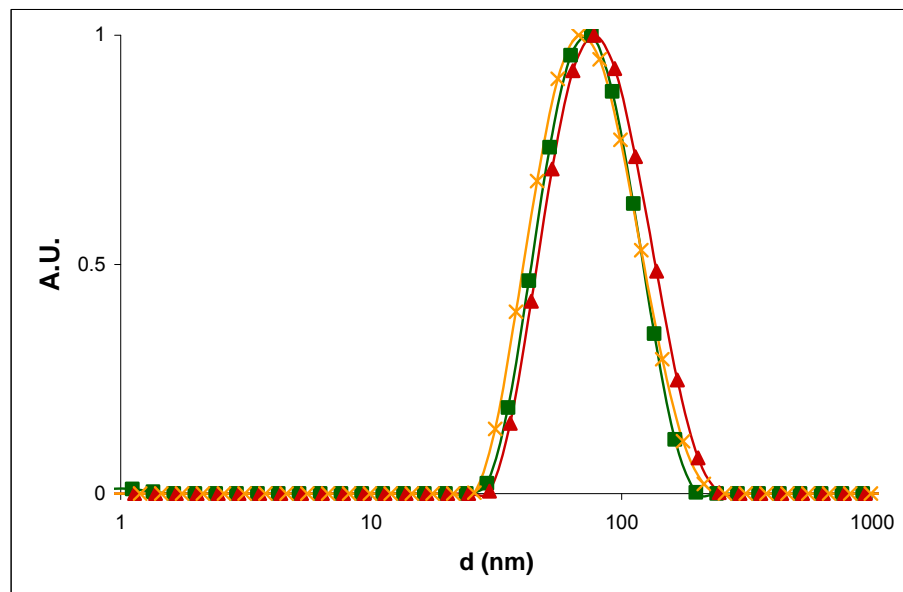


Figure 34: DLS distribution curves of M100 from repeated measurements of one sample

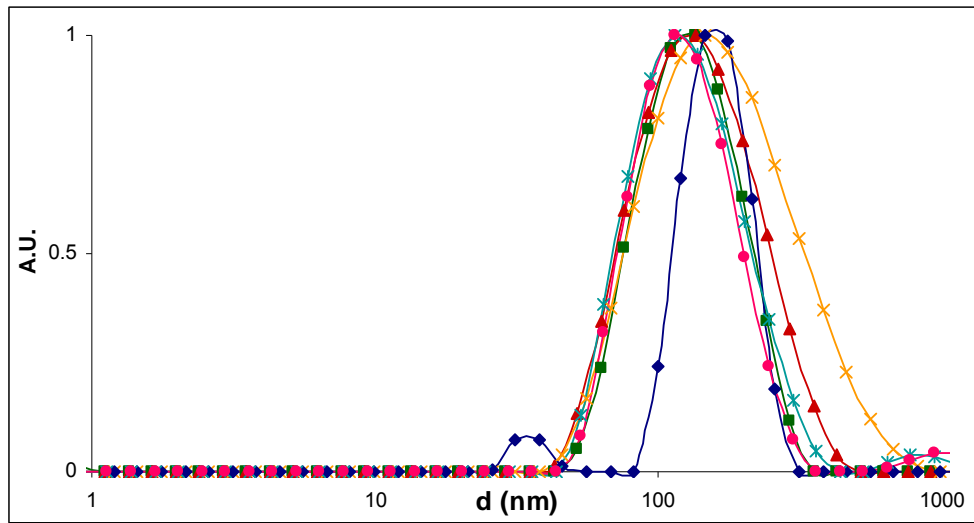


Figure 35: DLS distribution curves of M150 from repeated measurements of one sample

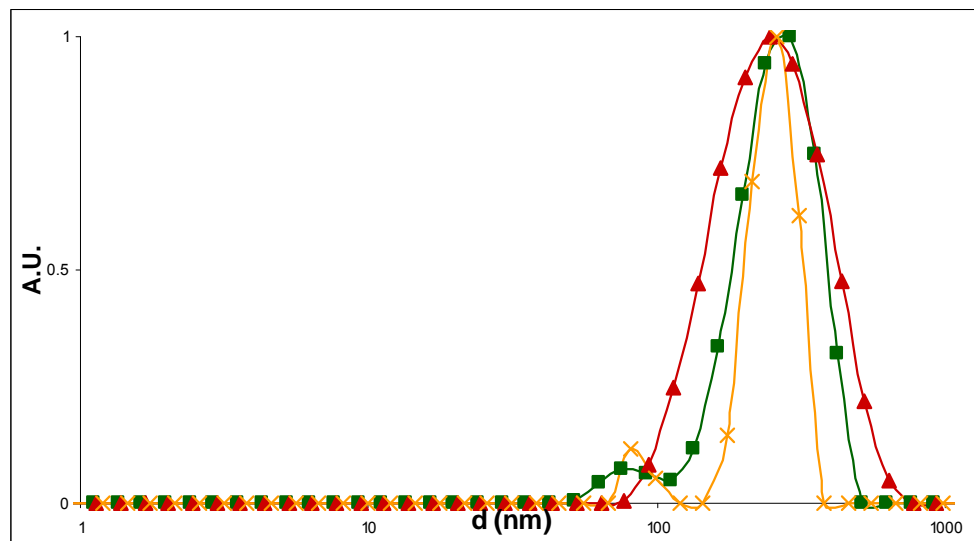


Figure 36: DLS distribution curves of M250 from repeated measurements of one sample

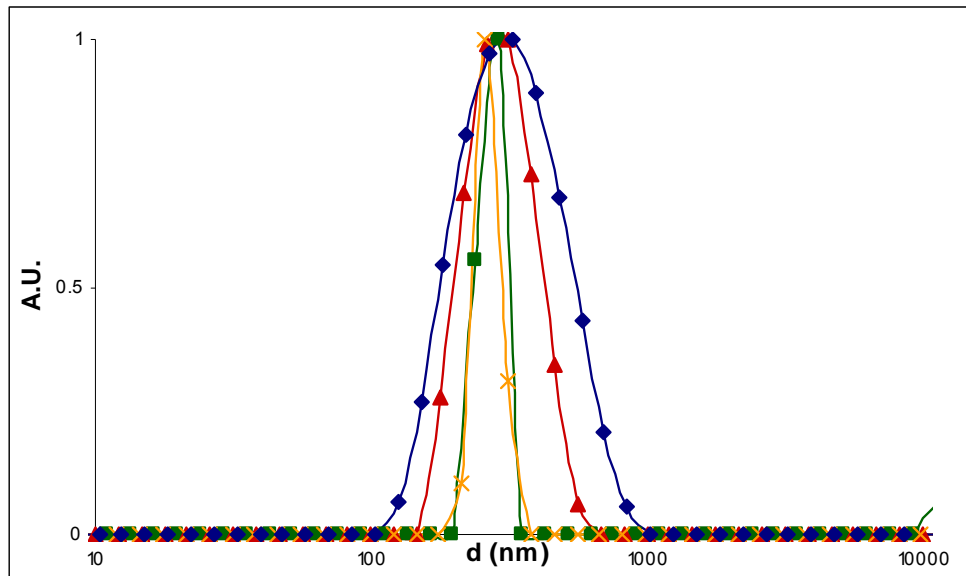


Figure 37: DLS distribution curves of M300 from repeated measurements of one sample

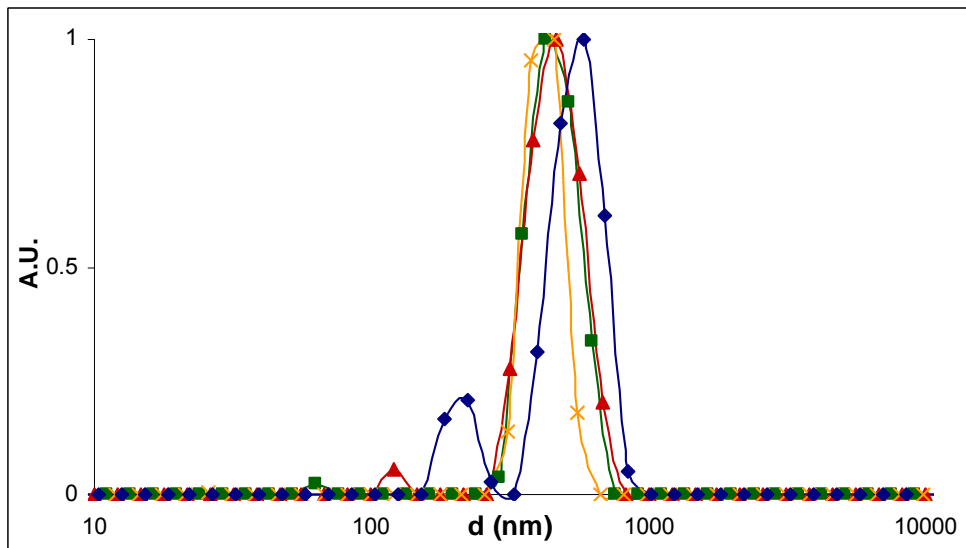


Figure 38: DLS distribution curves of M400 from repeated measurements of one sample

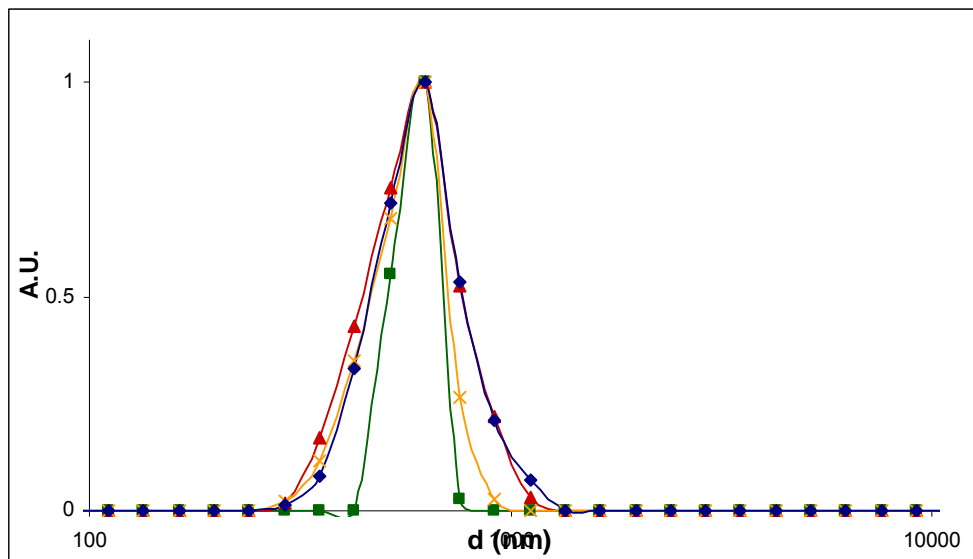


Figure 39: DLS distribution curves of M600 from repeated measurements of one sample

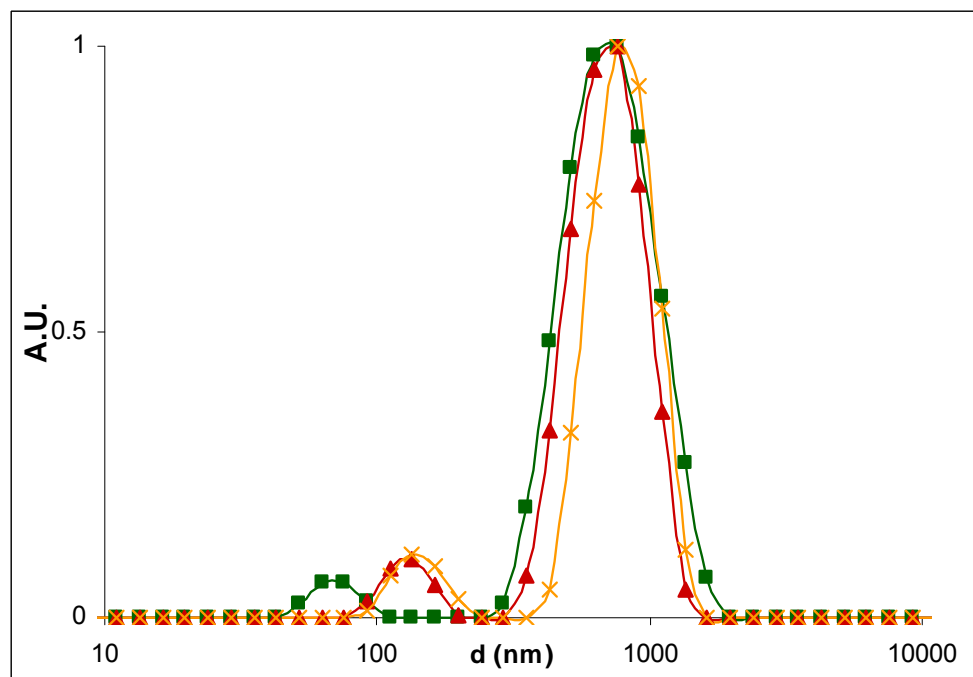


Figure 40: DLS distribution curves of M750 from repeated measurements of one sample

3.3.6 Relaxation

The $R2^*$ and $R2$ relaxation rates were obtained from the GRE and CPMG images, respectively. When the $R2^*$ or $R2$ relaxation rates of each bottle were plotted against its concentration, the slopes representing the $r2^*$ and $r2$ relaxivities were obtained by linear regression, from which the relaxation rates at 0.1 mM Fe were derived. The following plot for M250 is shown as an example.

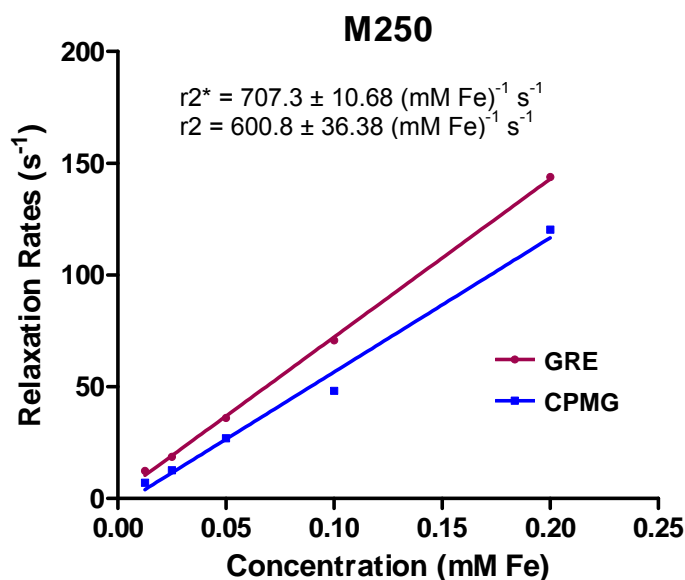


Figure 41: Example of a plot of relaxation rates against concentration to determine relaxivity. The gradient of CPMG relaxation rates and GRE relaxation rates corresponded to relaxivity $r2$ and $r2^*$, respectively.

The $T2$ and $T2^*$ relaxivity ($r2$ and $r2^*$, respectively) of the samples were measured. A GRE sequence was used to obtain $r2^*$, while a CPMG sequence with a $TE = 15$ ms was used to obtain the $r2$. The relaxation rates at 0.1 mM Fe ($R2$ and $R2^*$), obtained by interpolation of the relaxivity data, were plotted against particle DLS diameters, d_H on log-log scales. It was found that $R2$ and $R2^*$ increased with d_H , reaching a plateau for particles of diameter greater than 150 nm. For particles of diameter greater than 300 nm, $R2$ decreased while $R2^*$ remained constant.

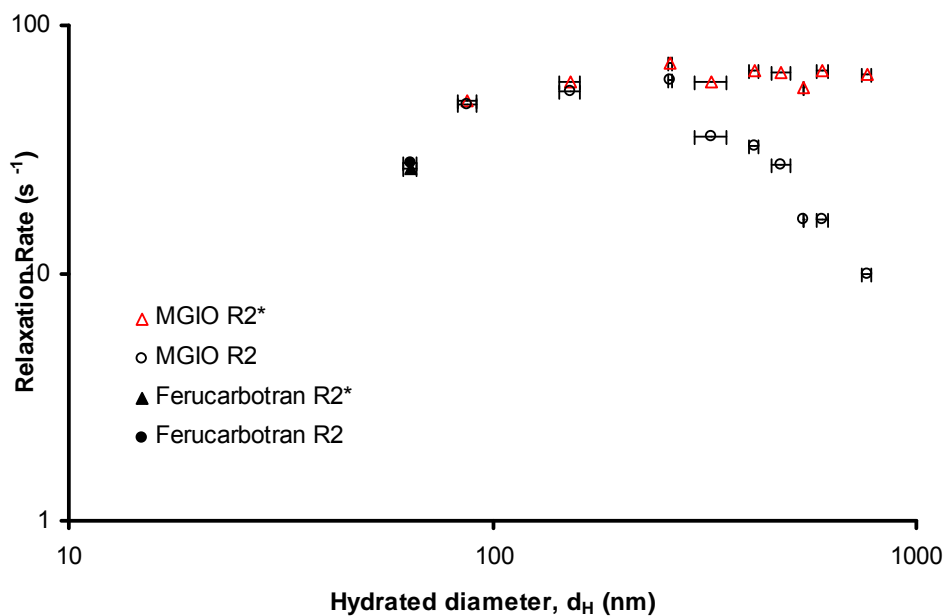


Figure 42: Relaxation rates of particles at 0.1mM Fe. R2* increased with diameter and reaches a plateau at M250. R2 is the same as R2* but as diameters increased beyond M250, R2 decreased.

The variation of MGIO relaxation rate with particle size is consistent with various theoretical MR relaxation models for magnetised particles. Relaxation rates of magnetised spheres like MGIO have been predicted to vary with particle diameters. The relationship can be classified into the distinct regimes of MAR, SDR and ELR proposed by Gillis et al (Gillis, 2002) and Brooks et al (Brooks, 2001) depending on the particle diameter. Several parameters were required by the models to compare them against the measure relaxation rates. An important parameter is the equatorial offset frequency, $\delta\omega$. It has been assigned the value of $3.4 \times 10^{-7} \text{ rad s}^{-1}$, the same value was used when theoretical values of magnetite particles were compared against Monte Carlo simulations (Muller, 1991; Ziener, 2005; Yablonskiy, 1994; Brown, 1993). The equatorial field, B_{eq} of magnetite was reported to be about 0.13 T (Gillis, 2002; Yung, 2003; Gillis, 1987), which corresponded to the above value through the

relationship $\delta\omega = \gamma B_{eq}$ (Yablonskiy, 1994), where the nuclear gyromagnetic ratio of ^1H , γ is $2.675 \times 10^{-8} \text{ rad s}^{-1} \text{ T}^{-1}$. Another required parameter is the concentration of iron oxide used, which at 0.1 mM Fe is equivalent to a volume fraction of 1.52ppm or 1.52×10^{-6} .

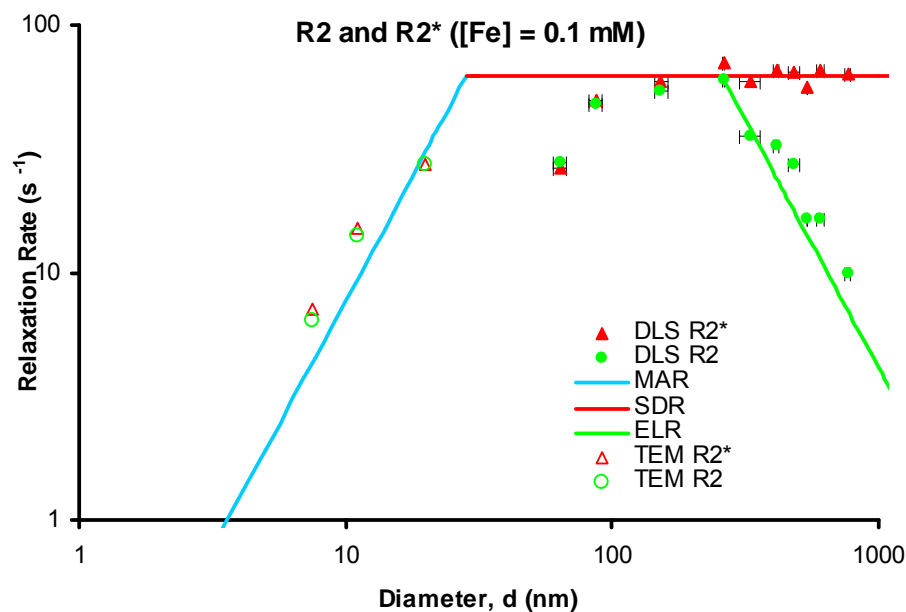


Figure 43: Comparison of relaxation rates to distinct regimes theory of motional averaging (MAR), static dephasing (SDR) and echo limited regime (ELR). Measurement fit the theoretical models in general.

The criterion for SDR is that the particle correlation time, $\tau_D > \pi\sqrt{15} / (4\Delta\omega_r)$ or $d_H > 25.46 \text{ nm}$, according to the relationship $\tau_D = d_H^2 / (4D)$, where D is the diffusion coefficient of water ($2.025 \text{ m}^2/\text{s}$ at 20°C). This suggests that all measured particles are in the SDR. However, the plateauing of $R2^*$ from M150 or larger diameters suggests that only these particles are operating in SDR. The average $R2^*$ of M150 to M750 was $63.0 \pm 1.6 \text{ s}^{-1}$, exceeding the theoretical value of 62.3 s^{-1} by 1.12%. The elevation of measured $R2^*$ was reported by other authors. Bowen and colleagues observed an elevation of 21% for SPIO/USPIO labelled cells (Bowen, 2002), Brooks

and colleagues a 33% with Monte Carlo simulations (Brooks, 2001). A lower increment of 10% between the Monte Carlo simulations and calculations was reported by Muller and colleagues (Muller, 1991; Yablonskiy, 1994). Brooks suggested that they used an overly large volume fraction of 0.5% in their simulation, violating the dilute perturber approximation implicit in the SDR theory. At high concentrations, the field profiles of different particles overlap, such that spins far from one particle is perturbed by another particle destroying signal and increasing relaxation rate. Indeed, lesser elevations were observed by Bowen and Muller who used 0.2% and 2ppm respectively. Our results obtained at 1.52ppm have the smallest elevation.

Comparing R2 measurements with predictions, the R2 of M400 and larger particles showed a moderate fit to ELR and decreased with $1/d^2$ in accordance with the model. M400 and larger particles had R2 that was 38% below the calculated value. The R2 of M250 and M300 did not agree with the model. The poor agreement is expected, as the ELR predicts R2 of large particles and does not model the behaviour of intermediately-sized particles with diameters near the intersect between SDR and ELR ($d = 251$ nm). The R2 behaviour of such particles has never been modelled.

The poor fit of ferucarbotran and M100 relaxation to the MAR predictions require further analysis. The particles may be operating at the intermediate region between MAR and SDR and the MAR criterion of $\tau_D \ll (1/\delta\omega)$ or $d \ll 15.43$ nm is not met by the DLS diameters of ferucarbotran and M100. The intermediate region has been modelled by a continuous empirical model by Yung (Yung, 2003). The R2* and R2 are predicted to be the same in MAR and SDR, but this model shows a difference between R2* and R2 of up to 20% (at $d = 25$ nm), raising questions about its reliability. Nonetheless, Monte Carlo simulation results with spherical particles that fit the MAR

were shown to be in agreement with the $R2^*$ empirical model in the intermediate region as well (Figure 44) (Yung, 2003; Muller, 1991). Therefore the existing models and simulation data are in agreement with one another, but the relaxation data of ferucarbotran and M100 do not fit any of them.

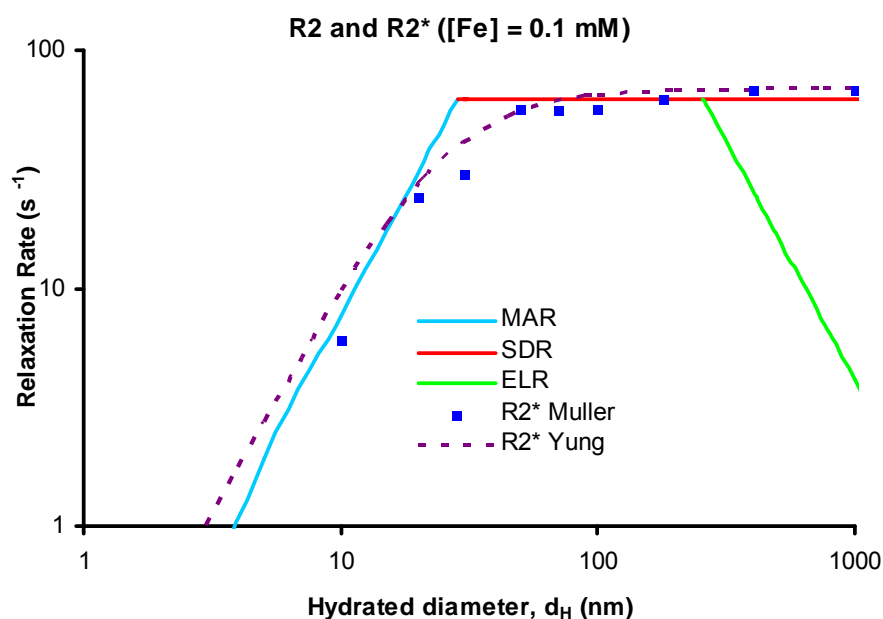


Figure 44: Comparison of Muller’s simulation, distinct regime and continuous theory. Muller’s simulated relaxation rates fit both theories better than the measurements of MGIO.

The disparity between MAR and the relaxation rates of ferucarbutran and M100 may be due to the overestimation of effective magnetic perturber size of small particles. Ferucarbotran and MGIO consist of multiple primary iron oxide nanoparticle cores (PIO) held together by a polymeric matrix of carboxy-dextran and PMG, respectively. The magnetic perturbers in theoretical models and Monte Carlo simulations were homogenous spheres of diameter d_{mag} . Although structurally different, it is proposed that the relaxation behaviour of large MGIO is similar. This proposal is supported by the observation that cells labelled with SPIO are inhomogenous intracellularly but

undergo $R2^*$ relaxation in the SDR like large homogenous particles (Bowen, 2002). This means that a composite particle with iron oxide cores (PIO) held together by a polymer matrix (eg MGIO) (A) of diameter d_{DLS} , is an equivalent magnetic perturber as a particle with a single homogenous core (B) of diameter, d_{mag} (Figure 45). The homogenous core is made up of a magnetic material of lower iron concentration such that the iron concentration per particles remains the same.

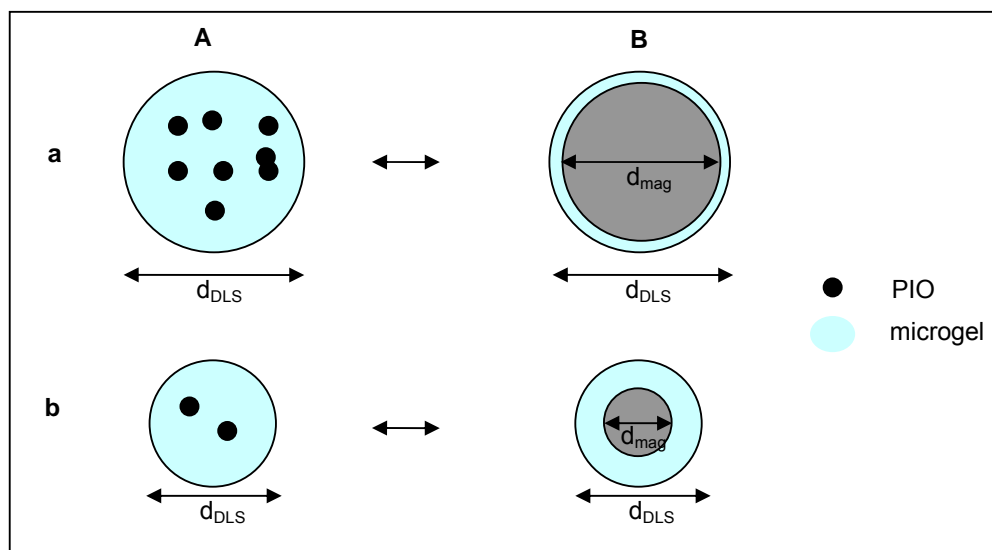


Figure 45: Representative sketch of composite particles such as MGIO that consist of multiple primary iron oxide nanoparticle cores (PIO) held together by a polymer matrix like microgel. Each composite particle is equivalent to one with a single homogenous core with diameter d_{mag} . (a) For large MGIO, the diameter determined by dynamic light scattering (d_{DLS}) approximates d_{mag} . (b) For ferucarbotran or small MGIO, d_{DLS} and d_{mag} deviates.

Dynamic light scattering was used to measure the particle hydrodynamic diameters, which is based on the refraction at the interface between the polymer matrix and surrounding water where the refractive indices are different. For large MGIO, d_{DLS} approximates d_{mag} because PIO were distributed relatively close to the particle surface (Figure 45a). However, this approximation fails with small particles like ferucarbotran or M100 as PIO are few and are distributed relatively further from the surface leading to a large error between d_{DLS} and d_{mag} (Figure 45b). This is probably the case for

ferucarbutran and M100. The overestimation of d_{mag} by d_{DLS} is the likely cause of disagreement between MAR and the measurements of ferucarbotran and M100.

It is hypothesized that the diameters of PIO clusters measured by TEM, d_{TEM} is a better approximation of d_{mag} for particles in the MAR. To verify this hypothesis, the relaxation rates of three more particles, each smaller than ferucarbotran were added to Figure 43. Through TEM analysis (not shown) each particle contains one to several electron-dense PIO, clustered in the centre of each particle such that the respective d_{TEM} can be determined. The particles contain PIO coated by i) hyperbranched polyglycerol ($d_{\text{TEM}} = 7.5\text{nm}$) (Wang *Advanced Functional Materials* 09 in press), ii) poly(ethyleneglycol) monomethacrylate (11nm) (Fan, 2007) and iii) silica (20nm) (Ding et al unpublished data). Using the d_{TEM} , the relaxation measurements of these particles were indeed in better agreement with MAR.

The relative proximity of PIO to the particle surface is also dependent on the synthesis route. The synthesis process of MGIO results in the co-precipitation of iron oxide near the surface of preformed microgel precursors. Conversely, ferucarbotran and other mentioned particles were formed by encapsulation of single or clustered PIO with a coating of polymer or silica of up tens of nm in thickness. This gives rise to the large difference between their d_{TEM} and d_{DLS} . When the d_{TEM} of ferucarbotran is unavailable, its relaxation measurements are expected to be closer to the MAR predictions.

3.4 Discussion

MGIO has been synthesized by alkaline co-precipitation of iron salts in preformed PMG. A wide size range of PMG was synthesized by selecting reagent mass ratios that vary the micellar seeds available for polymerisation (micellar ratio). Large PMG were intended for synthesizing large MGIO, but with only two measurements of PMG diameters made, the micellar ratio was used as the indicator of PMG sizes. Resulting MGIO were indeed larger when large PMG were used.

As expected, TEM showed that the structure of air-dried MGIO consists of numerous primary iron oxide nanoparticles (PIO) held by a polymer matrix that measures 50-80nm in diameter. However, DLS measurement showed that MGIO were 89 to 765nm, which means a nine-fold change of particle diameter between water-suspended and air-dried states and a huge 1000-fold change in volume. Although TEM showed separated MGIO and DLS samples are sonicated in water bath prior to each measurement to disperse aggregates, the possibility that the various MGIO models were actually stable aggregates of different sizes cannot be ruled out.

Magnetization measurements by VSM and SQUID showed that MGIO possess remenance at room temperature and are not superparamagnetic. This implies that MGIO exert interparticle attractive forces, but the implication on cell labelling is unknown. Being non-superparamagnetic is not necessarily a shortcoming for MGIO in the application of *in vitro* cell labelling as the overall remenance of the labelled cell is probably a more important parameter that may affect cellular function. It is also unknown if cells loaded with superparamagnetic particles become non-superparamagnetic themselves. If MGIO is conjugated to a targeting moiety as a long

circulating, *in vivo* targeting agent, non-superparamagnetism may be a disadvantage as poorer particle dispersion usually leads to higher undesired uptake by the reticuloendothelial system and lower accumulation at the intended target cells.

The relaxation rate measurements of large MGIO were closer than small MGIO to theoretical models of magnetic relaxation by homogenous magnetic spheres. This shows that DLS measurements of large MGIO approximate the effective “relaxation-inducing” diameters. Since this approximation failed for small MGIO, an alternative method of obtaining the effective diameters will be needed. One suggestion is to freeze a suspension of MGIO, followed by lyophilisation and scanning or transmission electron microscopy. Such a procedure may retain the water-suspended structure of small MGIO when they are lyophilised so that the water-suspended separation of PIO can be observed.

An application of the relaxation regimes is the differentiation between intact cells with compartmentalised iron oxide particles and lysed cells with free particles. Interestingly, when cells are loaded with iron oxide particles, they seem to have relaxation properties similar to those large magnetic spheres. When ferumoxtran or ferucarbotran were compartmentalised in cells, they produced less signal on T2-weighted images but similar signal T2*-weighted images (Simon, 2006; Henning, 2009). These results suggest that the labelled cells, like large magnetic spheres, produce relaxation in the ELR regime.

Chapter 4 Results II: Labelling of Stem Cells

The application of MGIO as a cell label was demonstrated on human fetal mesenchymal stem cells (fMSC) and endothelial progenitor cells (EPC). In order to test the utility of MGIO as a cell label for primary cells, labelling efficiency was compared against a clinically-available particle. To determine if labelling with MGIO caused deleterious effects, the cells were evaluated on functional characteristics such as proliferation rate, multi-lineage differentiation potential and gene expression differences.

Hypothesis: MGIO can be used as a label for non-phagocytic cell type, such as fMSC and provide better labelling efficiency than clinically-available labels, such as ferucarbotran, without deleterious effects to the cells

4.1 Isolation and Characterisation of fMSC

fMSC appeared as plastic-adherent spindle-shaped cells in culture. They have an immunophenotype which was negative for haemopoietic and endothelial markers CD14, CD34, CD45, CD31, vWF and HLA II and positive for mesenchymal markers CD105, CD73; intracellular marker vimentin and laminin; cell adhesion molecules CD29, CD44, CD 106, CD 90; and HLA I as previously reported (Zhang, 2009; Chan, 2007). Under permissive induction media, they underwent osteogenic, adipogenic and chondrogenic differentiation, confirming their bona fide identity as MSC (Dominici, 2006).

4.2 Uptake of MGIO by fMSC

In order to test the utility of these novel particles, we labelled primary fMSC with MGIO of varying sizes and ferucarbotran, a clinically-available particle. By simple incubation of fMSC with MGIO or ferucarbotran (0.05 mg iron/ml) over 24 hours, we observed the incorporation of nanoparticles into the cytoplasm of fMSC (Figure 46a) by staining for iron with Prussian Blue. I found 97.3 ± 0.9 % M600-labelled cells staining positive for Prussian blue (range 21-38/low powered field (LPF), total cells counted = 212), and 98.2 ± 1.1 % (range 20-35 / LPF, total cells counted = 216) for ferucarbotran-labelled cells.

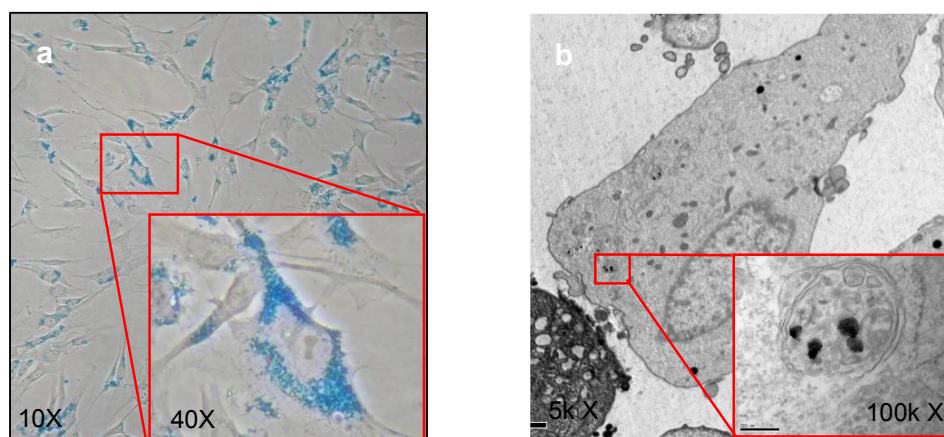


Figure 46: (a) Light micrograph of M600-labelled fMSC with iron stained with Prussian Blue. (b) TEM of labelled fMSC with insert showing MGIO in double-walled membrane organelle

In these experiments, the labelled cells tend to be “sticky” and have the tendency to form large and inseparable cellular aggregates when extracellular particles are present and allowed time to absorb on cellular surface. Obtaining labelled and freely suspendable cells is important for their application. For this reason, density centrifugation was added to further remove extracellular particles. The labelled cells

were also examined under on a haemocytometer to verify that they were separated cells (Figure 47).

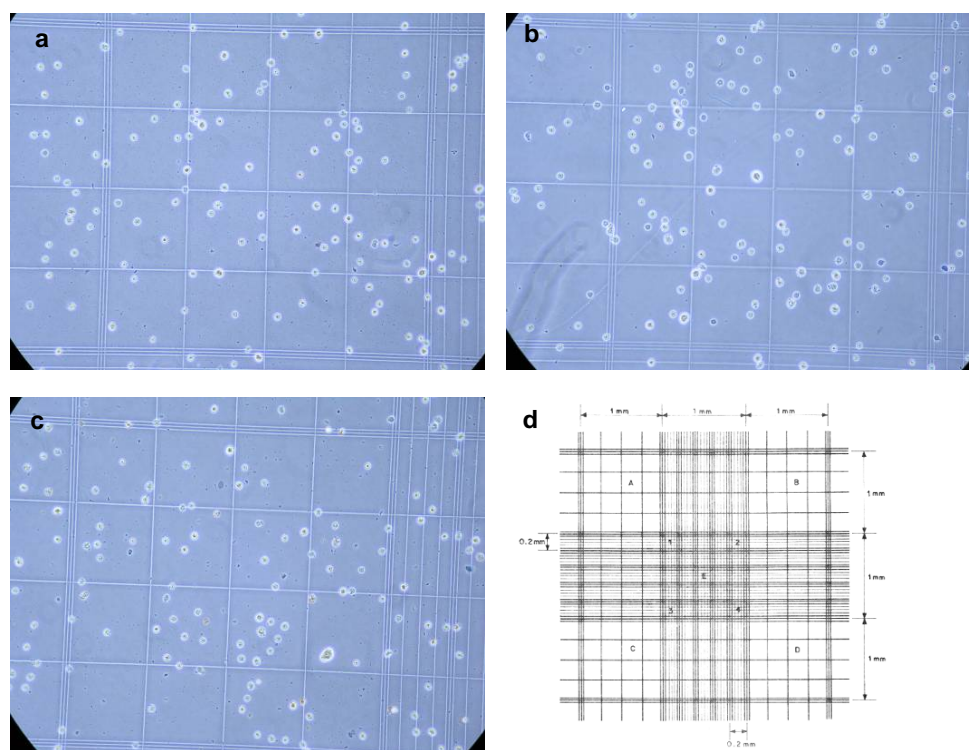


Figure 47: Micrographs of (a) M600, (b) mock and (c) ferucarbotran-labelled fMSC on a haemocytometer show that labeled cells are separated and their sizes in suspension remain 15-25 μm in diameter, as indicated by the lines of the (d) Neubauer haemocytometer, regardless of labelling.

To understand the intracellular location of MGIO, labelled-fMSC was visualized by TEM to reveal their localisation to endosomal structures (double-walled membrane, cytoplasmic organelles) (Figure 46b). This was consistent with the endocytotic mechanism for cellular uptake observed for ferucarbotran as well (Matuszewski, 2005).

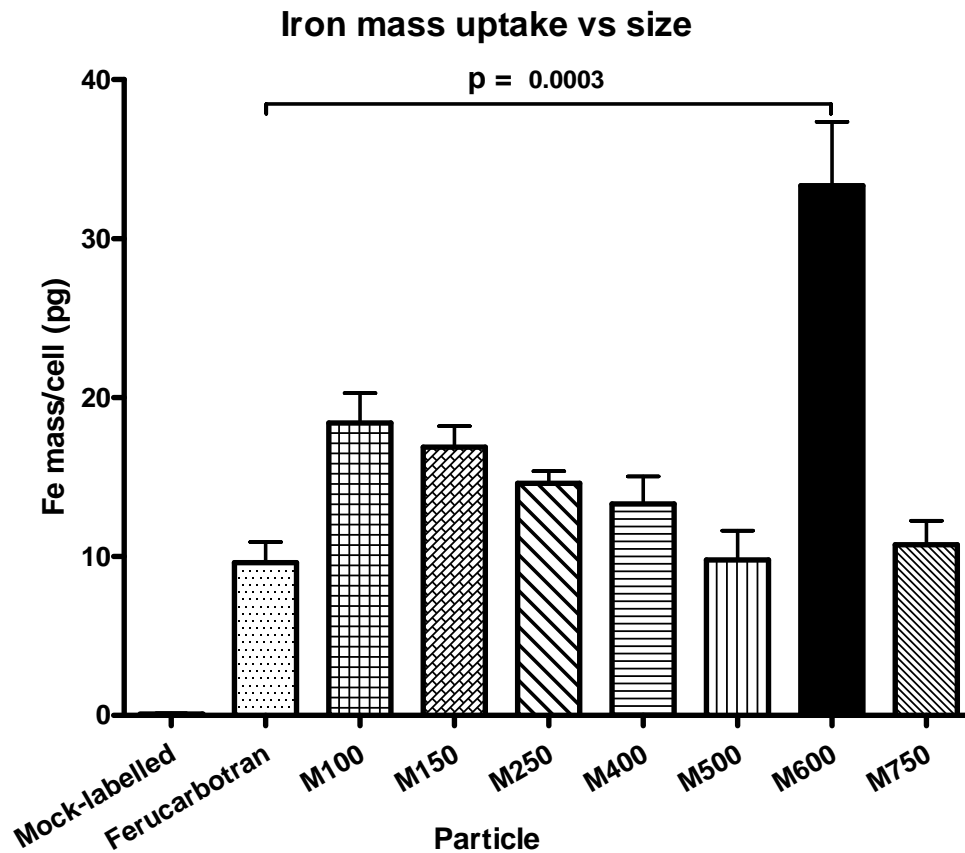


Figure 48: Intracellular iron mass when labelled with different particles showed a particle size-dependent quantity of uptake. All MGIO sizes showed the same or higher uptake than ferucarbotran with M600 providing the highest uptake.

Interestingly, a distinct size-dependent uptake of MGIO particles was observed. Using an initial iron concentration of 0.05 mg/ml, I consistently observed a three-fold greater cellular iron loading with M600 (33.3 ± 4.0 pg/cell) than with ferucarbotran (9.6 ± 1.3 pg/cell) ($p=0.0003$, $n=9$), and significantly higher iron loading for M600 than with MGIO of other sizes ($p<0.001$, Figure 48) was consistently observed.

This difference in iron uptake between M600 and ferucarbotran was even more marked on incubation with increasing iron concentrations. Up to a six-fold greater cellular iron loading was achieved at an incubation concentration of 0.2 mg iron/ml (Figure 49, 263 ± 27 pg/cell vs 41 ± 6 pg/cell, $n=3$, $p<0.001$).

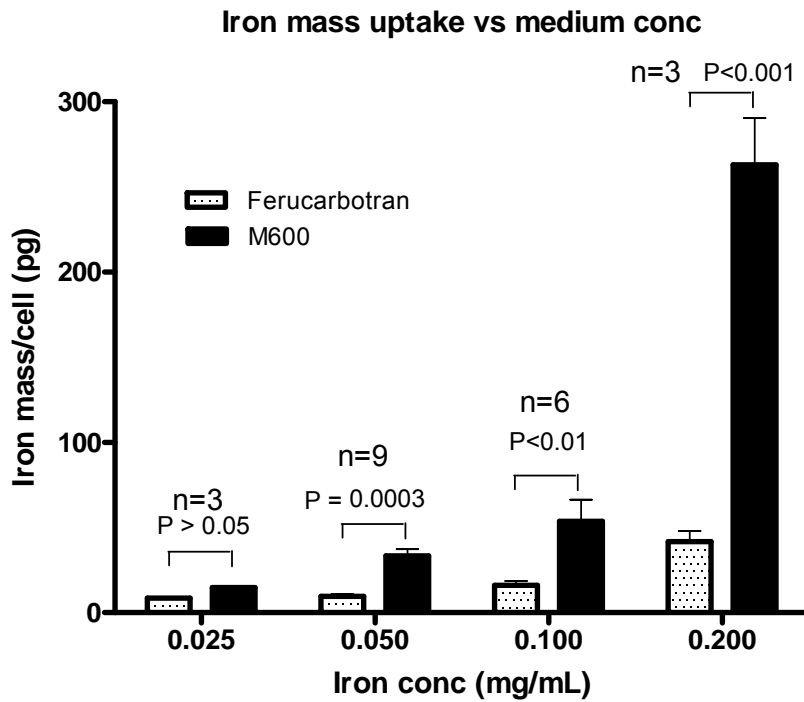


Figure 49: Intracellular iron as a function of labelling concentration. As iron concentration in the labeling medium was increased, the iron loading of the cells were increased and the difference in loading between ferucarbotran and M600 became more significant..

As shown in Figure 49, increasing labelling concentration to 0.1mg/ml or 0.2mg/ml resulted in more iron per cell.

4.3 Proliferation of Labelled fMSC

Cells labelled at passage 5 were cultured and sampled to have their intracellular iron content analysed for 3 more passages at 5, 8 and 11 days after labelling. We found that the half-life of the cellular iron content was approximately one population doubling, as can be expected when the iron labels from each cell are fully passed onto the two daughter cells (Figure 50).

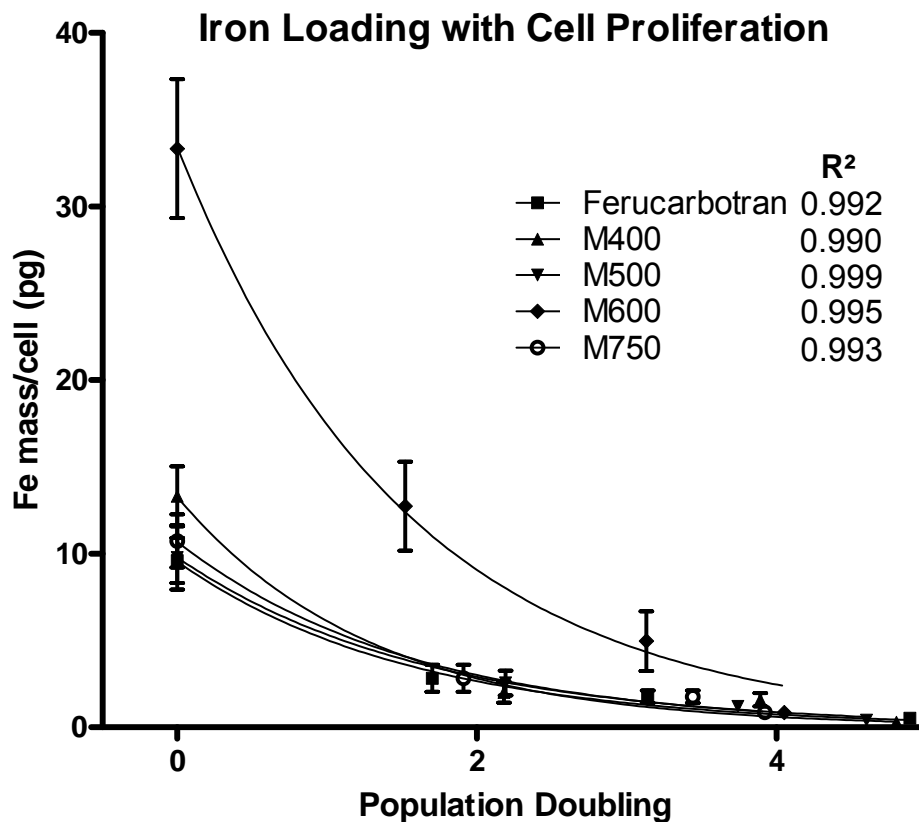


Figure 50: Retention of intracellular iron over 3 passages. Individual points indicate the quantity of iron at each particular population doubling. Lines are one-phase decay fits to each particle to show that intracellular iron was approximately halved each time a cell divided with R^2 showing goodness of fit.

The effects on stem cell properties were investigated when fMSC were labelled using MGIO from 400 to 750 nm and ferucarbotran. Labelling with either MGIO particles or ferucarbotran did not affect cell population doubling and viability (>95%) compared to the mock-labelled control. (Figure 51 and Figure 52)

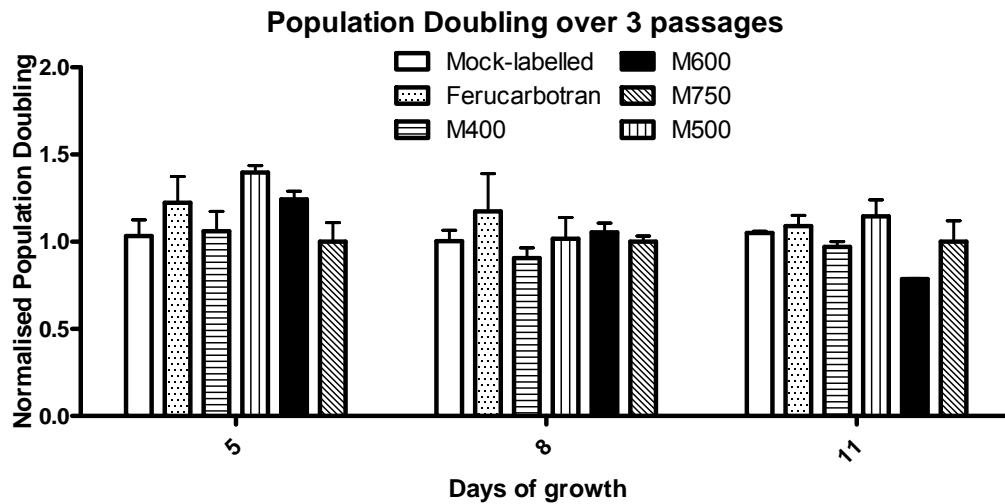


Figure 51: Population doublings at each passage. The number of population doubling at each of the three passages post-labelling were not affected by the particles used.

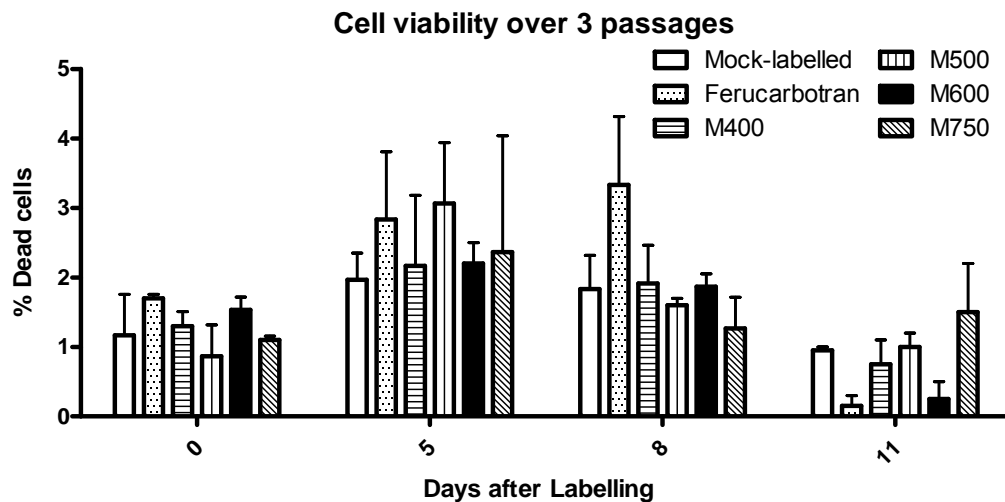


Figure 52: Cell viability at each passage. The effect of labelling on the cell viability, as assessed by Trypan blue exclusion assay, was insignificant for three passages post-labelling.

4.4 Multi-Lineage Differentiation of Labelled fMSC

Labelling of fMSC with M600 and ferucarbotran did not affect their tri-lineage differentiation capacity into osteoblasts, adipocytes and chondrocytes (Figure 53). A limitation of the present study is the lack of quantitation assays after staining for differentiation. From the optical micrographs of differentiation assays, M600 and ferucarbotran-labelled fMSC appeared to have undergone the same amount of differentiation as the mock-labelled control, but quantitation assays that measure the amount of stained products would have been an elegant proof.

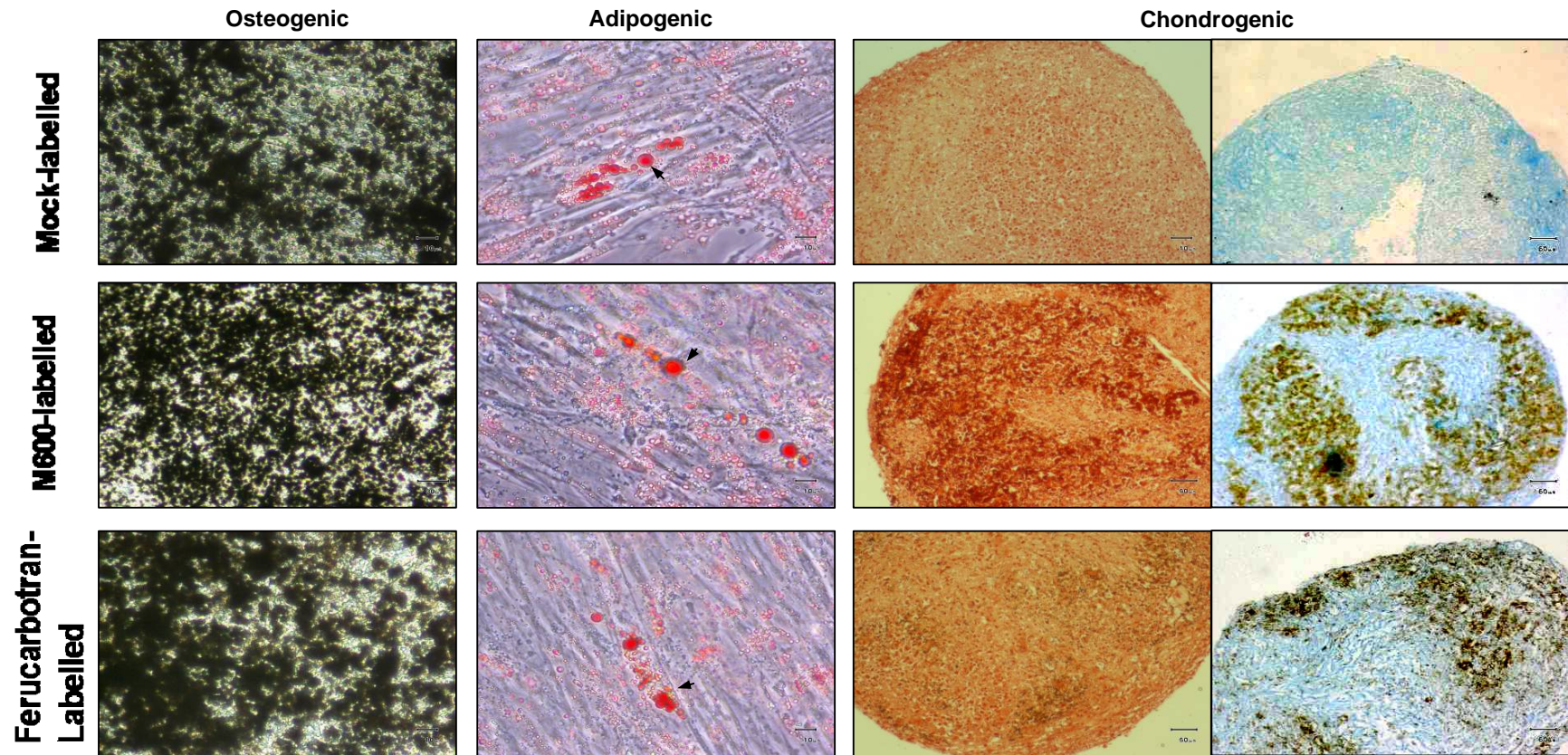


Figure 53: Trilineage differentiation of fMSC post-labelling. Labelling with either ferucarbotran or M600 did not affect the multipotent capacity of fMSC as shown by their differentiation into osteoblasts (black extracellular crystals by von Kossa staining), adipocytes (oil red O staining) or chondrocytes (micromass pellet cultures were stained red by Safranin O and blue by Alcian blue)

4.5 Microarray Analysis of Labelled fMSC

In order to broaden our understanding of the effects of iron-loading on fMSC, global gene expression analysis was performed using a genome-wide microarray. The RNA of labelled cells were extracted and their expression levels were compared to those of mock-labelled cells.

4.5.1 Development and Analysis of Microarray Data

Immediately after labelling, the total RNA of M600, ferucarbotran and mock-labelled fMSC was extracted and characterised for quantity, integrity and DNA contamination. cDNA was developed from total RNA, synthesised into Biotin-labelled, fragmented cRNA and hybridised on the microarrays. The gene expression data was imported into Genespring GX, which identified genes that have been altered by labelling. First, the control strength was determined from the maximum of base/proportional of the 3 samples groups (M600, ferucarbotran and mock-labelled) to be 64.47. By considering only probes with raw signals >64.47 in at least 1 out of 3 samples groups, the number of probes under consideration was reduced from 54675 to 30885. Next, the transcripts where triplicates from all sample groups were flagged absent were removed, to avoid unnecessary comparison of low signals, reducing the transcripts to 27344. A t-test was then performed to identify that 1504 M600-labelled probes (Figure 54) and 895 Ferucarbotran-labelled probes (Figure 55) had significant differences in expression with respect to mock-labelled probes ($p < 0.05$). Out of these, 114 and 102 probes were 2-fold up and down regulated, respectively, in M600-labelled samples compared with mock-labelled controls. And 32 and 29 probes were 2-fold up and down

regulated, respectively, in ferucarbotran-labelled samples compared with mock-labelled controls. The scatter plots with the 2-fold differential expression lines, heatmaps and the description of these probes are shown on the following pages.

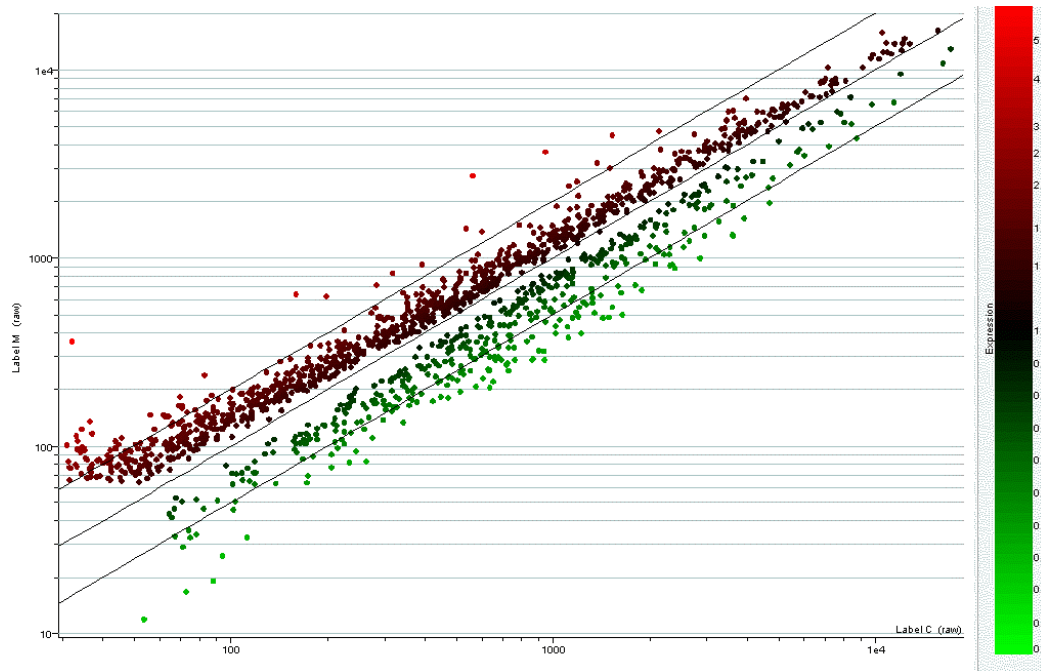


Figure 54: Scatter plot showing the 1504 M600-labelled probes that had significant difference in expression compared to the mock-labelled counterparts. Out of these probes, 114 were more than 2-fold upregulated and 102 were more than 2-fold downregulated.

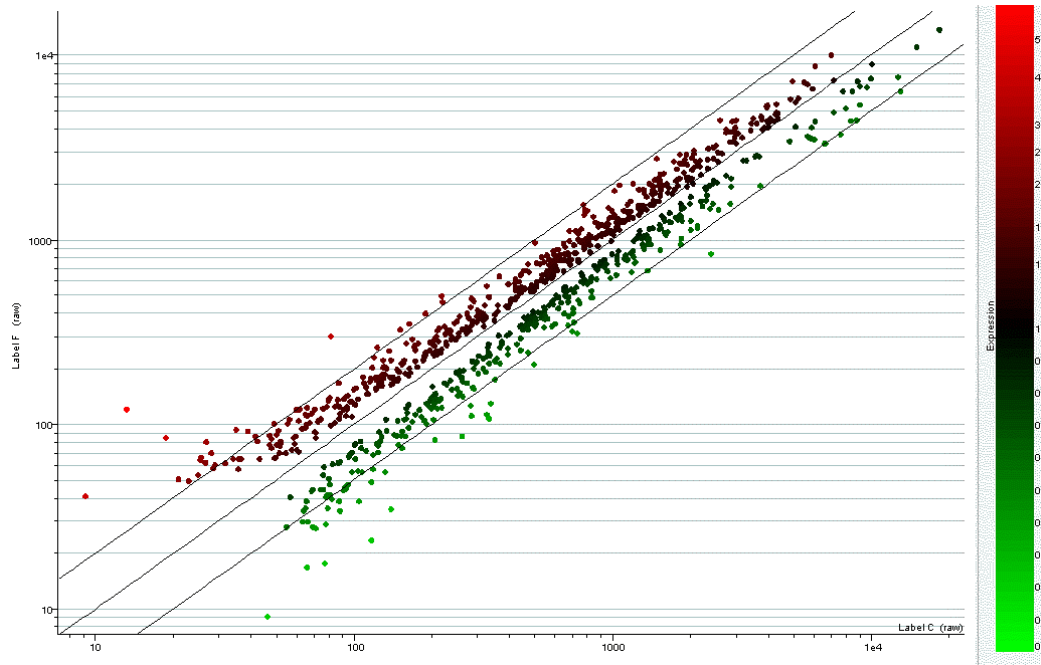


Figure 55: Scatter plot showing the 895 ferucarbotran-labelled probes that had significant difference in expression compared to the mock-labelled counterparts. Out of these probes, 32 were more than 2-fold upregulated and 29 were more than 2-fold downregulated.

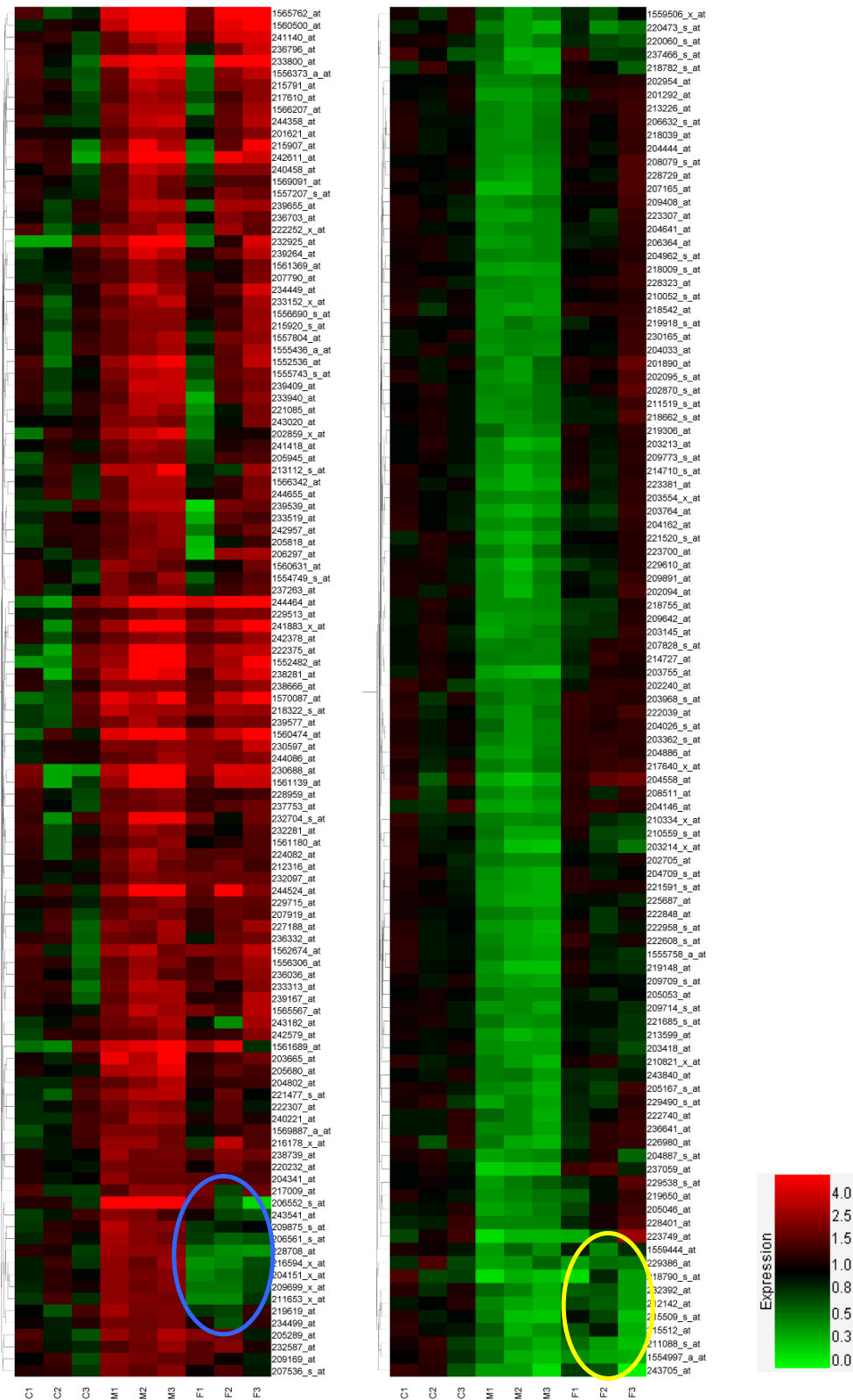


Figure 56: Heatmaps of 114 upregulated (left) and 102 downregulated (right) probes due to M600-labelling. Ferucarbotran-labelling resulted in the upregulation and downregulation of the same genes, except for the group circled blue and yellow.

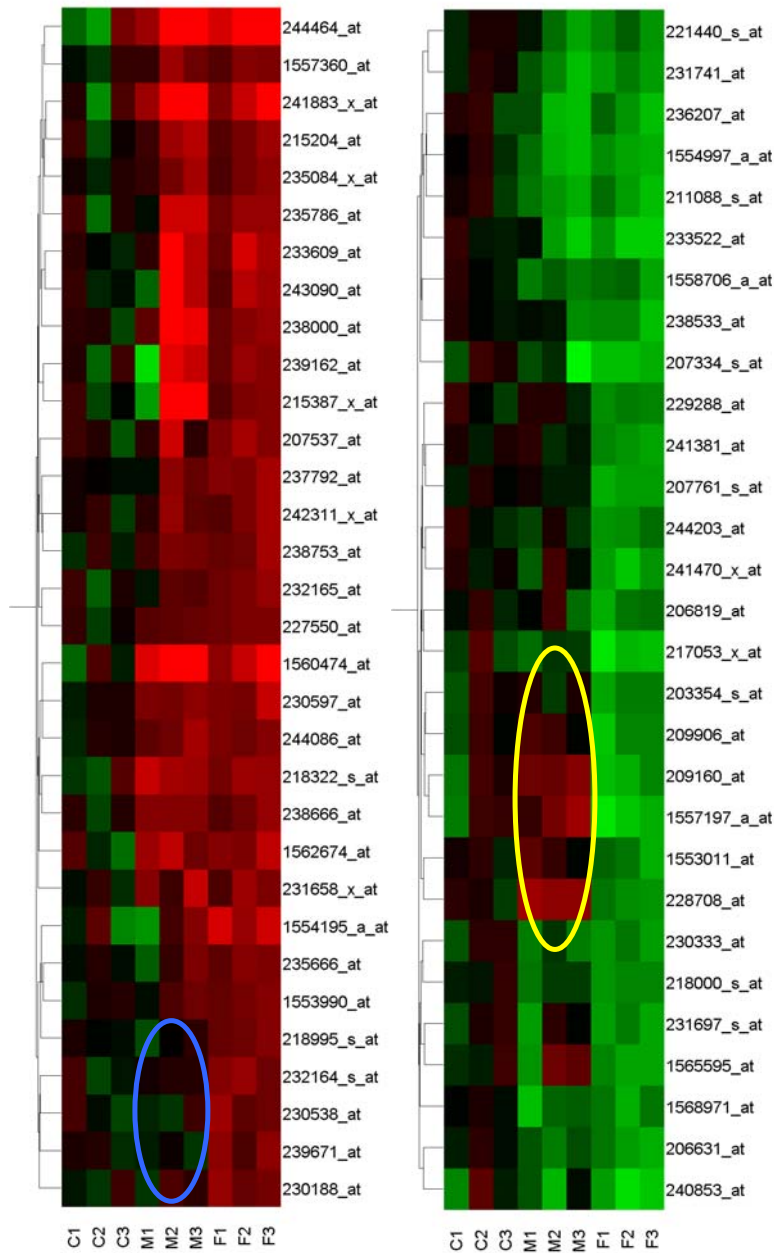


Figure 57: Heatmaps of 32 upregulated (left) and 29 downregulated (right) probes due to ferucarbotran-labelling. M600-labelling resulted in the upregulation of the same genes, except for the group circled blue. M600-labelling resulted in the downregulation of the same genes (circled in yellow) except the the uncircled group.

The nine lanes of the heatmaps belong to the triplicate samples from each group, ie from left to right are the triplicates of mock-labelled sample C1-3, M600-labelled sample M1-3 and ferucarbotran-labelled sample F1-3. On the right of each heatmap is the probe Affy-ID whose description and synonym can be found in the Appendix or via NetAffy™ the web tool from Affymetrix (<http://www.affymetrix.com>). The heatmaps of upregulated genes showed that largely the same genes were up-regulated by M600 and ferucarbotran labelling. This is with the exception of the small clusters of genes at the bottom (circled in blue in Figure 56 and Figure 57). On the other hand, different genes were down regulated by M600 and ferucarbotran labelling, except for the clusters circled in yellow. Therefore, the heatmaps suggested that the upregulated cellular functions were independent of the label used, but downregulated functions were specific to the label.

To establish the GO terms associated with the lists of differentially expressed genes (gene lists) and to enrich them in a process known as functional enrichment, the gene lists were imported into the web tool FatiGO (Al-Shahrour, 2006). During the process, the 114 genes up-regulated by M600-labelling were matched to the associated GO terms at the various GO levels while same was done for the rest of genes in the genome outside the list of 114 to produce the following table.

DB	List 1	Genome
GO biological process at level 3	29 / 114 25.44%	1804 / 31524 5.72%
GO biological process at level 4	28 / 114 24.56%	1787 / 31524 5.67%
GO biological process at level 5	27 / 114 23.68%	1733 / 31524 5.5%
GO biological process at level 6	25 / 114 21.93%	1632 / 31524 5.18%
GO biological process at level 7	21 / 114 18.42%	1472 / 31524 4.67%
GO biological process at level 8	18 / 114 15.79%	1246 / 31524 3.95%
GO biological process at level 9	13 / 114 11.4%	927 / 31524 2.94%
GO molecular function at level 3	28 / 114 24.56%	1732 / 31524 5.49%
GO molecular function at level 4	26 / 114 22.81%	1684 / 31524 5.34%
GO molecular function at level 5	25 / 114 21.93%	1551 / 31524 4.92%
GO molecular function at level 6	21 / 114 18.42%	1280 / 31524 4.06%
GO molecular function at level 7	12 / 114 10.53%	697 / 31524 2.21%
GO molecular function at level 8	3 / 114 2.63%	328 / 31524 1.04%
GO molecular function at level 9	0 / 114 0%	188 / 31524 0.6%
GO cellular component between at level 3	12 / 114 10.53%	511 / 31524 1.62%
GO cellular component between at level 4	11 / 114 9.65%	507 / 31524 1.61%
GO cellular component between at level 5	9 / 114 7.89%	492 / 31524 1.56%
GO cellular component between at level 6	9 / 114 7.89%	473 / 31524 1.5%
GO cellular component between at level 7	7 / 114 6.14%	436 / 31524 1.38%
GO cellular component between at level 8	6 / 114 5.26%	401 / 31524 1.27%
GO cellular component between at level 9	3 / 114 2.63%	345 / 31524 1.09%
KEGG	10 / 114 8.77%	1139 / 31524 3.61%
Interpro	43 / 114 37.72%	18273 / 31524 57.97%
Swissprot	35 / 114 30.7%	15171 / 31524 48.13%
MicroRNA	0 / 114 0%	469 / 31524 1.49%
BioCarta	3 / 114 2.63%	887 / 31524 2.81%
Transcription Factors	0 / 114 0%	0 / 31524 0%
cisRed	33 / 114 28.95%	13388 / 31524 42.47%

Table 10: Matching genes (column List 1) upregulated by M600 labelling to associated GO terms at various hierarchical levels and comparing the match with other genes in the genome (column Genome)

List 1 of Table 10 shows the number and percentage out of the 114 genes that were associated with each level of GO terms. For example, 29 out of 114 genes (25.44%) were associated with GO biological processes at level 3 and 1804 out of the 31524 unique probes in the microarray. Since genes have a many-to-many association with GO terms, each GO term was assigned a p-value and an adjusted p-value by Fatigo analysis. By considering only the three significant GO terms with adjusted $p < 0.05$, M600-labelling caused up-regulation of metal and cation-binding and increased penetration of phospholipid bilayer membrane (integral to membrane). Details of the significant GO terms are shown in the table below.

GO Term		List vs Genome	P-value	Adjusted P-value
GO cellular component at level 7				
integral to membrane	GO:0016021	89.9% 10.1%	6.79E-04	4.14E-02
GO molecular function at level 3				
ion binding	GO:0043167	95.97% 4.03%	5.22E-06	5.69E-04
GO molecular function at level 4				
metal ion binding	GO:0046872	96.71% 3.29%	2.12E-06	6.12E-04
cation binding	GO:0043169	95.57% 4.43%	6.77E-05	9.78E-03

Table 11: Significant GO terms that are associated with the upregulation of 114 genes due to M600-labelling

The same was done with the list of 102 genes down-regulated by M600-labelling to produce the tables in the following pages

























































DB	List 1	Genome
GO biological process at level 3	39 / 102  38.24%	1808 / 31524  5.74%
GO biological process at level 4	38 / 102  37.25%	1791 / 31524  5.68%
GO biological process at level 5	37 / 102  36.27%	1739 / 31524  5.52%
GO biological process at level 6	34 / 102  33.33%	1641 / 31524  5.21%
GO biological process at level 7	31 / 102  30.39%	1476 / 31524  4.68%
GO biological process at level 8	30 / 102  29.41%	1241 / 31524  3.94%
GO biological process at level 9	21 / 102  20.59%	922 / 31524  2.92%
GO molecular function at level 3	28 / 102  27.45%	1738 / 31524  5.51%
GO molecular function at level 4	27 / 102  26.47%	1691 / 31524  5.36%
GO molecular function at level 5	26 / 102  25.49%	1557 / 31524  4.94%
GO molecular function at level 6	19 / 102  18.63%	1285 / 31524  4.08%
GO molecular function at level 7	9 / 102  8.82%	705 / 31524  2.24%
GO molecular function at level 8	3 / 102  2.94%	329 / 31524  1.04%
GO molecular function at level 9	1 / 102  0.98%	188 / 31524  0.6%
GO cellular component between at level 3	20 / 102  19.61%	510 / 31524  1.62%
GO cellular component between at level 4	20 / 102  19.61%	505 / 31524  1.6%
GO cellular component between at level 5	18 / 102  17.65%	487 / 31524  1.54%
GO cellular component between at level 6	18 / 102  17.65%	464 / 31524  1.47%
GO cellular component between at level 7	17 / 102  16.67%	426 / 31524  1.35%
GO cellular component between at level 8	17 / 102  16.67%	389 / 31524  1.23%
GO cellular component between at level 9	14 / 102  13.73%	335 / 31524  1.06%
KEGG	5 / 102  4.9%	1139 / 31524  3.61%
Interpro	77 / 102  75.49%	18273 / 31524  57.97%
Swissprot	74 / 102  72.55%	15171 / 31524  48.13%
MicroRNA	0 / 102  0%	469 / 31524  1.49%
BioCarta	9 / 102  8.82%	887 / 31524  2.81%
Transcription Factors	11 / 102  10.78%	0 / 31524  0%
cisRed	59 / 102  57.84%	13388 / 31524  42.47%

Table 12: Matching genes (column List 1) downregulated by M600 labelling to associated GO terms at various hierarchical levels and comparing the match with other genes in the genome (column Genome)

GO Term		List vs Genome	P-value	Adjusted P-value
GO biological process at level 3				
cell cycle	GO:0007049	93.26% 6.74%	6.84E-15	5.20E-13
chromosome segregation	GO:0007059	95.86% 4.14%	7.45E-05	2.83E-03
cell division	GO:0051301	93.92% 6.08%	1.68E-03	4.26E-02
GO biological process at level 4				
mitotic cell cycle	GO:0000278	97.42% 2.58%	1.84E-19	3.95E-17
cell cycle process	GO:0022402	93.09% 6.91%	6.80E-14	7.31E-12
organelle organization and biogenesis	GO:0006996	77.33% 22.67%	2.89E-04	2.07E-02
GO biological process at level 5				
regulation of cell cycle	GO:0051726	96.25% 3.75%	3.83E-13	1.62E-10
cell cycle phase	GO:0022403	94.44% 5.56%	2.19E-12	4.63E-10
GO biological process at level 6				
regulation of progression through cell cycle	GO:0000074	96.5% 3.5%	1.53E-13	9.63E-11
M phase	GO:0000279	94.89% 5.11%	5.06E-10	1.59E-07
DNA replication	GO:0006260	94.61% 5.39%	1.65E-04	3.35E-02
microtubule-based process	GO:0007017	90.95% 9.05%	2.13E-04	3.35E-02
GO biological process at level 7				
M phase of mitotic cell cycle	GO:0000087	98.55% 1.45%	4.88E-14	3.49E-11

cell cycle checkpoint	GO:0000075	96.75% 3.25%	3.03E-06	1.08E-03
microtubule cytoskeleton organization and biogenesis	GO:0000226	94.45% 5.55%	2.50E-05	5.57E-03
positive regulation of progression through cell cycle	GO:0045787	99.3% 0.7%	3.11E-05	5.57E-03
sister chromatid segregation	GO:0000819	97.94% 2.06%	1.51E-04	2.17E-02
GO biological process at level 8				
mitosis	GO:0007067	98.34% 1.66%	1.80E-13	1.49E-10
spindle organization and biogenesis	GO:0007051	98.41% 1.59%	1.15E-04	4.76E-02
GO biological process at level 9				
regulation of mitosis	GO:0007088	99.43% 0.57%	5.93E-13	4.04E-10
mitotic sister chromatid segregation	GO:0000070	98.5% 1.5%	9.27E-05	3.16E-02

Table 13: Significant GO biological process terms that are associated with downregulation of 102 genes due to M600-labelling

GO Term		List vs Genome	P-value	Adjusted P-value
GO cellular component at level 3				
non-membrane-bound organelle	GO:0043228	75.74% 24.26%	1.05E-04	1.68E-03
GO cellular component at level 7				
intracellular non-membrane-bound organelle	GO:0043232	75.42% 24.58%	6.52E-05	3.98E-03
GO cellular component at level 8				
cytoskeleton	GO:0005856	82.73% 17.27%	5.19E-05	4.57E-03
GO cellular component at level 9				
microtubule cytoskeleton	GO:0015630	92.29% 7.71%	3.39E-07	2.85E-05
cytoskeletal part	GO:0044430	84.54% 15.46%	4.86E-05	2.04E-03
GO molecular function at level 3				
nucleic acid binding	GO:0003676	87.54% 12.46%	2.29E-04	2.49E-02

Table 14: Significant GO biological process and molecular function terms that are associated with downregulation of 102 genes by M600-labelling

There were 27 GO terms significantly associated with downregulation, compared to just three associated with upregulation, although on closer inspection the 27 GO terms were hierarchically associated and can be reduced to the three distinctive functions of lowered mitotic cell cycle, formation of microtubule cytoskeleton and nucleic acid binding. These GO terms suggest that M600-labelling of fMSC may

result in a lower proliferation rate, and possibly slower cellular migration than for unlabelled cells.

With ferucarbotran-labelling, 32 genes and 29 genes up-regulated and down-regulated by ferucarbotran labelling, respectively. The same FatgiGO analysis was applied to these genes to produces the following results.

























































DB	List 1	Genome
GO biological process at level 3	7 / 32  21.88%	1832 / 31524  5.81%
GO biological process at level 4	7 / 32  21.88%	1815 / 31524  5.76%
GO biological process at level 5	7 / 32  21.88%	1762 / 31524  5.59%
GO biological process at level 6	6 / 32  18.75%	1662 / 31524  5.27%
GO biological process at level 7	6 / 32  18.75%	1494 / 31524  4.74%
GO biological process at level 8	5 / 32  15.62%	1264 / 31524  4.01%
GO biological process at level 9	5 / 32  15.62%	935 / 31524  2.97%
GO molecular function at level 3	7 / 32  21.88%	1757 / 31524  5.57%
GO molecular function at level 4	6 / 32  18.75%	1709 / 31524  5.42%
GO molecular function at level 5	6 / 32  18.75%	1573 / 31524  4.99%
GO molecular function at level 6	5 / 32  15.62%	1295 / 31524  4.11%
GO molecular function at level 7	3 / 32  9.38%	706 / 31524  2.24%
GO molecular function at level 8	1 / 32  3.12%	330 / 31524  1.05%
GO molecular function at level 9	0 / 32  0%	188 / 31524  0.6%
GO cellular component between at level 3	6 / 32  18.75%	518 / 31524  1.64%
GO cellular component between at level 4	6 / 32  18.75%	513 / 31524  1.63%
GO cellular component between at level 5	5 / 32  15.62%	496 / 31524  1.57%
GO cellular component between at level 6	4 / 32  12.5%	476 / 31524  1.51%
GO cellular component between at level 7	3 / 32  9.38%	439 / 31524  1.39%
GO cellular component between at level 8	3 / 32  9.38%	402 / 31524  1.28%
GO cellular component between at level 9	3 / 32  9.38%	345 / 31524  1.09%
KEGG	1 / 32  3.12%	1139 / 31524  3.61%
Interpro	10 / 32  31.25%	18273 / 31524  57.97%
Swissprot	7 / 32  21.88%	15171 / 31524  48.13%
MicroRNA	0 / 32  0%	469 / 31524  1.49%
BioCarta	0 / 32  0%	887 / 31524  2.81%
Transcription Factors	0 / 32  0%	0 / 31524  0%
cisRed	8 / 32  25%	13388 / 31524  42.47%

Table 15: Matching genes (column List 1) upregulated by ferucarbotran labelling to associated GO terms at various hierarchical levels and comparing the match with other genes in the genome (column Genome)

GO Term		List vs Genome	P-value	Adjusted P-value
GO molecular function at level 3				
ion binding	GO:0043167	98.05% 1.95%	3.05E-05	3.32E-03
GO molecular function at level 4				
metal ion binding	GO:0046872	98.5% 1.5%	1.31E-05	3.79E-03

Table 16: Significant GO terms that are associated with upregulation of 32 genes due to ferucarbotran-labelling

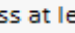

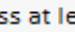

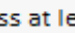

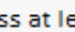

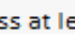

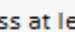

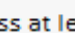

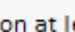

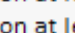

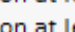

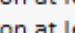

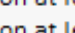

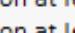

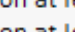

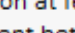

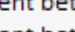

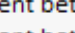

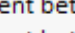

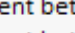

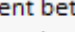

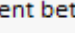

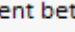

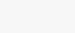

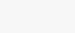

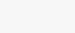

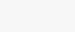

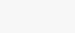

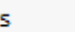

DB	List 1	Genome
GO biological process at level 3	12 / 29  41.38%	1833 / 31524  5.81%
GO biological process at level 4	12 / 29  41.38%	1816 / 31524  5.76%
GO biological process at level 5	12 / 29  41.38%	1764 / 31524  5.6%
GO biological process at level 6	12 / 29  41.38%	1664 / 31524  5.28%
GO biological process at level 7	10 / 29  34.48%	1494 / 31524  4.74%
GO biological process at level 8	8 / 29  27.59%	1263 / 31524  4.01%
GO biological process at level 9	5 / 29  17.24%	937 / 31524  2.97%
GO molecular function at level 3	12 / 29  41.38%	1750 / 31524  5.55%
GO molecular function at level 4	12 / 29  41.38%	1701 / 31524  5.4%
GO molecular function at level 5	12 / 29  41.38%	1564 / 31524  4.96%
GO molecular function at level 6	9 / 29  31.03%	1289 / 31524  4.09%
GO molecular function at level 7	8 / 29  27.59%	701 / 31524  2.22%
GO molecular function at level 8	3 / 29  10.34%	327 / 31524  1.04%
GO molecular function at level 9	4 / 29  13.79%	183 / 31524  0.58%
GO cellular component between at level 3	6 / 29  20.69%	522 / 31524  1.66%
GO cellular component between at level 4	6 / 29  20.69%	517 / 31524  1.64%
GO cellular component between at level 5	5 / 29  17.24%	499 / 31524  1.58%
GO cellular component between at level 6	5 / 29  17.24%	478 / 31524  1.52%
GO cellular component between at level 7	4 / 29  13.79%	440 / 31524  1.4%
GO cellular component between at level 8	3 / 29  10.34%	404 / 31524  1.28%
GO cellular component between at level 9	1 / 29  3.45%	348 / 31524  1.1%
KEGG	1 / 29  3.45%	1139 / 31524  3.61%
Interpro	16 / 29  55.17%	18273 / 31524  57.97%
Swissprot	15 / 29  51.72%	15171 / 31524  48.13%
MicroRNA	0 / 29  0%	469 / 31524  1.49%
BioCarta	2 / 29  6.9%	887 / 31524  2.81%
Transcription Factors	0 / 29  0%	0 / 31524  0%
cisRed	13 / 29  44.83%	13388 / 31524  42.47%

Table 17: Matching genes (column List 1) downregulated by ferucarbotran labelling to associated GO terms at various hierarchical levels and comparing the match with other genes in the genome (column Genome)

GO Term		List vs Genome	P-value	Adjusted P-value
GO biological process at level 9				
prostanoid metabolic process	GO:0006692	100% 0%	2.26E-05	0.015365

Table 18: Significant GO terms are associated with downregulation of 29 genes due to ferucarbotran-labelling

Therefore, only three significant GO terms were related to ferucarbotran-labelling compared to 30 for M600-labelling. Ion and metal ion binding genes were upregulated by ferucarbotran labelling which is similar to the effects of M600-labelling. Only genes related to the prostanoid metabolic process were down-regulated by ferucarbotran labelling.

The differences in gene expression profiles obtained may be due to the greater iron-loading of M600 labelled cells, or to differences in the polymeric content of M600 and ferucarbotran. M600 is made up of mainly MAA and EA and has an IO wt% of 43% while ferucarbotan is made of carboxy-dextran with an IO wt% of 58%.

Despite finding a greater number of differentially regulated genes when labelling with M600, no phenotypic difference was observed in the labelled cells in terms of proliferation rate over 3 passages, viability and differentiation capacity. The observed differential gene expression itself may be transient as total RNA was extracted immediately after labelling. The longer term effects are currently unknown, unless further test microarray analyses are done on cells several passages after labelling. There have been limited studies on the impact of iron oxide labelling on cellular gene expression reported in literature. Schafer et al demonstrated that the transferrin receptor was upregulated through flow cytometry after labelling of rat MSC with

SPIO (Schafer, 2007), while Berry et al. demonstrated that cytoskeleton and signalling genes were upregulated in human dermal fibroblasts after iron oxide labelling (Berry, 2004). To date, there has been no genome-wide array study performed in human MSC types after labelling with iron oxide particles.

4.6 Uptake of MGIO by EPC

In addition to labelling fMSC, we compared the utility of M600 particles with ferucarbotran for labelling umbilical cord blood-derived endothelial progenitor cells (EPC). By simple incubation of EPC with the particles (0.05 mg iron/ml) over 24 hours, we observed the incorporation of nanoparticles into the cytoplasm of EPC. This was consistent with the endocytotic mechanism for M600-labelling of fMSC and for cellular uptake previously described for ferucarbotran (Matuszewski, 2005). M600 particles were taken up with good efficiency (28.3 ± 1.6 pg/cell, n=3), a result is similar to that of ferucarbotran-labelling (25.8 ± 1.5 pg/cell, n=3) and both particles resulted in significantly more intracellular iron than mock-labelled EPC (1.43 ± 0.3 pg/cell, n=3).

4.7 Function of Labelled EPC

To determine if labelling with MGIO is deleterious to cellular function, M600-labelled EPC were phenotypically and functionally characterised, and the results were compared with those of ferucarbotran and mock-labelled EPC. Intracellular cellular iron was stained with Prussian blue and the labels appeared to reside in the cytoplasm, in agreement with their location in labelled fMSC. The cells were functionally tested to be able to form tubes on matrigel and able to take up acetylated low density lipoprotein and be stained for von Willebrand Factor (vWF) (Figure 58). They were also stained for phenotypic endothelial cell surface markers vascular-endothelial cadherin (CD144), and platelet/endothelial cell adhesion molecule-1 (PECAM-1/CD31) (Figure 59). The results of these stains were the same in all three groups, suggesting that labelling with M600 or ferucarbotran did not alter EPC phenotypically or functionally.

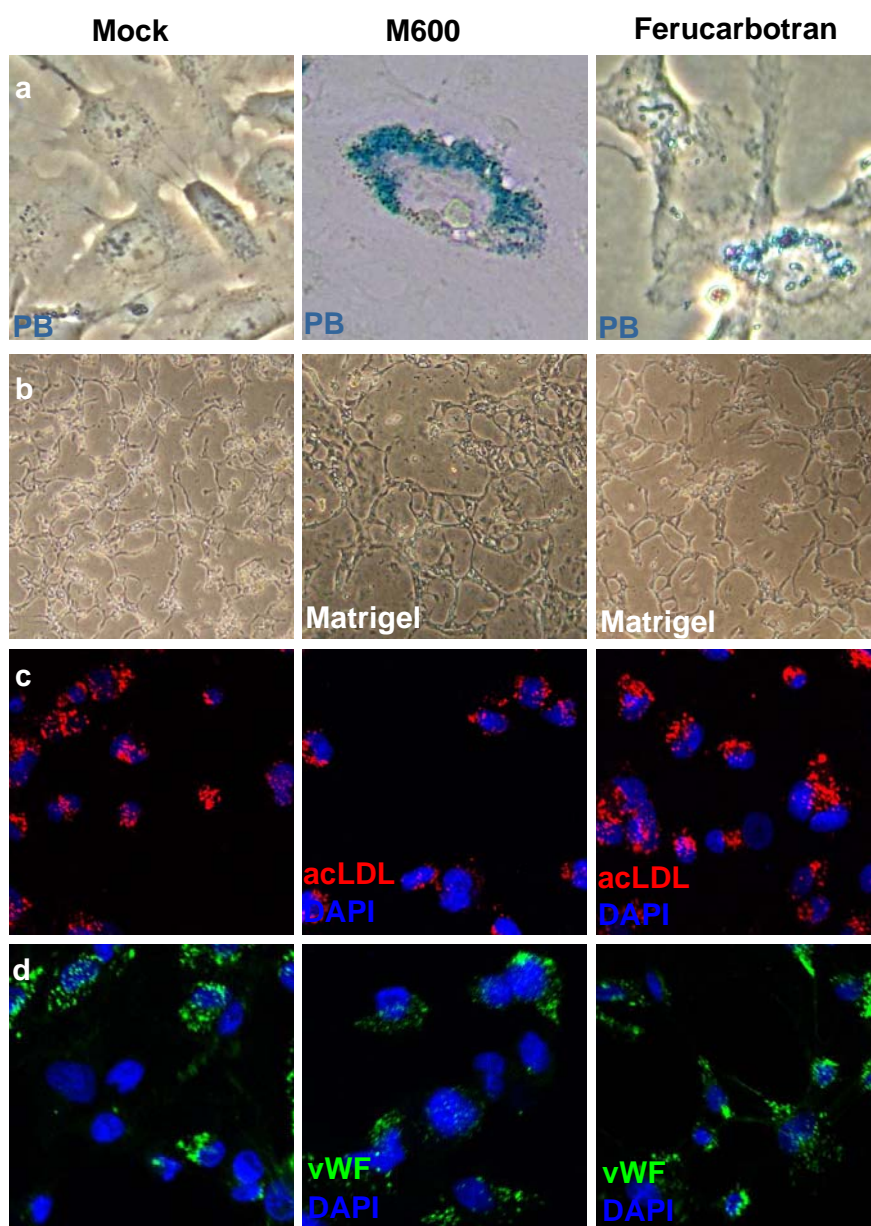


Figure 58: Staining of (a) intracellular iron by Prussian blue and (b-d) cellular function of mock, M600 and ferucarbotran-labelled EPC. Labelled EPC retained the capacity to (b) form tubes, (c) take up Dii-acLDL and (d) be stained for vWF.

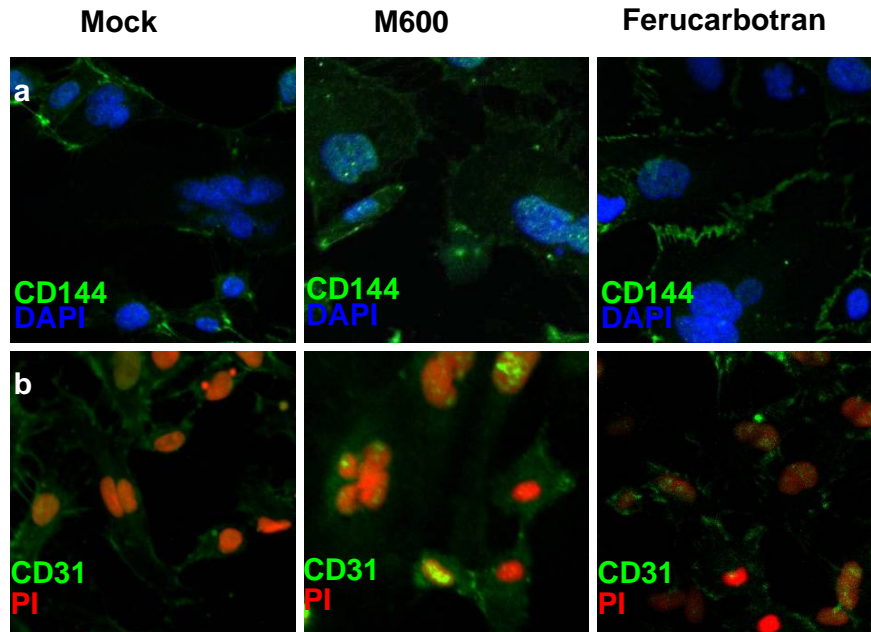


Figure 59: Staining of mock, M600 and ferucarbotran-labelled cells for endothelial phenotypic surface markers. Labelled EPC retained the expression of (a) CD144 and (b) CD31.

4.8 Discussion

Incubation of fMSC with MGIO resulted in its internalisation into endosomes, suggesting an endocytotic mechanism for cellular uptake as previously described for ferucarbotran (Matuszewski, 2005). The greater loading at high concentrations may be a result of greater availability of particles in the medium for interaction with the cells. There have been similar reports on incubation at high particle concentration in an attempt to increase intracellular iron load. It was shown that while human monocytes tolerated 0.1mg/ml of ferumoxide, 0.5mg/ml caused apoptosis but ferucarbotran at either concentration did not (Metz, 2004). Hsiao et al showed hMSC intracellular iron increased by 17 pg iron/cell and were >90% viability when labelled with ferucarbotran at 0.1mg/ml (Hsiao, 2007). Schafer labelled with ferucarbotran at concentrations up to 0.2mg/ml, obtained iron load increase of 24 pg iron / cell and showed that viability remained >90% at up to 20 days post-labelling in culture with no significant difference from unlabelled controls (Schafer, 2007).

The uptake of ferucarbotran and M600 did not show iron loadings that saturate with increasing iron concentration in medium. This is in contrast to reports that showed saturation at high concentrations for Hela cells and macrophages labelled with 30nm AMNP (Wilhelm, 2003) and for T cells labelled with sub-100 to 1.4µm particles (Thorek, 2008).

There are three possible explanations for the absence of saturated loading of fMSC. The first may be because fMSC loading is saturated only at concentrations beyond 0.2 mg/ml. Another possible reason is that the intracellular uptake pathway or space was already saturated at 0.1mg/ml. When more particles were introduced during labelling

concentration of 0.2mg/ml, the additional particles were merely attached to the cellular surface, with adhesion strong enough to resist removal by density centrifugation. Further TEM analysis will be required to verify presence of surface bound particles at 0.1 or 0.2 mg/ml labelling concentrations. The third possible reason is the activation of an alternate uptake mechanism at high concentrations. As particles have been shown to be adsorbed in aggregates on cellular surface prior to their internalisation (Wilhelm, 2003), the greater availability of particles at high concentration may have increased aggregate sizes. When presented with aggregates of larger sizes, alternative pathways may be activated, akin to the activation of caveolae mechanism on melanoma cells by large particles (Rejman, 2004). By determining the organelle that the particles reside, the pathway of internalisation may be uncovered (please see Section 1.6.6.2).

Although labelling at concentration beyond 0.2mg/ml was not studied, high concentrations such as 0.2mg/ml has been shown to associate with cytotoxicity (van den Bos, 2003; Neri, 2008). Most workers reported only cellular viability from Trypan blue exclusion or TUNEL assays without considering the functional effects of high labelling concentration. Our subsequent experiments used only cells labelled at 0.05mg/ml as this is a more commonly used concentration and to safeguard against possible functional deficit. This concentration already represents 5.6 times the plasma concentration when subjects are given the recommended dose of ferucarbotran i.v. [the recommended plasma concentration is 9µg/ml (Metz, 2004)].

The labelling of fMSC with ferucarbotran resulted in similar cellular loading as previously reported by Mailander et al using adult bone marrow derived MSC (9 pg/MSC) (Mailander, 2008), which is higher than that achieved with ultrasmall-SPIO

particle (3.8 pg/MSC) (Schafer, 2007) and the larger polystyrene particles (7.5 pg/MSC) (Stuckey, 2006). The unexpected finding of a three- to six-fold increase in uptake with M600 particles seem to reflect a size dependent effect which has been previously reported in the uptake of other nanoparticles by Hela (Chithrani, 2006) and T-cells (Thorek, 2008). The mechanisms for this preferential uptake at 600 nm are presently unknown, but may in part be explained by the differences in pathways involved in endocytotic uptake with different particle sizes. For example, 500nm polystyrene particles undergo uptake via a caveolae-mediated pathway, while those measuring 50 to 200 nm are taken up by cells through a clathrin-mediated pathway (Rejman, 2004). The lower uptake of the larger M750 particles may be explained in part by a size limitation of the endocytotic machinery of non-phagocytotic cell types (Rejman, 2004). Without considering M600, the differences in uptake between the other MGIO models are insignificant, but further trends in uptake with particle diameters may be elucidated with a wider range of MGIO diameters.

Labelling of fMSC with either MGIO or ferucarbotran did not affect either cellular proliferation in culture or tri-lineage differentiation. This finding is in contrast to the report by Kostura et al. that showed reduced chondrogenic differentiation potential of ferumoxide labelled adult MSC labelled with ferumoxide (Kostura, 2004), although it remains uncertain whether the cause lies with the particle type used, or the choice of transfection agent (poly-L-lysine) used to increase particle uptake (Arbab, 2005). However, my microarray analysis picked up possible cell cycle downregulation after M600-labelling. This may be due to the difference in chemical composition of M600 and ferucarbotran, or the greater amount or total particle mass or iron oxide mass per cell resulting from M600 labelling. The latter can be controlled by labelling fMSC at M600 concentrations lower than 0.05mg/ml to achieve similar particle or iron mass

loading per cell at 0.05mg/ml. A separate gene expression analysis of fMSC labelled with different particles but with the same particle or iron loading per cells will shed light on the cause of the apparent cell cycle downregulation by M600-labelling.

M600 and ferucarbotran were taken up in similar quantity into EPC cytoplasm, as compared to the three-fold greater uptake of M600 compared to ferucarbotran by fMSC. This suggests that the effect of particle size on uptake is dependent on cell type. Each cell type may have an optimum uptake particle size, which for fMSC is 600nm, but this size has yet been determined for EPC. Labelling EPC with M600 and ferucarbotran did not affect the cellular function and phenotypic surface marker expression. This shows that MGIO is a suitable label that does not affect cellular characteristics after labelling across multiple cell types.

Chapter 5 Results III: MR Tracking of MGIO-fMSC

Through the cell culture experiments described in Section Chapter 4, M600 was shown to provide higher iron loading in fMSC than ferucarbotran, without affecting stem cell properties. To verify whether fMSC is a cell label superior to ferucarbotran, *in vivo* MR tracking of the labelled cells was demonstrated in this section. A cerebral injury model was created to obtain damaged tissue that induced fMSC homing. Animals were imaged by MRI at regular time points before and up to weeks after stem cell injections to identify the location of the stem cells. The cellular locations given by MR images were verified by histology to determine the accuracy of cellular tracking achieved.

Hypothesis: MGIO-labelled fMSC can be transplanted to an animal model of cerebral stroke such that the cellular migration to the injury site can be tracked by MRI

5.1 Cellular Migration Stroke Model

Stroke was created via two methods: the ligation of internal or middle cerebral artery (ICA/MCA), and the focal photochemical induction of cerebral thrombosis.

5.1.1 Internal and Middle Cerebral Artery Occlusion

Stroke induction through MCA occlusion by advancing suture method was attempted on one animal (Rat1). The ICA was exposed but the suture could not be guided into the lumen of the artery. As no personnel with such microsurgery experience was available, the technique was deemed to be accomplishable only through the practice on tens of animals, which was not feasible ethically. Occlusion by arterial ligation was next attempted. A unilateral ICA ligation was performed on one animal (Rat2) for 30min but no stroke was observed when the brain was stained with 2,3,5-triphenyltetrazolium (TTC). Stroke confirmation by perfusing the animal with TTC was preferred over methods that yield greater histological details (ie paraffin or cryo-sectioning), as TTC staining provided almost immediate feedback on the stroke parameters, without the need for fixation and sectioning. Bilateral ICA ligation was attempted on another animal (Rat3) in a procedure that took over an hour to complete, but the animal died shortly after the procedure. The invasiveness of the ligation procedure and the duration required due to lack of surgery experience may have been the cause of death. Yet again, practice with numerous animals, with simultaneous ligation of the vertebral arteries may be required to obtain reproducible infarcts (Yamaguchi, 2005)

5.1.2 Photochemical Cerebral Thrombosis

After induction of the photo-thrombotic stroke, perfusion with TTC stains mitochondrial activity distinctly red to verify that cortical infarcts measuring 4 to 5 mm across (Figure 60) could be consistently produced.



Figure 60: Consecutive 2mm brain sections of rats with photo-thrombotic stroke were stained by TTC. Mitochondria activity is stained red while the infarct region remains colourless.

Infarct region demarcated by TTC staining was compared against T2-weighted fast spin echo MR images. This MR sequence shows infarcts as hyperintense regions due to its sensitivity to accumulated water (Figure 61). The strong corroboration between TTC stains and T2 images with suggests that TTC is a convenient method to verify stroke creation in our *in vivo* model.

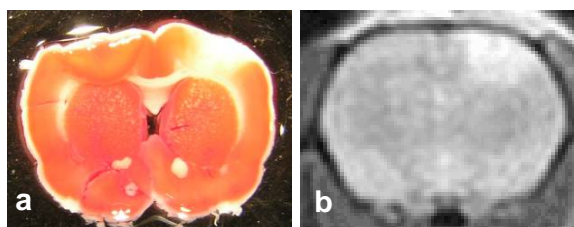


Figure 61: Comparison of (a) TTC stain and (b) T2-weighted MR image of the approximate section shows that TTC can reliably verify infarct extent

Seven animals (Rat 4 to 9, Rat 14) were used to establish the parameters and gain the technical experience required to create reproducible infarcts. Although reproducible, critics of this model may argue that reperfusion is not possible and the mechanism of infarction is different from the one experienced by stroke victims. The MCAo

generates cerebral ischemia in the region normally perfused by the MCA, but the photochemical method causes thrombosis to all vessels in the light-exposed region. However, there are clinical scenarios where focal, primarily cortical or peripheral strokes can occur, especially in the setting of embolic disease or vasculitis. Nevertheless, the aim is the reliable creation of an injury model that allows the observation of cellular migration, which is already achieved with the photochemically-induced thrombotic model. However, during the assessment of the therapeutic potential of fMSC towards cerebral remodelling in typical stroke victims, the MCAo may be a more suitable model.

5.2 Tracking fMSC in Stroke Animals

One day after creation of a Rose Bengal-induced photo-thrombotic injury to the cerebral cortex (Day -1), the ischemic region was visualised on MR imaging through a TSE (yellow arrowheads Figure 62) sequence as a wedge shaped focal hyperintense region, involving the cortex predominantly.

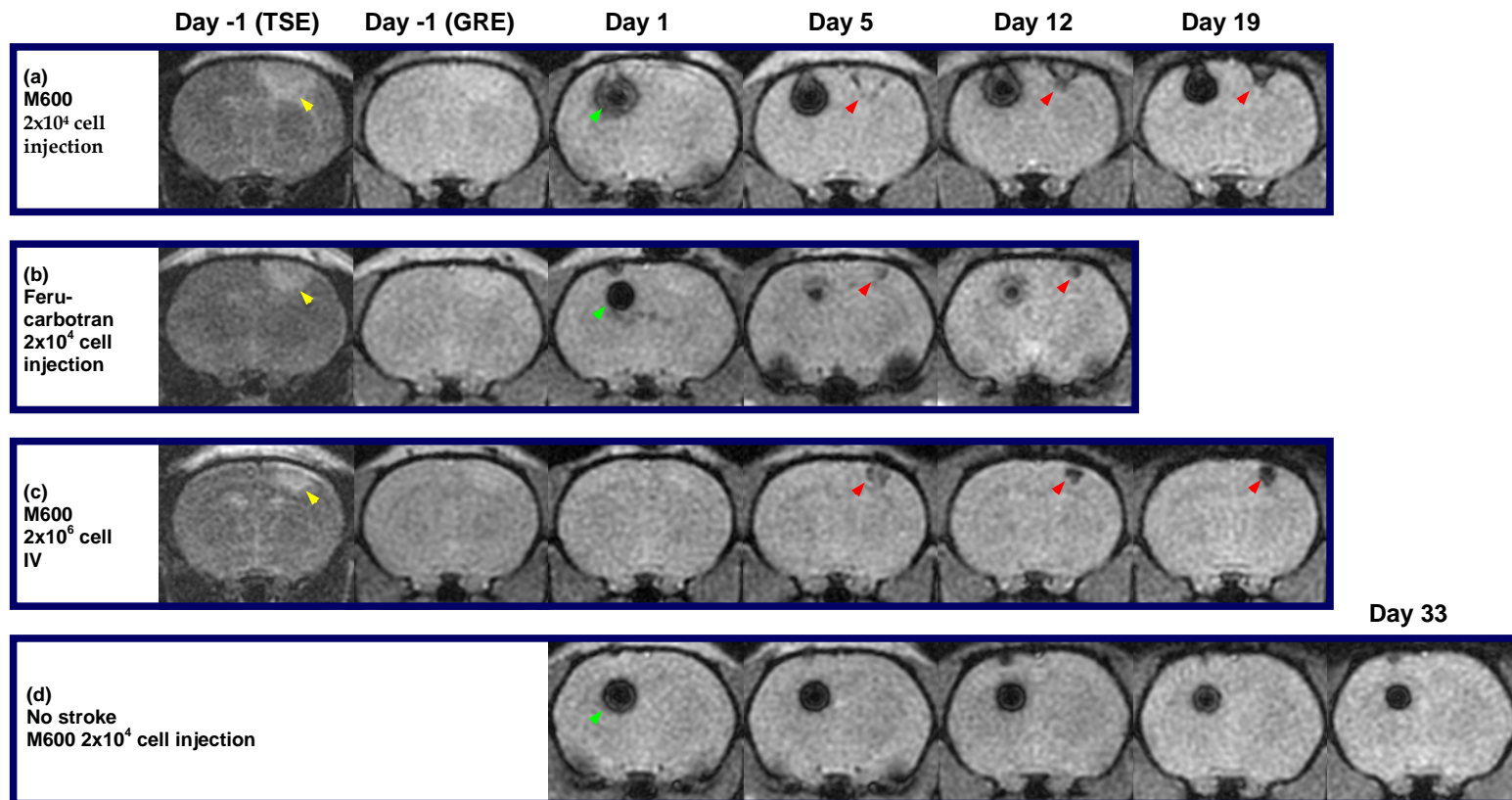


Figure 62: *In vivo* imaging with turbo spin echo (TSE, Day -1) and gradient echo sequence (GRE, Day -1 through Day 12). A focal cortical stroke (yellow arrows) was induced at Day -2 and cellular transplantation took place on Day 0 by contralateral intracerebral (green arrows) or systemic injection (IV) (a) An area of hypointensity appeared in the area of the stroke (red arrows) noticeable at Day 5, and increased over time to Day 12 in M600-fMSC injected animals. (b) A similar observation was made in Ferucarbotran-fMSC injected animals, albeit with a smaller area of hypointensity seen. (c) Animals injected with M600-fMSC intravenously showed appearance of hypointensity in the stroke region by Day 5, which increased over time to Day 12. (d) In comparison, there was no hypointensity at the contralateral cerebral cortex where no stroke injury had been induced.

In the M600-fMSC group, intracerebrally-transplanted cells (Figure 62a green arrowhead) appeared as hypointense regions in gradient echo (GRE) images on the transplanted side of the brain. By day 5, a small area of hypointensity could be seen around the peripheral region of the stroke (Figure 62a red arrowhead), suggesting the migration of M600-fMSC cells to the stroke site. On day 12, the area of hypointensity around the injury could be clearly seen encompassing the periphery of the stroke (Figure 62a red arrowheads).

In keeping with the higher iron loading of fMSC with the use of M600 particles over ferucarbotran, the hypointensities developing in the stroke region appeared more striking in animals transplanted with M600 than ferucarbotran-labelled fMSC. By using the Rose criterion (Rose, 1948) to obtain an image-based quantitative assessment for cellular detection, animals transplanted with M600-fMSC had greater numbers of hypointense voxels at Day 5 (average hypointense voxels per image 106.2 ± 15.2 (n=5) vs 14.0 ± 5.5 (n=3); $p=0.002$) and at Day 12 (235.3 ± 64.7 (n=4) vs 44.0 ± 22.1 (n=3); $p=0.03$) at the stroke region compared with animals transplanted with ferucarbotran-fMSC. Thus, M600-labelling provided a six- to seven-fold higher sensitivity for cellular detection at both time-points, which should provide more reliable detection of transplanted cells.

Intravenous delivery of M600-fMSC was well-tolerated, and resulted in the appearance of hypointensity by Day 5 at the site of the stroke, which increased from Day 5 to 12 on GRE images (Figure 62c). MR imaging of control animals transplanted with M600-fMSC but without a contralateral stroke demonstrated no development of hypointensity in the contralateral cerebral cortex (Figure 62d).

In order to quantify the improvement in cell detection with M600-labelling over ferucarbotran-labelling, we measured the signal-to-noise ratio (SNR) in our GRE images to be 15.2 ± 0.2 (Firbank, 1999). By applying the detection threshold reported by Heyn et al (Heyn, 2005), the detection limit was calculated to be 777 ± 126 pg Fe per voxel. In terms of cell numbers, the lower limit at which M600-fMSC (33.3pg/cell) can therefore be detected is ~ 23 cells, compared to ~ 81 cells for ferucarbotran-fMSC (9pg/cell). Under micro-imaging conditions, possibly with research scanners or custom-built hardware (100 μm isotropic voxel dimensions and SNR=60) (Heyn, 2005), the detection limit would be lowered from 777 to 1.34 ± 0.22 pg Fe per voxel, which should allow a single M600-fMSC to be detected even after four cellular divisions, assuming that the intracellular iron halves with each cellular division.

Brain images captured with SSFP sequence provided similar indications of cellular migration (Figure 63). However, the infarct areas were less hyperintense compared to TSE images, and the suggested cellular locations were also less hypointense. This 3D sequence is highly sensitive to water and should give better SNR than a GRE sequence in theory. In our SSFP sequence setup, I have chosen higher spatial resolution over the GRE sequence while maintaining similar SNR. However, the sequence was affected by respiration-induced motion artefact, which was evident in the artefacts that extended radially from the brain stem. Susceptibility artefact is characteristic of this sequence and in this case, GRE images were deemed more suitable for the image analysis and hence preferred over the SSFP images.

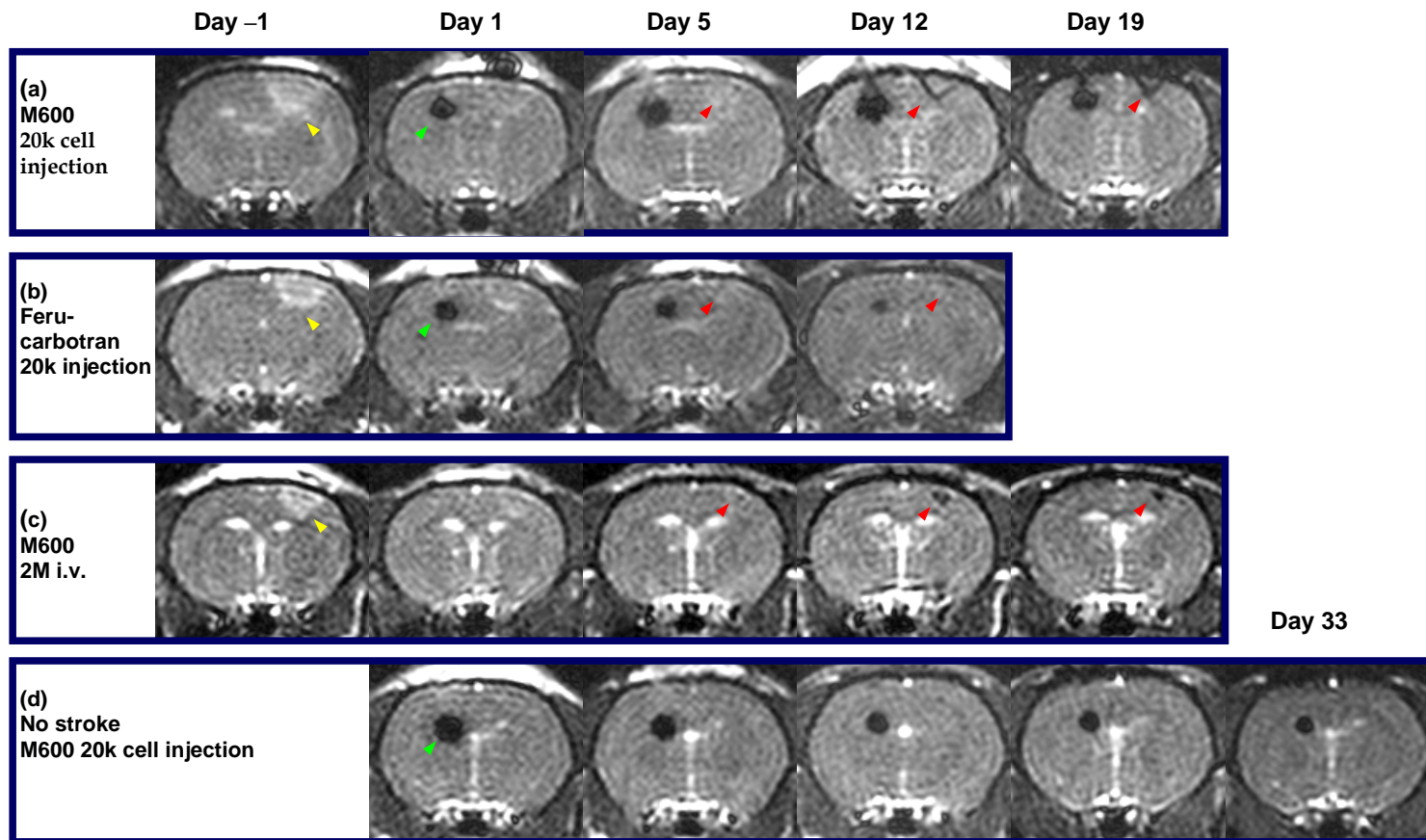


Figure 63: *In vivo* imaging with SSFP sequence. The images are of the same animals and were taken immediately after those in Figure 62. A focal cortical stroke (yellow arrows) was induced at Day -2 and cellular transplantation took place on Day 0 by contralateral intracerebral (green arrows) or systemic injection (IV) (a) An area of hypointensity appeared in the area of the stroke (red arrows) noticeable at Day 5, and increased over time to Day 12 in M600-fMSC injected animals. (b) A similar observation was made in Ferucarbotran-fMSC injected animals, albeit with a smaller area of hypointensity seen. (c) Animals injected with M600-fMSC intravenously showed appearance of hypointensity in the stroke region by Day 5, which increased over time to Day 12. (d) In comparison, there was no hypointensity at the contralateral cerebral cortex where no stroke injury had been induced.

5.3 Histology

We sacrificed the animals in the M600-fMSC group and harvested the brains to correlate the MRI findings with histologic and immunostaining evidence of cellular and label fate. On Day 1, Prussian blue-positive cells (staining for iron) could be seen only at the injection site (blue stain, Figure 64a), but not at the stroke site (Figure 64b,c). Double immuno-staining of the injection site revealed fMSC as human vimentin-positive cells among an infiltration of host ED1 positive macrophages (Figure 64d-f) with a discernible shift of cells from the injected site towards the stroke area at Day 1. There were only ED1-positive host macrophages, with no vimentin-positive cells at the stroke site at Day 1 (Figure 64g-h).

By Day 5, in keeping with MRI findings, iron-labelled DAB-enhanced Prussian blue-positive cells appeared at the periphery of the stroke injury (Figure 65a-c) and the appearance of vimentin-positive human cells together with a heavy infiltration of host ED1-positive cells (Figure 65d-f). Histologic sections at Day 12 showed an abundance of globular heavily Prussian blue positive cells (Figure 66a-c), correlating well with the increase in hypointensity on MR imaging. However, immunostaining revealed only ED1-positive cells at the stroke area and no human vimentin positive cells (Figure 66d-e). Inspection of the injection site revealed only few vimentin-positive cells (Figure 66f) amid a large infiltrate of ED1-positive cells.

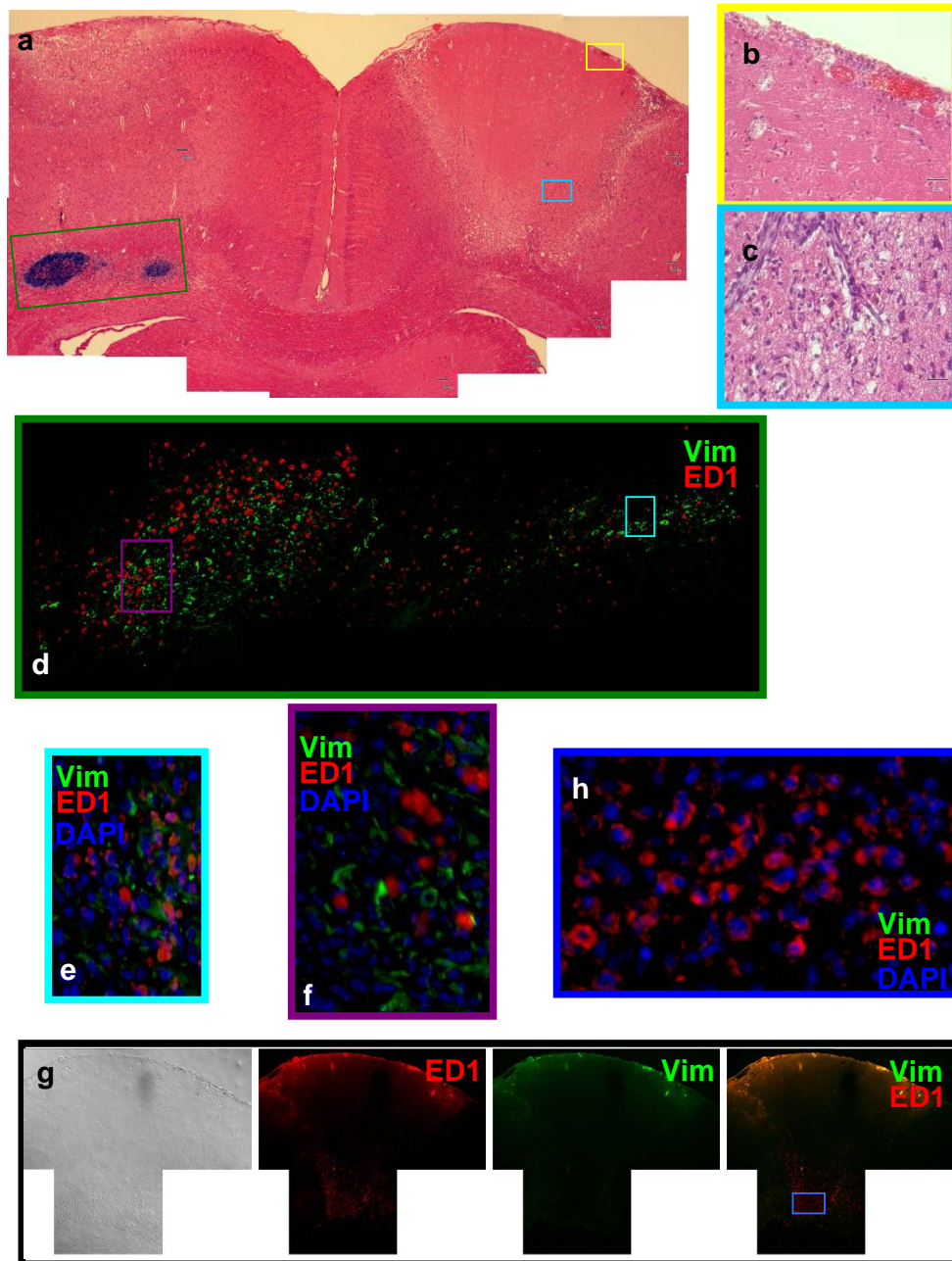


Figure 64: Immunohistological analysis of animals transplanted with 2×10^4 M600-fMSC on Day 1. (a-c) Prussian blue/haematoxylin-eosin staining demonstrated iron-laden cells at the injection site, but not the stroke site. (d-f) Immunohistochemical staining of adjacent sections showed these to be mainly human vimentin-positive fMSC (green), infiltrated by ED1-positive rat macrophages (red). (g-h) Examination of the stroke area demonstrates presence of ED1-positive cells and no vimentin-positive fMSC. Nuclei were stained with DAPI (blue).

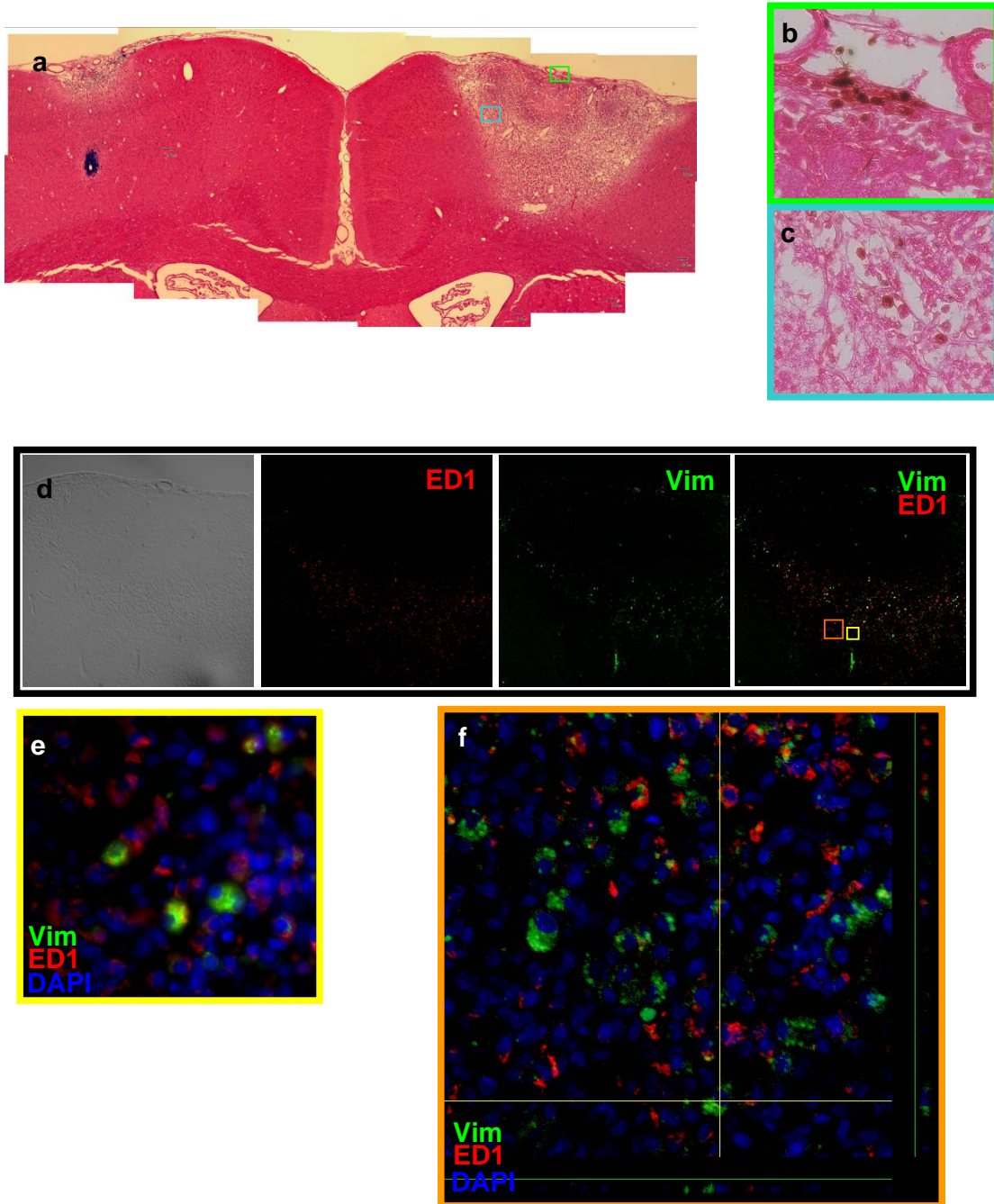


Figure 65: Immunohistological analysis of animals transplanted with 2×10^4 M600-fMSC on Day 5. By Day 5, (a-c) the presence of iron-laden cells can be seen at the stroke site through DAB enhancement of Prussian blue staining (brown, b-c). (d-f) Immunohistological staining of adjacent sections showed the presence of fMSC (green vimentin positive cells, f, z-stacked confocal) surrounded with ED1-positive macrophages at the stroke site.

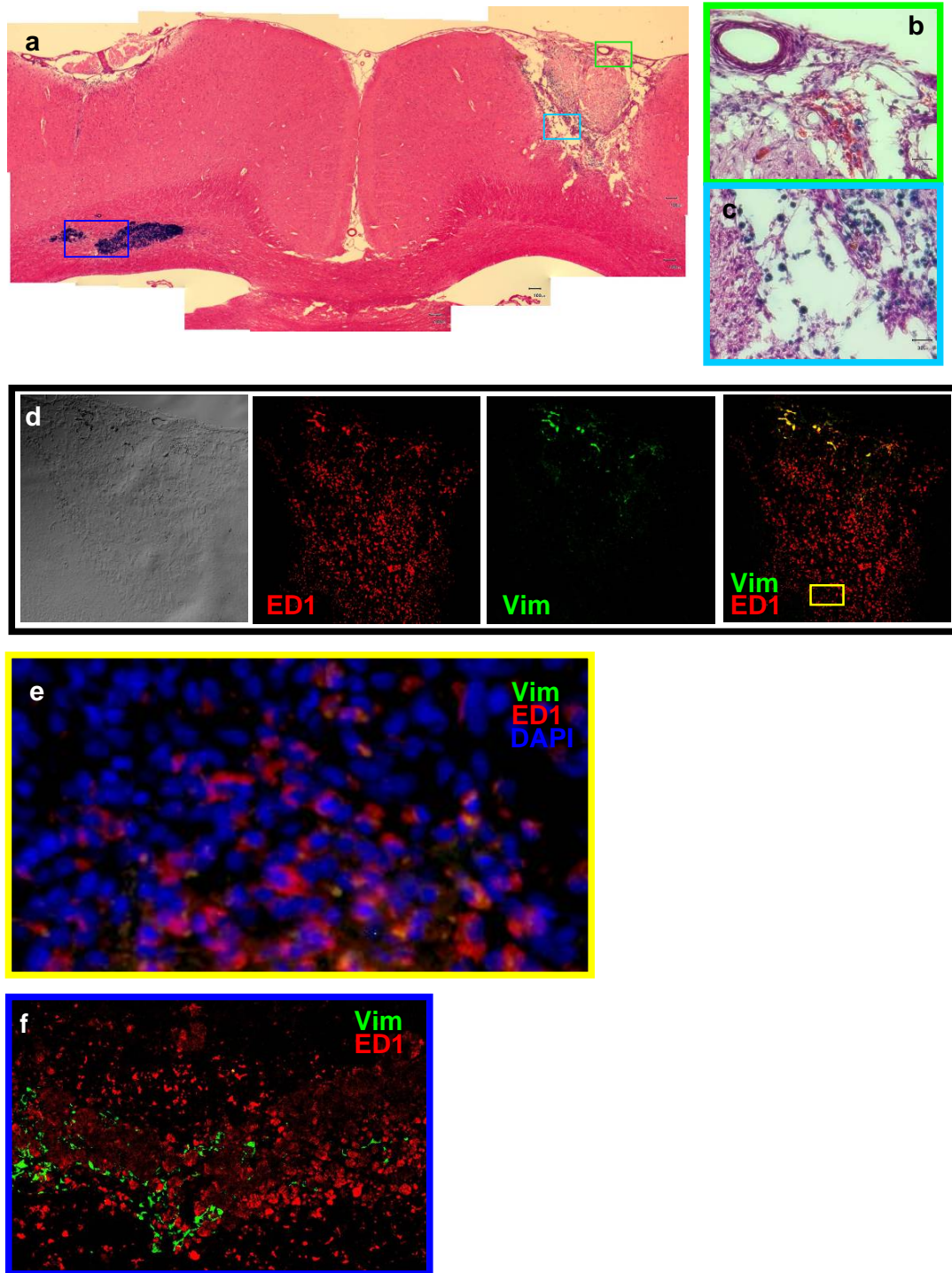


Figure 66: Immunohistological analysis of animals transplanted with 2×10^4 M600-fMSC on Day 12. By Day 12, Prussian blue staining demonstrated increased iron-laden cells at the stroke site (a-c), which were exclusively ED1-positive when stained for both ED1 and human vimentin on adjacent sections (d-e). Both vimentin-positive and ED1-positive cells were found in the injection site (f).

In animals transplanted with ferucarbotran-fMSC, immunohistologic staining at Day 12 similarly showed Prussian blue positive and ED1-positive cells at the stroke site (Figure 67a-e), and a few vimentin-positive human cells among a majority of ED1-positive macrophages at the injection site (Figure 67f). In animals that had been transplanted with M600-fMSC through tail vein injection, analysis at day 19 demonstrated similar findings of iron-ladened macrophages at the stroke site, again with no visible human cells (Figure 68a-e).

Transplantation of mock-labelled fMSC into the contralateral cerebral cortex resulted in no MRI-hypointense regions at either the injection or the stroke sites, with infiltration of Prussian blue-negative ED1 positive cells into both injection and stroke sites, and only a few vimentin-positive human cells at the injection site by Day 12 (Figure 69a-e). Histology of animals without stroke but with transplantation of M600-labelled fMSC at Day 19 revealed small number of surviving fMSC at the injection site with no non-specific migration to other regions of the brain. (Figure 70). Examination of animals with a stroke injury but without cellular transplantation also demonstrated no MRI hypointensity at either sites, with infiltration of only ED1-positive cells, and no vimentin-positive cells at the stroke site by Day 12 (Figure 71).

Immunostaining for host CD8⁺ cells revealed an increasing infiltrate at the stroke region between Day 5 and 12, but were not found at the injection sites (Figure 72).

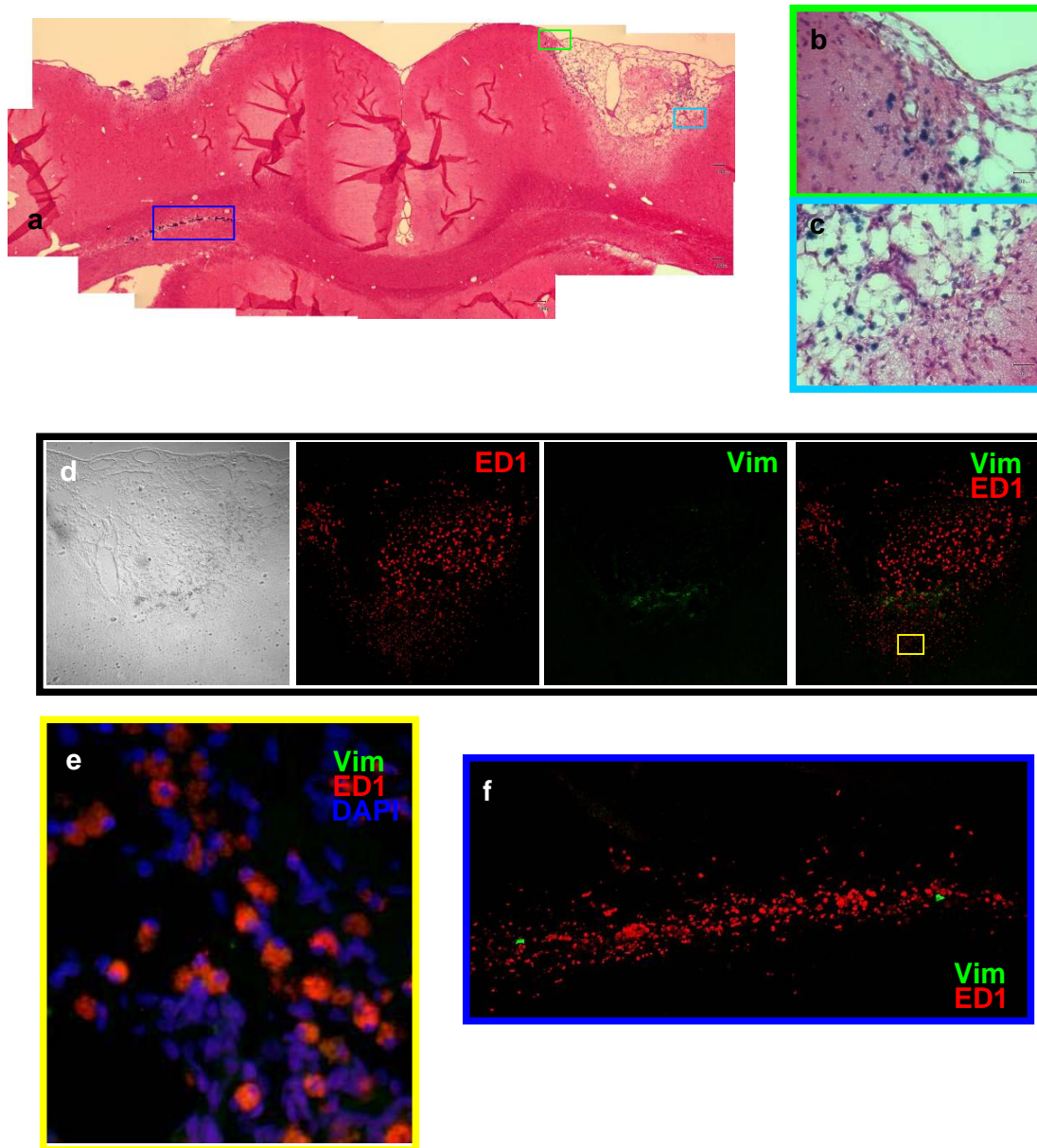


Figure 67: Immunohistological analysis of animals transplanted with 2×10^4 ferucarbotran-fMSC on Day 12. (a-c) Prussian blue/haematoxylin-eosin staining demonstrated a large number of iron-laden cells at the stroke site. (d-e) Immunohistochemical staining of adjacent sections at the stroke site revealed a large infiltrate of ED1 positive cells with no human-vimentin positive fMSC seen at the stroke site. Nuclei were stained with DAPI (blue).

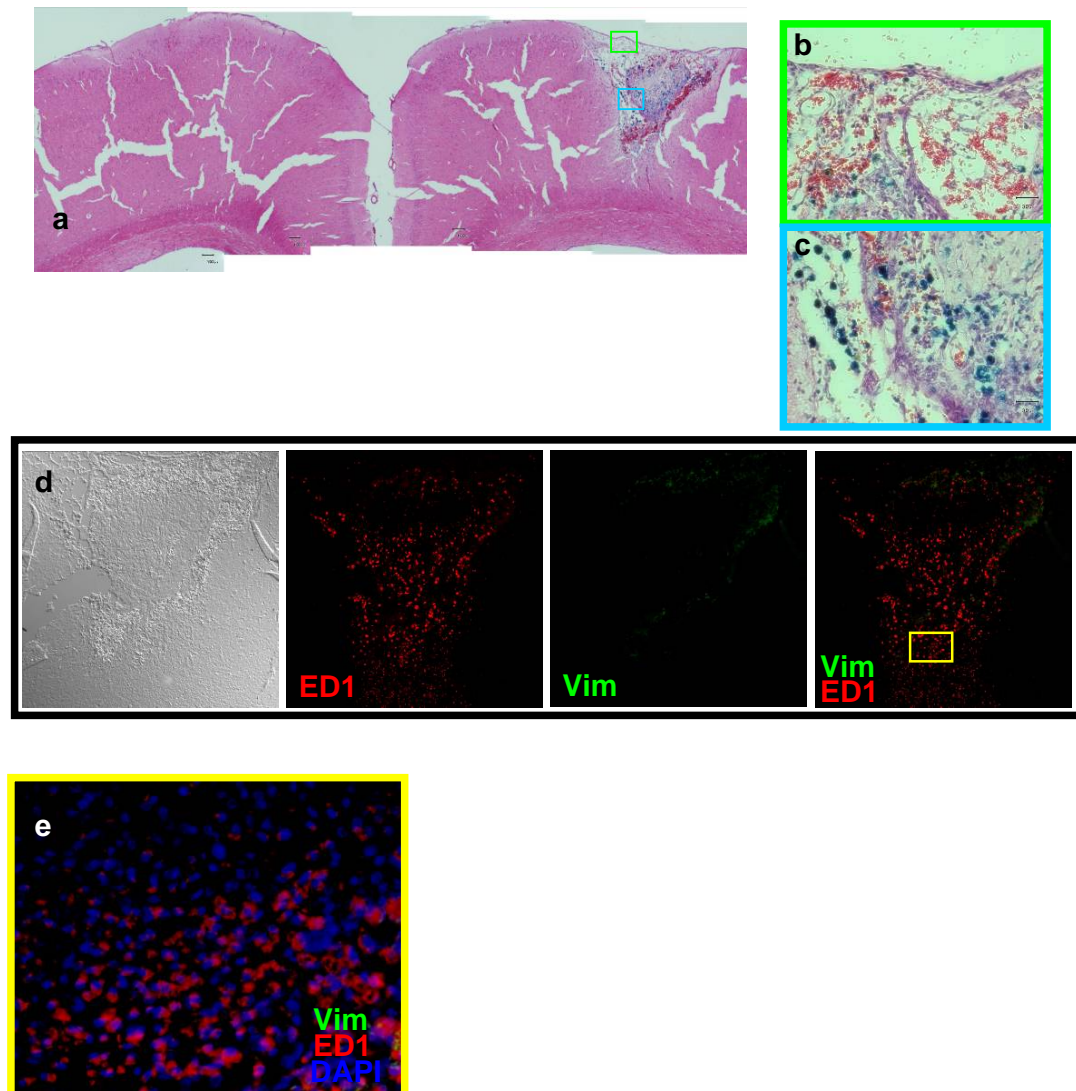


Figure 68: Immunohistological analysis of animals transplanted with 2×10^6 M600-fMSC by tail vein injection on Day 19. (a-c) Prussian blue/haematoxylin-eosin staining demonstrated iron-laden cells at the stroke site. (d-f) Immunohistochemical staining of adjacent sections revealed that these cells to be ED1 positive macrophages. There were no human vimentin positive fMSC cells seen at the stroke area. Nuclei were stained with DAPI (blue).

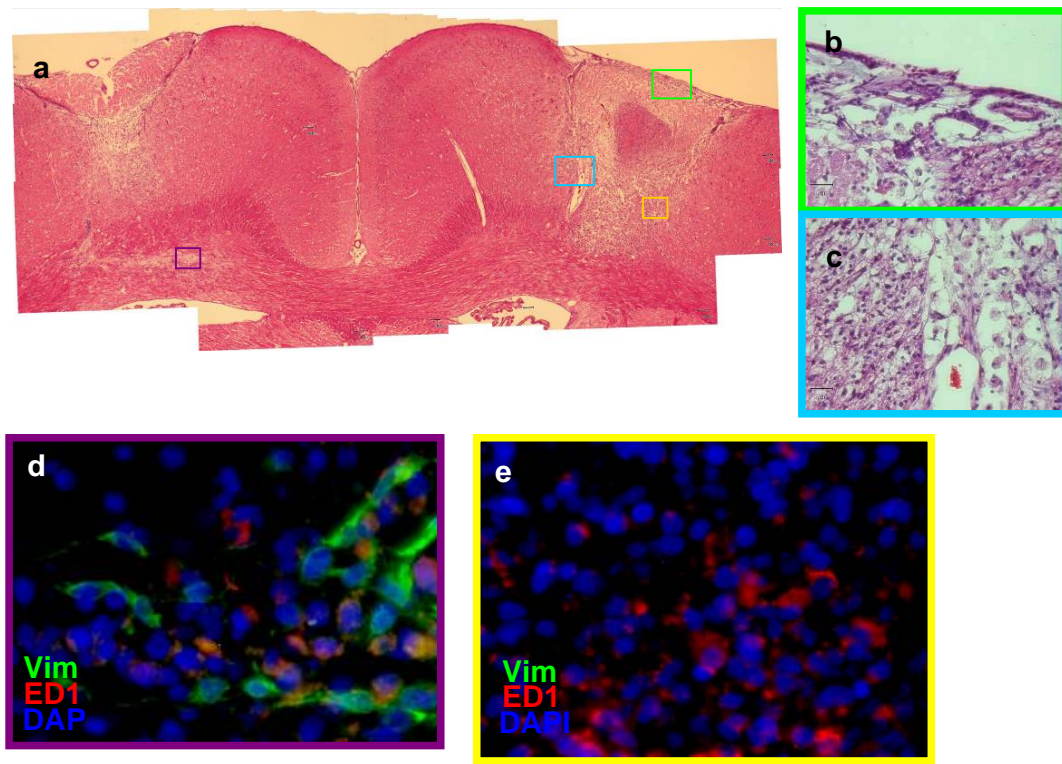


Figure 69: Immunohistological analysis of animals transplanted with 2×10^4 mock-labelled-fMSC at Day 12. (a-c) Prussian blue/haematoxylin-eosin staining demonstrated absence of iron-laden cells at the injection and stroke site. (d-e) Immunohistochemical staining of adjacent sections revealed infiltration of ED1 positive cells with a few human vimentin-positive fMSC (green) at the (d) injection site but not the (e) stroke site. Nuclei were stained with DAPI (blue).

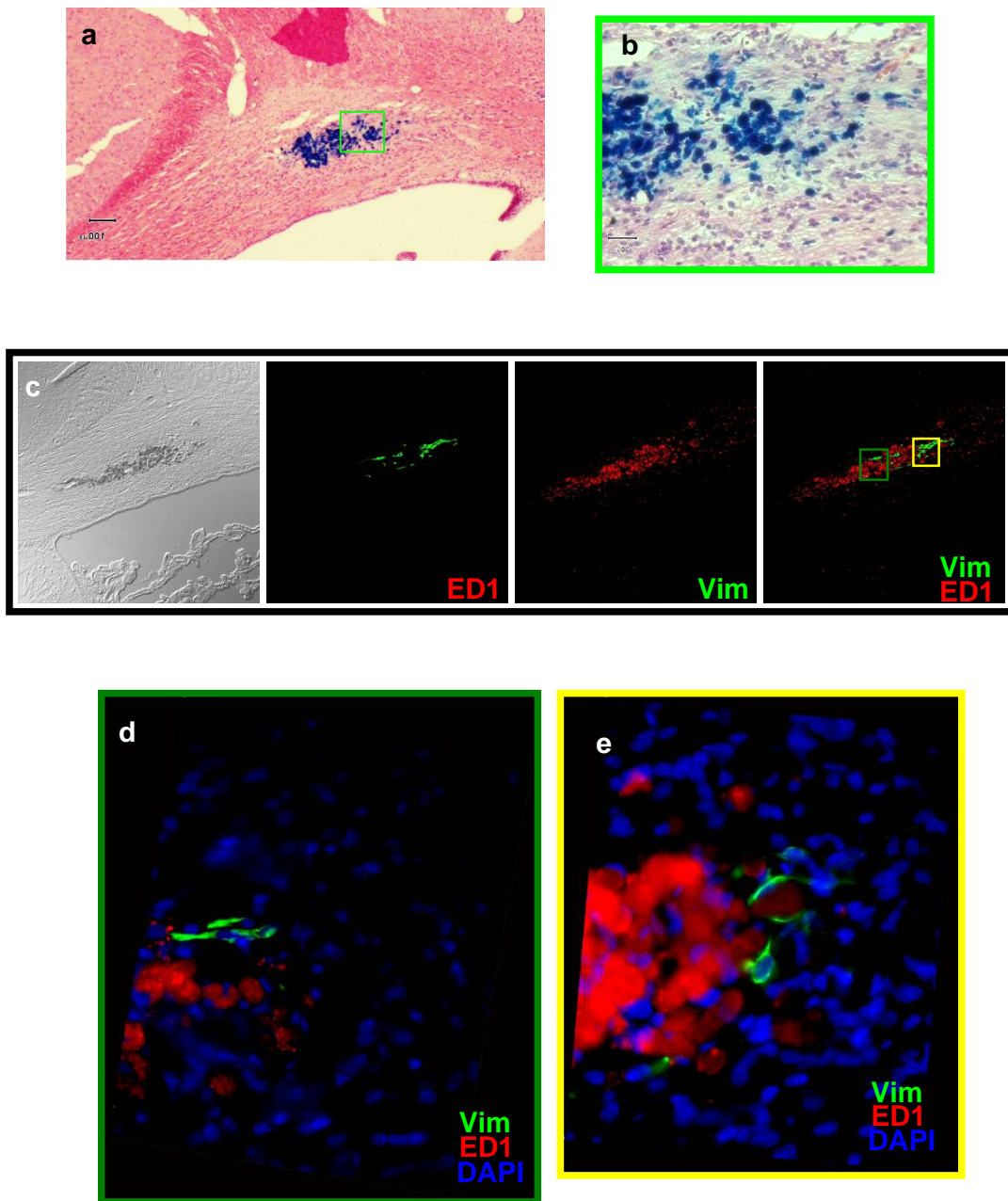


Figure 70: Immunohistological analysis of animals without stroke but transplanted with 2×10^4 M600-fMSC on Day 19. (a-b) Prussian blue/haematoxylin-eosin staining demonstrated iron-laden cells at the injection site, but not the contralateral site. (c-e) Immunohistochemical staining of adjacent sections showed infiltration of ED1-positive rat macrophages (red) and presence of human vimentin-positive fMSC (green) at the injection area. (g-h) Magnified images shows many ED1-positive cells and only few vimentin-positive fMSC. Nuclei were stained with DAPI (blue).

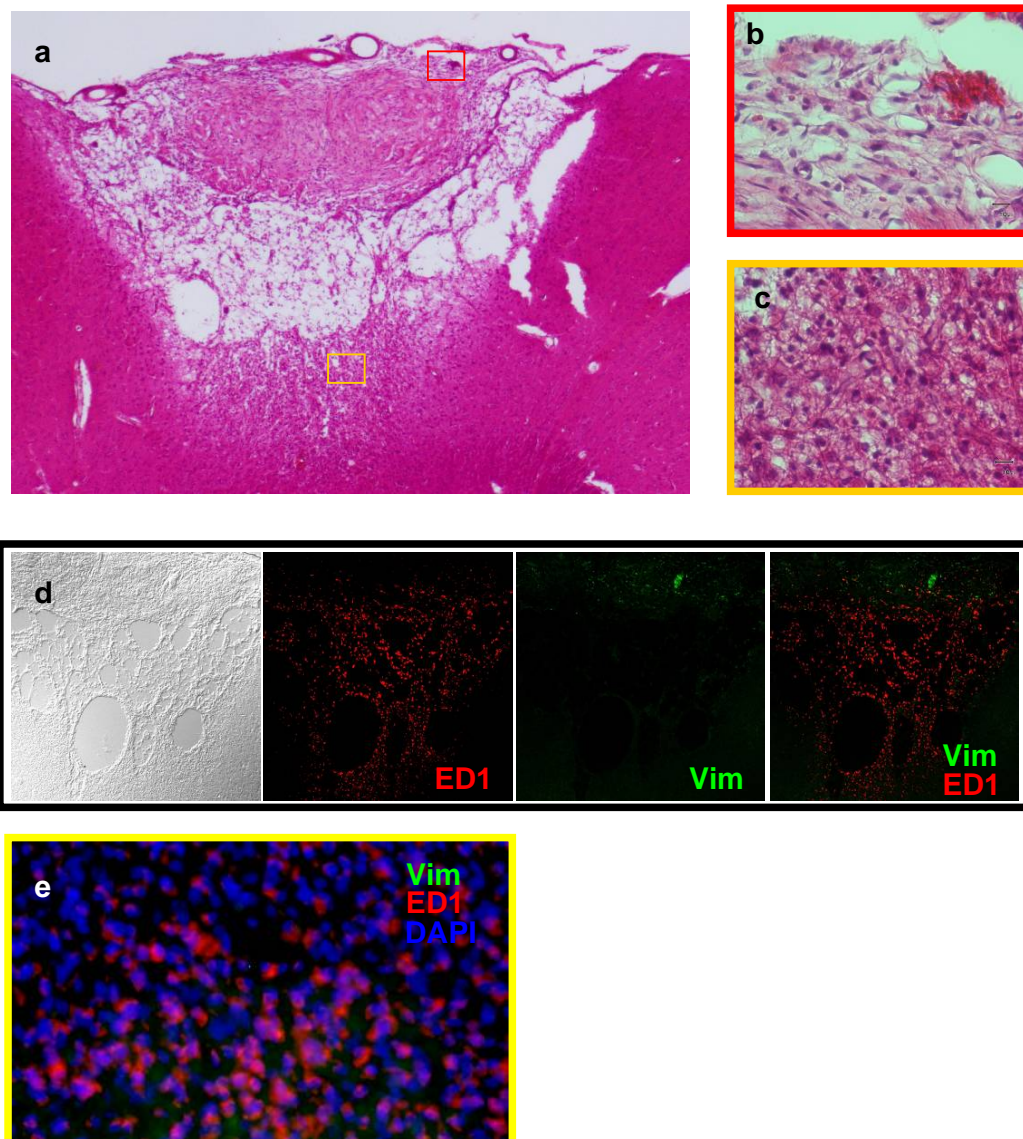


Figure 71: Histological sections on Day 12 of animal with stroke induced but no injection. (a-c) No iron-laden cells were found at the Prussian blue/haematoxylin-eosin staining. (d-e) Immunohistochemical staining of adjacent sections shows infiltration of ED1-positive rat macrophages (red) but no human vimentin-positive fMSC (green) at the stroke area. (e) Magnification of the stroke area shows many ED1-positive cells and no vimentin-positive fMSC. Nuclei were stained with DAPI (blue).

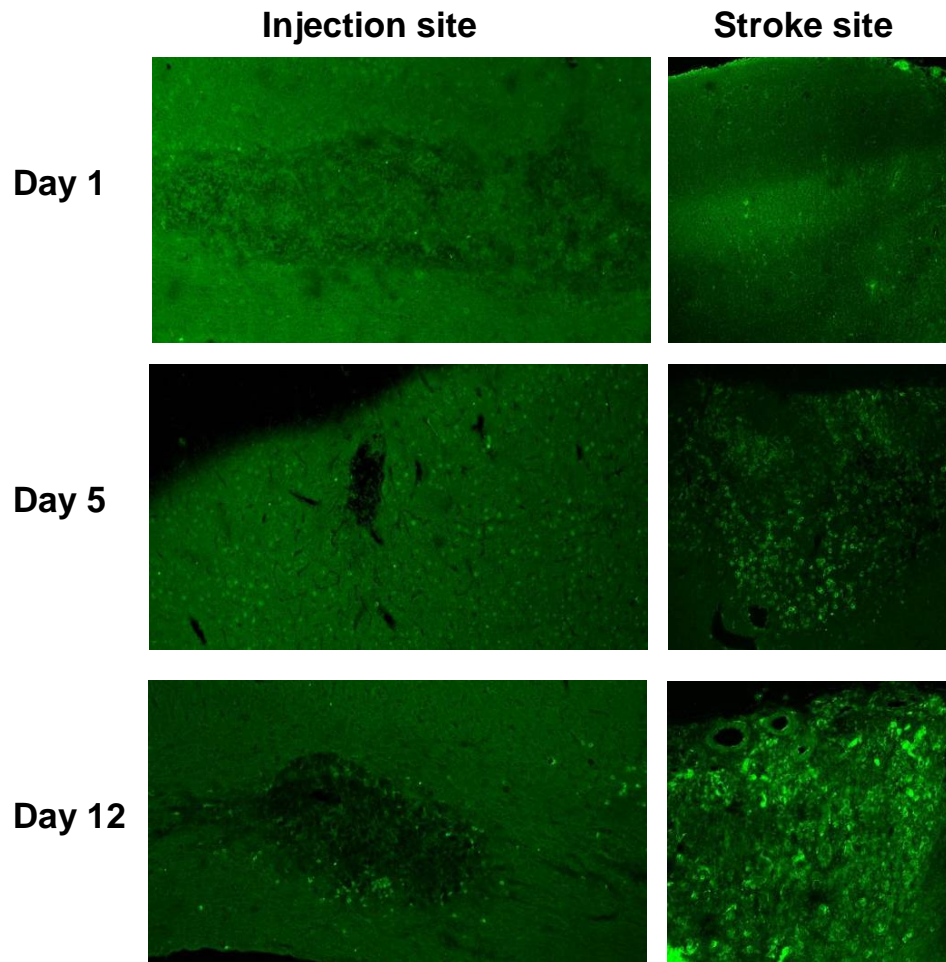


Figure 72: Immunohistochemical analysis of various animals with stroke induced and transplanted with 2×10^4 M600-fMSC and sacrificed at Day 1, 5 or 12. Sections, adjacent those shown in Figure 64 to Figure 66, demonstrate progressive increase of CD8 (green) cytotoxic T cell in stroke site from Day 1 to 12 but only negligible change of CD8+ cells in the injection site, suggesting that an adapted immune response was mounted against the stroke site only but not the injection site.

5.4 Discussion

Taken together, histological analysis of the harvested brain suggests that M600-fMSC migrated towards the injury from Day 1 and arrived at the stroke area by Day 5 as confirmed by both MRI and immuno-histological findings. However, by Day 12 none of the fMSC at the stroke site had survived, and their label had been ingested by host ED1 positive macrophages, which appeared as heavily label-laden Prussian blue positive cells. This in turn was matched by the disappearance of human cells at injection site and corresponding macrophage infiltration. The increase in hypointense voxels in the stroke region between Day 5 and 12 is therefore most likely a result of migration of host ED1 positive macrophages, following ingestion of iron-label from necrosed fMSC at the injection site.

This unexpected finding may have been caused by acute graft cellular apoptosis associated with cellular transplantation paradigms (Beauchamp, 1999; Skuk, 2003), resulting in the infiltration of host macrophages to areas of cell death as early as day 1 after cellular transplantation. Coyne et al and Amsalem et al had previously documented inflammatory rejection of allogeneic rat MSC post transplantation into neural and cardiac injury models (Coyne, 2006; Amsalem, 2007), and thus this phenomenon is not limited to xenotransplantation models.

There was no heavy mono-nuclear cellular infiltrate into the stroke or injection areas to suggest an adaptive immune response, which would normally take between 10-14 days to develop. Moreover, the observation that cytotoxic CD8⁺ T-cells were found only at the stroke sites on Day 5 and 12, and not at the injection sites, suggested that the T-cell infiltrate occurred in response to the stroke and not to the cellular

transplantation (Figure 72). The use of combined immunosuppressive agent reportedly allows longer graft survival than just Cyclosporin A alone (Yan, 2006; Wennberg, 2001). However, we used a Cyclosporin A immunosuppressive dose which has been previously shown to enable human-rat xeno-tolerance for up to six weeks (Wennersten, 2004; Zhao, 2002; Guo, 2007). Identification of grafted cells was attempted using human pan-centromeric FISH probes, but cells with human DNA could not be identified. The failure is likely attributed to the paraffin embedding, which available probes are not designed to stain.

Previously, fMSC survival in a fetal-to-fetal human-mouse xenotransplantation paradigm with chimerisms of up to 5% for up to 19 weeks duration was demonstrated by members in the research group (Chan, 2007; Guillot, 2008). Intracerebral fetal injections in a similar model led to oligodendrocytic differentiation and survival for at least 35 days (Kennea, 2009). Indeed post-natal transplantation of fMSC in adult *scid* mouse muscle was associated with their survival up to 28 days post transplantation (Chan, 2006). The observed cell death cannot be attributed to label toxicity, as a similar finding occurred in both ferucarbotran and M600-labelled, and mock-labelled fMSC (Figure 69), and therefore is probably due to a difference in the host environment specific to this model.

Chapter 6 General Discussion

Future cellular therapy can be aided by imaging tools that allow clinicians to follow the whereabouts of transplanted cells. Magnetic resonance imaging is a high resolution imaging modality without ionising radiation that provides excellent anatomical details of soft tissue. When cells are sufficiently loaded with iron oxide particles, they can be tracked throughout the therapeutic period. However, non-phagocytic cells such as fMSC take up insufficient amounts of small clinically-available particles (<100nm diameter) or large commercial particles (>900nm) to enable tracking of small groups of cells. Particles with diameters between 100 to 900nm have not been previously explored as a cell label.

The key requirement of a useful MR cell label is to enable sufficient labelling efficiency without affecting viability or function of the cells. The new label should demonstrate improved *in vivo* reporting of cellular location that is verifiable with histological analysis of sacrificed animals.

6.1 Hypothesis

The aim of the thesis is to develop a new label that provides better labelling efficiency than clinically-available agents. (i) Magnetic microgel iron oxide particles (MGIO) can be synthesized to have diameters over the range of 100nm to 1 μ m, a size range not previously explored as cell labels. (ii) With MGIO of various sizes, theoretical models of MR relaxation can be verified. (iii) The labelling efficiency of MGIO can be tested on a non-phagocytic cell type, such as fMSC, to show better labelling efficiency without deleterious effects to cells. (iv) The utility of MGIO can be demonstrated in the tracking of fMSC migration in an animal stroke model.

6.2 Summary of Findings

MGIO in the sub-micron diameter range was synthesized by *in situ* co-precipitation of preformed precursor microgel. The iron oxide weight content varied among MGIO models from 33 to 82 wt%. The structure of MGIO consists of numerous primary iron oxide nanoparticles held by a polymer matrix. MGIO has a high average magnetization of about 86 Am²/kg of iron oxide, and although not superparamagnetic, the remnant magnetization is low. The diameters of water-suspended MGIO were 87 to 765nm as measured by DLS. The MR relaxation of M250 and larger particles are in good agreement to theoretical values from relaxation model. The poor agreement of M150 and smaller particles is probably due to the failure of DLS to estimate their effective sizes.

When MGIO was used to label fMSC by simple incubation, the labelling efficiency depended on the particle diameter. M600 provide three- to six-fold increase in iron loading compared to ferucarbotran or other models of MGIO. The difference in loading is significant and may be attributed to size-dependent activation of endocytic pathways. M600-labelled fMSC retained their proliferation rates and multi-lineage differentiation capacity but showed down regulation of cell cycle related genes, possibly due to the transient effect of exposure to labels in the medium. As an alternative cell model, EPC were efficiently labelled by M600 and retained phenotypical and functional properties.

A photochemical cerebral thrombosis rat model was successfully created as a platform for verifying the capacity of MGIO. M600-labelled fMSC injected intracerebrally or intravenously migrated to the stroke site over 12 days and were

tracked by MR. Compared to ferucarbotran-labelling, M600-labelling provided six to seven fold higher sensitivity for cellular detection. Histology analysis showed that fMSC survived for up to five days post transplantation at the stroke site and were rejected by Day 12, regardless of whether they were labelled. The cause is most likely acute immune rejection of fMSC due to incomplete immunosuppression in the xenotransplantation model used. Nonetheless, the superiority of M600 over ferucarbotran as a label for MR tracking was demonstrated.

6.3 Limitations

A limitation of synthesis result is that each PMG and MGIO model was synthesised only once, with the exception of M600 which was synthesised three times under the same conditions. However, all physicochemical characterisation of M600, with the exception of TGA was performed only on the first batch synthesised. All three batches were used for cell labelling experiments, including the labelling of MSC transplanted into animals, and the results with different batches were pooled and treated as replicates. The tight standard deviation of the iron mass loading with M600 may indicate the reproducibility of the synthesis method, but thorough characterisation of each batch will be a better proof of reproducibility.

The structure of MGIO has not been thoroughly understood through current physicochemical analysis. The 10-fold difference between diameters reported by TEM and DLS suggest that MGIO has exceptional swelling capacity, or else MGIO models are actually aggregates of different diameters. MGIO was suggested to be the first verification of theoretical MR relaxation model with a set of synthesised particles with similar composition over the sub-micron diameter range. Although MGIO may

aggregate, they are stable aggregates that are inseparable by ultrasonic agitation, unlike the inducible and dynamic aggregation of SPIO that have relaxation rates that vary with aggregate sizes (Roch, 2005).

More models of MGIO could have been synthesized with smaller separation of diameters, if not for the limited time available to experiment with different synthesis formulae. With more MGIO models, the MR relaxation models could be more thoroughly tested, especially at the inter-regime diameters. Furthermore, fMSC can be labelled with more models of MGIO with diameters between 500 to 700nm to confirm and understand the extensive uptake observed at with M600. The distribution of MGIO diameters were unimodal but were wide and overlapping between adjacent models. Post-synthesis method such as gradient centrifugation can be employed to obtain MGIO with narrowly distributed diameters, which may help to uncover the mechanism of the size-dependent uptake. The attachment of fluorosphores to MGIO will also help the analysis of their uptake mechanism. Live confocal microscopy can help to visualise cellular response to MGIO labels. For example, if endosomes and MGIO were fluorescent at two different channels, their fusion could be observed during endocytosis.

Since the zeta-potential of MGIO was never measured, the various models may have different zeta-potential especially when the proportions of MAA to EA are different. Presence of particle surface charge can alter the quantity of uptake, probably due to alternation of particle aggregation in culture medium by electrostatic repulsion. Therefore, the zeta-potential is an important property that may affect particle uptake and explain the exceptional performance of M600. Moreover, the reported DLS measurements were performed with particles suspended in water instead of culture

medium used during cell labelling. The actual and relative diameter of the various models of MGIO during cell labelling may be different, especially if the zeta-potentials were different. This means that M750 is not necessarily larger than M600 in culture medium and therefore peak uptake could be at greater diameters. Labelling for durations of 6h, 12h and 48h with analysis of cell loading and proliferations will also strengthen the choice of 24h as the optimum labelling duration.

The down regulation of cell cycle related genes due to M600-labelling may in part be due to the reagents used to synthesise MGIO. Although a month-long dialysis was performed to remove unreacted reagent from PMG, minute amounts may remain. Even polymerised monomers may be subjected to rare depolymerisation. The most dangerous reagent is EA, an irritant with an Acute Exposure Guideline Level One of 6.3 ppm according to US Environment Protection Agency. Although current evidence is inconclusive about the classification of EA as a carcinogen, its capacity to affect cellular function cannot be ruled out.

The results reported by microarray analysis may be due to transient effects of cell labelling. This can be confirmed by passaging labelled cells for cell cycle or microarray analysis. While the current analysis method has only looked at gene ontology related to mRNA expression, pathway analysis of the mRNA expression or proteomic analysis may reveal the effects of labelling. The labelled cells have not been tested in a cell migration assay such as Boyden chamber or chemotactic microfluidic device, where the remnant magnetization in MGIO may affect the motility of labelled cells.

Iron loading was increased by increasing M600 concentration in the labelling medium. No saturation of uptake was observed even at 0.2 mg/ml, suggesting that either the

saturation concentration has not been reached, or that particles were attached to cellular surface rather than internalised into fMSC. The compartmentalisation of M600 can be analysed by TEM of cells labelled at various concentrations.

MR tracking with M600 was demonstrated for up to only 5 days post-transplantation. A longer period of monitoring is required in clinical applications. The reason for rejection of the grafts was most likely the acute immune rejection of xenoantigen, and further histology analysis include staining for HLA-I and II can be carried out to confirm this. To demonstrate long term cellular tracking with MGIO, rat MSC can be labelled by M600 for allogeneic transplantation where better survival can be expected. However, rodent MSC is known to have rather different characteristics compared to their human counter part. The most probable cell source for clinical trials is autologous or allogeneic MSC, rather than xenogeneic MSC. As a compromise between graft acceptance and accuracy of the preclinical model, the labelling non-human primates MSC for allo-transplantation can also be created to determine if the rejection of M600 is species or xenograft-related. The issue of label transfer may require prior transgenic marking of transplanted cells or sex-mismatched transplantation to enable immunohistology analysis for the co-localisation of transgenic markers and MGIO. Transgenic labels are useful although some questions may remain as to the effect of transgenic labels like GFP to mammalian cell systems.

6.4 Future Directions for Research

MGIO models of more discrete diameter distribution and at more closely spaced diameters need to be developed by fine-tuning of synthesis formulae and post-synthesis purification. Further analysis by TEM is required to understand the structure

of water-suspended MGIO. Fluorophores should be conjugated to MGIO to assist localization of the particles during live confocal imaging of the uptake process or histology of animal model. Rodent or non-human primate MSC should be labelled and allo-transplanted to demonstrate if the rejection of fMSC in rats is model- or species-related. A research MR scanner with dedicated coils can be used to enable high resolution localization of small groups of M600-labelled cells and determine the minimum cell count detectable *in vivo*.

6.5 Conclusion

A new class of MGIO nanoparticles was synthesised to diameters of approximately 100 to 750nm, for the application of verification of MR relaxation models, cellular labelling and MR tracking. High iron-loading of M600 particles in fMSC was demonstrated. Despite gene expression analysis showing greater numbers of differentially regulated genes after MGIO-labelling compared to ferucarbotran-labelling, the stem cell properties of self-renewal and differentiation in culture were unaffected. The difference in gene expression may be transient and may have been the result of either differences in iron loading or particle composition. Although acute cellular death of fMSC is evident in our rat stroke model, we found imaging and histological evidence of engrafted cellular migration to a thrombotic stroke after M600-labelling. With M600, MR detection of migrated cells at the stroke site was improved. The greater detection sensitivity available with MGIO labelling of fMSC should allow better MRI tracking of small numbers of migrating stem cells. This technology could enable *in vivo* monitoring of cell therapy on standard, widely available clinical 1.5T MR scanners.

Chapter 7 Appendix

7.1 List of Overexpressed genes

Here are the lists of up and downregulated genes that have been passed the filtering process by Genespring GX. The lists have been sorted in the order of fold-change with respect to the mock-labelled control.

7.1.1 M600-Labeling Up-Regulated Genes (Top 50)

Fold Change	Affy ProbeID	Genbank	Gene Symbol	Description
13.1	1565762_at	AK074233	RABGAP1L	RAB GTPase activating protein 1-like
12.7	233800_at	AA805082	AP2B1	Adaptor-related protein complex 2, beta 1 subunit
11.5	244464_at	AA668789	UBE2E2	Ubiquitin-conjugating enzyme E2E 2 (UBC4/5 homolog, yeast)
11.3	232925_at	AU156822	EGFR	Epidermal growth factor receptor (erythroblastic leukemia viral (v-erb-b) oncogene homolog, avian)
13.1	1565762_at	AK074233	RABGAP1L	RAB GTPase activating protein 1-like
12.7	233800_at	AA805082	AP2B1	Adaptor-related protein complex 2, beta 1 subunit
11.5	244464_at	AA668789	UBE2E2	Ubiquitin-conjugating enzyme E2E 2 (UBC4/5 homolog, yeast)
11.3	232925_at	AU156822	EGFR	Epidermal growth factor receptor (erythroblastic leukemia viral (v-erb-b) oncogene homolog, avian)
7.8	1561139_at	AF086372	COMMD1	Copper metabolism (Murr1) domain containing 1
7.6	1561689_at	AL832561		MRNA; cDNA DKFZp547G1518 (from clone DKFZp547G1518)
7.5	222375_at	AW970944	PPIG	Peptidyl-prolyl isomerase G (cyclophilin G)
7.2	1560500_at	BC039395		CDNA clone IMAGE:5299346
7.1	1560474_at	BM728509	NIPBL	Nipped-B homolog (Drosophila)
6.5	238281_at	BF593928	RBMS1	RNA binding motif, single stranded interacting protein 1
5.9	244524_at	AI587332	PAX8	Paired box gene 8
5.9	242611_at	BF112104	DOCK7	Dedicator of cytokinesis 7
5.9	1570087_at	BC017431		Homo sapiens, clone IMAGE:4717361, mRNA
5.0	203665_at	NM_002133	HMOX1	heme oxygenase (decycling) 1
4.5	232704_s_at	AK025207	LRRFIP2	leucine rich repeat (in FLII) interacting protein 2
4.4	1552536_at	NM_145206	VTI1A	vesicle transport through interaction with t-SNAREs homolog 1A (yeast)
4.2	202859_x_at	NM_000584	IL8	interleukin 8
4.2	213112_s_at	N30649	SQSTM1	sequestosome 1
3.9	205680_at	NM_002425	MMP10	matrix metalloproteinase 10 (stromelysin 2)
3.7	1556373_a_at	AF086212	MGC35361	Hypothetical protein MGC35361
3.7	215907_at	AK027193	BACH2	BTB and CNC homology 1, basic leucine zipper transcription factor 2
3.5	218322_s_at	NM_016234	ACSL5	acyl-CoA synthetase long-chain family member 5
3.4	241140_at	AA702962	LMO7	LIM domain 7
3.3	239264_at	AW973078	SEC8L1	SEC8-like 1 (S. cerevisiae)
3.3	221477_s_at	BF575213	MGC5618	hypothetical protein MGC5618
3.3	1555743_s_at	U92816		
3.2	244358_at	AW372457		
3.2	239409_at	AA828280	RAP1A	RAP1A, member of RAS oncogene family
3.1	239539_at	AI291210	NEK3	NIMA (never in mitosis gene a)-related kinase 3

3.1	234449_at	AL137625		MRNA; cDNA DKFZp434O0212 (from clone DKFZp434O0212)
3.0	1562674_at	BC034299		Hypothetical gene supported by AK001966
3.0	1566207_at	BQ286789	TCEA1	transcription elongation factor A (SII), 1
3.0	233313_at	AU158316	PTPRA	Protein tyrosine phosphatase, receptor type, A
2.9	233940_at	AK022801	EML4	Echinoderm microtubule associated protein like 4
2.9	240458_at	AI242023	ITPR2	Family with sequence similarity 20, member C
2.8	239655_at	AA744843	PRDM2	PR domain containing 2, with ZNF domain
2.8	1565567_at	AF075045	STX7	Syntaxin 7
2.8	205289_at	AA583044	BMP2	bone morphogenetic protein 2
2.8	222252_x_at	AK023354	UBQLN4 ; UBQLN4P	ubiquilin 4 ; ubiquilin 4 pseudogene
2.8	233152_x_at	AL049979	TNKS	Tankyrase, TRF1-interacting ankyrin-related ADP-ribose polymerase
2.8	215791_at	AF003738	ITSN1	Intersectin 1 (SH3 domain protein)
2.8	221085_at	NM_005118	TNFSF15	tumor necrosis factor (ligand) superfamily, member 15
2.7	209875_s_at	M83248	SPP1	secreted phosphoprotein 1 (osteopontin, bone sialoprotein I, early T-lymphocyte activation 1)
2.7	1566342_at	R34841		Transcribed locus
2.7	228708_at	BF438386		Clone 25194 mRNA sequence
2.6	227188_at	AI744591	C21orf63	chromosome 21 open reading frame 63

7.1.2 M600-Labeling Down-regulated Genes (Top 50)

Fold Change	Affy ProbeID	Genbank	Gene Symbol	Description
0.23	218790_s_at	NM_018196	TMLHE	trimethyllysine hydroxylase, epsilon
0.23	223749_at	AF329836	C1QTNF2	C1q and tumor necrosis factor related protein 2
0.24	237059_at	AA423893		Transcribed locus
0.27	243705_at	AW183689	DDHD1	DDHD domain containing 1
0.30	203214_x_at	NM_001786	CDC2	cell division cycle 2, G1 to S and G2 to M
0.31	215509_s_at	AL137654	BUB1	BUB1 budding uninhibited by benzimidazoles 1 homolog (yeast)
0.31	219148_at	NM_018492	PBK	PDZ binding kinase
0.31	204558_at	NM_003579	RAD54L	RAD54-like (S. cerevisiae)
0.33	223381_at	AF326731	CDCA1	cell division cycle associated 1
0.33	207165_at	NM_012485	HMMR	hyaluronan-mediated motility receptor (RHAMM)
0.34	203755_at	NM_001211	BUB1B	BUB1 budding uninhibited by benzimidazoles 1 homolog beta (yeast)
0.35	203764_at	NM_014750	DLG7	discs, large homolog 7 (Drosophila)
0.35	225687_at	BC001068	C20orf129	chromosome 20 open reading frame 129
0.35	213599_at	BE045993	OIP5	Opa interacting protein 5
0.35	222958_s_at	AK000490	DEPDC1	DEP domain containing 1
0.36	221591_s_at	BC005004	FAM64A	family with sequence similarity 64, member A
0.36	221520_s_at	BC001651	CDCA8	cell division cycle associated 8
0.36	212142_at	AI936566	MCM4	MCM4 minichromosome maintenance deficient 4 (S. cerevisiae)
0.36	1554997_a_at	AY151286	PTGS2	prostaglandin-endoperoxide synthase 2 (prostaglandin G/H synthase and cyclooxygenase)
0.36	218009_s_at	NM_003981	PRC1	protein regulator of cytokinesis 1
0.36	229610_at	AW088063	FLJ40629	hypothetical protein FLJ40629
0.37	204146_at	BE966146	RAD51AP1	RAD51 associated protein 1
0.37	203213_at	AL524035	CDC2	Cell division cycle 2, G1 to S and G2 to M
0.37	204709_s_at	NM_004856	KIF23	kinesin family member 23
0.37	222608_s_at	AK023208	ANLN	anillin, actin binding protein (scraps homolog, Drosophila)
0.38	218542_at	NM_018131	C10orf3	chromosome 10 open reading frame 3
0.38	214710_s_at	BE407516	CCNB1	cyclin B1
0.38	220473_s_at	NM_014150	ZCCHC4	zinc finger, CCHC domain containing 4
0.39	218782_s_at	NM_014109	ATAD2	ATPase family, AAA domain containing 2

0.39	202094_at	AA648913	BIRC5	baculoviral IAP repeat-containing 5 (survivin)
0.39	237466_s_at	AW444502	HHIP	hedgehog interacting protein
0.39	229490_s_at	AW271106	IQGAP3	IQ motif containing GTPase activating protein 3
0.39	210821_x_at	BC002703	CENPA	centromere protein A, 17kDa
0.39	209709_s_at	U29343	HMMR	hyaluronan-mediated motility receptor (RHAMM)
0.39	226980_at	AK001166	DEPDC1B	DEP domain containing 1B
0.40	203418_at	NM_001237	CCNA2	cyclin A2
0.40	209714_s_at	AF213033	CDKN3	cyclin-dependent kinase inhibitor 3 (CDK2-associated dual specificity phosphatase)
0.40	205167_s_at	NM_001790	CDC25C	cell division cycle 25C
0.40	210559_s_at	D88357	CDC2	cell division cycle 2, G1 to S and G2 to M
0.41	204887_s_at	NM_014264	PLK4	polo-like kinase 4 (Drosophila)
0.41	228729_at	N90191	CCNB1	cyclin B1
0.41	210052_s_at	AF098158	TPX2	TPX2, microtubule-associated, homolog (Xenopus laevis)
0.41	201292_at	AL561834	TOP2A	topoisomerase (DNA) II alpha 170kDa
0.42	209642_at	AF043294	BUB1	BUB1 budding uninhibited by benzimidazoles 1 homolog (yeast)
0.42	204886_at	AL043646	PLK4	polo-like kinase 4 (Drosophila)
0.42	1555758_a_at	AF213040	CDKN3	cyclin-dependent kinase inhibitor 3 (CDK2-associated dual specificity phosphatase)
0.42	206364_at	NM_014875	KIF14	kinesin family member 14
0.42	209891_at	AF225416	SPBC25	spindle pole body component 25 homolog (S. cerevisiae)
0.42	223307_at	BC002551	CDCA3	cell division cycle associated 3
0.42	208079_s_at	NM_003158	STK6	serine/threonine kinase 6

7.1.3 Ferucarbotran-Labeling Up-regulated Genes

Fold Change	Affy ProbeID	Genbank	Gene Symbol	Description
11.6	244464_at	AA668789	UBE2E2	Ubiquitin-conjugating enzyme E2E 2 (UBC4/5 homolog, yeast)
4.7	241883_x_at	R54203		
4.7	1560474_at	BM728509	NIPBL	Nipped-B homolog (Drosophila)
4.3	1554195_a_at	BC021680	MGC23985	similar to AVLV472
3.0	1562674_at	BC034299		Hypothetical gene supported by AK001966
3.0	233609_at	AU145587	PTPRK	Protein tyrosine phosphatase, receptor type, K
2.7	218322_s_at	NM_016234	ACSL5	acyl-CoA synthetase long-chain family member 5
2.7	230597_at	AI963203	SLC7A3	solute carrier family 7 (cationic amino acid transporter, y+ system), member 3
2.7	207537_at	NM_002625	PFKFB1	6-phosphofructo-2-kinase/fructose-2,6-biphosphatase 1
2.6	235786_at	AI806781	RABEP1	Rabaptin, RAB GTPase binding effector protein 1
2.6	243090_at	AA534466	KIAA0427	KIAA0427
2.5	237792_at	R95743		Transcribed locus, strongly similar to XP_529427.1 PREDICTED: hypothetical protein XP_529427 [Pan troglodytes]
2.4	232164_s_at	AL137725	EPPK1	epiplakin 1
2.4	232165_at	AL137725	EPPK1	epiplakin 1
2.4	239162_at	H04394	DAPK1	Death-associated protein kinase 1
2.3	238000_at	BF195340	KIAA0265	KIAA0265 protein
2.2	242311_x_at	H37943	WHSC1	Wolf-Hirschhorn syndrome candidate 1
2.2	230538_at	AI027957	RaLP	rai-like protein
2.2	244086_at	AA872567	KIAA1363	Arylacetamide deacetylase-like 1
2.2	230188_at	AW138350	ICHTHYIN	ichthyin protein
2.2	238753_at	AI079596	FREQ	Frequenin homolog (Drosophila)
2.2	227550_at	AW242720	LOC143381	hypothetical protein LOC143381
2.2	239671_at	AV703555	CDNA FLJ31085	CDNA FLJ31085 fis, clone IMR321000037
2.2	215204_at	AU147295	SEN6	SUMO1/sentrin specific peptidase 6
2.1	231658_x_at	BG151154	LOC127295 ; LOC391209	similar to 60S ribosomal protein L36 ; similar to ribosomal protein L36; 60S ribosomal protein L36
2.1	235666_at	AA903473		Transcribed locus, moderately similar to NP_055301.1 neuronal thread protein AD7c-

NTP [Homo sapiens]				
2.1	215387_x_at	AK021505	GPC6	Glypican 6
2.1	1553990_at	BC039154	MGC21830	hypothetical protein MGC21830
2.0	238666_at	BF438300	FDFT1	Farnesyl-diphosphate farnesyltransferase 1
2.0	235084_x_at	AI809831	TRIM38	Tripartite motif-containing 38
2.0	218995_s_at	NM_001955	EDN1	endothelin 1
2.0	1557360_at	CA430402	LRPPRC	leucine-rich PPR-motif containing

7.1.4 Ferucarbotran-Labeling Down-regulated Genes

Fold Change	Affy ProbeID	Genbank	Gene Symbol	Description
0.21	1557197_a_at	AW085690	LGALS3	Lectin, galactoside-binding, soluble, 3 (galectin 3)
0.21	217053_x_at	X87175	ETV1	ets variant gene 1
0.25	240853_at	BF224109		
0.25	233522_at	AL050132		CDNA FLJ43429 fis, clone OCBBF2027511
0.27	207334_s_at	NM_003242	TGFBR2	transforming growth factor, beta receptor II (70/80kDa)
0.33	241470_x_at	R97781		Transcribed locus
0.37	209160_at	AB018580	AKR1C3	aldo-keto reductase family 1, member C3 (3-alpha hydroxysteroid dehydrogenase, type II)
0.37	207761_s_at	NM_014033	DKFZP586	
0.37	1554997_a_at	AY151286	PTGS2	prostaglandin-endoperoxide synthase 2 (prostaglandin G/H synthase and cyclooxygenase)
0.38	238533_at	AA651750	EPHA7	EPH receptor A7
0.38	211088_s_at	Z25433	PLK4	polo-like kinase 4 (Drosophila) ; polo-like kinase 4 (Drosophila)
0.39	209906_at	U62027	C3AR1	complement component 3a receptor 1
0.39	1565595_at	AU144979	SLC6A16	Solute carrier family 6, member 16
0.4	206631_at	NM_000956	PTGER2	prostaglandin E receptor 2 (subtype EP2), 53kDa
0.41	231697_s_at	AV660825	VMP1	Transmembrane protein 49
0.42	241381_at	W35132	CXorf36	chromosome X open reading frame 36
0.42	236207_at	BE083088	SSFA2	sperm specific antigen 2
0.42	231741_at	NM_005226	EDG3	endothelial differentiation, sphingolipid G-protein-coupled receptor, 3
0.46	206819_at	NM_014549	DKFZP43	
0.46	218000_s_at	NM_007350	PHLDA1	pleckstrin homology-like domain, family A, member 1
0.46	203354_s_at	AW117368	PSD3	pleckstrin and Sec7 domain containing 3
0.46	1568971_at	BE564868	C14orf135	Chromosome 14 open reading frame 135
0.46	230333_at	BE326919	SAT	Spermidine/spermine N1-acetyltransferase
0.47	244203_at	AI082507		Transcribed locus
0.47	228708_at	BF438386		Clone 25194 mRNA sequence
0.48	1553011_at	NM_153809	TAF1L	TAF1-like RNA polymerase II, TATA box binding protein (TBP)-associated factor, 210kDa
0.49	229288_at	BF439579	EPHA7	EPH receptor A7
0.49	1558706_a_at	AL831857	ATOX8	Atonal homolog 8 (Drosophila)
0.5	221440_s_at	NM_006606	RBBP9	retinoblastoma binding protein 9

7.2 Record of Experimental Animals

The following experimental groups were established to demonstrate to evaluate MR tracking with M600.

- Group 0: Verification of stroke model
- Group 1: Stroke induced, M600-fMSC injected contralaterally
- Group 2: Stroke induced, ferucarbotran-fMSC injected contralaterally
- Group 3: Stroke induced, M600-fMSC injected intravenously
- Group 4: No stroke, M600-fMSC injected
- Group 5: Stroke induced, no cells injected
- Group 6: Stroke induced, mock-labelled fMSC injected contralaterally

Group 1 and 2 are needed to demonstrate that M600-labelling improves the detection of cellular migration when compared with ferucarbotran-labelling. Group 3 is needed to show that M600-fMSC can home when delivered in a clinically-relevant route. Group 4 is a negative control on the stroke model to show that cellular homing is specific to the stroke. Group 5 is a control to show the host response to the stroke alone. Group 6 is a control to show that host response to cells alone without the effects of labels.

Group Name	Description	Rats attempted
0a	Unsuccessful stroke by MCAo	1
0b	Unsuccessful stroke by ICA ligation	2-3
0c	Stroke by photo-thrombosis	4-9
0d	Injection of 10^3 , 10^4 and 10^5 M600-fMSC	10
0e	Stroke by photo-thrombosis, T2 MRI then TTC	14
1a	Stroke induced at Day-2 $2 \cdot 10^4$ M600-fMSC injected contralaterally at Day 0 sacrificed at Day 12	11, 15, 17, 21, 29, 32, 37, 40, 46- 48, 50, 56- 59, 64, 66, 67, 70-72
1b	Same as Group 1 but animal was sacrificed at Day 1	73
1c	Same as Group 1 but animal was sacrificed at Day 5	74
2a	Stroke induced at Day-2 $2 \cdot 10^4$ ferucarbotran-fMSC injected contralaterally at Day 0 sacrificed at Day 12	12, 20, 28, 31, 43, 44, 45,
2b	Same as Group 2a but $2 \cdot 10^5$ cells injected	34
3	Stroke induced at Day -2 $2 \cdot 10^6$ M600-fMSC injected intravenously at Day 0 Sacrificed at Day 19	36, 39, 41, 49
4a	No stroke induced. $2 \cdot 10^4$ M600-fMSC injected contralaterally at Day 0 Sacrificed at Day12	18, 38, 69
4b	Same as Group 4a but $2 \cdot 10^4$ ferucarbotran-fMSC injected	33
5	Stroke induced at Day -2 No cells injected	16, 19, 25, 26, 30, 35, 62, 63, 65, 68
6	Stroke induced at Day -2 $2 \cdot 10^4$ mock-labelled fMSC injected contralaterally at Day 0 sacrificed at Day 12	75

Table 19: Record of experimental animals used in our study classified by the experimental groups.

7.3 Publications

The following publications and presentations were achieved during the preparation of this thesis.

Journal Publications

- Eddy SM Lee**, J Chan, B Shuter, LG Tan, MSK Chong, DL Ramachandra, GS Dawe, J Ding, SH Teoh, O Beuf, A Briguet, KC Tam, M Choolani, SC Wang. Microgel Iron Oxide Nanoparticles For Tracking Human Fetal Mesenchymal Stem Cells Through Magnetic Resonance Imaging. **Stem Cells** 2009;27:1921-1931 Accepted 30 Apr 2009
- Eddy SM Lee**, B. Shuter, J Chan, MSK Chong, J Ding, SH Teoh, Olivier Beuf, Andre Briguet, KC Tam, M Choolani, SC Wang. The use of Microgel Iron Oxide Nanoparticles in the Studies of Magnetic Resonance Relaxation and Endothelial Progenitor Cell Labelling. **Biomaterials** (In Press) Accepted 10 Jan 2010
- ZY Zhang, SH Teoh, MSK Chong, **Eddy SM Lee**, LG Tan, C Mattar, NM Fisk, M Choolani, J Chan. Neo-vascularization and bone formation mediated by fetal mesenchymal stem cell tissue-engineered bone grafts in critical-size femoral defects. **Biomaterials** 2010; 31; 608-620 Accepted 21 Sep 2009

Oral Presentations

- 27th International Fetal Medicine and Surgery Society (IFMSS), Athens, Greece** Sep 2008
Travel award for the presentation on "MRI Tracking of Fetal Mesenchymal Stem Cells" (Group Prize) – Best Young Investigator (Jerry Chan)
- 6th Singapore Congress in O&G, Singapore** 21 - 25 Mar 2007
2nd prize for best oral presentation on "MRI of fMSC with Microgel-Iron Oxide Particles"
- Contrast Media Research, Evian, France** Oct 2005
Awarded Young Investigator Award for oral presentation on "Biodistribution of Anionic Magnetic Nanoparticle"

Poster Presentations

- 7th Annual Meeting of the ISSCR, Barcelona, Spain** 8 - 11 Jul 2009
Poster on "MRI Tracking of Human Fetal Mesenchymal Stem Cells"
- World Molecular Imaging Congress, Nice, France** 10 - 13 Sep 2008
Poster on "In Vivo Tracking of Human Fetal Stem Cells With a Magnetic Microgel: Histological Evaluation"
- Joint Molecular Imaging Conference, Rhode Island, USA** 8 – 11 Sep 2007
Poster on "In Vivo Tracking of Human Fetal Stem Cells With a

Magnetic Microgel”

5th Annual Meeting of the ISSCR, Cairns, Australia

11 - 14 Jun 2007

Poster on “MRI of human fetal MSC using magnetic microgels on a clinical scanner”

4th Annual Meeting of Molecular Imaging, Cologne, Germany

7 - 10 Sep 2005

Poster on “Analysis of Hepatic Uptake of Anionic Magnetic Nanoparticles”

References

1. Ahrens ET, Feili-Hariri M, Xu H, Genove G and Morel PA (2003). "Receptor-mediated endocytosis of iron-oxide particles provides efficient labeling of dendritic cells for in vivo MR imaging." *Magnetic Resonance in Medicine* **49** 1006-1013.
2. Ahrens ET, Flores R, Xu H and Morel PA (2005). "In vivo imaging platform for tracking immunotherapeutic cells." *Nature Biotechnology* **23** 983-987.
3. Aime S, Carrera C, Delli CD, Geninatti CS and Terreno E (2005). "Tunable imaging of cells labeled with MRI-PARACEST agents." *Angew Chem Int Ed Engl* **44** 1813-5.
4. Almeida-Porada G, El SD, Porada C and Zanjani ED (2002). "Differentiative potential of human metanephric mesenchymal cells." *Experimental Hematology* **30** 1454-1462.
5. Aloisi F (2001). "Immune function of microglia." *Glia* **36** 165-179.
6. Al-Shahrour F, Minguez P, Tarraga J, Montaner D, Alloza E, Vaquerizas JM, Conde L, Blaschke C, Vera J and Dopazo J (2006). "BABELOMICS: a systems biology perspective in the functional annotation of genome-scale experiments." *Nucleic Acids Research* **34** W472.
7. Amsalem Y, Mardor Y, Feinberg MS, Landa N, Miller L, Daniels D, Ocherashvilli A, Holbova R, Yosef O, Barbash IM and Leor J (2007). "Iron-oxide labeling and outcome of transplanted mesenchymal stem cells in the infarcted myocardium." *Circulation* **116** I38-I45.
8. Anderson SA, Glod J, Arbab AS, Noel M, Ashari P, Fine HA and Frank JA (2005). "Noninvasive MR imaging of magnetically labeled stem cells to directly identify neovasculature in a glioma model." *Blood* **105** 420-5.
9. Apte RS, Sinha D, Mayhew E, Wistow GJ and Niederkorn JY (1998). Cutting Edge: Role of Macrophage Migration Inhibitory Factor in Inhibiting NK Cell Activity and Preserving Immune Privilege 1, *Am Assoc Immunol.* **160**: 5693-5696.
10. Aranguren XL, Luttun A, Clavel C, Moreno C, Abizanda G, Barajas MA, Pelacho B, Uriz M, Arana M and Echavarri A (2007). "In vitro and in vivo arterial differentiation of human multipotent adult progenitor cells." *Blood* **109** 2634-42.
11. Arbab AS, Bashaw LA, Miller BR, Jordan EK, Lewis BK, Kalish H and Frank JA (2003). "Characterization of biophysical and metabolic properties of cells labeled with superparamagnetic iron oxide nanoparticles and transfection agent for cellular MR imaging." *Radiology* **229** 838-846.
12. Arbab AS and Frank JA (2008). "Cellular MRI and its role in stem cell therapy." *Regen Med* **3** 199-215.
13. Arbab AS, Yocum GT, Kalish H, Jordan EK, Anderson SA, Khakoo AY, Read EJ and Frank JA (2004). "Efficient magnetic cell labeling with protamine sulfate complexed to ferumoxides for cellular MRI." *Blood* **104** 1217-1223.
14. Arbab AS, Yocum GT, Rad AM, Khakoo AY, Fellowes V, Read EJ and Frank JA (2005). "Labeling of cells with ferumoxides-protamine sulfate complexes does not inhibit function or differentiation capacity of hematopoietic or mesenchymal stem cells." *NMR Biomed* **18** 553-9.
15. Arbab AS, Janic B, Knight RA, Anderson SA, Pawelczyk E, Rad AM, Read EJ, Pandit SD and Frank JA (2008). "Detection of migration of locally implanted AC133+ stem cells

- by cellular magnetic resonance imaging with histological findings." *FASEB J.* **22** 3234-3246.
16. Arnold IC (1991). "Mesenchymal stem cells." *Journal of Orthopaedic Research* **9** 641-650.
 17. Aurich I, Mueller LP, Aurich H, Luetzkendorf J, Tisljar K, Dollinger MM, Schormann W, Walldorf J, Hengstler JG and Fleig WE (2007). "Functional integration of hepatocytes derived from human mesenchymal stem cells into mouse livers." *Gut* **56** 405-15.
 18. Baggiolini M (2001). "Chemokines in pathology and medicine." *Journal of Internal Medicine* **250** 91-104.
 19. Bajaj P, Coyal M and Chavan RB (1994). "Thermal Behavior of Methacrylic Acid-Ethyl Acrylate Copolymers." *Journal of Applied Polymer Science* **51** 423-433.
 20. Bakker CJ, Seppenwoolde JH and Vincken KL (2006). "Dephased MRI." *Magn Reson Med* **55** 92-7.
 21. Balsam LB, Wagers AJ, Christensen JL, Kofidis T, Weissman IL and Robbins RC (2004). "Haematopoietic stem cells adopt mature haematopoietic fates in ischaemic myocardium." *Nature* **428** 668-673.
 22. Banas A, Teratani T, Yamamoto Y, Tokuhara M, Takeshita F, Quinn G, Okochi H and Ochiya T (2007). "Adipose tissue-derived mesenchymal stem cells as a source of human hepatocytes." *Hepatology* **46** 219-28.
 23. Bang OY, Lee JS, Lee PH and Lee G (2005). "Autologous mesenchymal stem cell transplantation in stroke patients." *Ann Neurol* **57** 874-882.
 24. Bartholomew A, Sturgeon C, Siatskas M, Ferrer K, McIntosh K, Patil S, Hardy W, Devine S, Ucker D and Deans R (2002). "Mesenchymal stem cells suppress lymphocyte proliferation in vitro and prolong skin graft survival in vivo." *Experimental Hematology* **30** 42-48.
 25. Batlle X and Labarta A (2002). "Finite-size effects in fine particles: magnetic and transport properties." *Journal of Physics D: Applied Physics* **35** R15-R42.
 26. Bazyliński DA and Frankel RB (2004). "Magnetosome formation in prokaryotes." *Nat Rev Microbiol* **2** 217-30.
 27. Bean CP and Livingston JD (1959). "Superparamagnetism." *Journal of Applied Physics* **30** S120.
 28. Beauchamp JR, Morgan JE, Pagel CN and Partridge TA (1999). "Dynamics of Myoblast Transplantation Reveal a Discrete Minority of Precursors with Stem Cell-like Properties as the Myogenic Source." *J Cell Biol* **144** 1113-1122.
 29. Bechmann I, MOR GI, NILSEN JO, ELIZA M, NITSCH R and NAFTOLIN F (1999). "FasL (CD95L, Apo1L) Is Expressed in the Normal Rat and Human Brain." *GLIA* **27** 62-74.
 30. Bendszus M, Kleinschnitz C and Stoll G (2007). "Iron-Enhanced MRI in Ischemic Stroke: Intravascular Trapping Versus Cellular Inflammation." *Stroke* **38** e12.
 31. Benjamini Y and Hochberg Y (1995). "Controlling the false discovery rate: a practical and powerful approach to multiple testing." *Journal of the Royal Statistical Society. Series B (Methodological)* 289-300.
 32. Bennett KM, Shapiro EM, Sotak CH and Koretsky AP (2008). "Controlled Aggregation of Ferritin to Modulate MRI Relaxivity." *Biophys. J.* **95** 342-351.

33. Berry CC, Charles S, Wells S, Dalby MJ and Curtis AS (2004). "The influence of transferrin stabilised magnetic nanoparticles on human dermal fibroblasts in culture." *International Journal of Pharmaceutics* **269** 211-225.
34. Bieback K, Kern S, Kluter H and Eichler H (2004). "Critical Parameters for the Isolation of Mesenchymal Stem Cells from Umbilical Cord Blood." *Stem Cells* **22** 625.
35. Bizdoaca EL, Spasova M, Farle M, Hilgendorff M, Liz-Marzan LM and Caruso F (2003). "Self-assembly and magnetism in core-shell microspheres." *Journal of Vacuum Science and Technology, A: Vacuum, Surfaces, and Films* **21** 1515-1518.
36. Borlongan CV, Hadman M, Sanberg CD and Sanberg PR (2004). "Central nervous system entry of peripherally injected umbilical cord blood cells is not required for neuroprotection in stroke." *Stroke* **35** 2385-9.
37. Borlongan CV, Lind JG, Dillon-Carter O, Yu G, Hadman M, Cheng C, Carroll J and Hess DC (2004). "Bone marrow grafts restore cerebral blood flow and blood brain barrier in stroke rats." *Brain Research* **1010** 108-116.
38. Bowen CV, Zhang X, Saab G, Gareau PJ and Rutt BK (2002). "Application of the static dephasing regime theory to superparamagnetic iron-oxide loaded cells." *Magn Reson Med* **48** 52-61.
39. Bradley RH, Kent TA, Eisenberg HM, Quast MJ, Ward GA, Campbell GA and Hillman G (1989). "Middle cerebral artery occlusion in rats studied by magnetic resonance imaging." *Stroke* **20** 1032-1036.
40. Briel A, Gleich B, WeizeneckerJürgen, Rohrer M, Weinmann H, Pietsch H, LawaczekRüdiger, Rothe M and Thomsen J (2007). "Compositions Containing Magnetic Iron Oxide Particles, And Use Of Said Compositions In Magnetic Particle Imaging." WIPO Patent Filing WO/2007/000350.
41. Brooks RA, Moyny F and Gillis P (2001). "On T2-shortening by weakly magnetized particles: the chemical exchange model." *Magn Reson Med* **45** 1014-20.
42. Brown RJ (1993). "Some contrast agents in oil well logging and in medical MRI." *Magn Reson Med* **29** 551-2.
43. Brown RJ (1961). "Distribution of Fields from Randomly Placed Dipoles: Free-Precession Signal Decay as Result of Magnetic Grains." *Phys. Rev.* **121** 1379.
44. Alberts B, Bray D, Lewis J, Raff M, Roberts K and Watson AJD (2007). *Molecular Biology of the Cell*, Garland Publishing, Incorporated.
45. Bulte JW and Kraitchman DL (2004). "Iron oxide MR contrast agents for molecular and cellular imaging." *NMR in Biomedicine* **17** 484-499.
46. Bulte JW, Douglas T, Witwer B, Zhang SC, Strable E, Lewis BK, Zywicke H, Miller B, van GP, Moskowitz BM, Duncan ID and Frank JA (2001). "Magnetodendrimers allow endosomal magnetic labeling and in vivo tracking of stem cells." *Nat Biotech* **19** 1141-1147.
47. Bulte JW, Kraitchman DL, Mackay AM, Pittenger MF, Arbab AS, Yocum GT, Kalish H, Jordan EK, Anderson SA, Khakoo AY, Read EJ and Frank JA (2004). "Chondrogenic differentiation of mesenchymal stem cells is inhibited after magnetic labeling with ferumoxides." *Blood* **104** 3410-3413.
48. Burns TC, Ortiz-Gonzalez XR, Gutierrez-Perez M, Keene CD, Sharda R, Demorest ZL, Jiang Y, Nelson-Holte M, Soriano M and Nakagawa Y (2006). "Thymidine Analogs Are Transferred from Prelabeled Donor to Host Cells in the Central Nervous System After Transplantation: A Word of Caution." *Stem Cells* **24** 1121-1127.

49. Butcher EC (1991). "Leukocyte-endothelial cell recognition: three (or more) steps to specificity and diversity." *Cell* **67** 1033.
50. Calandra T and Roger T (2003). "Macrophage migration inhibitory factor: a regulator of innate immunity." *Nature Reviews Immunology* **3** 791-800.
51. Callera F and de Melo CM (2007). "Magnetic Resonance Tracking of Magnetically Labeled Autologous Bone Marrow CD34+ Cells Transplanted into the Spinal Cord via Lumbar Puncture Technique in Patients with Chronic Spinal Cord Injury: CD34+ Cells' Migration into the Injured Site." *Stem Cells and Development* **16** 461-466.
52. Campagnoli C, Fisk N, Overton T, Bennett P, Watts T and Roberts I (2000). "Circulating hematopoietic progenitor cells in first trimester fetal blood." *Blood* **95** 1967.
53. Campagnoli C, Roberts IA, Kumar S, Bennett PR, Bellantuono I and Fisk NM (2001). "Identification of mesenchymal stem/progenitor cells in human first-trimester fetal blood, liver, and bone marrow." *Blood* **98** 2396-402.
54. Cao F, Lin S, Xie X, Ray P, Patel M, Zhang X, Drukker M, Dylla SJ, Connolly AJ and Chen X (2006). "In vivo visualization of embryonic stem cell survival, proliferation, and migration after cardiac delivery." *Circulation* **113** 1005-14.
55. Caplan AI (1991). "Mesenchymal stem cells." *J Orthop Res* **9** 641-50.
56. Caplan AI (2005). "Review: Mesenchymal Stem Cells: Cell-Based Reconstructive Therapy in Orthopedics." *Tissue Engineering* **11** 1198-1211.
57. Carr DH, Brown J, Bydder GM, Steiner RE, Weinmann HJ, Speck U, Hall AS and Young IR (1984). "Gadolinium-DTPA as a contrast agent in MRI: initial clinical experience in 20 patients." *American Journal of Roentgenology* **143** 215-224.
58. Castro-Malaspina H, Gay RE, Resnick G, Kapoor N, Meyers P, Chiarieri D, McKenzie S, Broxmeyer HE and Moore MA (1980). "Characterization of human bone marrow fibroblast colony-forming cells (CFU-F) and their progeny." *Blood* **56** 289-301.
59. Chamberlain G, Fox J, Ashton B and Middleton J (2007). "Concise review: mesenchymal stem cells: their phenotype, differentiation capacity, immunological features, and potential for homing." *Stem cells* **25** 2739-2749.
60. Chan J, O Donoghue K, de la Fuente J, Roberts IA, Kumar S, Morgan JE and Fisk NM (2005). "Human fetal mesenchymal stem cells as vehicles for gene delivery." *Stem Cells* **23** 93-102.
61. Chan J, O Donoghue K, Gavina M, Torrente Y, Kennea N, Mehmet H, Stewart H, Watt DJ, Morgan JE and Fisk NM (2006). "Galectin-1 induces skeletal muscle differentiation in human fetal mesenchymal stem cells and increases muscle regeneration." *Stem Cells* **24** 1879-91.
62. Chan J, Waddington SN, ODonoghue K, Kurata H, Guillot PV, Gotherstrom C, Themis M, Morgan JE and Fisk NM (2007). "Widespread distribution and muscle differentiation of human fetal mesenchymal stem cells after intrauterine transplantation in dystrophic mdx mouse." *Stem Cells* **25** 875-84.
63. Chen J, Li Y, Wang L, Zhang Z, Lu D, Lu M and Chopp M (2001). "Therapeutic benefit of intravenous administration of bone marrow stromal cells after cerebral ischemia in rats." *Stroke* **32** 1005-11.
64. Chen J, Li Y, Zhang R, Katakowski M, Gautam SC, Xu Y, Lu M, Zhang Z and Chopp M (2004). "Combination therapy of stroke in rats with a nitric oxide donor and human bone marrow stromal cells enhances angiogenesis and neurogenesis." *Brain Research* **1005** 21-28.

-
65. Chen J, Zhang ZG, Li Y, Wang L, Xu YX, Gautam SC, Lu M, Zhu Z and Chopp M (2003). Intravenous Administration of Human Bone Marrow Stromal Cells Induces Angiogenesis in the Ischemic Boundary Zone After Stroke in Rats, *Am Heart Assoc.* **92**: 692-699.
 66. Chen Z and Palmer TD (2008). "Cellular repair of CNS disorders: an immunological perspective." *Human molecular genetics* **17** R84-R92.
 67. Chithrani BD, Ghazani AA and Chan WC (2006). "Determining the size and shape dependence of gold nanoparticle uptake into mammalian cells." *Nano Lett* **6** 662-668.
 68. Cho KJ, Trzaska KA, Greco SJ, McArdle J, Wang FS, Ye JH and Rameshwar P (2005). "Neurons Derived From Human Mesenchymal Stem Cells Show Synaptic Transmission and Can Be Induced to Produce the Neurotransmitter Substance P by Interleukin-1 {alpha}." *Stem Cells* **23** 383.
 69. Cobo F, Garc C, Talavera P, Ruiz-Cabello F, Bravo J and Concha A (2008). "Diffuse large B-cell lymphoma in a renal allograft associated with Epstein-Barr virus in the recipient: a case report and a review of lymphomas presenting in a transplanted kidney." *Clinical transplantation*.
 70. Cohen B, Dafni H, Meir G, Harmelin A and Neeman M (2005). "Ferritin as an endogenous MRI reporter for noninvasive imaging of gene expression in C6 glioma tumors." *Neoplasia* **7** 109-17.
 71. Cohen B, Ziv K, Plaks V, Israely T, Kalchenko V, Harmelin A, Benjamin LE and Neeman M (2007). "MRI detection of transcriptional regulation of gene expression in transgenic mice." *Nat Med* **13** 498-503.
 72. Coyne TM, Marcus AJ, Woodbury D and Black IB (2006). "Marrow stromal cells transplanted to the adult brain are rejected by an inflammatory response and transfer donor labels to host neurons and glia." *Stem Cells* **24** 2483-92.
 73. Cozzi A, Corsi B, Levi S, Santambrogio P, Albertini A and Arosio P (2000). "Overexpression of Wild Type and Mutated Human Ferritin H-chain in HeLa Cells IN VIVO ROLE OF FERRITIN FERROXIDASE ACTIVITY." *Journal of Biological Chemistry* **275** 25122-25129.
 74. Cullity BD and Cullity LC (1972). *Introduction to Magnetic Materials*. Reading, MA, Addison-Wesley.
 75. Cunningham CH, Arai T, Yang PC, McConnell MV, Pauly JM and Conolly SM (2005). "Positive contrast magnetic resonance imaging of cells labeled with magnetic nanoparticles." *Magn Reson Med* **53** 999-1005.
 76. da Silva Meirelles L, Chagastelles PC and Nardi NB (2006). "Mesenchymal stem cells reside in virtually all post-natal organs and tissues." *J Cell Sci* **119** 2204-13.
 77. Dahnke H, Liu W and Frank J (2006). Optimal positive contrast of labeled cells via conventional 3D imaging.
 78. Dahnke H and Schaeffter T (2005). "Limits of detection of SPIO at 3.0 T using T2 relaxometry." *Magn Reson Med* **53** 1202-6.
 79. Daldrup-Link HE, Meier R, Rudelius M, Piontek G, Piert M, Metz S, Settles M, Uherek C, Wels W and Schlegel J (2005). "In vivo tracking of genetically engineered, anti-HER2/neu directed natural killer cells to HER2/neu positive mammary tumors with magnetic resonance imaging." *Eur Radiol* **15** 4-13.
 80. Daldrup-Link HE, Rudelius M, Oostendorp RA, Settles M, Piontek G, Metz S, Rosenbrock H, Keller U, Heinzmann U and Rummeny EJ (2003). "Targeting of hematopoietic progenitor cells with MR contrast agents." *Radiology* **228** 760-7.

81. Davies KJ, Wells S and Charles SW (1993). "The effect of temperature and oleate adsorption on the growth of maghemite particles." *Journal of Magnetism and Magnetic Materials* **122** 24-28.
82. De Coppi P, Bartsch JG, Siddiqui MM, Xu T, Santos CC, Perin L, Mostoslavsky G, Serre AC, Snyder EY and Yoo JJ (2007). "Isolation of amniotic stem cell lines with potential for therapy." *Nature biotechnology* **25** 100.
83. de la Fuente J, O Donoghue K, Kumar S, Chan J, Fisk NM and Roberts IA (2002). "Ontogeny-related changes in integrin expression and cytokine production by fetal mesenchymal stem cells (MSC)." *Blood* **100** 526a.
84. de Vries I, Lesterhuis WJ, Barentsz JO, Verdijk P, van KJ, Boerman OC, Oyen WJ, Bonenkamp JJ, Boezeman JB and Adema GJ (2005). "Magnetic resonance tracking of dendritic cells in melanoma patients for monitoring of cellular therapy." *Nat Biotechnol* **23** 1407-1413.
85. Deans AE, Wadghiri YZ, Bernas LM, Yu X, Rutt BK and Turnbull DH (2006). "Cellular MRI contrast via coexpression of transferrin receptor and ferritin." *Magn Reson Med* **56** 51-9.
86. DiGirolamo CM, Stokes D, Colter D, Phinney DG, Class R and Prockop DJ (1999). "Propagation and senescence of human marrow stromal cells in culture: a simple colony-forming assay identifies samples with the greatest potential to propagate and differentiate." *Br J Haematol* **107** 275-281.
87. DiPpolito G, Diabira S, Howard GA, Menei P, Roos BA and Schiller PC (2004). "Marrow-isolated adult multilineage inducible (MIAMI) cells, a unique population of postnatal young and old human cells with extensive expansion and differentiation potential." *J Cell Sci* **117** 2971-81.
88. Dirnagl U, Iadecola C and Moskowitz MA (1999). "Pathobiology of ischaemic stroke: an integrated view." *Trends in Neurosciences* **22** 391-397.
89. Djouad F, Plence P, Bony C, Tropel P, Apparailly F, Sany J, Noel D and Jorgensen C (2003). "Immunosuppressive effect of mesenchymal stem cells favors tumor growth in allogeneic animals." *Blood* **102** 3837.
90. Dominici M, Le Blanc K, Mueller I, Slaper-Cortenbach I, Marini F, Krause D, Deans R, Keating A, Prockop D and Horwitz E (2006). "Minimal criteria for defining multipotent mesenchymal stromal cells. The International Society for Cellular Therapy position statement." *Cytotherapy* **8** 315 - 317.
91. Thomas ED, Blume KG, Forman SJ and Appelbaum FR (2008). *Thomas' Hematopoietic Cell Transplantation*. F. R. Appelbaum. Malden, Wiley-Blackwell.
92. Eliopoulos N, Stagg J, Lejeune L, Pommey S and Galipeau J (2005). "Allogeneic marrow stromal cells are immune rejected by MHC class I-and class II-mismatched recipient mice." *Blood* **106** 4057.
93. Erices A, Conget P and Minguell JJ (2000). "Mesenchymal progenitor cells in human umbilical cord blood." *Br J Haematol* **109** 235-42.
94. Fan QL, Neoh KG, Kang ET, Shuter B and Wang SC (2007). "Solvent-free atom transfer radical polymerization for the preparation of poly (poly (ethyleneglycol) monomethacrylate)-grafted Fe₃O₄ nanoparticles: synthesis, characterization and cellular uptake." *Biomaterials* **28** 5426-5436.
95. Farina C, Aloisi F and Meinl E (2007). "Astrocytes are active players in cerebral innate immunity." *Trends in Immunology* **28** 138-145.

-
96. Ferrara JL and Reddy P (2006). "Pathophysiology of graft-versus-host disease." *Semin Hematol* **43** 3-10.
 97. Firbank MJ, Coulthard A, Harrison RM and Williams ED (1999). "A comparison of two methods for measuring the signal to noise ratio on MR images." *Phys Med Biol* **44** N261-N264.
 98. Fischer HG and Bielinsky AK (1999). Antigen presentation function of brain-derived dendriform cells depends on astrocyte help, *Jpn Soc Immunol.* **11**: 1265-1274.
 99. Fleige G, Seeberger F, Laux D, Kresse M, Taupitz M, Pilgrimm H and Zimmer C (2002). "In vitro characterization of two different ultrasmall iron oxide particles for magnetic resonance cell tracking." *Invest Radiol* **37** 482-8.
 100. Fontaine R, Viscogliosi N, Semmaoui H, B F, Lemieux F, T MA, Michaud JB, B P, Cadorette J and Pepin CM (2007). "Digital signal processing applied to crystal identification in Positron Emission Tomography dedicated to small animals." *Nuclear Inst. and Methods in Physics Research, A* **571** 385-388.
 101. Forsmo SP (2005). "Oxidation of magnetite concentrate powders during storage and drying." *International Journal of Mineral Processing* **75** 135-144.
 102. Frank JA, Miller BR, Arbab AS, Zywicke HA, Jordan EK, Lewis BK, Bryant LH and Bulte JW (2003). "Clinically Applicable Labeling of Mammalian and Stem Cells by Combining Superparamagnetic Iron Oxides and Transfection Agents." *Radiology* **228** 480-487.
 103. Friedenstein AJ, Chailakhjan RK and Lalykina KS (1970). "The development of fibroblast colonies in monolayer cultures of guinea-pig bone marrow and spleen cells." *Cell Proliferation* **3** 393-403.
 104. Friedenstein AJ, Petrakova KV, Kurolesova AI and Frolova GP (1968). "Heterotopic of bone marrow. Analysis of precursor cells for osteogenic and hematopoietic tissues." *Transplantation* **6** 230-47.
 105. Gafni Y, Turgeman G, Liebergal M, Pelled G, Gazit Z and Gazit D (2004). "Stem cells as vehicles for orthopedic gene therapy." *Gene Ther* **11** 417-26.
 106. Gang EJ, Jeong JA, Hong SH, Hwang SH, Kim SW, Yang IH, Ahn C, Han H and Kim H (2004). Skeletal Myogenic Differentiation of Mesenchymal Stem Cells Isolated from Human Umbilical Cord Blood, *AlphaMed Press.* **22**: 617-624.
 107. Gao F, Kar S, Zhang J, Qiu B, Walczak P, Larabi M, Xue R, Frost E, Qian Z and Bulte JW (2007). "MRI of intravenously injected bone marrow cells homing to the site of injured arteries." *NMR Biomed* **20** 673-81.
 108. Geiser M, Rothen-Rutishauser B, Kapp N, Schurch S, Kreyling W, Schulz H, Semmler M, Im HV, Heyder J and Gehr P (2005). "Ultrafine particles cross cellular membranes by nonphagocytic mechanisms in lungs and in cultured cells." *Environ Health Perspect* **113** 1555-60.
 109. Ghosh P, Hawrylak N, Broadus J, Greenough WT and Lauterbur PC (1990). NMR imaging of transplanted iron oxide-labelled cells in the rat brain.
 110. Gillis P and Koenig SH (1987). "Transverse relaxation of solvent protons induced by magnetized spheres: application to ferritin, erythrocytes, and magnetite." *Magn Reson Med* **5** 323-45.
 111. Gillis P, Moiny F and Brooks RA (2002). "On T(2)-shortening by strongly magnetized spheres: a partial refocusing model." *Magn Reson Med* **47** 257-63.
 112. Goodwin HS, Bicknese AR, Chien SN, Bogucki BD, Oliver DA, Quinn CO and Wall DA (2001). "Multilineage differentiation activity by cells isolated from umbilical cord
-

- blood: Expression of bone, fat, and neural markers." *Biology of Blood and Marrow Transplantation* **7** 581-588.
113. Gossuin Y, Roch A, Muller RN and Gillis P (2000). "Relaxation induced by ferritin and ferritin-like magnetic particles: The role of proton exchange." *Magnetic Resonance in Medicine* **43** 237-243.
114. Gotherstrom C, Ringden O, Tammik C, Zetterberg E, Westgren M and Le BK (2004). "Immunologic properties of human fetal mesenchymal stem cells." *Am J Obstet Gynecol* **190** 239-45.
115. Gotherstrom C, Ringden O, Westgren M, Tammik C and Le BK (2003). "Immunomodulatory effects of human foetal liver-derived mesenchymal stem cells." *Bone Marrow Transplant* **32** 265-72.
116. Grabill C, Silva AC, Smith SS, Koretsky AP and Rouault TA (2003). "MRI detection of ferritin iron overload and associated neuronal pathology in iron regulatory protein-2 knockout mice." *Brain Research* **971** 95-106.
117. Grabowski M, Johansson BB and Brundin P (1994). "Survival of fetal neocortical grafts implanted in brain infarcts of adult rats: the influence of postlesion time and age of donor tissue." *Exp Neurol* **127** 126-36.
118. Groman EV, Josephson L and Lewis JM (1989). "Biologically degradable superparamagnetic materials for use in clinical applications." US Patent **4827945** Section 7.1.
119. Guillot PV, Abass O, Bassett JH, Shefelbine SJ, Bou-Gharios G, Chan J, Kurata H, Williams GR, Polak J and Fisk NM (2008). "Intrauterine transplantation of human fetal mesenchymal stem cells from first-trimester blood repairs bone and reduces fractures in osteogenesis imperfecta mice." *Blood* **111** 1717-25.
120. Guillot PV, Gotherstrom C, Chan J, Kurata H and Fisk NM (2007). "Human First-Trimester Fetal MSC Express Pluripotency Markers and Grow Faster and Have Longer Telomeres Than Adult MSC." *Stem Cells* **25** 646-654.
121. Guo C, Haider HK, Shim WS, Tan RS, Ye L, Jiang S, Law PK, Wong P and Sim EK (2007). "Myoblast-based cardiac repair: xenomyoblast versus allomyoblast transplantation." *J Thorac Cardiovasc Surg* **134** 1332-9.
122. Guzman R, Uchida N, Bliss TM, He D, Christopherson KK, Stellwagen D, Capela A, Greve J, Malenka RC and Moseley ME (2007). "Long-term monitoring of transplanted human neural stem cells in developmental and pathological contexts with MRI." *Proc Natl Acad Sci US A* **104** 10211-6.
123. Haacke M, Brown R, Thompson M, Venkatesan R, Haacke M, Brown R, Thompson M and Venkatesan R (1999). *Magnetic Resonance Imaging: Physical Principles and Sequence Design*, Wiley-Liss.
124. Hallikas O, Palin K, Sinjushina N, Rautiainen R, Partanen J, Ukkonen E and Taipale J (2006). "Genome-wide prediction of mammalian enhancers based on analysis of transcription-factor binding affinity." *Cell* **124** 47-59.
125. Hann IM, Bodger MP and Hoffbrand AV (1983). "Development of pluripotent hematopoietic progenitor cells in the human fetus." *Blood* **62** 118.
126. Harrison PM and Arosio P (1996). "The ferritins: molecular properties, iron storage function and cellular regulation." *BBA-Bioenergetics* **1275** 161-203.
127. Harrower TP, Richards A, Cruz G, Copeman L, Dunnett SB and Barker RA (2004). "Complement regulatory proteins are expressed at low levels in embryonic human, wild type and transgenic porcine neural tissue." *Xenotransplantation* **11** 60-71.

128. Harush-Frenkel O, Debotton N, Benita S and Altschuler Y (2007). "Targeting of nanoparticles to the clathrin-mediated endocytic pathway." *Biochemical and Biophysical Research Communications* **353** 26-32.
129. Heyn C, Bowen CV, Rutt BK and Foster PJ (2005). "Detection threshold of single SPIO-labeled cells with FIESTA." *Magn Reson Med* **53** 312-20.
130. Heyn C, Ronald JA, Mackenzie LT, MacDonald IC, Chambers AF, Rutt BK and Foster PJ (2006). "In Vivo Magnetic Resonance Imaging of Single Cells in Mouse Brain with Optical Validation." *Magn Reson Med* **55** 23.
131. Hickey WF, Hsu BL and Kimura H (1991). "T-lymphocyte entry into the central nervous system." *Journal of Neuroscience Research* **28** 254-260.
132. Hill JM, Dick AJ, Raman VK, Thompson RB, Yu ZX, Hinds KA, Pessanha BS, Guttman MA, Varney TR and Martin BJ (2003). "Serial cardiac magnetic resonance imaging of injected mesenchymal stem cells." *Circulation* **108** 1009.
133. Himmelreich U, Weber R, Ramos-Cabrer P, Wegener S, Kandal K, Shapiro EM, Koretsky AP and Hoehn M (2005). "Improved stem cell MR detectability in animal models by modification of the inhalation gas." *Mol Imaging* **4** 104-9.
134. Hinds KA, Hill JM, Shapiro EM, Laukkanen MO, Silva AC, Combs CA, Varney TR, Balaban RS, Koretsky AP and Dunbar CE (2003). "Highly efficient endosomal labeling of progenitor and stem cells with large magnetic particles allows magnetic resonance imaging of single cells." *Blood* **102** 867-72.
135. Hocht-Zeisberg E, Kahnert H, Guan K, Wulf G, Hemmerlein B, Schlott T, Tenderich G, Korfer R, Raute-Kreinsen U and Hasenfuss G (2004). "Cellular repopulation of myocardial infarction in patients with sex-mismatched heart transplantation." *Eur Heart J* **25** 749-58.
136. Hoehn M, Kustermann E, Blunk J, Wiedermann D, Trapp T, Wecker S, Focking M, Arnold H, Hescheler J and Fleischmann BK (2002). "Monitoring of implanted stem cell migration in vivo: A highly resolved in vivo magnetic resonance imaging investigation of experimental stroke in rat." *Proceedings of the National Academy of Sciences* **99** 16267-16272.
137. Honeczarenko M, Le Y, Swierkowski M, Ghiran I, Glodek AM and Silberstein LE (2006). "Human bone marrow stromal cells express a distinct set of biologically functional chemokine receptors." *Stem Cells* **24** 1030-41.
138. Horwitz EM, Gordon PL, Koo WK, Marx JC, Neel MD, McNall RY, Muul L and Hofmann T (2002). "Isolated allogeneic bone marrow-derived mesenchymal cells engraft and stimulate growth in children with osteogenesis imperfecta: Implications for cell therapy of bone." *Proc Natl Acad Sci US A* **99** 8932-7.
139. Horwitz EM, Le BK, Dominici M, Mueller I, Slaper-Cortenbach I, Marini FC, Deans RJ, Krause DS and Keating A (2005). "Clarification of the nomenclature for MSC: The International Society for Cellular Therapy position statement." *Cytotherapy* **7** 393-395.
140. Horwitz EM, Prockop DJ, Fitzpatrick LA, Koo WW, Gordon PL, Neel M, Sussman M, Orchard P, Marx JC and Pyeritz RE (1999). "Transplantability and therapeutic effects of bone marrow-derived mesenchymal cells in children with osteogenesis imperfecta." *Nat Med* **5** 309-13.
141. Horwitz EM, Prockop DJ, Gordon PL, Koo WW, Fitzpatrick LA, Neel MD, McCarville ME, Orchard PJ, Pyeritz RE and Brenner MK (2001). "Clinical responses to bone marrow transplantation in children with severe osteogenesis imperfecta." *Blood* **97** 1227-1231.

142. Houghton J, Stoicov C, Nomura S, Rogers AB, Carlson J, Li H, Cai X, Fox JG, Goldenring JR and Wang TC (2004). "Gastric cancer originating from bone marrow-derived cells." *Science (New York, NY)* **306** 1568.
143. Hsiao JK, Tai MF, Chu HH, Chen ST, Li H, Lai DM, Hsieh ST, Wang JL and Liu HM (2007). "Magnetic nanoparticle labeling of mesenchymal stem cells without transfection agent: cellular behavior and capability of detection with clinical 1.5 T magnetic resonance at the single cell level." *Magnetic Resonance in Medicine* **58** 717.
144. Hu Y, Liao L, Wang Q, Ma L, Ma G, Jiang X and Zhao RC (2003). "Isolation and identification of mesenchymal stem cells from human fetal pancreas." *The Journal of Laboratory and Clinical Medicine* **141** 342-349.
145. Huang J, Upadhyay UM and Tamargo RJ (2006). "Inflammation in stroke and focal cerebral ischemia." *Surgical neurology* **66** 232.
146. Hunter RJ (1995). *Foundations of colloid science*. Oxford, Clarendon Press.
147. Hyeon T, Lee SS, Park J, Chung Y and Na HB (2001). "Synthesis of highly crystalline and monodisperse maghemite nanocrystallites without a size-selection process." *Journal of the American Chemical Society* **123** 12798-12801.
148. Imbeaud S, Graudens E, Boulanger V, Barlet X, Zaborski P, Eveno E, Mueller O, Schroeder A and Auffray C (2005). "Towards standardization of RNA quality assessment using user-independent classifiers of microcapillary electrophoresis traces." *Nucleic Acids Res* **33** e56.
149. in't Anker PS, Scherjon SA, C KK, de Groot-Swings GM, Claas FH, Fibbe WE and Kanhai HH (2004). "Isolation of Mesenchymal Stem Cells of Fetal or Maternal Origin from Human Placenta." **22** 1338-1345.
150. Ingram DA, Caplice NM and Yoder MC (2005). "Unresolved questions, changing definitions, and novel paradigms for defining endothelial progenitor cells." *Blood* **106** 1525-1531.
151. Irons H, Lind JG, Wakade CG, Yu G, Hadman M, Carroll J, Hess DC and Borlongan CV (2004). "Intracerebral xenotransplantation of GFP mouse bone marrow stromal cells in intaCell Transplantation and stroke rat brain: graft survival and immunologic response." *Cell Transplant* **13** 283-294.
152. Ishikawa T, Nakazaki H, Yasukawa A, Kandori K and Seto M (1998). "Structure and properties of magnetite formed in the presence of nickel (II) ions." *Materials Research Bulletin* **33** 1609-1619.
153. Jake J (1995). "Regularized Positive Exponential Sum (REPES) Program - A Way of Inverting Laplace Transform Data Obtained by Dynamic Light Scattering." *Collection of Czechoslovak Chemical Communications* **60** 1781-1797.
154. Javazon EH, Beggs KJ and Flake AW (2004). "Mesenchymal stem cells: paradoxes of passaging." *Experimental Hematology* **32** 414-425.
155. Jendelova P, Herynek V, DeCroos J, Glogarova K, Andersson B, Hajek M and Sykova E (2003). "Imaging the fate of implanted bone marrow stromal cells labeled with superparamagnetic nanoparticles." *Magn Reson Med* **50** 767-76.
156. Jendelova P, Herynek V, Urdzikova L, Glogarova K, Kroupova J, Andersson B, Bryja V, Burian M, Hajek M and Sykova E (2004). "Magnetic resonance tracking of transplanted bone marrow and embryonic stem cells labeled by iron oxide nanoparticles in rat brain and spinal cord." *J Neurosci Res* **76** 232-43.
157. Jiang Y, Jahagirdar BN, Reinhardt RL, Schwartz RE, Keene CD, Ortiz-Gonzalez XR, Reyes M, Lenvik T, Lund T, Blackstad M, Du J, Aldrich S, Lisberg A, Low WC,

- Largaespada DA and Verfaillie CM (2002). "Pluripotency of mesenchymal stem cells derived from adult marrow." *Nature* **418** 41-49.
158. Jung CW and Jacobs P (1995). "Physical and chemical properties of superparamagnetic iron oxide MR contrast agents: Ferumoxides, ferumoxtran, ferumoxsil." *Magnetic Resonance Imaging* **13** 661-674.
159. Kawaguchi H, Koiwai N, Ohtsuka Y, Miyamoto M and Sasakawa S (1986). "Phagocytosis of latex particles by leucocytes. I. Dependence of phagocytosis on the size and surface potential of particles." *Biomaterials* **7** 61-66.
160. Kelly S, Bliss TM, Shah AK, Sun GH, Ma M, Foo WC, Masel J, Yenari MA, Weissman IL and Uchida N (2004). "Transplanted human fetal neural stem cells survive, migrate, and differentiate in ischemic rat cerebral cortex." *Proceedings of the National Academy of Sciences* **101** 11839-11844.
161. Kennan RP, Zhong J and Gore JC (1994). "Intravascular susceptibility contrast mechanisms in tissues." *Magn Reson Med* **31** 9-21.
162. Kennea NL, Fisk NM, Edwards AD and Mehmet H (2003). "Neural cell differentiation of fetal mesenchymal stem cells." *Early Hum Dev* **73** 121a-122a.
163. Kennea N, Waddington SN, Chan J, Keelin O'Donoghue, Yeung D, Taylor DL, Al-Allaf FA, Pirianov G, Themis M, Edwards AD, Fisk NM and Mehmet H (2009). "Differentiation Of Human Fetal Mesenchymal Stem Cells Into Cells With An Oligodendrocyte Phenotype." *Cell Cycle* **8** 1069-1079.
164. Kim DK, Mikhaylova M, Zhang Y and Muhammed M (2003). "Protective coating of superparamagnetic iron oxide nanoparticles." *Chemistry of materials* **15** 1617-1627.
165. Kim GW, Sugawara T and Chan PH (2000). "Involvement of oxidative stress and caspase-3 in cortical infarction after photothrombotic ischemia in mice." *Journal of cerebral blood flow and metabolism: official journal of the International Society of Cerebral Blood Flow and Metabolism* **20** 1690.
166. Kim H (2008). Comparison of the Biological Properties of Human Mesenchymal Stem Cells Labeled with Different Iron Oxide Nanoparticles. World Molecular Imaging Conference, Nice, France, Poster No. 1071.
167. Kleinschnitz C, Bendszus M, Frank M, Solymosi L, Toyka KV and Stoll G (2003). "In Vivo Monitoring of Macrophage Infiltration in Experimental Ischemic Brain Lesions by Magnetic Resonance Imaging." *Journal of Cerebral Blood Flow & Metabolism* **23** 1356-1361.
168. Kleinschnitz C, Sch A, N I, Horn T, Frank M, Solymosi L, Stoll G and Bendszus M (2005). "In vivo detection of developing vessel occlusion in photothrombotic ischemic brain lesions in the rat by iron particle enhanced MRI." *Journal of Cerebral Blood Flow & Metabolism* **25** 1548-1555.
169. Ko IK, Song HT, Cho EJ, Lee ES, Huh YM and Suh JS (2007). "In vivo MR imaging of tissue-engineered human mesenchymal stem cells transplanted to mouse: a preliminary study." *Ann Biomed Eng* **35** 101-8.
170. Koc ON, Gerson SL, Cooper BW, Dyhouse SM, Haynesworth SE, Caplan AI and Lazarus HM (2000). "Rapid hematopoietic recovery after coinfusion of autologous-blood stem cells and culture-expanded marrow mesenchymal stem cells in advanced breast cancer patients receiving high-dose chemotherapy." *J Clin Oncol* **18** 307-16.
171. Kooi ME, Cappendijk VC, Cleutjens K, Kessels AG, Kitslaar P, Borgers M, Frederik PM, Daemen M and van EJ (2003). Accumulation of Ultrasmall Superparamagnetic

- Particles of Iron Oxide in Human Atherosclerotic Plaques Can Be Detected by In Vivo Magnetic Resonance Imaging, *Am Heart Assoc.* **107**: 2453-2458.
172. Kostura L, Kraitchman DL, Mackay AM, Pittenger MF and Bulte JW (2004). "Feridex labeling of mesenchymal stem cells inhibits chondrogenesis but not adipogenesis or osteogenesis." *NMR in Biomedicine* **17** 513-517.
173. Kraitchman DL, Heldman AW, Atalar E, Amado LC, Martin BJ, Pittenger MF, Hare JM and Bulte JW (2003). "In vivo magnetic resonance imaging of mesenchymal stem cells in myocardial infarction." *Circulation* **107** 2290-3.
174. Kraitchman DL, Tatsumi M, Gilson WD, Ishimori T, Kedziorek D, Walczak P, Segars WP, Chen HH, Fritzges D and Izbudak I (2005). "Dynamic imaging of allogeneic mesenchymal stem cells trafficking to myocardial infarction." *Circulation* **112** 1451-61.
175. Krampera M, Glennie S, Dyson J, Scott D, Laylor R, Simpson E and Dazzi F (2003). "Bone marrow mesenchymal stem cells inhibit the response of naive and memory antigen-specific T cells to their cognate peptide." *Blood* **101** 3722.
176. Krampera M, Pasini A, Pizzolo G, Cosmi L, Romagnani S and Annunziato F (2006). "Regenerative and immunomodulatory potential of mesenchymal stem cells." *Current opinion in pharmacology* **6** 435.
177. Kuhlper R, Dahnke H, Matuszewski L, Persigehl T, von WA, Allkemper T, Heindel WL, Schaeffter T and Bremer C (2007). "R2 and R2* mapping for sensing cell-bound superparamagnetic nanoparticles: in vitro and murine in vivo testing." *Radiology* **245** 449.
178. Lai E and van ZJ (2001). "Monitoring DNA/Poly-L-Lysine Polyplex Formation with Time-Resolved Multiangle Laser Light Scattering." *Biophysical Journal* **80** 864-873.
179. Laurent S, Forge D, Port M, Roch A, Robic C, Vander EL and Muller RN (2008). "Magnetic iron oxide nanoparticles: synthesis, stabilization, vectorization, physicochemical characterizations, and biological applications." *Chemical reviews* **108** 2064.
180. Lawrence JM, Morris RJ, Wilson DJ and Raisman G (1990). "Mechanisms of allograft rejection in the rat brain." *Neuroscience* **37** 431-62.
181. Lazarus HM, Haynesworth SE, Gerson SL, Rosenthal NS and Caplan AI (1995). "Ex vivo expansion and subsequent infusion of human bone marrow-derived stromal progenitor cells (mesenchymal progenitor cells): implications for therapeutic use." *Bone Marrow Transplant* **16** 557-64.
182. Lazarus HM, Koc ON, Devine SM, Curtin P, Maziarz RT, Holland HK, Shpall EJ, McCarthy P, Atkinson K and Cooper BW (2005). "Cotransplantation of HLA-identical sibling culture-expanded mesenchymal stem cells and hematopoietic stem cells in hematologic malignancy patients." *Biology of blood and marrow transplantation: journal of the American Society for Blood and Marrow Transplantation* **11** 389.
183. Le Blanc K, Frassoni F, Ball L, Locatelli F, Roelofs H, Lewis I, Lanino E, Sundberg B, Bernardo ME and Remberger M (2008). "Mesenchymal stem cells for treatment of steroid-resistant, severe, acute graft-versus-host disease: a phase II study." *Lancet* **371** 1579.
184. Le Blanc K, Götherström C, Ringden O, Hassan M, McMahon R, Horwitz E, Anneren G, Axelsson O, Nunn J and Ewald U (2005). "Fetal Mesenchymal Stem-Cell Engraftment in Bone after In Utero Transplantation in a Patient with Severe Osteogenesis Imperfecta." *Transplantation* **79** 1607-1614.

185. Le Blanc K and Ringden O (2007). "Immunomodulation by mesenchymal stem cells and clinical experience." *J Intern Med* **262** 509-25.
186. Le Blanc K, Tammik C, Rosendahl K, Zetterberg E and Ringd O (2003). "HLA expression and immunologic properties of differentiated and undifferentiated mesenchymal stem cells." *Experimental Hematology* **31** 890-896.
187. Lee H, Lee E, Kim K, Jang NK, Jeong YY and Jon S (2006). "Antibiofouling polymer-coated superparamagnetic iron oxide nanoparticles as potential magnetic resonance contrast agents for in vivo cancer imaging." *J Am Chem Soc* **128** 7383-9.
188. Lee OK, Kuo TK, Chen WM, Lee KD, Hsieh SL and Chen TH (2004). "Isolation of multipotent mesenchymal stem cells from umbilical cord blood." *Blood* **103** 1669.
189. Lee ST, Jang JH, Cheong JW, Kim JS, Maeng HY, Hahn JS, Ko YW and Min YH (2002). "Treatment of high-risk acute myelogenous leukaemia by myeloablative chemoradiotherapy followed by co-infusion of T cell-depleted haematopoietic stem cells and culture-expanded marrow." *British Journal of Haematology* **118** 1128-1131.
190. Lee Y, Lee J, Bae CJ, Park JG, Noh HJ, Park JH and Hyeon T (2005). "Large-scale synthesis of uniform and crystalline magnetite nanoparticles using reverse micelles as nanoreactors under reflux conditions." *Advanced Functional Materials* **15** 503-509.
191. Lewin M, Carlesso N, Tung CH, Tang XW, Cory D, Scadden DT and Weissleder R (2000). "Tat peptide-derivatized magnetic nanoparticles allow in vivo tracking and recovery of progenitor cells." *Nature Biotechnology* **18** 410-414.
192. Li Y, Chen J, Chen XG, Wang L, Gautam SC, Xu YX, Katakowski M, Zhang LJ, Lu M and Janakiraman N (2002). "Human marrow stromal cell therapy for stroke in rat: neurotrophins and functional recovery." *Neurology* **59** 514-23.
193. Li Y, Chen J, Wang L, Lu M and Chopp M (2001). "Treatment of stroke in rat with intracarotid administration of marrow stromal cells." *Neurology* **56** 1666-72.
194. Lin CL, Lee CF and Chiu WY (2005). "Preparation and properties of poly (acrylic acid) oligomer stabilized superparamagnetic ferrofluid." *Journal of Colloid And Interface Science* **291** 411-420.
195. Lineweaver H and Burk D (1934). "The Determination of Enzyme Dissociation Constants." *Journal of the American Chemical Society* **56** 658-666.
196. Liu G, Molas M, Grossmann GA, Pasumarthy M, Perales JC, Cooper MJ and Hanson RW (2001). "Biological Properties of Poly-l-lysine-DNA Complexes Generated by Cooperative Binding of the Polycation." *Journal of Biological Chemistry* **276** 34379-34387.
197. Liu H, Honmou O, Harada K, Nakamura K, Houkin K, Hamada H and Kocsis JD (2006). "Neuroprotection by PIGF gene-modified human mesenchymal stem cells after cerebral ischaemia." *Brain* **129** 2734-45.
198. Liu W, Dahnke H, Jordan EK, Schaeffter T and Frank JA (2007). "In vivo MRI using positive-contrast techniques in detection of cells labeled with superparamagnetic iron oxide nanoparticles." *NMR Biomed.*
199. Longa EZ, Weinstein PR, Carlson S and Cummins R (1989). "Reversible middle cerebral artery occlusion without craniectomy in rats." *Stroke; a journal of cerebral circulation* **20** 84.
200. Lu D, Mahmood A, Qu C, Hong X, Kaplan D and Chopp M (2007). "Collagen Scaffolds Populated with Human Marrow Stromal Cells Reduce Lesion Volume and Improve Functional Outcome after Traumatic Brain Injury." **63** 596-603.

201. Lunde K, Solheim S, Aakhus S, Arnesen H, Abdelnoor M, Egeland T, Endresen K, Ilebakk A, Mangschau A and Fjeld JG (2006). "Intracoronary injection of mononuclear bone marrow cells in acute myocardial infarction." *N Engl J Med* **355** 1199-209.
202. Macek M, Rezacova D and Kotasek A (1973). "[Smear method of collection and cultivation of embryonal and fetal tissue]." *Cesk Pediatr* **28** 281-3.
203. Mailander V, Lorenz MR, Holzzapfel V, Musyanovych A, Fuchs K, Wiesneth M, Walther P, Landfester K and Schrezenmeier H (2008). "Carboxylated Superparamagnetic Iron Oxide Particles Label Cells Intracellularly Without Transfection Agents." *Molecular Imaging and Biology* **10** 138-146.
204. Maity D, Choo SG, Yi J, Ding J and Xue JM (2008). "Synthesis of magnetite nanoparticles via a solvent-free thermal decomposition route." *Journal of Magnetism and Magnetic Materials* **321** 1256-1259.
205. Mani V, Briley-Saebo KC, Itskovich VV, Samber DD and Fayad ZA (2006). "Gradient echo acquisition for superparamagnetic particles with positive contrast (GRASP): sequence characterization in membrane and glass superparamagnetic iron oxide phantoms at 1.5 T and 3T." *Magn Reson Med* **55** 126-35.
206. Mareschi K, Biasin E, Piacibello W, Aglietta M, Madon E and Fagioli F (2001). "Isolation of human mesenchymal stem cells: bone marrow versus umbilical cord blood." *Haematologica* **86** 1099.
207. Mason DW, Charlton HM, Jones AJ, Lavy CB, Puklavec M and Simmonds SJ (1986). "The fate of allogeneic and xenogeneic neuronal tissue transplanted into the third ventricle of rodents." *Neuroscience* **19** 685-694.
208. Massa PT, Ozato K and McFarlin DE (1993). "Cell type-specific regulation of major histocompatibility complex(MHC) Class I gene expression in astrocytes, oligodendrocytes, and neurons." *Glia* **8** 201-207.
209. Massart R (1981). "Preparation of aqueous magnetic liquids in alkaline and acidic media." *Magnetics, IEEE Transactions on* **17** 1247-1248.
210. Matuszewski L, Persigehl T, Wall A, Schwindt W, Tombach B, Fobker M, Poremba C, Ebert W, Heindel W and Bremer C (2005). "Cell Tagging with Clinically Approved Iron Oxides: Feasibility and Effect of Lipofection, Particle Size, and Surface Coating on Labeling Efficiency." *Radiology* **235** 155-161.
211. Maurer JJ, Eustace DJ and Ratcliffe CT (1987). "Thermal characterization of poly(acrylic acid)." *Macromolecules* **20** 196-202.
212. Medawar PB (1948). "The fate of skin homografts transplanted to the brain, to subcutaneous tissue, and to the anterior chamber of the eye." *Br. J. Exp. Pathol* **29** 58-69.
213. Mendonca DM and Lauterbur PC (1986). "Ferromagnetic particles as contrast agents for magnetic resonance imaging of liver and spleen." *Magnetic resonance in medicine: official journal of the Society of Magnetic Resonance in Medicine/Society of Magnetic Resonance in Medicine* **3** 328-330.
214. Mendonca ML, Freitas GR, Silva SA, Manfrim A, Falcao CH, Gonzales C, Andre C, Dohmann HF, Borojevic R and Otero RM (2006). "Safety of intra-arterial autologous bone marrow mononuclear cell transplantation for acute ischemic stroke." *Arq Bras Cardiol* **86** 52-5.
215. Menzies SA, Hoff JT and Betz AL (1992). "Middle cerebral artery occlusion in rats: a neurological and pathological evaluation of a reproducible model." *Neurosurgery* **31** 100.

216. Metz S, Bonaterra G, Rudelius M, Settles M, Rummeny EJ and Daldrup-Link HE (2004). "Capacity of human monocytes to phagocytose approved iron oxide MR contrast agents in vitro." *Eur Radiol* **14** 1851-8.
217. Meyer GP, Wollert KC, Lotz J, Steffens J, Lippolt P, Fichtner S, Hecker H, Schaefer A, Arseniev L, Hertenstein B, Ganser A and Drexler H (2006). "Intracoronary Bone Marrow Cell Transfer After Myocardial Infarction: Eighteen Months' Follow-Up Data From the Randomized, Controlled BOOST (BOne marrOw transfer to enhance ST-elevation infarct regeneration) Trial." *Circulation* **113** 1287-1294.
218. Mills PH, Wu YJ, Ho C and Ahrens ET (2008). "Sensitive and automated detection of iron-oxide-labeled cells using phase image cross-correlation analysis." *Magnetic resonance imaging*.
219. Modo M, Cash D, Mellodew K, Williams SC, Fraser SE, Meade TJ, Price J and Hodges H (2002). "Tracking transplanted stem cell migration using bifunctional, contrast agent-enhanced, magnetic resonance imaging." *Neuroimage* **17** 803-11.
220. Modo M, Rezaie P, Heuschling P, Patel S, Male DK and Hodges H (2002). "Transplantation of neural stem cells in a rat model of stroke: assessment of short-term graft survival and acute host immunological response." *Brain Research* **958** 70-82.
221. Montet-Abou K, Montet X, Weissleder R and Josephson L (2007). "Cell internalization of magnetic nanoparticles using transfection agents." *Mol Imaging* **6** 1-9.
222. Moore A, Josephson L, Bhorade RM, Basilion JP and Weissleder R (2001). "Human transferrin receptor gene as a marker gene for MR imaging." *Radiology* **221** 244-50.
223. Moore A, Weissleder R and Bogdanov A (1997). "Uptake of Dextran-Coated Monocrystalline Iron Oxides in Tumor Cells and Macrophages." *Journal of Magnetic Resonance Imaging* **7** 1140-1145.
224. Morup S, Bodker F, Hendriksen PV and Linderorth S (1995). "Spin-glass-like ordering of the magnetic moments of interacting nanosized maghemite particles." *Physical Review B: Condensed Matter* **52** 287-294.
225. Muller FJ, Laurent LC, Kostka D, Ulitsky I, Williams R, Lu C, Park IH, Rao MS, Shamir R, Schwartz PH, Schmidt NO and Loring JF (2008). "Regulatory networks define phenotypic classes of human stem cell lines." *Nature* **455** 401-405.
226. Muller RN, Gillis P, Moyny F and Roch A (1991). "Transverse relaxivity of particulate MRI contrast media: from theories to experiments." *Magn Reson Med* **22** 178-82.
227. Muller WA (1995). "The role of PECAM-1 (CD31) in leukocyte emigration: studies in vitro and in vivo." *Journal of leukocyte biology* **57** 523.
228. Muraglia A (2000). Clonal mesenchymal progenitors from human bone marrow differentiate in vitro according to a hierarchical model. **113**: 1161-1166.
229. Murbe J, Rechtenbach A and Tjörg (2008). "Synthesis and physical characterization of magnetite nanoparticles for biomedical applications." *Materials Chemistry and Physics* **110** 426-433.
230. Murry CE, Soonpaa MH, Reinecke H, Nakajima H, Nakajima HO, Rubart M, Pasumarthi KB, Ismail VJ, Bartelmez SH, Poppa V, Bradford G, Dowell JD, Williams DA and Field LJ (2004). "Haematopoietic stem cells do not transdifferentiate into cardiac myocytes in myocardial infarcts." *Nature* **428** 664-668.
231. Myriam Ricarda Lorenza,b, Verena Holzapfelb, Anna Musyanovychb (2008). "Uptake of functionalized, fluorescent-labeled polymeric particles in." .

-
232. Nasef A, Ashammakhi N and Fouillard L (2008). "Immunomodulatory effect of mesenchymal stromal cells: possible mechanisms." *Regen. Med.* **3** 531-546.
233. Nath N, Hyun J, Ma H and Chilkoti A (2004). "Surface engineering strategies for control of protein and cell interactions." *Surface Science* **570** 98-110.
234. Nayak S and Lyon LA (2005). "Soft nanotechnology with soft nanoparticles." *Angewandte Chemie (International ed. in English)* **44** 7686.
235. Nelson GN, Roh JD, Mirensky TL, Wang Y, Yi T, Tellides G, Pober JS, Shkarin P, Shapiro EM, Saltzman WM, Papademetris X, Fahmy TM and Breuer CK (2008). "Initial evaluation of the use of USPIO cell labeling and noninvasive MR monitoring of human tissue-engineered vascular grafts in vivo." *FASEB J.* **22** 3888-3895.
236. Nelson KL, Gifford LM, Lauber-Huber C, Gross CA and Lasser TA (1995). "Clinical safety of gadopentetate dimeglumine." *Radiology* **196** 439-443.
237. Nelson PT, Kondziolka D, Wechsler L, Goldstein S, Gebel J, DeCesare S, Elder EM, Zhang PJ, Jacobs A and McGrogan M (2002). "Clonal human (hNT) neuron grafts for stroke therapy: neuropathology in a patient 27 months after implantation." *Am J Pathol* **160** 1201-6.
238. Neri M, Maderna C, Cavazzin C, Deidda-Vigoriti V, Politi LS, Scotti G, Marzola P, Sbarbati A, Vescovi AL and Gritti A (2008). "Efficient In Vitro Labeling of Human Neural Precursor Cells with Superparamagnetic Iron Oxide Particles: Relevance for In Vivo Cell Tracking." *Stem Cells* **26** 505-516.
239. Niederkorn JY (2006). "See no evil, hear no evil, do no evil: the lessons of immune privilege." *Nature Immunology* **7** 354-359.
240. Nimmerjahn A, Kirchhoff F and Helmchen F (2005). Resting Microglial Cells Are Highly Dynamic Surveillants of Brain Parenchyma in Vivo, *American Association for the Advancement of Science.* **308**: 1314-1318.
241. Norman AB, Thomas SR, Pratt RG, Lu SY and Norgren RB (1992). "Magnetic resonance imaging of neural transplants in rat brain using a superparamagnetic contrast agent." *Brain Res* **594** 279-83.
242. O Donoghue K and Chan J (2006). "Human Fetal Mesenchymal Stem Cells." *Curr Stem Cell Res Ther* **1** 371-86.
243. Oertel J, Samii M and Walter GF (2004). "Fetal allogeneic dopaminergic cell suspension grafts in the ventricular system of the rat: characterization of transplant morphology and graft-host interactions." *Acta Neuropathologica* **107** 421-427.
244. Olson JK and Miller SD (2004). "Microglia Initiate Central Nervous System Innate and Adaptive Immune Responses through Multiple TLRs 1." *The Journal of Immunology* **173** 3916-3924.
245. Orlic D, Kajstura J, Chimenti S, Bodine DM, Leri A and Anversa P (2003). "Bone marrow stem cells regenerate infarcted myocardium." *Pediatr Transplant* **7** 86-8.
246. Pakzaban P and Isacson O (1994). "Neural xenotransplantation: reconstruction of neuronal circuitry across species barriers." *Neuroscience* **62** 989-1001.
247. Pardoe H, Chua-anusorn W, St PT and Dobson J (2001). "Structural and magnetic properties of nanoscale iron oxide particles synthesized in the presence of dextran or polyvinyl alcohol." *Journal of Magnetism and Magnetic Materials* **225** 41-46.
248. Park C, Ma YD and Choi K (2005). "Evidence for the Hemangioblast." *Experimental Hematology* **33** 965-970.
-

-
249. Park J, An K, Hwang Y, Park JG, Noh HJ, Kim JY, Park JH, Hwang NM and Hyeon T (2004). "Ultra-large-scale syntheses of monodisperse nanocrystals." *Nat Mater* **3** 891-5.
250. Park J, Lee E, Hwang NM, Kang M, Kim SC, Hwang Y, Park JG, Noh HJ, Kim JY and Park JH (2005). "One-Nanometer-Scale Size-Controlled Synthesis of Monodisperse Magnetic Iron Oxide Nanoparticles." *Angew Chem Int Ed Engl* **44** 2872-2877.
251. Park SJ, Leslie RW, Huh S, Kagan H, Honscheid K, Burdette D, Chesi E, Lacasta C, Llosa G and Mikuz M (2007). "A prototype of very high-resolution small animal PET scanner using silicon pad detectors." *Nuclear Inst. and Methods in Physics Research, A* **570** 543-555.
252. Pawelczyk E, Arbab AS, Pandit S, Hu E and Frank JA (2006). "Expression of transferrin receptor and ferritin following ferumoxides-protamine sulfate labeling of cells: implications for cellular magnetic resonance imaging." *NMR Biomed* **19** 581-92.
253. Perry MM and Gilbert AB (1979). "Yolk transport in the ovarian follicle of the hen (*Gallus domesticus*): lipoprotein-like particles at the periphery of the oocyte in the rapid growth phase." *J Cell Sci* **39** 257-272.
254. Phinney DG and Prockop DJ (2007). "Concise review: mesenchymal stem/multipotent stromal cells: the state of transdifferentiation and modes of tissue repair-current views." *Stem Cells* **25** 2896-902.
255. Pintaske J, Muller-Bierl B and Schick F (2006). "Geometry and extension of signal voids in MR images induced by aggregations of magnetically labelled cells." *Phys Med Biol* **51** 4707-18.
256. Pittenger MF, Mackay AM, Beck SC, Jaiswal RK, Douglas R, Mosca JD, Moorman MA, Simonetti DW, Craig S and Marshak DR (1999). "Multilineage Potential of Adult Human Mesenchymal Stem Cells." *Science* **284** 143.
257. Polkinghorne JC (1989). Review of the Guidance on the Research Use of Fetuses and Fetal Material, Her Majesty's Stationary Office, London, U.K.
258. Ponte AL, Marais E, Gallay N, Langonne A, Delorme B, Herault O, Charbord P and Domenech J (2007). "The in vitro migration capacity of human bone marrow mesenchymal stem cells: comparison of chemokine and growth factor chemotactic activities." *Stem Cells* **25** 1737-45.
259. Posse S (1992). "Direct imaging of magnetic field gradients by group spin-echo selection." *Magn Reson Med* **25** 12-29.
260. Pratten MK and Lloyd JB (1986). "Pinocytosis and phagocytosis: the effect of size of a particulate substrate on its mode of capture by rat peritoneal macrophages cultured in vitro." *Biochim Biophys Acta* **881** 307-13.
261. Prockop DJ (2009). "Repair of Tissues by Adult Stem/Progenitor Cells (MSCs): Controversies, Myths, and Changing Paradigms." *Molecular Therapy* **17** 939-946.
262. Qiu B, Gao F, Walczak P, Zhang J, Kar S, Bulte JW and Yang X (2007). "In vivo MR imaging of bone marrow cells trafficking to atherosclerotic plaques." *J Magn Reson Imaging* **26** 339-43.
263. Ramirez LP and Landfester K (2003). "Magnetic polystyrene nanoparticles with a high magnetite content obtained by miniemulsion processes." *Macromolecular Chemistry and Physics* **204** 22-31.
264. Raynal I, Prigent P, Peyramaure S, Najid A, Rebuzzi C and Corot C (2004). "Macrophage endocytosis of superparamagnetic iron oxide nanoparticles: mechanisms and comparison of ferumoxides and ferumoxtran-10." *Invest Radiol* **39** 56-63.
-

-
265. Reimer P and Balzer T (2003). "Ferucarbotran (Resovist): a new clinically approved RES-specific contrast agent for contrast-enhanced MRI of the liver: properties, clinical development, and applications." *European Radiology* **13** 1266-1276.
266. Reimer P, Rummeny EJ, Daldrup HE, Balzer T, Tombach B, Berns T and Peters PE (1995). "Clinical results with Resovist: a phase 2 clinical trial." *Radiology* **195** 489-96.
267. Reimer P and Tombach B (1998). "Hepatic MRI with SPIO: detection and characterization of focal liver lesions." *Eur Radiol* **8** 1198-204.
268. Rejman J, Oberle V, Zuhorn IS and Hoekstra D (2004). "Size-dependent internalization of particles via the pathways of clathrin- and caveolae-mediated endocytosis." *Biochem J* **377** 159-69.
269. Reyes M, Dudek A, Jahagirdar B, Koodie L, Marker PH and Verfaillie CM (2002). "Origin of endothelial progenitors in human postnatal bone marrow." *J Clin Invest* **109** 337-46.
270. Reyes M, Lund T, Lenvik T, Aguiar D, Koodie L and Verfaillie CM (2001). "Purification and ex vivo expansion of postnatal human marrow mesodermal progenitor cells." *Blood* **98** 2615-25.
271. Ries C, Egea V, Karow M, Kolb H, Jochum M and Neth P (2007). "MMP-2, MT1-MMP, and TIMP-2 are essential for the invasive capacity of human mesenchymal stem cells: differential regulation by inflammatory cytokines." *Blood* **109** 4055-63.
272. Ringden O, Uzunel M, Rasmusson I, Remberger M, Sundberg B, Lonnie H, Marschall HU, Dlugosz A, Szakos A and Hassan Z (2006). "Mesenchymal stem cells for treatment of therapy-resistant graft-versus-host disease." *Transplantation* **81** 1390-7.
273. Ringe J, Strassburg S, Neumann K, Endres M, Notter M, Burmester GR, Kaps C and Sittlinger M (2007). "Towards in situ tissue repair: human mesenchymal stem cells express chemokine receptors CXCR1, CXCR2 and CCR2, and migrate upon stimulation with CXCL8 but not CCL2." *J Cell Biochem* **101** 135-46.
274. Rivera M, Talens-Visconti R, Jordan A, Sirera R, Sevilla B, Climent V, Rosello E, Paya R, Cortes R and Sancho-Tello MJ (2006). "Myocardial remodeling and immunologic activation in patients with heart failure." *Rev Esp Cardiol* **59** 911-8.
275. Roch A, Gossuin Y, Muller RN and Gillis P (2005). "Superparamagnetic colloid suspensions: Water magnetic relaxation and clustering." *Journal of Magnetism and Magnetic Materials* **293** 532-539.
276. Rogers WJ and Basu P (2005). "Factors regulating macrophage endocytosis of nanoparticles: implications for targeted magnetic resonance plaque imaging." *Atherosclerosis* **178** 67-73.
277. Rose A (1948). "The sensitivity performance of the human eye on an absolute scale." *J. Opt. Soc. Am* **38** 196-208.
278. Rosenzweig A (2006). "Cardiac Cell Therapy--Mixed Results from Mixed Cells." *New England Journal of Medicine* **355** 1274.
279. Roser M, Fischer D and Kissel T (1998). "Surface-modified biodegradable albumin nano- and microspheres. II: effect of surface charges on in vitro phagocytosis and biodistribution in rats." *European Journal of Pharmaceutics and Biopharmaceutics* **46** 255-263.
280. Rothberg KG, Heuser JE, Donzell WC, Ying YS, Glenney JR and Anderson RG (1992). "Caveolin, a protein component of caveolae membrane coats." *Cell* **68** 673-82.
-

-
281. Ruehm SG, Corot C, Vogt P, Kolb S and Debatin JF (2001). Magnetic Resonance Imaging of Atherosclerotic Plaque With Ultrasmall Superparamagnetic Particles of Iron Oxide in Hyperlipidemic Rabbits, *Am Heart Assoc.* **103**: 415-422.
 282. Ruster B, Gottig S, Ludwig RJ, Bistrrian R, Muller S, Seifried E, Gille J and Henschler R (2006). "Mesenchymal stem cells display coordinated rolling and adhesion behavior on endothelial cells." *Blood* **108** 3938-3944.
 283. Ryffel B, Mihatsch MJ and Fisher GL (1992). "Immunosuppression and cancer: the ciclosporin case." *Drug and chemical toxicology* **15** 95.
 284. Rzhaininova AA, Gornostaeva SN and Gol DV (2005). "Isolation and phenotypical characterization of mesenchymal stem cells from human fetal thymus." *Bulletin of Experimental Biology and Medicine* **139** 134-140.
 285. Sadan O, Shemesh N, Barzilay R, Bahat-Stromza M, Melamed E, Cohen Y and Offen D (2008). "Migration of neurotrophic factors-secreting mesenchymal stem cells towards a quinolinic acid lesion as viewed by MRI." *Stem Cells*.
 286. Saini S, Stark DD, Brady TJ, Wittenberg J and Ferrucci JJ (1986). "Dynamic spin-echo MRI of liver cancer using Gadolinium-DTPA: animal investigation." *AJR Am J Roentgenol* **147** 357-62.
 287. Saini S, Stark DD, Hahn PF, Wittenberg J, Brady TJ and Ferrucci JJ (1987). "Ferrite particles: a superparamagnetic MR contrast agent for the reticuloendothelial system." *Radiology* **162** 211-216.
 288. Saleh A, Schroeter M, Jonkmanns C, Hartung HP, Modder U and Jander S (2004). "In vivo MRI of brain inflammation in human ischaemic stroke." *Brain* **127** 1670.
 289. Santambrogio L, Belyanskaya SL, Fischer FR, Cipriani B, Brosnan CF, Ricciardi-Castagnoli P, Stern LJ, Strominger JL and Riese R (2001). "Developmental plasticity of CNS microglia." *Proceedings of the National Academy of Sciences* **98** 6295.
 290. Schachinger V, Erbs S, Elsasser A, Haberbosch W, Hambrecht R, Holschermann H, Yu J, Corti R, Mathey DG and Hamm CW (2006). "Intracoronary Bone Marrow-Derived Progenitor Cells in Acute Myocardial Infarction." *New England Journal of Medicine* **355** 1210.
 291. Schafer R, Kehlbach R, Wiskirchen J, Bantleon R, Pintaske J, Brehm BR, Gerber A, Wolburg H, Claussen CD and Northoff H (2007). "Transferrin Receptor Upregulation: In Vitro Labeling of Rat Mesenchymal Stem Cells with Superparamagnetic Iron Oxide." *Radiology* **244** 514-523.
 292. Schild HG (1993). "Thermal Degradation of Poly (Methacrylic Acid): Further Studies Applying TGA/FTIR." *Journal of Polymer Science, Polymer Chemistry(USA)* **31** 2403-2405.
 293. Schroeter M, Saleh A, Wiedermann D, Hoehn M and Jander S (2004). "Histochemical detection of ultrasmall superparamagnetic iron oxide (USPIO) contrast medium uptake in experimental brain ischemia." *Magn Reson Med* **52** 403-406.
 294. Seaton TA, Cooper JM and Schapira AH (1998). "Cyclosporin inhibition of apoptosis induced by mitochondrial complex I toxins." *Brain Research* **809** 12-17.
 295. Seppenwoolde JH, Viergever MA and Bakker CJ (2003). "Passive tracking exploiting local signal conservation: The white marker phenomenon." *Magnetic Resonance in Medicine* **50** 784-790.
 296. Serafini M, Dylla SJ, Oki M, Heremans Y, Tolar J, Jiang Y, Buckley SM, Pelacho B, Burns TC and Frommer S (2007). "Hematopoietic reconstitution by multipotent adult

- progenitor cells: precursors to long-term hematopoietic stem cells." *The Journal of Experimental Medicine* **204** 129.
297. Sharma R, Saini S, Ros PR, Hahn PF, Small WC, de LE, Stillman AE, Edelman RR, Runge VM and Outwater EK (1999). "Safety profile of ultrasmall superparamagnetic iron oxide ferumoxtran-10: phase II clinical trial data." *Journal of magnetic resonance imaging: JMRI* **9** 291.
298. Shen LH, Li Y, Chen J, Zacharek A, Gao Q, Kapke A, Lu M, Raginski K, Vanguri P and Smith A (2007). "Therapeutic benefit of bone marrow stromal cells administered 1 month after stroke." *Journal of Cerebral Blood Flow & Metabolism* **27** 6-13.
299. Shen LH, Li Y, Chen J, Zhang J, Vanguri P, Borneman J and Chopp M (2006). "Intracarotid transplantation of bone marrow stromal cells increases axon-myelin remodeling after stroke." *Neuroscience* **137** 393-9.
300. Shen T, Weissleder R, Papisov M, Bogdanov JA and Brady TJ (1993). "Monocrystalline iron oxide nanocompounds (MION): physicochemical properties." *Magn Reson Med* **29** 599-604.
301. Shukla R, Bansal V, Chaudhary M, Basu A, Bhonde RR and Sastry M (2005). "Biocompatibility of gold nanoparticles and their endocytotic fate inside the cellular compartment: a microscopic overview." *Langmuir* **21** 10644-10654.
302. Skuk D, Caron NJ, Goulet M, Roy B and Tremblay JP (2003). "Resetting the problem of cell death following muscle-derived cell transplantation: detection, dynamics and mechanisms." *J Neuropathol Exp Neurol* **62** 951-67.
303. Song M, Moon WK, Kim Y, Lim D, Song IC and Yoon BW (2007). "Labeling efficacy of superparamagnetic iron oxide nanoparticles to human neural stem cells: comparison of ferumoxides, monocrystalline iron oxide, cross-linked iron oxide (CLIO)-NH₂ and tat-CLIO." *Korean J Radiol* **8** 365-71.
304. Springer TA (1994). "Traffic signals for lymphocyte recirculation and leukocyte emigration: the multistep paradigm." *Cell* **76** 301.
305. Stearns RC, Paulauskis JD and Godleski JJ (2001). "Endocytosis of Ultrafine Particles by A549 Cells." *American Journal of Respiratory Cell and Molecular Biology* **24** 108-115.
306. Steingen C, Brenig F, Baumgartner L, Schmidt J, Schmidt A and Bloch W (2008). "Characterization of key mechanisms in transmigration and invasion of mesenchymal stem cells." *J Mol Cell Cardiol.*
307. Stroh A, Faber C, Neuberger T, Lorenz P, Sieland K, Jakob PM, Webb A, Pilgrimm H, Schober R and Pohl EE (2005). "In vivo detection limits of magnetically labeled embryonic stem cells in the rat brain using high-field (17.6 T) magnetic resonance imaging." *Neuroimage* **24** 635-645.
308. Stuber M, Gilson WD, Schar M, Kedziorek DA, Hofmann LV, Shah S, Vonken EJ, Bulte JW and Kraitchman DL (2007). "Positive contrast visualization of iron oxide-labeled stem cells using inversion-recovery with ON-resonant water suppression (IRON)." *Magn Reson Med* **58** 1072-7.
309. Stuckey DJ, Carr CA, Martin-Rendon E, Tyler DJ, Willmott C, Cassidy PJ, Hale SJ, Schneider JE, Tatton L and Harding SE (2006). "Iron Particles for Noninvasive Monitoring of Bone Marrow Stromal Cell Engraftment into, and Isolation of Viable Engrafted Donor Cells from, the Heart." *Stem Cells* **24** 1968-1975.
310. Swenson ES, Price JG, Brazelton T and Krause DS (2007). "Limitations of green fluorescent protein as a cell lineage marker." *Stem Cells* **25** 2593-600.

-
311. Tabata Y and Ikada Y (1988). "Effect of the size and surface charge of polymer microspheres on their phagocytosis by macrophage." *Biomaterials* **9** 356-362.
312. Takenaka S, Karg E, Kreyling W, Lentner B, M W, Behnke-Semmler M, Jennen L, Walch A, Michalke B and Schramel P (2006). "Distribution Pattern of Inhaled Ultrafine Gold Particles in the Rat Lung." *Inhalation Toxicology* **18** 733-740.
313. Tan BH, Tam KC, Lam YC and Tan CB (2004). "A semi-empirical approach for modeling charged soft microgel particles." *Journal of Rheology* **48** 915-926.
314. Tan BH, Tam KC, Lam YC and Tan CB (2005). "Osmotic compressibility of soft colloidal systems." *Langmuir: the ACS journal of surfaces and colloids* **21** 4283.
315. Tan BH, Tam KC, Lam YC and Tan CB (2004). "Dynamics and microstructure of charged soft nano-colloidal particles." *Polymer* **45** 5515-5523.
316. Tao K, Dou H and Sun K (2008). "Interfacial coprecipitation to prepare magnetite nanoparticles: Concentration and temperature dependence." *Colloids and Surfaces A: Physicochemical and Engineering Aspects* **320** 115-122.
317. Taupitz M, Schnorr J, Abramjuk C, Wagner S, Pilgrimm H, Hunigen H and Hamm B (2000). "New generation of monomer-stabilized very small superparamagnetic iron oxide particles (VSOP) as contrast medium for MR angiography: preclinical results in rats and rabbits." *J Magn Reson Imaging* **12** 905-11.
318. Terrovitis JV, Bulte JW, Sarvananthan S, Crowe LA, Sarathchandra P, Batten P, Sachlos E, Chester AH, Czernuszka JT and Firmin DN (2006). "Magnetic resonance imaging of ferumoxide-labeled mesenchymal stem cells seeded on collagen scaffolds-relevance to tissue engineering." *Tissue Eng* **12** 2765-75.
319. Testa AM, Foglia S, Suber L, Fiorani D, Casas L, Roig A, Molins E, Greneche JM and Tejada J (2001). "Unconventional magnetic behavior of iron-oxide nanoparticles in polymeric matrices." *Journal of Applied Physics* **90** 1534-1539.
320. Thompson WG (1890). "Successful brain grafting." *NY Med J* **51** 701-702.
321. Thomson JA, Itskovitz-Eldor J, Shapiro SS, Waknitz MA, Swiergiel JJ, Marshall VS and Jones JM (1998). "Embryonic stem cell lines derived from human blastocysts." *Science* **282** 1145-7.
322. Thorek DL and Tsourkas A (2008). "Size, charge and concentration dependent uptake of iron oxide particles by non-phagocytic cells." *Biomaterials* **29** 3583-3590.
323. Tokumitsu H, Ichikawa H and Fukumori Y (1999). "Chitosan-gadopentetic acid complex nanoparticles for gadolinium neutron-capture therapy of cancer: preparation by novel emulsion-droplet coalescence technique and characterization." *Pharm Res* **16** 1830-5.
324. Tsai MS, Lee JL, Chang YJ and Hwang SM (2004). "Isolation of human multipotent mesenchymal stem cells from second-trimester amniotic fluid using a novel two-stage culture protocol." *Human reproduction (Oxford, England)* **19** 1450.
325. Tse WT, Pendleton JD, Beyer WM, Egalka MC and Guinan EC (2003). "Suppression of allogeneic T-cell proliferation by human marrow stromal cells: implications in transplantation." *Transplantation* **75** 389.
326. Unfried K, Albrecht C, Klotz LO, Von MA, Grether-Beck S and Schins RP (2007). "Cellular responses to nanoparticles: Target structures and mechanisms." *Nanotoxicology* **1** 52 - 71.
327. Urist MR and McLean FC (1952). "Osteogenetic Potency And New-Bone Formation By Induction In Transplants To The Anterior Chamber Of The Eye." *The Journal of Bone and Joint Surgery* **34** 443.
-

-
328. van Dekken H, Hagenbeek A and Bauman JG (1989). "Detection of host cells following sex-mismatched bone marrow transplantation by fluorescent in situ hybridization with a Y-chromosome specific probe." *Leukemia* **3** 724-8.
329. van den Bos EJ, Baks T, Moelker AD, Kerver W, van GR, van GW, Duncker DJ and Wielopolski PA (2006). "Magnetic resonance imaging of haemorrhage within reperfused myocardial infarcts: possible interference with iron oxide-labelled cell tracking?" *Eur Heart J* **27** 1620-6.
330. van den Bos EJ, Wagner A, Mahrholdt H, Thompson RB, Morimoto Y, Sutton BS, Judd RM and Taylor DA (2003). "Improved efficacy of stem cell labeling for magnetic resonance imaging studies by the use of cationic liposomes." *Cell Transplant* **12** 743-56.
331. Van Den Heuvel R, Versele S, Schoeters G and J VO (1987). "Stromal stem cells (CFU-f) in yolk sac, liver, spleen and bone marrow of pre-and postnatal mice." *British Journal of Haematology* **66** 15-20.
332. von Bonin M, Stolzel F, Goedecke A, Richter K, Wuschek N, Holig K, Platzbecker U, Illmer T, Schaich M, Schetelig J, Kiani A, Ordemann R, Ehninger G, Schmitz M and Bornhauser M (2009). "Treatment of refractory acute GVHD with third-party MSC expanded in platelet lysate-containing medium." *Bone Marrow Transplant* **43** 245-251.
333. von Zur Muhlen C, von ED, Bassler N, Neudorfer I, Steitz B, Petri-Fink A, Hofmann H, Bode C and Peter K (2007). "Superparamagnetic iron oxide binding and uptake as imaged by magnetic resonance is mediated by the integrin receptor Mac-1 (CD11b/CD18): implications on imaging of atherosclerotic plaques." *Atherosclerosis* **193** 102-11.
334. Walczak P, Kedziorek DA, Gilad AA, Lin S and Bulte JW (2005). "Instant MR labeling of stem cells using magnetoelectroporation." *Magn Reson Med* **54** 769-774.
335. Walczak P, Zhang J, Gilad AA, Kedziorek DA, Ruiz-Cabello J, Young RG, Pittenger MF, van ZP, Huang J and Bulte JW (2008). "Dual-Modality Monitoring of Targeted Intraarterial Delivery of Mesenchymal Stem Cells After Transient Ischemia." *Stroke* **39** 1569.
336. Watson BD, Dietrich WD, Busto R, Wachtel MS and Ginsberg MD (1985). "Induction of reproducible brain infarction by photochemically initiated thrombosis." *Ann Neurol* **17** 497-504.
337. Weissleder R, Elizondo G, Wittenberg J, Lee AS, Josephson L and Brady TJ (1990). "Ultrasmall superparamagnetic iron oxide: an intravenous contrast agent for assessing lymph nodes with MR imaging." *Radiology* **175** 494-8.
338. Weissleder R, Moore A, Mahmood U, Bhorade R, Benveniste H, Chioocca EA and Basilion JP (2000). "In vivo magnetic resonance imaging of transgene expression." *Nature medicine* **6** 351.
339. Weissleder R, Wittenberg J, Rabito CA and Bengel HH (1990). "Ultrasmall Superparamagnetic Iron Oxide: Characterization of a New Class of Contrast Agents for MR Imaging." *Radiology* **175** 489-493.
340. Wennberg L, Czech KA, Larsson LC, Mirza B, Bennet W, Song Z and Widner H (2001). "Effects Of Immunosuppressive Treatment On Host Responses Against Intracerebral Porcine Neural Tissue Xenografts In Rats." *Transplantation* **71** 1797.
341. Wennersten A, Meier X, Holmin S, Wahlberg L and Mathiesen T (2004). "Proliferation, migration, and differentiation of human neural stem/progenitor cells after transplantation into a rat model of traumatic brain injury." *J Neurosurg* **100** 88-96.
-

-
342. Wiart M, Davoust N, Pialat JB, Desestret V, Moucharaffie S, Cho TH, Mutin M, Langlois JB, Beuf O and Honnorat J (2007). "MRI Monitoring of Neuroinflammation in Mouse Focal Ischemia." *Stroke* **38** 131.
343. Wilfinger WW, Mackey K and Chomeczynski P (1997). "Effect of pH and ionic strength on the spectrophotometric assessment of nucleic acid purity." *BioTechniques* **22** 474-481.
344. Wilhelm C, Billotey C, Roger J, Pons JN, Bacri JC and Gazeau F (2003). "Intracellular uptake of anionic superparamagnetic nanoparticles as a function of their surface coating." *Biomaterials* **24** 1001-1011.
345. Wilhelm C and Gazeau F (2008). "Universal cell labelling with anionic magnetic nanoparticles." *Biomaterials*.
346. Wislet-Gendebien S, Hans G, Leprince P, Rigo JM, Moonen G and Rogister B (2005). "Plasticity of Cultured Mesenchymal Stem Cells: Switch from Nestin-Positive to Excitable Neuron-Like Phenotype." *Stem Cells* **23** 392.
347. Wollert KC, Meyer GP, Lotz J, Ringes LS, Lippolt P, Breidenbach C, Fichtner S, Korte T, Hornig B, Messinger D, Arseniev L, Hertenstein B, Ganser A and Drexler H (2004). "Intracoronary autologous bone-marrow cell transfer after myocardial infarction: the BOOST randomised controlled clinical trial." *The Lancet* **364** 141-148.
348. Wu H, Pal D, O SJ and Tai YC (2008). "A Feasibility Study of a Prototype PET Insert Device to Convert a General-Purpose Animal PET Scanner to Higher Resolution." *J Nucl Med* **49** 79-87.
349. Yablonskiy DA and Haacke EM (1994). "Theory of NMR signal behavior in magnetically inhomogeneous tissues: the static dephasing regime." *Magn Reson Med* **32** 749-63.
350. Yamaguchi M, Calvert JW, Kusaka G and Zhang JH (2005). "One-stage anterior approach for four-vessel occlusion in rat." *Stroke; a journal of cerebral circulation* **36** 2212.
351. Yan J, Xu L, Welsh AM, Chen D, Hazel T, Johe K and Koliatsos VE (2006). "Combined immunosuppressive agents or CD4 antibodies prolong survival of human neural stem cell grafts and improve disease outcomes in amyotrophic lateral sclerosis transgenic mice." *Stem Cells* **24** 1976-85.
352. Yeh TC, Zhang W, Ildstad ST and Ho C (1993). "Intracellular labeling of T-cells with superparamagnetic contrast agents." *Magn Reson Med* **30** 617-25.
353. Yung KT (2003). "Empirical models of transverse relaxation for spherical magnetic perturbers." *Magn Reson Imaging* **21** 451-63.
354. Zhang X, Bowen CV, Gareau P and Rutt BK (2001). "Quantitative Analysis of SPIO and USPIO Uptake Rate by Macrophages: Effects of Particle Size, Concentration, and Labeling Time." **9** 880.
355. Zhang ZY, Teoh SH, Chong MS, Schantz JT, Fisk NM, Choolani MA and Chan J (2009). "Superior Osteogenic Capacity for Bone Tissue Engineering of Fetal Compared To Perinatal and Adult Mesenchymal Stem Cells." *Stem Cells* **27** 126 -137.
356. Zhao LR, Duan WM, Reyes M, Keene CD, Verfaillie CM and Low WC (2002). "Human bone marrow stem cells exhibit neural phenotypes and ameliorate neurological deficits after grafting into the ischemic brain of rats." *Exp Neurol* **174** 11-20.
357. Zhao P, Ise H, Hongo M, Ota M, Konishi I and Nikaido T (2005). "Human Amniotic Mesenchymal Cells Have Some Characteristics of Cardiomyocytes." *Transplantation* **79** 528.
-

358. Zhao Z, Liao L, Cao Y, Jiang X and Zhao RC (2005). "Establishment and properties of fetal dermis-derived mesenchymal stem cell lines: plasticity in vitro and hematopoietic protection in vivo." *Bone Marrow Transplantation* **36**.
359. Zhu J, Zhou L and XingWu FG (2006). "Tracking Neural Stem Cells in Patients with Brain Trauma." *New England Journal of Medicine* **355** 2376.
360. Ziener CH, Bauer WR and Jakob PM (2005). "Transverse relaxation of cells labeled with magnetic nanoparticles." *Magn Reson Med* **54** 702-706.
361. Zurkiya O and Hu X (2006). "Off-resonance saturation as a means of generating contrast with superparamagnetic nanoparticles." *Magn Reson Med* **56** 726-32.
362. Zurkiya O, Chan AWS and Hu X (2008). "MagA is sufficient for producing magnetic nanoparticles in mammalian cells, making it an MRI reporter." *Magnetic Resonance in Medicine* **59** 1225-1231.